

## Durham E-Theses

---

### *The Structure and Dynamics of Ions at Aqueous Interfaces Studied via Atomic Force Microscopy*

TREWBY, WILLIAM,JOHN

#### How to cite:

---

TREWBY, WILLIAM,JOHN (2019) *The Structure and Dynamics of Ions at Aqueous Interfaces Studied via Atomic Force Microscopy*, Durham theses, Durham University. Available at Durham E-Theses Online: <http://etheses.dur.ac.uk/13149/>

#### Use policy

---

The full-text may be used and/or reproduced, and given to third parties in any format or medium, without prior permission or charge, for personal research or study, educational, or not-for-profit purposes provided that:

- a full bibliographic reference is made to the original source
- a [link](#) is made to the metadata record in Durham E-Theses
- the full-text is not changed in any way

The full-text must not be sold in any format or medium without the formal permission of the copyright holders.

Please consult the [full Durham E-Theses policy](#) for further details.

DURHAM UNIVERSITY

---

**Structure and Dynamics of Ions at  
Aqueous Interfaces Studied *via* Atomic  
Force Microscopy**

---

*Author:*

William John Trewby

*Primary Supervisor:*

Dr. Kislou Voitchovsky

A thesis presented for the degree of  
*Doctor of Philosophy*



Centre for Materials Physics  
Department of Physics and Astronomy

Stockton Road  
Durham  
DH1 3LE

June 6, 2019



# ABSTRACT

The organisation and kinetics of charges at solid and soft interfaces play a central role in biological signalling processes and are vital for energy storage technologies as well as our understanding of heterogeneous catalysis. At the molecular-scale, such interfacial behaviour remains stubbornly difficult to characterise, due to the short-ranged interactions between ions, their aqueous solvent and surface groups. Thus, continuum-scale models quickly break down, especially close to the interface and with high charge densities.

This thesis addresses the question of ionic organisation using atomic force microscopy (AFM), which uniquely combines sub-nanometre spatial resolution and the ability to probe relatively long timescales. The use of small oscillation amplitudes allows the topography of the ionic layer to be mapped while simultaneously extracting physical properties from the sample or the interface itself, with time resolution spanning from tens of milliseconds to minutes.

The structure of ions at hydrophilic interfaces is shown to be delicately sensitive to the charges' molecular structure (in the case of larger buffering agents) and their charge density (for simple alkali cations). Specifically, the cations' interactions with a model lipid membrane and the waters around it lead to an attractive correlation energy which generates nanoscale networks that evolve over the course of many seconds. These ionic structures directly reduce the effective stiffness of the lipids, providing a mechanism for the spontaneous control of membranes' mechanical properties.

These ionic networks are significant in the case of confined fluids and provide an efficient means of lubrication even under high pressures in sub-nanometre gaps. When sheared, such fluid films are revealed to be non-Newtonian, with dynamics that depend on the velocity and lengthscale of the motion. The results highlight the greatly damped kinetics of ions and water molecules at interfaces, and shed light on the mechanisms behind their transport through and along biomolecules.



## ACKNOWLEDGEMENTS

First and foremost, my utmost thanks go to my supervisor Kislun Voitchovsky, without whom I wouldn't have been able to begin (or indeed complete) this journey. I am indebted to him for his guidance through the often murky worlds of soft matter and high-resolution AFM, especially in periods when questions were many and answers seemed few and far between. His enthusiastic and dedicated approach to research is contagious and has played a major role in shaping my own approach to biophysics. On top of this, his pastoral support and general advice proved invaluable (especially when it comes to choosing a good whisky).

Thanks must also go to my collaborators, both near and far. Jordi Faraudo provided the brilliant MD simulations that helped bring the bilayer cations to life, and my appreciation of cantilever dynamics was strengthened through my many chats with Amir Payam. I think everyone in the group – Ethan Miller, Will Foster, Miro Cafolla and Luca Piantanida – has had to endure my habit of wandering into offices and waffling about my experiments but to their credit, the response was always insightful help and advice (rather than the irritated huff that I probably deserved!). Our lab-siblings in the Staykova group have also received their fair share of my ramblings, and Liam Stubbington was always able to keep the spirits high in OC14.

The superconductive residents of 144B have put up with me for over four years now and deserve an acknowledgement for providing a warm, friendly environment that was not *too* judgemental about the softness of my research field. Frank Ridgeon especially deserves thanks; he was one of the first people I met at Durham and very quickly became a great friend. His enforcement of the 11:00 and 16:00 coffee break was important, both for research chat and general peace of mind. The formation of the Slack Squadron (with T-shirt designs for when fame hit) also deserves a mention. I'm grateful to all friends and colleagues across the department, especially those associated with Friday pub outings and the daily crossword (far too many to list – you know who you are), who have widened my perspectives and given me frequent reasons to laugh. I'll miss you all.

Thanks, of course, to my parents who have always supported me, giving me advice and

well-needed perspective when things were tough. The prospect of a roast dinner in Yorkshire at the end of the week always managed to rejuvenate my enthusiasm! I especially appreciated their continued determination to understand what I actually did, day-to-day.

Finally, a huge thank-you to Keecia, who has been there for me throughout my PhD, even more so during the crucial months of thesis-writing (when sometimes it would be with a glass of wine). Her patience and confidence in me has been rock-steady and has seen me through these years.

# DECLARATION

The work presented in this thesis has been developed under the supervision of Dr. Kislun Voitchovsky of the Department of Physics and Astronomy at Durham University. All text and figures are the work of the author, unless otherwise stated. The specific contributions of other researchers to the work presented is detailed in the next section. No part of this thesis has been presented for any other degree or qualification.

**Copyright © 2019** William J. Trewby

*The copyright of this thesis rests with the author. No quotation from it should be published without the author's prior written consent and information derived from it should be acknowledged.*



## CONTRIBUTIONS

- Section 2.4.3: A. F. Payam developed the equations used to calibrate the cantilevers' spring constants. All experiments and numerical analysis were performed by the author. The author, A. F. Payam and K. Voitchovsky subsequently contributed to writing "Determining the spring constant of arbitrarily shaped cantilevers in viscous environments".
- Section 3.1: the author carried out all experiments and analysis, with additional help from M.-C. Pope when performing the ellipsometry measurements (Fig. 3.7). The author and K. Voitchovsky wrote "Buffering agents modify the hydration landscape at charged interfaces".
- Section 3.2: A. F. Payam developed the equations used to evaluate the properties of the fluids. All experiments and numerical analysis were performed by the author. The author, A. F. Payam and K. Voitchovsky wrote "Simultaneous viscosity and density measurement of small volumes of liquids using a vibrating microcantilever" together.
- Section 4.1: M. Ricci and K. Voitchovsky performed the experiments regarding diffusion of  $\text{Rb}^+$ , the author performed those relating to the dynamic hydration layer (Fig. 4.4) and C. Cafolla performed those determining the AFM drift. The data was analysed using algorithms written by K. Voitchovsky and the paper "Direct observation of the dynamics of single metal ions at the interface with solids in aqueous solutions" was written by M. Ricci and K. Voitchovsky.
- Section 4.2: the author performed all experiments and numerical analysis. SEM imaging was carried out with the help of L. Bowen.
- Chapter 5: the author performed all experiments and numerical analysis apart from the molecular dynamics simulations of section 5.3.2, which were conducted by J. Faraudo.



## PUBLICATIONS

- **W. Trewby**, D. Livesey and K. Voitchovsky, “Buffering agents modify the hydration landscape at charged interfaces”, *Soft Matter*, **2016**, 12, 2642-2651. This work is shown in section 3.1.
- E. J. Miller, **W. Trewby**, A. Farokh Payam, L. Piantanida, C. Cafolla and K. Voitchovsky, “Sub-nanometer Resolution Imaging with Amplitude-modulation Atomic Force Microscopy in Liquid”, *J. Vis. Exp.*, **2016**, 1–10. This work forms part of section 2.3.
- M. Ricci, **W. Trewby**, C. Cafolla and K. Voitchovsky, “Direct observation of the dynamics of single metal ions at the interface with solids in aqueous solutions”, *Sci. Rep.*, **2017**, 7, 43234. This work forms part of section 4.1
- J. Sturala, M. K. Etherington, A. N. Bismillah, H. F. Higginbotham, **W. Trewby**, J. A. Aguilar, E. H. C. Bromley, A. J. Avestro, A. P. Monkman and P. R. McGonigal, “Excited-State Aromatic Interactions in the Aggregation-Induced Emission of Molecular Rotors”, *J. Am. Chem. Soc.*, **2017**, 139, 17882–17889.
- A. F. Payam, **W. Trewby** and K. Voitchovsky, “Simultaneous viscosity and density measurement of small volumes of liquids using a vibrating microcantilever” *Analyst*, **2017**, 142, 1492–1498. This work is discussed in section 3.2.
- A. F. Payam, **W. Trewby** and K. Voitchovsky, “Determining the spring constant of arbitrarily shaped cantilevers in viscous environments” *Appl. Phys. Lett.*, **2018**, 112, 083101. This work is discussed in section 2.4.
- **W. Trewby**, J. Faraudo and K. Voitchovsky, “Long-lived ionic nano-networks modulate the stiffness of lipid membranes”, *Nanoscale* [accepted]. This work forms the basis of chapter 5.



# CONTENTS

1. <i>Introduction</i> . . . . .	1
1.1 Ion-water interactions in bulk aqueous solutions . . . . .	2
1.2 Ions' altered behaviour at the interface with solid and soft matter . . . . .	5
1.2.1 Continuum influence of surfaces on ionic behaviour . . . . .	5
1.2.2 Breakdown of continuum approximations . . . . .	7
1.3 Solvated ions at solid-liquid interfaces: insights from the main techniques . . . . .	9
1.3.1 X-ray based techniques . . . . .	10
1.3.2 Non-linear optics techniques . . . . .	13
1.3.3 Molecular dynamics . . . . .	14
1.3.4 Force-based interfacial studies: the surface force balance . . . . .	16
1.3.5 Force-based interfacial studies: atomic force microscopy . . . . .	18
1.4 Dynamics of aqueous solutions of ions . . . . .	22
1.4.1 Short Timescale Dynamics . . . . .	22
1.4.2 Long Timescale Dynamics . . . . .	23
1.5 Conclusions . . . . .	26
2. <i>Dynamic AFM: techniques and cantilever calibration</i> . . . . .	35
2.1 Features, observables and modes of AFM operation . . . . .	35
2.1.1 Contact mode AFM . . . . .	36
2.1.2 Frequency modulation AFM . . . . .	37
2.1.3 Amplitude modulation AFM . . . . .	38
2.2 Approximating dynamic cantilever motion: harmonic oscillators and beyond . . . . .	40
2.2.1 Phase-contrast imaging; extracting mechanical and energetic properties with high lateral resolution . . . . .	41
2.2.2 Alternative descriptions of cantilever dynamics . . . . .	42
2.3 Approaches for obtaining high resolution in dynamic AFM . . . . .	44
2.3.1 Solvation forces and vertical resolution . . . . .	44
2.3.2 Anharmonic cantilever motion: the importance of small amplitudes . . . . .	46
2.4 Calibrating the flexural stiffness of AFM cantilevers . . . . .	47
2.4.1 The thermal method . . . . .	48

---

2.4.2	The Sader method . . . . .	50
2.4.3	A shape-independent method for calculating the cantilever stiffness . . . . .	51
2.5	Conclusions . . . . .	55
3.	<i>Dynamic AFM: example applications</i> . . . . .	63
3.1	Buffering agents at hydrophilic interfaces: a high resolution AFM study . . . . .	64
3.1.1	Buffer organisation on mesoscopic length scales . . . . .	66
3.1.2	Buffer organisation on molecular length scales . . . . .	67
3.1.3	Impact on biomimetic membranes . . . . .	70
3.1.4	Conclusions: buffers at hydrophilic interfaces . . . . .	74
3.1.5	Materials and methods: section 3.1 . . . . .	74
3.2	Viscometry and density sensing of fluids using a vibrating lever . . . . .	77
3.2.1	Development of analytic equations for viscosity and density . . . . .	78
3.2.2	Experimental verification of the method . . . . .	79
3.2.3	Conclusions: dynamic cantilevers as viscometers . . . . .	84
4.	<i>Diffusion, friction and viscoelasticity of ions at solid-liquid interfaces</i> . . . . .	89
4.1	Lateral diffusion of individual $\text{Rb}^+$ ions within the Stern layer . . . . .	90
4.1.1	Residence timescale of adsorbed rubidium . . . . .	92
4.1.2	Dynamic hydration behaviour at the mica surface . . . . .	96
4.2	Confined electrolytes: scale-dependent friction and viscoelasticity . . . . .	99
4.2.1	Friction: origins and models . . . . .	100
4.2.2	Dynamic response of confined ultrapure water and 150 mM KCl . . . . .	105
4.2.3	Stern layer structure and fluidity: $\text{K}^+$ concentration and lengthscale dependence . . . . .	110
4.2.4	Impact of finite tip size . . . . .	114
4.2.5	Nanoconfinement against amorphous interfaces . . . . .	119
4.2.6	Frequency- and velocity-dependence of dynamic behaviour . . . . .	122
4.3	Conclusions . . . . .	130
4.4	Materials and methods: chapter 4 . . . . .	131
4.4.1	Sample preparation . . . . .	131
4.4.2	Time-resolved AM-AFM Imaging (section 4.1) . . . . .	131
4.4.3	Shear-force spectroscopy . . . . .	133
5.	<i>Ionic impact upon biomimetic membranes</i> . . . . .	145
5.1	Coordination of ions at lipid headgroups . . . . .	146
5.2	Global interactions of alkali cations with DPPA; electrophoresis and continuum models . . . . .	148
5.2.1	Vesicle $\zeta$ -potential and charge density in electrolyte solutions . . . . .	148

---

5.2.2	Calculation of cation binding constants . . . . .	149
5.3	Molecular-scale structure and dynamics of ions around lipids . . . . .	152
5.3.1	Small amplitude AFM imaging and spectroscopy of DPPA-electrolyte interface . . . . .	153
5.3.2	Molecular dynamics simulations . . . . .	158
5.3.3	Time-resolved evolution of ionic domains . . . . .	162
5.4	Mechanical perturbation of membranes by ions . . . . .	165
5.4.1	Extraction of bilayer mechanical parameters with AFM . . . . .	165
5.5	Conclusions . . . . .	172
5.6	Materials and methods: chapter 5 . . . . .	173
5.6.1	Sample preparation . . . . .	173
5.6.2	Electrophoresis . . . . .	176
5.6.3	AFM imaging and spectroscopy . . . . .	176
5.6.4	Image analysis . . . . .	177
6.	<i>Summary and Conclusions</i> . . . . .	187
7.	<i>Outlook and Further Work</i> . . . . .	189



# 1.0 INTRODUCTION

Solvated ions are truly abundant in the natural world; it is impossible to find aqueous systems that do not contain some form of mobile charges. The oceans – and the biological organisms that evolved from them – tend to contain monovalent ions at concentrations of hundreds of millimolar, and even nominally pure water will contain dissociating protons and hydroxide ions. As such, it is vital to understand the behaviour and interactions of these ions, not just with themselves, but also with the surrounding waters and interfaces at the edge of the fluid phase. These interfacial systems are staggeringly common, from the boundary between the Earth’s mineral crust and the sea, to the sub-nanometre channel of a transmembrane protein. They present altered symmetry, electrostatics and chemistry compared with the bulk, which can dramatically influence the ions’ dynamics, solvation behaviour and general organisation, providing fertile ground for research in molecular biology, battery and energy storage technologies and the earth sciences to name just a few.

This chapter will review our current understanding of how ions interact with water, both in bulk and at the interface, especially highlighting the limits of modern theory and experiments. Firstly, the molecular-level interactions of water with ions will be briefly introduced, along with properties that depend on the species of ion in solution. These properties can be loosely categorised through the so-called Hofmeister series, which was originally conceived to rank ions based on their ability to disrupt protein hydration shells, and shall be reviewed in greater detail. We shall then discuss the perturbations induced by solid surfaces on ionic distributions, the continuum-level theories devised to describe them and the limits of their applicability. Over the past few decades, many experimental techniques have been developed that can probe the molecular-level structure of the electrolyte and thus illuminate the gaps in current theoretical understanding. These will be reviewed, with particular focus on state-of-the-art developments in atomic force microscopy that allow direct characterisation of ionic behaviour with unprecedented spatial resolution. Finally, the (often conflicting) dynamic picture of interfacial fluid as measured by different techniques will be presented, highlighting current discrepancies in the literature and how atomic force microscopy (AFM) is well-poised to explore aspects that remain challenging to address through other approaches.

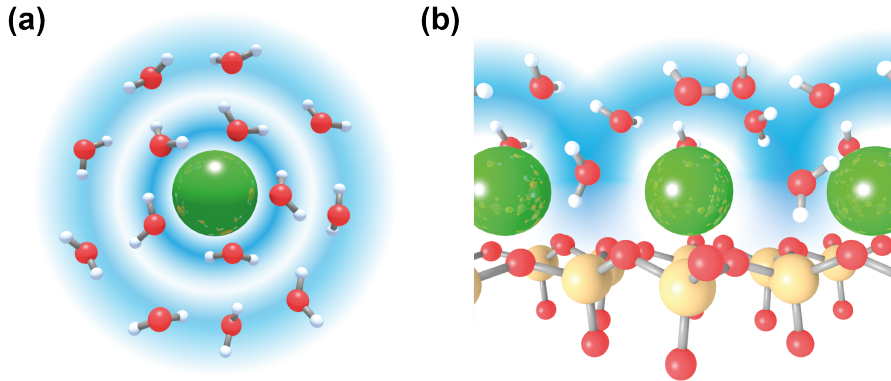


*Fig. 1.1:* Schematic illustrating the altered symmetry and density of water molecules around dissolved cations (green). (a) A cation in bulk water: the waters’ oxygens (red beads) are more likely to orient towards the positive charge and can form as many as two solvation shells (blue gradient) that are distinguishable from bulk  $\text{H}_2\text{O}$ . (b) Cations adsorbed into a cavity in a crystalline solid. The interface breaks the spherical symmetry of (a), and the solvation shells are affected by both the ions and the crystal’s periodicity.

## 1.1 Ion-water interactions in bulk aqueous solutions

Many of water’s physical and chemical properties derive from its polar nature – the characteristic angle and separation between its two hydrogens and central oxygen atom define a permanent dipole, which is strongly sensitive to nearby electric fields. Thus the inclusion of charged ions in liquid water dramatically affects both its bulk and molecular-level properties; oxygens re-orientate towards cations and hydrogens prefer to point towards anions. This leads to the concept of a hydration/solvation shell – the spherical lattice of water molecules surrounding an ion that is in some manner distinct from bulk water (illustrated schematically in Fig. 1.1(a)). That the dissolved ions induce a variation in the *macroscopic* properties of water such as its viscosity [1] and air-fluid surface tension [2] has indeed been known for over eighty years, but there continues to be fierce debate over the molecular-level structural and dynamical changes that occur [3–5].

Historically, much has been made of ions’ ability to alter the native structure of pure water. Ions were typically placed into one of two categories, depending on their capacity to either increase the organisation of bulk water (“structure-making”) or disrupt it (“structure-breaking”). Examples of the former category often included relatively small ( $\text{Na}^+$ ,  $\text{F}^-$ ) or highly charged ( $\text{Mg}^{2+}$ ) ions that increase water’s rotational correlation time [4], decrease its exchange rate between hydration shell and bulk [3] or bind it so strongly that it cannot be externally polarized [6]. Conversely, bulkier ions with lower charge-densities (e.g.  $\text{Rb}^+$ ,  $\text{NH}_4^+$ ) are usually defined as being structure-breaking as they can enhance the self-diffusion of water [3], leading to a more disordered liquid. This

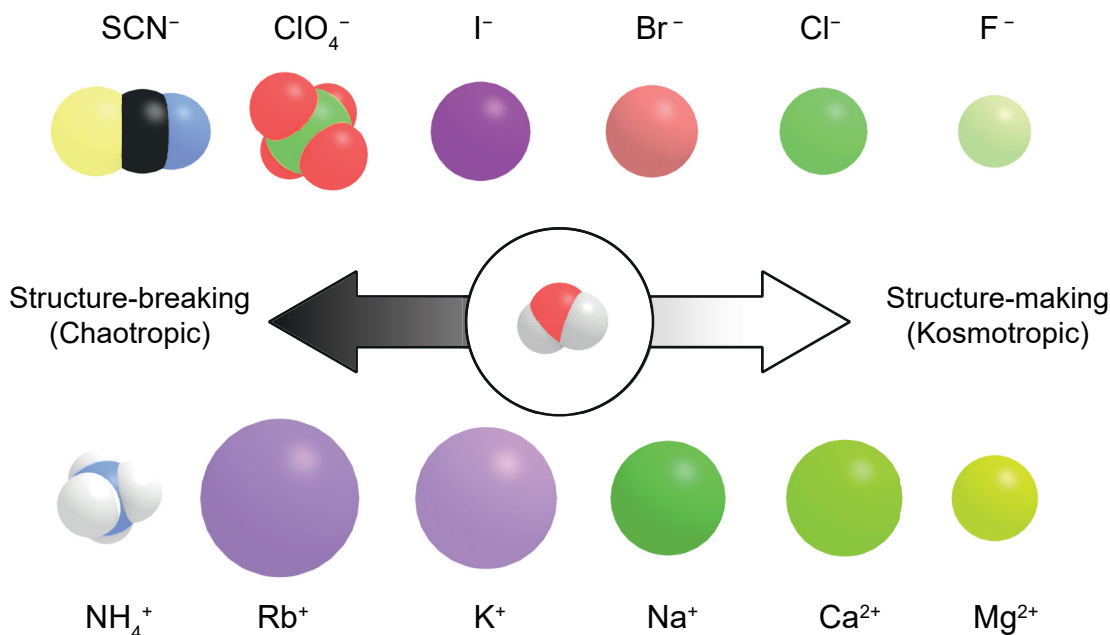


Fig. 1.2: Partial representation of the Hofmeister series for anions (upper) and cations (lower). Ions and water molecule (centre) are shown approximately to scale, with atoms represented by their neutral van der Waals radii. The series reflects the fact that smaller ions with large charge densities tend to structure nearby waters to a greater extent than their larger, weakly charged relatives.

method of characterising ions is often discussed in the context of the so-called Hofmeister Series [7, 8] (Fig. 1.2), which originally was a ranking of cations and anions based on their ability to stabilise proteins (egg globulin) in solution. The solubility of an amphiphilic protein is dependent upon the access its surface has to water, and it was therefore postulated that certain ions caused precipitation by “robbing” them of water, which is intrinsically related to the extent of a hydration of a charge. Since its discovery in the late 19<sup>th</sup> century, the series has been observed in many diverse scenarios, including colloidal mobility, lipid hydration and binding and air-water surface tension. The ubiquity of Hofmeister effects in aqueous systems comes from the fact that the dominant interactions are either ion-ion or water-ion [9], which allows many subtleties of the surface (protein, air, crystal etc.) to be simplified. The precise hydration of an ion, and the implications for its surface affinity and dynamic behaviour at the interface will be explored in greater depth in section 1.3 and 1.4.

Perhaps due to its enticing simplicity, the Hofmeister classification of ions by their effect on the organisation of water has endured, and the description of structure-maker/breaker is commonplace in the literature. As is often the case however, aqueous solutions of ions are too complex to allow such a straightforward classification; structural effects are

strongly concentration-dependent (with studies frequently investigating near the salt's saturation limit [3]); their long-range effect on water is highly contentious [10–13] and non-linear, cooperative behaviour between anions and cations is often exhibited [14, 15]. Further, the series can often be observed in different orders (either reversed or partially reversed) depending on the pH, polarity and charge of the surface [16, 17], resulting in a rather under-defined picture of the series. The long-lived nature of this debate is due, in part, to different sensitivities in the experimental and computational techniques used to probe it. For example, nuclear magnetic resonance (NMR) and X-ray and neutron scattering tend to probe timescales on the order of nanoseconds to microseconds (essentially static relative to the exchange time of waters between hydration shells and their bulk [5]). The use of terahertz-frequency radiation and femtosecond pump-probe spectroscopy [14] conversely, can achieve the picosecond time resolution necessary to study the dynamics of water around ions. However, their interrogation of contrasting aspects of water (or semi-heavy water, HDO<sup>1</sup>) – the permanent dipole direction and O–H stretch, respectively – render comparison with other techniques troublesome. Even molecular dynamics (MD) simulations resist quantitative comparison with other techniques due to ambiguous definitions of hydration shells, the simplicity of the chosen interaction model [5] and the challenge of including grand canonical variables such as pH and electric potentials [18].

This being said, there are general features of water's behaviour when interacting with ions that have become well-accepted over time and will be of further interest when discussing interfaces in section 1.3. These include observations made from X-ray diffraction that, for a given charge and geometry, the average distance between a metal ion,  $M$ , and the water oxygens in its first hydration shell,  $r_{M-O}$ , increases with its size due to straightforward steric hindrance. This is especially significant for the the alkali-halides; their single charge means their electrostatic perturbation of water, which decays rapidly as  $R^{-4}$  when interacting with a freely-rotating dipole [11, 19], is very sensitive to  $r_{M-O}$ . In the case of alkali cations,  $r_{M-O}$  increases monotonically from  $\sim 190$  pm for  $\text{Li}^+$  to 295 – 315 pm for  $\text{Cs}^+$  (with typical accuracies in the tens of pm [4]). As well as the inclusion of salts altering the time-averaged structure of  $\text{H}_2\text{O}$ , its *dynamics* are accepted to be distinct from that of neat water. Thus, polarizability [20], residence times [5], occurrence of “slow” waters [14] and self-diffusion coefficient of water [21] are all distinct from neat water and ion-dependent.

---

<sup>1</sup> Studies that probe vibrational modes of water molecules are often forced to use dilute mixtures of HDO in heavy water ( $\text{D}_2\text{O}$ ) to ensure that only a single O–H bond per molecule is excited, thereby avoiding resonant transfer between both O–H bonds of  $\text{H}_2\text{O}$ .

## 1.2 Ions' altered behaviour at the interface with solid and soft matter

As illustrated in Fig. 1.1(b), an interface between the fluid phase and a solid or soft surface distorts the spherical symmetry of simple ions and their solvation shells. The precise effect of the surface depends on the ion's size and charge as above, but also on the chemistry and periodicity of the molecules making up the interfacial region [18]. This is typically discussed in terms of hydrophilicity and hydrophobicity – i.e. the affinity of water for a particular molecule or material. It becomes especially important when discussing the structuring of ions against surfaces [16, 22], as H<sub>2</sub>O will compete with ions for access to surface sites, and the interplay between electrostatics and water's affinity is a strong determiner of interfacial behaviour. Before exploring this concept further in section 1.3, it is necessary to discuss the continuum-level descriptions of how charged surfaces affect the distribution of ions in solution. These models are in fact remarkably successful and only begin to break down within a few nanometres of the surface, where molecular-level effects become readily apparent.

### 1.2.1 Continuum influence of surfaces on ionic behaviour

#### *Poisson-Boltzmann theory and the Grahame equation*

The vast majority of solids when immersed in water will develop a charge, regardless of whether they are electrostatically neutral in a vacuum, due to the dissociation of surface groups or interaction with protons/hydroxyl ions from the fluid phase. Thus an electrostatic perturbation of the bulk liquid is generated perpendicular to the plane of the interface. Although the neat water screens the electric fields to some extent, ions with the same charge sign as the surface (coions) will be repelled into the bulk, while those with the opposite sign (counterions) will be attracted to the surface. The extent of this depletion or enhancement in ion density,  $\rho(z)$ , and its dependence on the separation from the surface,  $z$ , can be readily modeled by assuming the charges have negligible volume and are dissolved in a continuous solvent that they do not perturb. Clearly neither of these assumptions is strictly valid, but they enable a powerful framework to be developed, from which the molecular-level effects of ions at interfaces can be then discussed.

The ionic density is first assumed to have a Boltzmann distribution that depends on the electric potential at that point,  $\psi(z)$ , such that  $\rho(z) = \rho_\infty \exp(-Ze\psi(z)/k_B T)$ . Here,  $\rho_\infty$  is the bulk ionic density,  $Z$  is the ion's valency,  $e$  is the fundamental unit of electric charge,  $k_B$  is the Boltzmann constant and  $T$  is the absolute temperature. This can be

then combined with the one-dimensional Poisson equation,  $d^2\psi(z)/dz^2 = -Ze\rho/\varepsilon_0\varepsilon$ , to give the so-called Poisson-Boltzmann equation:

$$\frac{d^2\psi(z)}{dz^2} = -\frac{Ze\rho_\infty}{\varepsilon_0\varepsilon} \exp\left(-\frac{Ze\psi(z)}{k_B T}\right). \quad (1.1)$$

The relative dielectric permittivity of the fluid and that of free space are given by  $\varepsilon$  and  $\varepsilon_0$  respectively, and emphasize that this theory relies on the treatment of the solvent as continuous, with no ion-solvent interactions. Next, by integrating the ionic charge density from the surface to the bulk solution where, by electroneutrality, the potential is assumed to decay to zero, the density of ions can be related to the surface charge density,  $\sigma$ , by  $\sum_i \rho_{0,i} = \sum_i \rho_{\infty,i} + \sigma^2/2\varepsilon_0\varepsilon k_B T$ , where the summation is over each species of ion,  $i$ , in solution. Finally, by rearranging this and using the Boltzmann expression above, a relationship between the surface charge density and surface potential can be arrived at, known as the Grahame equation [19]. It is illustrated here for monovalent, symmetric ions:

$$\sigma = \sqrt{8\varepsilon_0\varepsilon\rho_\infty k_B T} \sinh\left(\frac{e\psi_0}{2k_B T}\right) \approx \varepsilon_0\varepsilon\kappa\psi_0. \quad (1.2)$$

The similarity is valid for small (25 mV) surface potentials,  $\psi_0$ , such that  $(e\psi_0/2k_B T) \ll 1$ . The constant  $\kappa^{-1}$  is known as the Debye length and satisfies

$$\kappa^2 = \sum_i \frac{\rho_{\infty,i}(Z_i e)^2}{\varepsilon_0\varepsilon k_B T}. \quad (1.3)$$

In the Grahame equation, we have a straightforward way of estimating the charge density at a surface, knowing just the potential produced by it and the bulk density and valency of ions in solution. The low-potential result of equation 1.2 is also physically intuitive; the surface charge is directly proportional to the potential in the same manner as a parallel-plate capacitor of separation  $\kappa^{-1}$  and with plate charge densities  $\pm\sigma$ . The potential's rate of decay in the bulk fluid can be found from combining the Boltzmann distribution of ions with the gradient  $d\psi(x)/dz$  from equation 1.1 to give [19]:

$$\psi(z) = \frac{2k_B T}{e} \ln \left[ \frac{1 + \gamma e^{-\kappa z}}{1 - \gamma e^{-\kappa z}} \right], \quad (1.4)$$

with the definition  $\gamma \equiv \tanh(e\psi_0/4k_B T)$ . The behaviour predicted by these equations is highlighted in Fig. 1.3 for a 50 mM solution of symmetric, monovalent ions (e.g. NaCl) and surface charge density  $\sigma = -0.0621 \text{ C m}^{-2}$ , for which the Debye length,  $\kappa^{-1} = 1.36 \text{ nm}$ . It's clear that the presence of a charged surface (here equivalent to  $\sim 0.39 \text{ e/nm}^2$ ) induces an order of magnitude enhancement in counterion concentration close to the surface and subsequent reduction in coion density.

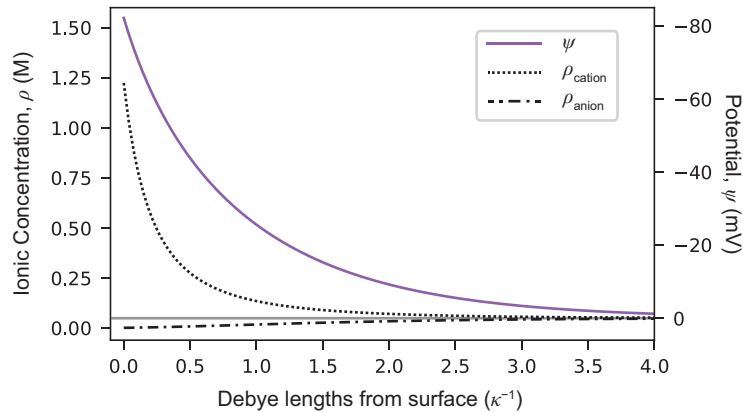


Fig. 1.3: The potential decay (purple) away from surface of charge density  $\sigma = -0.0621 \text{ C m}^{-2}$  in a monovalent ionic solution of bulk concentration 50 mM according to equation 1.2 and 1.4. The effect on the cation and anion densities (dashed and dash-dotted lines) is also shown and compared to the bulk value (grey horizontal bar).

It can be seen that, despite the potential dropping off much less rapidly than the ion density ( $\psi(z) \propto \exp(-\kappa z)$ ), bulk conditions of  $\rho$  and  $\psi$  are reached already by  $4\kappa^{-1} \sim 5.44 \text{ nm}$ . Hence in these conditions of moderate ionic strength, there is very little long-range perturbation of the bulk fluid, but for  $\sim$  millimolar concentrations and below, the interface's influence will extend many tens of nanometres into the fluid.

### 1.2.2 Breakdown of continuum approximations

The results above are referred to as Gouy-Chapman theory, and describe very well the ionic distribution in the vicinity of a charged surface, especially its capacitance [23]. Even next to biological membranes, ions have been shown to obey this distribution at separations of above 2 nm [24]. However, at distances smaller than a nanometre, Gouy-Chapman theory becomes increasingly invalid. This is because these lengthscales are comparable to those of the ions and the solvent molecules themselves, and specific surface details become increasingly dominant [22]. For example, Fig. 1.3 shows that, for  $z \leq 0.4 \text{ nm}$  ( $\sim 0.3 \kappa^{-1}$ ),  $\rho_{\text{cation}}$  smoothly increases up to 1.22 M, despite this surface separation being smaller than a hydrated ion. Thus, any meaningful interpretation of  $\rho_{\text{cation}}$  at this scale is rendered unlikely.

The Poisson-Boltzmann approach gives no way to encode the plane of closest approach of ions, never mind accounting for their different effective radii or hydration levels that were discussed in section 1.1. These become increasingly significant as the surface charge and bulk ion concentration increase; for the case of  $\sigma = -100 \text{ mV}$  and  $\rho_{\infty} = 150 \text{ mM}$ , the predicted distance between adsorbed ions is  $< 1 \text{ nm}$ , meaning that specific molecular effects and non-Coulombic interactions can no longer be ignored. Further problems are encountered when there are two interfaces in close proximity – i.e. in the case of strongly

confined ionic solutions. Here, when the surfaces' double layers overlap, an extra electrostatic pressure is generated that may force ions to condense from solution onto the surface [25]. These act like reversible chemical reactions [26] and can change the sign of the attractive/repulsive forces between surfaces [27], as well alter the interfacial fluid's dynamics [28]. This be discussed in much greater depth in chapter 4, where we will probe the viscoelastic properties of strongly-confined electrolytes, as well as their impact on the friction between two surfaces. Finally, implicit in Fig. 1.3 is that there is only variation in  $\psi$  and  $\rho_{\text{ion}}$  *perpendicular* to the surface. While this may be an acceptable approximation many Debye lengths from the solid where the charge can be treated as smeared-out, chemical heterogeneities [16] and ion-ion correlations [29] induce in-plane variations in  $\rho_{\text{ion}}$  that do not fit such a continuous model.

Many of these problems can be addressed with a simple, semi-empirical extension of the Gouy-Chapman theory by introducing a static layer of adsorbed ions between the solid and the electrolyte, named the Stern layer. In the simplest description of the Stern layer, there is just one layer of adsorbed counterions that specifically adsorb onto the solid. The centres of these ions, at  $z = \delta$ , represents the plane of closest approach, after which the potential decays according to equation 1.4, but with a modified contact potential,  $\psi_\delta$ , used instead of  $\psi_0$ . More complex Stern layer models allow for indirectly adsorbed ions that retain their hydration shell (Fig. 1.4) and adsorb at a larger separation,  $\delta'$  but are similar in principle. Stern models typically assume that adsorbed ion layers act as capacitors (of capacitance  $C_{\text{St}}$ ) in series with that of the Gouy-Chapman distribution of ions ( $C_{\text{GC}}$ ).

Together, the Stern layer and the diffuse layer of ions are known as the electric double layer (EDL). Conceptually, the EDL provides a useful framework from which to begin investigating the structure and dynamics of ions at charged interfaces, and is invaluable in the description of e.g. electrokinetic phenomena [30–33], but there remains the problem of the EDL essentially being a one-dimensional model, which pays no attention to the in-plane dynamics or correlations of ions. This severely restricts discussion of more dynamic interfacial processes such as charge regulation or competition with  $\text{OH}^-/\text{H}^+$  for binding sites [25, 34]. Further, despite the acknowledgment of ions binding indirectly via their hydration shells, there is still no explicit treatment of the solvent in EDL models, which limits their ability to describe the underlying molecular drivers for interfacial charge phenomena.

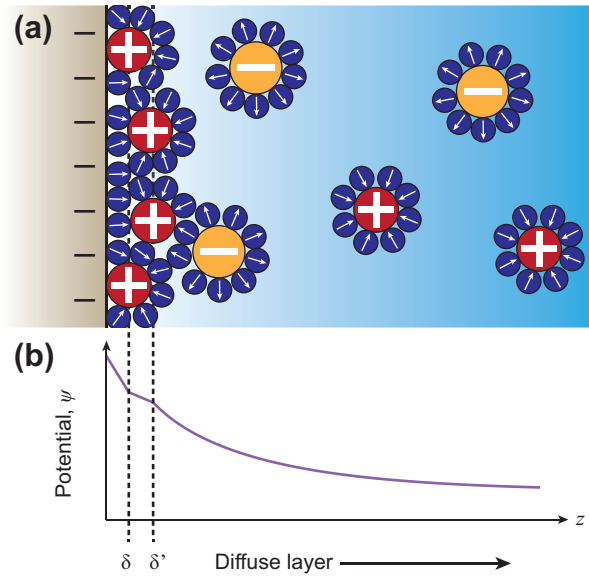


Fig. 1.4: The introduction of a Stern layer to a model negative interface and its impact on the potential decay. (a) The centres of specifically adsorbed counterions (red) define the plane at  $\delta$ , but in more complex models, ions can also adsorb indirectly *via* a water molecule (blue, dipole moment indicated by arrows), defined by a second plane,  $\delta'$ . (b) These planes alter the rate of decay of potential in the same way as parallel-plate capacitors – i.e. with a linear region of  $\psi(z)$ . Figure partially adapted from ref. [23]

### 1.3 Solvated ions at solid-liquid interfaces: insights from the main techniques

In this section, we will move away from theoretical, continuum approaches to studying the behaviour of electrolytes, and focus more on experimental techniques that do not rely so heavily on approximations which become increasingly invalid at the fluid's edge. Techniques with single molecule/ion resolution normal to the surface (i.e.  $z$  in Fig. 1.4), but requiring in-plane averaging, will initially be discussed. Such methods usually involve scattering or adsorption of radiation, and are extremely powerful as they describe equilibrium interfacial structure with long time averages and statistics built up over at least hundreds of square microns of the interface. Following this, the insight gained from more “local” techniques will be addressed. This includes *in silico* simulations, which offer microscopic analyses of the Stern layer, and also ground-breaking atomic force microscopy (AFM) developments that allow Ångström-scale lateral resolution while probing timescales orders of magnitude greater than the computational methods. Throughout this section, we shall see that these methods reveal that the molecular characteristics of the surface and the influence they have on interfacial fluid must be considered to build up a realistic picture of the interface. The effect of the interface's chemical make-up, geometry and physical properties such as stiffness on the structure of the fluids and ions will be especially highlighted.

### 1.3.1 X-ray based techniques

We first focus on the use of X-ray reflectivity (XR) to analyse the structure of aqueous electrolytes at solid interfaces. X-rays are powerful tools in this context, as they are able to penetrate millimetres of fluid and have sub-nanometre resolution normal to the surface, with atomic specificity in some cases [35]. A large portion of the progress in this field begins with the work of Cheng *et al.* [36], which unveiled the structure of pure water in ambient conditions at the surface of muscovite mica (a hydrophilic, atomically flat aluminosilicate). The authors used synchrotron radiation to probe the oxygen distribution in the first  $\sim 10$  Å above the mica. While an interfacial model with which to fit the data is still required (solid line in Fig. 1.5(a)), it was found that simplistic, structure-less or oscillatory profiles could not satisfactorily describe the system. Instead, three components of the oxygen distribution were required; a strongly adsorbed molecular film of water, a “hydration” layer, and finally density oscillations close to the bulk fluid (shown in Fig. 1.5(b)). It was found that one  $\text{H}_2\text{O}$  or  $\text{H}_3\text{O}^+$  molecule adsorbed per ditrigonal cavity of mica and hydrogen bonded with the layer above it, with both layers having a density approximately double that of bulk water. Similar results were found by X-ray scattering on calcite ( $\text{CaCO}_3$ ) [37]. These revealed the presence of two independently adsorbed water species that were vertically and laterally distinct, as well as significant surface reconstruction of interfacial  $\text{Ca}^{2+}$  and  $\text{CO}_3^{2-}$ . Thus, the presence of a non-trivial interfacial structure was found at ambient pressures that could not be adequately described without acknowledging both the solid’s structure and the solvent’s propensity for H-bonding.

Since then, there have been a plethora of reflectivity studies that have aimed to further reveal the breakdown of continuum theories at the solid-liquid interface, especially in the case of ionic distributions [38–40]. Resonant anomalous X-ray reflectivity (RAXR), which scans X-ray energy for a given momentum transfer,  $\underline{q}$ , allows the interrogation of individual ion species independently from the hydration structure. It was found that  $\text{Rb}^+$  ions in solution adsorb and disrupt the native hydration structure of mica and do so by losing part of their hydration shell (so-called “inner-sphere” configuration; equivalent to ions adsorbed at  $\delta$  in Fig. 1.4).  $\text{Sr}^{2+}$  ions can, in addition to this, adsorb without losing any waters (“outer-sphere”). This behaviour of divalent ions – the formation of two adsorption states with similar occupancies – seemingly contradicts strontium’s relatively high energy of hydration ( $\sim -1445$  kJ mol $^{-1}$ ) and implies the existence of more complex interfacial phenomena, such as a dramatic drop in water’s dielectric permittivity near the solid [41–43]<sup>2</sup>.

<sup>2</sup> In fact, this dielectric drop can be described in an identical manner to Stern’s strongly-adsorbed layer of counterions (see Fig. 1.4), but in this case, the drop reflects the interfacial water’s reduced rotational degrees of freedom, rather than the surface charge being counterbalanced by ions.

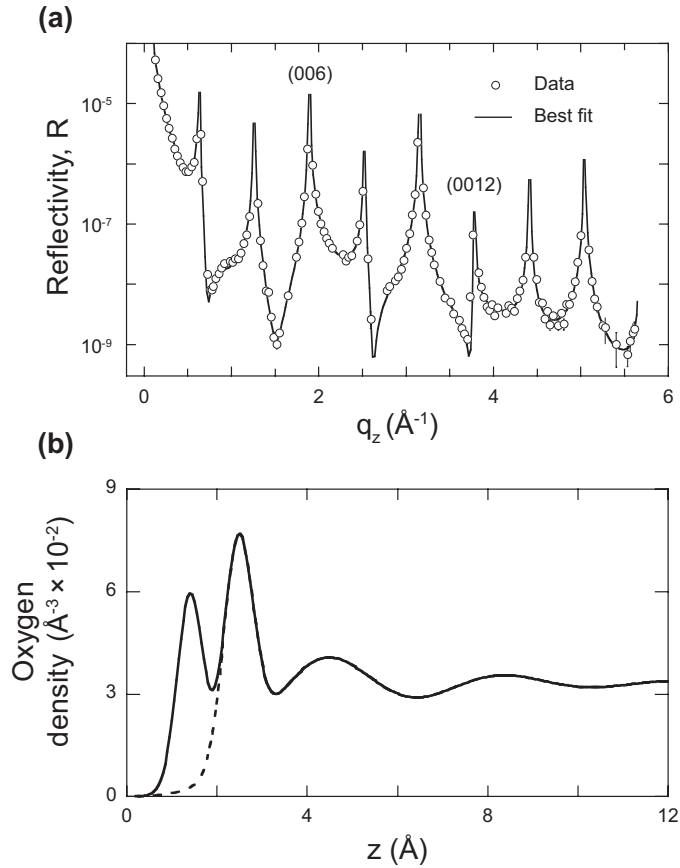


Fig. 1.5: X-ray reflectivity (XR) allows the electron density in the first few Ångströms above solid surfaces to be probed. (a) Reflectivity as a function of momentum transfer normal to the mica interface,  $q_z$ , in pure water. The best fit (solid line) based on modelling interfacial layers allows the distribution of oxygens in the interfacial layer (b) to be calculated. Dashed line indicates tail of Gaussian function used to model the mica's "hydration layer". Figures adapted from [36].

As discussed in section 1.1, water's interaction with an ion depends strongly on the latter's valency (as expected from electrostatic considerations) but also on its *species*. Thus, while divalent ions regularly form inner- and outer-sphere configurations on mica, the proportional occupancy of these states and the energy required to transfer between them varies in accordance with the hydration enthalpy of each ion [40]. The same is also true of monovalent ions, typically with stronger species-dependent effects, due their smaller charge. In fact, reflectivity studies showed that the larger alkali ions  $\text{K}^+$ ,  $\text{Rb}^+$  and  $\text{Cs}^+$  adsorbed almost entirely with inner-sphere coordination, whereas  $\text{Li}^+$  and  $\text{Na}^+$  behaved more like divalent ions, with a mix of inner- and outer-sphere adsorption profiles [44]. This is evident in Fig. 1.6(a), where rubidium adsorbs overwhelmingly in inner-sphere configuration, but sodium has a much more complex adsorption profile. A more recent reflectivity study found similar discrepancies between alkali ions of different sizes, but used

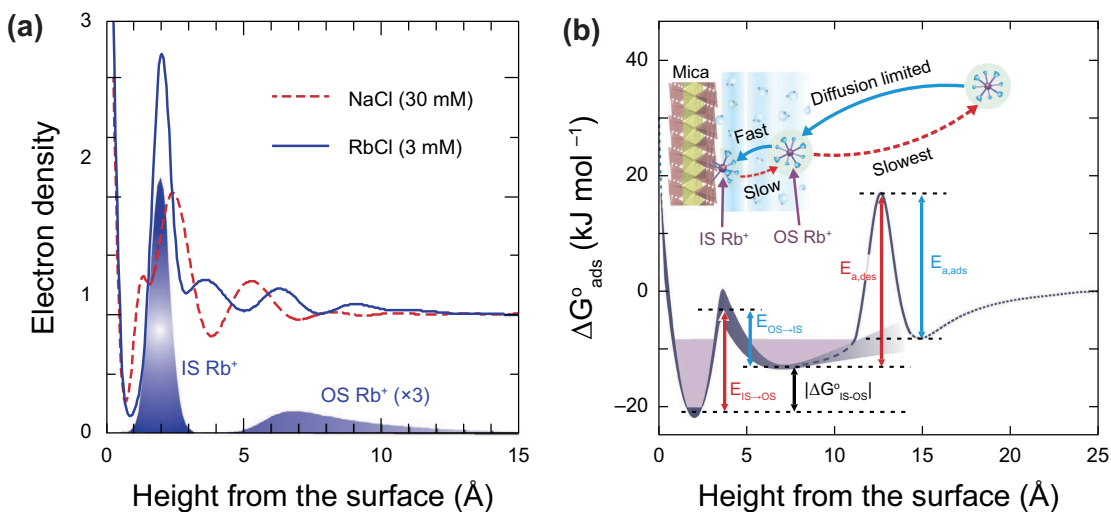


Fig. 1.6: Resonant anomalous X-ray reflectivity can be used to gain additional, element specific information about the Stern layer, shown in (a) for  $\text{Rb}^+$ , leading to a dynamic picture of ion adsorption being mediated by water (cartoon in (b)). Here, rubidium's hydration waters generate an asymmetric free energy ( $\Delta G^0$ ) landscape through formation of inner-sphere (IS) and outer-sphere (OS) configurations that result in remarkably slow desorption rates of  $\sim$  seconds. Figures adapted from [48].

complementary MD simulations to show that  $\text{Li}^+$  and  $\text{Na}^+$  bound directly to mica's triad of surface oxygens, rather than its ditrigonal cavities [45]. The somewhat surprising consequence of these results is that smaller cations with higher charge densities can have lower effective surface binding affinities than their larger counterparts, due to strongly-bound hydration water that prevents direct ion-surface contact. This effect is not solely limited to crystalline materials however; X-ray standing wave measurements of oxide-water interfaces [46, 47] have shown similar ion-size dependencies of adsorption locations.

X-ray reflectivity is also well suited to study softer interfaces that bear relevance to biological systems. For example, lipid monolayers can be spread at the air-electrolyte interface and provide a useful model for how cell or organelle compartments respond to different solutions. Lipids' dynamic nature and often complex headgroup chemistry allow for more subtle interactions with ions in solution than for hard minerals. In particular, evidence has been found for charge inversion [49] (counterions overcompensating for the surface charge), charge regulation [50] (counterions controlling the protonation state of the interface) and ionic binding specificity [51] at the lipid-electrolyte interface. These effects are non-trivial and require the cations' binding to be correlated, either with themselves, with anions (typically  $\text{Cl}^-$  or  $\text{OH}^-$ ) or with the surface headgroups. These interactions with soft surfaces have been validated by X-ray diffraction experiments that emphasise the ability of ions to form ordered sub-phases above the lipids [52], and also to penetrate deep into the headgroup region [53]. The latter case highlights the ability of ions not

just to alter water structure, as we have seen previously, but to dramatically remodel the interface itself by changing the packing of the monolayer as well as its thickness.

### 1.3.2 *Non-linear optics techniques*

The X-ray studies discussed above tend to require high-intensity synchrotron sources in order to build up enough statistics from the small angle reflections. In contrast, lower-energy photons in the visible spectrum are simpler to produce at high intensities, but lack intrinsic surface specificity. This problem can be bypassed using non-linear techniques, such as sum frequency generation (SFG) spectroscopy. Here, an infrared laser (of frequency  $\omega_{\text{IR}}$ ) is incident on molecules at the interface, and its energy up-converted by a second incident visible-range photon (frequency  $\omega_{\text{v}}$ ). The reflected sum-frequency signal is proportional to the surface non-linear polarisation at  $\omega_{\text{SFG}} = \omega_{\text{v}} + \omega_{\text{IR}}$ . This effect is directly reliant on the second-order susceptibility,  $\chi^{(2)}$ , which, crucially, vanishes in situations with spherical symmetry. As the SFG signal is strongly enhanced when the IR photon excites vibrational modes of the interfacial species, the technique is well placed for investigating changes in H<sub>2</sub>O molecules' dynamics due to the interface or dissolved salts.

SFG is commonly used to probe two peaks associated with water structure in the 3000-3700 cm<sup>-1</sup> band. The first, at  $\sim 3200$  cm<sup>-1</sup>, relates to the symmetric OH stretch of tetrahedrally coordinated water molecules and therefore is used as a measure of how "ice-like" the water becomes when in contact with a charged surface. This has been used to show the orientation and in-plane bonding of H<sub>2</sub>O is severely dependent on the surface charge (and therefore the pH) at oxide surfaces [54, 55]. In fact, the waters' dipole orientation reverses entirely when the surface polarity is changed [56]. The second peak, at  $\sim 3450$  cm<sup>-1</sup>, is less well-defined, and usually associated with asymmetrically hydrogen-bonded water, i.e. less structured fluid. In a similar manner to the X-ray studies discussed above, once the pure water-solid interaction has been understood, the disruptive effect of different ions on this structuring can be probed [57–59]. In particular, Jena *et al.* found that the SFG signal only significantly changes for ionic strengths,  $I > 0.7$  mM, where the signal intensity drops dramatically [58]. This is due to a combination of the ions neutralising the static electric field produced by the solid, which affects the third order susceptibility,  $\chi^{(3)}$  contributions, and also the interfacial fluid being structured, which impacts solely  $\chi^{(2)}$ . SFG signals originating from the Stern layer have successfully unveiled the complex water-proton-cation interactions at soft interfaces of COOH-terminated fatty acids [60] and phospholipids [61], with the latter highlighting the importance of counterion condensation on modulating the response, both of the lipids and the interfacial water.

There are numerous other examples of spectroscopic techniques that have been utilised to investigate the structure of aqueous electrolytes at interfaces, including nuclear magnetic resonance (NMR) [62, 63], adapted infrared spectroscopies [64] and neutron diffraction [65], but for a more thorough discussion of available techniques and key results, the reader is pointed to the review of ref. [66].

### 1.3.3 *Molecular dynamics*

The previous techniques discussed, while being able to access molecular-level details of the ions or water, all require averaging of some form, typically over macroscopic in-plane areas and many seconds of data acquisition. This results in the loss of structural information *parallel* to the interface, especially organisation related to surface heterogeneity or lateral correlations. Molecular dynamics simulations provide powerful insight into these systems while bypassing many of the problems mentioned above. In short, these *in silico* experiments comprise solving Newton's equations of motion for particles, typically atoms (although this depends on the level of coarse-graining). The potentials between each particle species are chosen either to reflect the nature of the system (such as covalent bonding in a crystal with well-defined lattice angles) or to satisfy some known thermodynamic constraint (e.g. surface tension or melting point of a liquid). As long as the system is large enough, and sufficiently small time steps are used ( $\sim$  fs), MD can provide microscopic information about the structure of every species within the interfacial fluid at any time or position within the simulation. Modern simulations can easily run to hundreds of nanoseconds in length and therefore can address many of the uncertainties associated with the spectroscopies above, including the dynamics of particular species (discussed in greater detail in section 1.4) and hydrogen-bonding characteristics at the interface. The limitations of MD studies typically relate to the subtle effects due to the choice of water model used, capturing chemical reactions realistically and ensuring that the system size is large enough avoid artefacts.

Mica has been a much-studied model surface in MD, partly because of how well-characterised it has been through other methods. Simulations of systems similar to those studied *via* XR have allowed the direct evaluation of the types of binding available to ions [67–70]. Broadly speaking, these results agree with those produced experimentally; cations' specific interactions with water ensure that those with relatively high charge densities have heterogeneous adsorption behaviours due to their increased affinity for both the solvent and the surface. MD simulations can go much further than adding weight to experimental data however; the artificial tweaking of interaction parameters allows deep insight into the origin of interfacial effects. For example, Fitzner *et al.* [71] disentangled

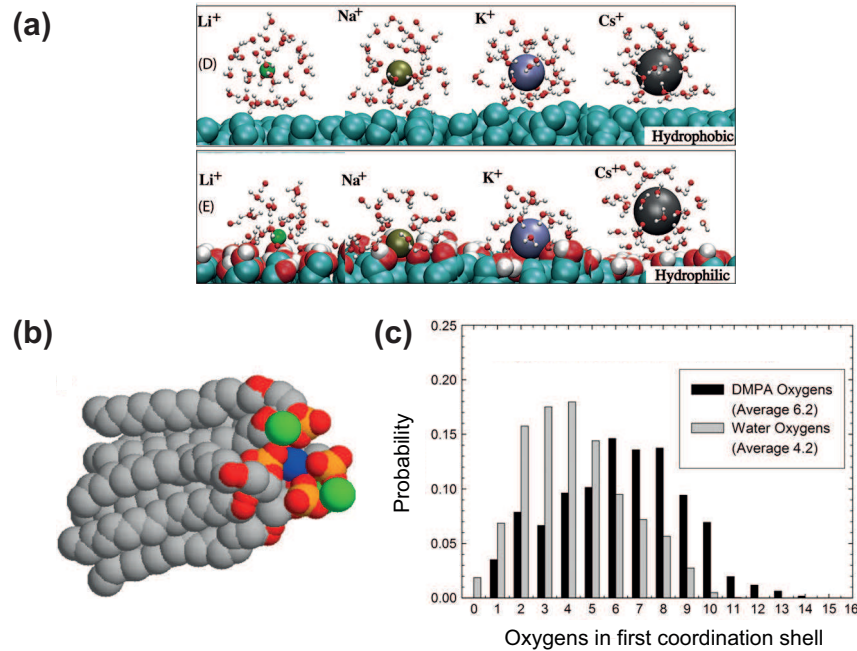


Fig. 1.7: Molecular dynamics allows atomic-level insight into the binding modes and behaviours of different ions (a) as well as providing conformational snapshots (b) and the analysis of specific atoms (c) at any time within the simulation. (a) adapted from ref. [16] and shows ions at heights of  $z = 0.75$  nm (upper segment) and  $z = 0.55$  nm ( $\text{Cs}^+$ , lower segment)/ $z = 0.2$  nm ( $\text{Li}^+$ ,  $\text{Na}^+$ ,  $\text{K}^+$ , lower segment). (b) shows the lipid carbon chains in grey; phosphate groups in orange/red;  $\text{Cl}^-$  ions in green and a  $\text{Ba}^{2+}$  ion in blue. (b) and (c) adapted from ref. [72]

the contributions of interaction energy and interface morphology in the formation of ice at a crystalline surface by adjusting the lattice parameter and adsorption energy continuously. This revealed the importance of the epitaxial arrangement of the first water layer on the remaining bulk fluid’s interaction with the surface. Similarly, the work of Schwierz *et al.* [16, 17] involved tuning the polarity and charge of a surface in aqueous electrolyte in order to ascertain how differences in these material properties drives their startlingly diverse interactions with series of cations and anions. Snapshots from these are shown in Fig. 1.7(a) for a hydrophobic (upper) and hydrophilic surface (lower), illustrating how ion size and surface chemistry can substantially alter the proximal water structure.

MD also provides insight into the surface restructuring of soft surfaces that experimental techniques can typically only explore indirectly. Phospholipid membranes are a key model surface in this context and there has been a great deal of exploration of their interaction with different ions and water. The review of Berkowitz *et al.* in ref. [24] highlights how MD has revealed the “overscreening” of their dipole potential by water, which results in even globally neutral phosphatidylcholine (PC) lipids having a negative potential in aqueous solutions. This drives remarkably specific interactions with cations

(especially  $\text{Na}^+$ ), leading to them penetrating deep into the membrane as well as forming complexes as they tightly bind with three lipids on average [73]. MD simulations have also confirmed experimental findings of charge inversion with  $\text{La}^{3+}$  ions, with the intriguing result that this behaviour is unaffected by the concentration of “background” monovalent salts, unlike for solid systems [74]. Further exotic behaviour has been observed in simulations of negatively charged lipids with the divalent counter ions  $\text{Mg}^{2+}$ ,  $\text{Ca}^{2+}$  and  $\text{Ba}^{2+}$ , including the binding of many lipids to a single charge (as illustrated in Fig. 1.7(b)-(c)), which has important implications for domain formation and lipid organisation in biological membranes [72, 75].

### 1.3.4 Force-based interfacial studies: the surface force balance

The previous experimental techniques relied in some way on chemical interrogation of the interface, whether the electron distribution in the case of XR, or the molecular vibrational modes in SFG. The surface force balance (SFB) and atomic force microscope in contrast, can directly measure the physical force between two surfaces which (for the purposes of this discussion at least) are separated by an aqueous electrolyte. The instruments’ focus on a non-specific interaction potential means they are versatile and are not limited to specific elements or systems. However, the requirement of a physical probe means that the interfaces investigated may not be in their equilibrium, native state, especially if large confining pressures are imposed.

The SFB is principally composed of two curved mica surfaces which are oriented in a crossed-cylinder geometry (illustrated in Fig. 1.8(a)), such that the equivalent interaction energy per unit area of two planar surfaces,  $E_{\text{int}}$ , can be directly related to the normal force,  $F_N$ , between the two by  $F_N/R = 2\pi E_{\text{int}}$ , known as the Derjaguin approximation [19] (here,  $R$  is the radius of curvature of the cylinders). The force is measured via a stiff spring coupled to one of the cylinders and the separation between the plates can be determined to  $\sim 0.1$  nm resolution by monitoring the interference fringes generated by light reflected on the mica surfaces. The SFB has allowed the direct testing of colloidal interaction models such as that of Derjaguin, Landau, Verwey and Overbeek (so-called DLVO theory). This theory assumes that at large separations, two surfaces in solution will primarily interact electrostatically *via* their double layers, but when brought into close proximity, attractive quantum-mechanical effects – the van der Waals force – dominate the surfaces’ response. SFB studies routinely use DLVO theory to extract the apparent surface potential from  $F_N/R$  versus  $d$  curves (see e.g. the inset to Fig. 1.8(c)) with excellent accuracy and the ability to observe *in situ* dynamic surface charging/regulation events [76]. Although the theory includes short-ranged interactions, it relies on a pair-wise integration over atoms

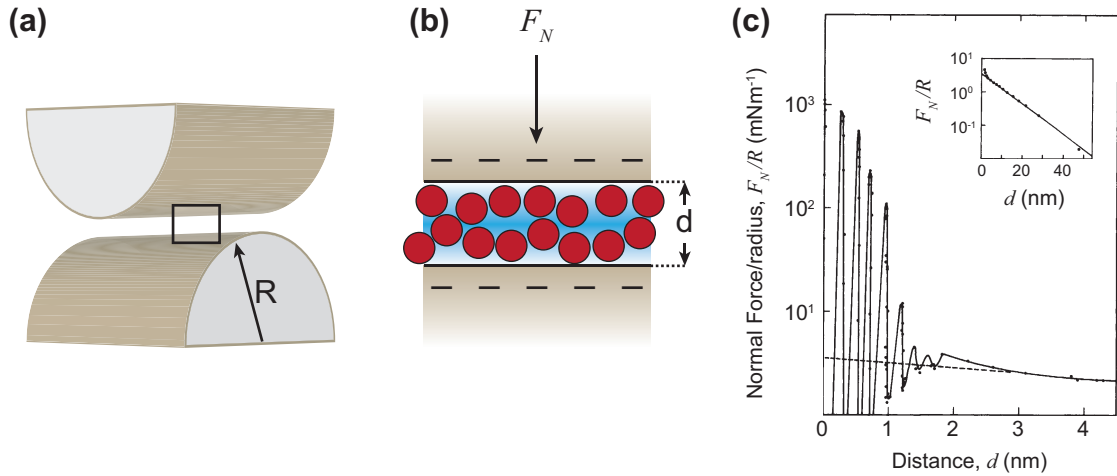


*Fig. 1.8:* The surface force balance as a tool to investigate structure at confined interfaces. (a) The crossed-cylinder geometry (radius  $R$ ) of curved mica plates allows the interaction energy to be calculated (see text). Typical radii of curvature are  $\sim 1$  cm. (b) Zoomed-in schematic of box in (a) showing idealised liquid molecules (red) forced into a more structured ensemble due to the normal force,  $F_N$  applied by the mica sheets. (c) The interaction force observed in pure water by Israelachvili and Pashley demonstrates oscillations at small separations  $d$ , with a periodicity similar to the diameter of a water molecule [77]. The inset shows that the long-range force for  $d > 3$  nm agrees well with DLVO theory (solid line).

within the surface but typically *not* in the intervening solvent (except indirectly *via* the so-called Hamaker constant). Thus, as with the Gouy-Chapman theory of subsection 1.2.1, specific dielectric and steric behaviour of the fluid at small separations is not considered.

This was highlighted by the work of Pashley which observed an additional repulsive force, not predicted by DLVO, between the mica surfaces of an SFB separated by an aqueous solution, but only when dissolved ions were present [78, 79]. This so-called hydration force decayed exponentially with separation over less than a nanometre and depended on the concentration and type of ions in solution. It was postulated to be related to strongly bound ions resisting desorption from the mica but later work showed that hydration repulsion could still be observed in pure water [77] and even demonstrated an oscillatory profile with a period commensurate with the diameter of an  $\text{H}_2\text{O}$  molecule ( $\sim 0.25$  nm, see Fig. 1.8(c)). The similar periodicity indicates that the force is generated by the progressive squeezing out of layers of ordered water from between the mica plates. That is, the confinement induced by the SFB at small separations reduces the degrees of freedom of the water and requires work to be done to remove molecules from the gap, an effect expected for “simple” liquids in atomically smooth gaps [80] (illustrated in Fig. 1.8(b)). Unsurprisingly, given the nanometre-scale separations investigated by SFB, the precise nature of the hydration forces strongly depends upon the surface’s chemistry and the extent to which it induces ordering of water. For example, the oscillatory force profile is

usually superimposed upon a long range, monotonic force that may either be attractive or repulsive, depending on the local density and orientation of the water molecules at the surfaces [81]. Despite this system of mica and pure water being over-idealised, it appears that a “primary” hydration decay of the order of a few Ångströms is remarkably universal in biological systems, including lipids, proteins, polysaccharides and nucleic acids, even ones containing very low water fractions [82].

The versatility of SFB studies has allowed the chemical structure and behaviour of diverse systems to be uncovered. This includes the surface restructuring of silica under water to form a nanometre-thick “gel” layer of silanol (Si–OH) groups [83], as well as the behaviour of electrolytes at the interfaces with conducting surfaces such as graphene and gold [76, 84]. These latter examples present the intriguing possibility of being able to reversibly control the interfacial structure by straightforwardly altering the surface potential. While the technique has allowed the observation of complex local correlations between ions [85], its  $\sim \mu\text{m}^2$  interaction areas provide no way to determine how heterogeneous such interfaces are; that is, how smeared out the ionic behaviour is within the Stern layer or the lateral dimensions of such variation.

### 1.3.5 Force-based interfacial studies: atomic force microscopy

Atomic force microscopy in many ways is very similar to the surface force balance; it principally relies on the interaction force between two surfaces to provide interfacial information, and thus can be used in similarly varied systems as SFB. However, rather than macroscopic mica plates, AFM measures the force between a sample and a sharp tip (radii of curvature of  $\mathcal{O}(10 \text{ nm})$  or less) attached to a flexible cantilever, reducing the effective contact area by orders of magnitude compared with its larger cousin. This allows it to derive local information normal to the interface with sub-nanometre lateral precision (especially since asperities on the tip often mean there are only a few atoms interacting with the sample at any one time). Further, the tip can be raster-scanned across the sample, allowing the direct imaging of lateral variation in ionic interfaces with solid and soft samples, often with Ångström-level resolution. Since its development three decades ago, dynamic modes of AFM operation have flourished [86, 87] (which will be discussed in greater detail in chapter 2) and are now the norm when it is necessary to extract quantitative information about the topography or material properties about a sample with nanoscale resolution.

Many AFM studies of the structure of the aqueous interfaces have focused on using force-distance spectroscopy, wherein the cantilever is lowered towards the sample and either its deflection, or dynamic properties such as oscillation amplitude are monitored as a

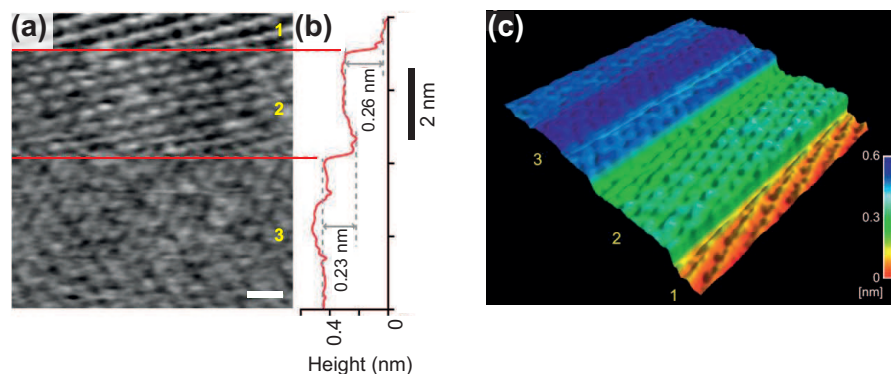


Fig. 1.9: Dynamic AFM provides sub-nanometre resolution mapping of the hydration landscape. (a) Molecular resolution topographic imaging of a DPPC bilayer on mica with strongly-bound water by FM-AFM (line-by-line flattened). Transitions between imaging lipids and hydration shells are highlighted by the red lines, reflecting height transitions shown in (b): each jump corresponds to the diameter of a water molecule. (c) 3D representation of topographic data in (a) highlighting stable imaging hydration “terraces” in blue, green and orange. Adapted from ref. [93]; scale bar in (a) corresponds to 1 nm

function of distance. This allows similar information to be collected as that of Fig. 1.8(c) but there is no requirement for the molecules/interfaces of interest to be grafted or evaporated onto curved mica or for them to be atomically flat. For instance, static force measurements have investigated hydration forces at calcite [88], gibbsite [26] and more complex systems containing proteins [89]. The use of dynamic AFM modes when performing spectroscopy with sharp probes allows for more nuanced investigations of the interface, including charge regulation [26] and dielectric measurements [90, 91] in ionic solutions. At the Ångström end of the scale, Kilpatrick *et al.* [92] measured the average hydration forces presented by  $\text{Na}^+$  and  $\text{Mg}^{2+}$  above a mica surface. They observed a monotonic primary hydration force as well as an oscillatory “structural” hydration force, in an analogous manner to similar SFB results, but the authors argued that AFM effectively measured an unperturbed interface, due to the small dimensions of the tip (2 nm radius of curvature) and its slow oscillation dynamics ( $\sim \mu\text{s}$ ) compared to that of the water’s diffusion ( $\sim \text{ns}$ ). However, this discussion assumed that water retained (and could accurately be described by) its bulk diffusion coefficient in the presence of the AFM tip, which is not necessarily so obvious, as we shall see in section 1.4.

The true power of AFM in interfacial studies lies in its ability to image and extract quantitative topographical and mechanical properties from samples with sub-nanometre lateral resolution. This atomic- or molecular-level resolution has only really become routinely possible in the last decade or so (at least immersed in water, at ambient temperatures), with work by the likes of Higgins [94] and Fukuma *et al.* [93, 95, 96]. These authors were able to directly image the hydration structure on mica and a gel-phase lipid

bilayer using frequency modulation (FM, see subsection 2.1.2) AFM, which showed that oscillatory forces were responsible for the stable imaging of water and ions in the Stern layer over many seconds of imaging time, as illustrated in Fig. 1.9. This was significant because it was now possible to produce real-space mapping with unprecedented resolution of the interfaces between solids and liquids, directly exploiting the strongly-bound hydration water that exists at the interface of many minerals [97] and bio-molecules [98]. The results also held consequences for image interpretation of similar AFM studies; variations in topography must acknowledge not only the molecular structure of the solid, but also the specific organisation of the solvent as well as ions dissolved within it. Further work in the group of Jarvis emphasised the role of hydration water mediated interactions in the mesoscale organisation of both gel-phase [99] and liquid-crystalline [100] lipid membranes.

These initial developments in dynamic imaging of the hydration structure of the liquid interface focused more on the implications for strongly-bound *water*, partly due to the  $\sim 0.3$  nm force periodicity which implied that the key activity was between the  $\text{H}_2\text{O}$  molecule and the surface. Studies did specifically address the impact of ions on the interfacial structure however, with the variation in apparent topography in solutions of common mono- and divalent cations systematically compared at the mica interface [101] and a 1,2-dipalmitoyl-*sn*-glycero-3-phosphatidylcholine (DPPC) lipid bilayer in gel phase [102]. These two studies complemented one another; both systematically measured ionic interfacial effects, but the former probed the adsorption location of ions on a fixed surface with negligible flexibility, while the lipids in the latter were shown to alter their headgroup dipole orientation in response to the differing adsorption locations of  $\text{Ca}^{2+}$  compared with  $\text{Na}^+$  and in response to different concentrations of ions.

Following these results, and deeper understanding of the mechanism behind this enhanced resolution at smaller amplitudes [104, 105], more detailed studies of the local, non-averaged organisation of single ions were carried out using dynamic AFM [34, 103, 106, 107]. Consistently with the previous work we have seen in this section, continuum models and assumptions were seen to break down dramatically within a nanometre of solid surfaces. The reactivity and adsorption structure of dissolved ions was seen to depend far more on the ion species and concentration than on “intrinsic” features of the solid such as its surface charge or  $\text{p}K_a$  [34]. This was further emphasised by the breakthrough of being able to image singly-adsorbed  $\text{Rb}^+$  ions in liquid [103]. Through assessment of the rubidium coverage at varying bulk concentrations (Fig. 1.10) and complementary molecular dynamic simulations, Ricci *et al.* were able to show that the ions preferentially adsorb in laterally ordered structures at the interface, despite their electrostatic repulsion. This process was driven in great part by the hydration energy – that is, the free energy con-

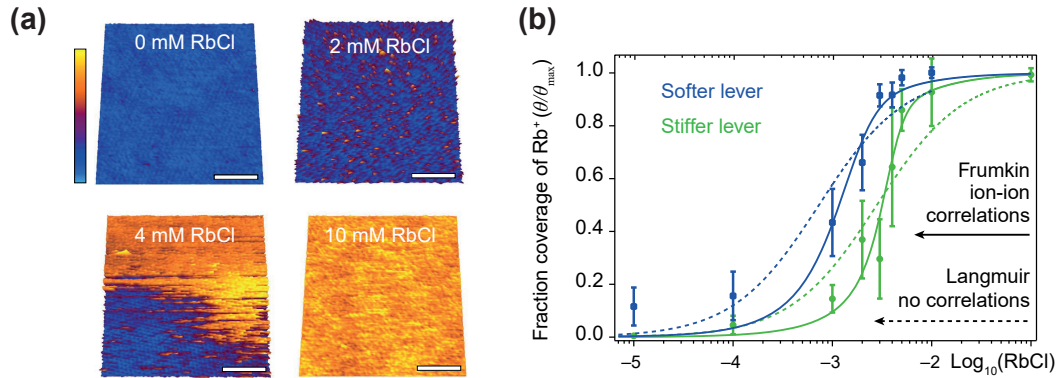


Fig. 1.10: Individual adsorbed  $\text{Rb}^+$  ions can be resolved *via* AM-AFM (a) and their profiles tracked as a function of bulk concentration. (b) Measuring the relative rubidium coverage ( $\theta/\theta_{\max}$ ) with cantilevers of various stiffness allows adsorption models to be used that highlight the need to include ionic correlations in descriptions of Stern layer. Figures adapted from ref. [103]; scale bar in (a) corresponds to 5 nm.

tribution between the ions and their surrounding waters – and in fact was shown to be remarkably general and not limited to charged, crystalline surfaces.

Clearly, from the myriad independent studies of this chapter, a thorough characterisation of water and ionic structure requires examining both  $z$  and  $x$ - $y$  simultaneously. This problem has been approached in recent years by the development of three-dimensional (3D) AFM, which builds on Hölscher *et al.*'s 3D force field approach [108] and was pioneered by Fukuma *et al.* [109]. While imaging, three distinct motions are applied to the tip; vertical driving of the cantilever at resonance with small ( $< 1$  nm) amplitudes; modulating the  $z$  position of the cantilever with a sinusoidal motion at a much lower frequency ( $\sim 200$  Hz) over a few nanometres and finally the conventional raster-scanning. Most commonly, this procedure is undertaken in frequency-modulation mode [109–115], so that the change in resonance frequency,  $\Delta f$ , of the cantilever in each voxel can be directly converted into a force by the method of Sader and Jarvis [116], allowing a “force volume” to be constructed. In principle, however, the technique can be combined with any dynamic AFM mode, as has been demonstrated using AM-AFM [117, 118] and also bimodal operation [119]. These volumes are typically of  $\mathcal{O}(\text{nm}^3)$  and retain molecular-level resolution in every dimension. As is common with AFM studies however, interpretation of the measured forces is rarely straightforward. In analogy to the 1D cases of the SFB and AFM force spectroscopy, oscillatory forces with periods close to the size of a water molecule ( $\sim 0.3$  nm) [109, 113, 117, 119], as well as ion-specific differences [112, 117] imply that the force is principally due to the tip penetrating strongly-adsorbed water layers. However, experiments on softer samples have revealed the importance of accounting for flexible surface groups, as well as bulk compressibility of the layer when assigning features in the force [111]. There are

also unresolved questions about the extent to which ions modify the measured hydration landscape, and how much we can infer about water structure from highly concentrated electrolyte solutions [114, 118, 120]. That being said, 3D AFM has shown exciting potential for directly quantifying the nanoscale properties of the solid-liquid interface; chemical differentiation between single ions [112] and identification of adsorbed  $K^+$  [118] has recently been made possible, as well as 3D mapping of the electrolyte-DNA boundary and heterogeneously charged interfaces [120, 121].

## 1.4 Dynamics of aqueous solutions of ions

Thus far, we have considered mostly the *time-averaged* picture of the solid-liquid interface, focusing on binding locations and geometries of ions, and how it depends on their interplay with water. Often this is because experimental techniques, such as those discussed above, either require in-plane averaging (and so lose dynamical information), or are assumed not to have the time resolution to track the ionic/hydration events. However, time-resolved information is crucial for understanding transport through e.g. pores [122, 123], in-plane motion along membranes that can drive energetic processes in biology [124, 125] and chemical reactions occurring at the interface [126]. Further, these kinetics must be considered if we are to understand the limitations of mean-field (equilibrium) approximations such as DLVO theory and the EDL. We shall discuss first the short-timescale dynamics of pure water and ions at interfaces, which are typically probed using simulations, vibrational spectroscopy or more indirect electrokinetic experiments. We will then move on to much slower dynamics that are accessible to techniques such as AFM. Latter such studies are often couched in terms of frictional forces transmitted by the fluid, or effective viscosities, but they provide important molecular insight onto the dynamic behaviour of the water and ions as well.

### 1.4.1 Short Timescale Dynamics

Molecular dynamics offers insight into the driving mechanisms behind the altered dynamics of interfacial species and, despite its limitations to nanoseconds of simulation time, has revealed the extent to which the proximal water layer's structure dictates the dynamics of subsequent layers, as well as dissolved ions. Rather counterintuitively, the first layer of water against a solid surface can, in some instances, make surfaces hydrophobic in a heterogeneous way, even on perfectly idealised substrates [127]. This Stern layer of water strongly affects in-plane diffusion of ions, which have ballistic motion ( $\langle \underline{r}(t)^2 \rangle \propto t^2$ ) at sub-picosecond timescales and diffusive ( $\langle \underline{r}(t)^2 \rangle \propto t$ ) thereafter, due to molecular “caging” [128]. Other simulations of a positively charged solid agreed with the nanosec-

ond diffusive behaviour and showed that the effective diffusion coefficient,  $D$ , was reduced by an order of magnitude for ions adsorbed to the surface ( $D_{\text{Cl}^-} \sim 2 \times 10^{-7} \text{ cm}^2 \text{ s}^{-1}$ ) compared with those interacting at a greater distance ( $D_{\text{Na}^+} \sim 2 \times 10^{-6} \text{ cm}^2 \text{ s}^{-1}$ ) [129]. These coefficients, as well as other experimental and *in silico* studies [68, 130–133], have confirmed that while the interface and often some degree of confinement certainly does retard the dynamics of the fluid (both ions and water) between a few times [133] and a few orders of magnitude [68], it is not immobilised in the manner implied by, say, Fig. 1.4. That being said, some groups have called into question the ability of MD timescales to fully equilibrate strongly-hydrated ions such as  $\text{Li}^+$ , which Hocine *et al.* estimated had a relaxation time on the order of seconds [134]. Further, the notion of a stagnant interfacial water layer which nevertheless allows finite ion mobilities (a common assumption in electrokinetic studies) seems unlikely in the face of many MD simulations [135] and appears to depend to a large extent on the model or technique used to probe the system. Generally however, studies which probe these ps-ns timescales appear to agree that ions and water exhibit reduced, but certainly finite, dynamics at the interface for a broad variety of surface charges, polarities and ion types.

### 1.4.2 Long Timescale Dynamics

The conclusions above imply that to any technique probing timescales greater than microseconds, the interfacial fluid will appear static, as the nanosecond dynamics will average out into a global equilibrium state with the bulk fluid and surface. Indeed, that is the underlying assumption of many of the conclusions of section 1.3 where, for example, the oscillatory motion of an AFM tip (frequencies of 10s of kHz to MHz) is slow enough such that the interfacial fluid can wholly rearrange itself in response (i.e. there are no viscoelastic effects), leaving a equilibrium picture of the molecular structure. However, we shall see that experiments have observed interfacial relaxation times many decades greater than this, on the order of milliseconds to seconds. Many of these investigate electrolytes restricted in  $z$  to just a few molecular layers (so-called “nanoconfined” fluids), which has clear implications for their ability to rearrange [136], but the shift to such dramatically long scales is still unexpected.

We shall begin with the case of nanoconfined water, partly because it is so commonplace in biological and chemical engineering [123, 137–139], but also because it remains a ill-defined and controversial topic among researchers [140–142]. For instance, SFB measurements that impose a shear with one mica plate with frequencies of  $\sim 0.5\text{-}1.0 \text{ Hz}$  (equivalent in their system to shear rates of  $\dot{\gamma}_s \equiv dv/dz = 10^4 \text{ s}^{-1}$ ) have shown that confined water retains essentially its bulk viscosity [28, 143–146]. This was predicted to

be related to the strong hydrogen bonding nature of  $\text{H}_2\text{O}$ ; confinement suppressed the hydrogen bond networks that would promote higher viscosities and longer relaxation times. The results qualitatively agreed with studies showing that confined water behaves as if it were supercooled – i.e. remaining fluid despite a temperature below freezing point [147]. Further, the authors surmised that this fluidity was maintained even in the presence of tenaciously adsorbed sodium, *via* the rapid exchange of water molecules between hydration shells of opposing  $\text{Na}^+$  ions. These studies placed an upper limit on the viscosity of water being at most thirty times greater than bulk, depending on the ionic content, although they could not discount the possibility of an additional monolayer of water being present in their determination of mica plate separation [28].

These results are powerful, but on first sight appear to contradict theoretical [42, 43] and experimental [41, 148] studies that show water’s dielectric permittivity,  $\varepsilon$ , to be greatly reduced from  $\sim 80$  in the bulk down to as low as  $\sim 2$  when confined or in close proximity to an interface. This dampening of  $\varepsilon$  is a direct measure of the loss of rotational freedom for water dipoles, at least perpendicular to the plane,  $\varepsilon_{\perp}$ , and implies a concomitant increase in viscosity. However, it should be noted that despite the decrease of  $\varepsilon_{\perp}$ , even for relatively liberal confinements of hundreds of nm [148], Fumagalli *et al.* attribute the dielectric changes to be governed by at most three layers of interfacial water. Thus, the global viscosity as measured by SFB may *not* be dramatically altered in the same manner as  $\varepsilon_{\perp}$ . Further, there is a clear disparity in frequency between the SFB results ( $\mathcal{O}(\text{Hz})$ ) to those of ref. [148] (kHz electric field modulation) and MD simulations which cover nanoseconds at most, and it is uncertain to what extent this would impact the conclusions reached.

More insight onto this discrepancy has been granted by studies using smaller probes, which reduce the extent of the fluid’s confinement. These include traditional AFM, but also adapted technologies that, for example use quartz tuning forks [149, 150] or optical fibres in so-called “transverse dynamic force microscopy” [151]. These have been able to explore many dynamic properties of nanoconfined water and ions, including the slip length [152], stiffness and damping [153–156], storage and loss moduli [157] and viscosities [150–152, 158], but have provided an even wider spread of conclusions regarding their time-dependent behaviour! Indeed, the effective viscosity of nanoconfined water,  $\eta_{\text{eff}} = \eta/\eta_0$ , (for bulk water viscosity at  $25^\circ\text{C}$ ,  $\eta_0 = 0.89 \text{ mPa}\cdot\text{s}$ ) has been variously measured as  $10^3$ ,  $10^4$ ,  $10^6$  and  $10^7$  [151, 152, 158–160], implying that the precise, chemical and physical nature of the confinement dramatically influences the measured dynamic profile. To some extent, these discrepancies regarding confined water have been put to bed by the work of Jeffery, Khan, Hoffmann *et al.* [153, 154, 161]. Their ultra-small amplitude ( $< 1 \text{ \AA}$ ), off-resonance AFM technique directly showed that water underwent “dynamic solidification” above certain

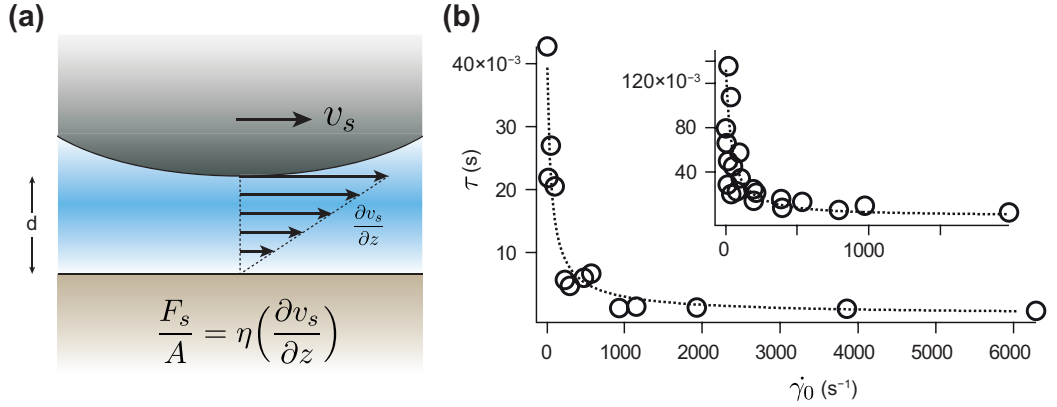


Fig. 1.11: AFM shearing experiments allow dynamic information about confined fluids to be recovered. (a) Schematic illustrating so-called “shear-force” spectroscopy, in which a nanoscale probe is moved parallel to the interface with velocity  $v_s$ . The viscosity of the fluid,  $\eta$ , is related to the velocity gradient,  $\partial v_s/\partial z$ , and the shear stress (lateral force per unit area),  $F_s/A$ . (b) By applying an oscillatory shear to tightly confined water ( $d = 0.4$  nm), Li *et al.* showed the fluid’s relaxation time,  $\tau$ , to dramatically increase at low shear rates,  $\dot{\gamma}$ . This reflected an “intrinsic” timescale for the restricted water of  $\tau_0 = 0.06 \pm 0.03$  s (dashed lines), orders of magnitude greater than that of bulk water. Schematic and graph adapted from from ref.s [152] and [162] respectively.

compression rates. This phenomena is characterised by a marked increase in the Maxwell relaxation time, which indicates slow stress dissipation and a more solid-like behaviour. Many of the inconsistencies in the long-timescale measurements of water’s dynamics could be encompassed by this perspective; the rapid jump-to-contact in SFB studies of Raviv *et al.* [144–146] promoted an elastic structure of water that had minimal fluid-like damping and thus no measurable increase in viscosity. Shearing AFM measurements [152, 157–159, 162] (for example, see Fig. 1.11) that confined the fluids in a slower, more controlled manner, conversely resulted in a highly viscous interaction with the structured water and large apparent values of  $\eta_{\text{eff}}$ .

Strong modification of the effective viscosity of interfacial water is likely to have a significant impact for the diffusion of ions within the Stern layer. This appears to be the case; AFM imaging can individuate single ions that remain stable over the multiple line scans at the imaging time scale (ms-s) [103], even for the nominally much slower 3D AFM [118]. This implies that the in-plane relaxation time of the Stern layer is at least on this timescale, and the observation of single ions [103] appears to contradict the interpretation of topography changes as just representing average ionic densities [101]. Indeed, recent RAXR results (significantly, with no confinement and thus an unperturbed interface) found relaxation timescales for  $\text{Rb}^+$  and  $\text{Na}^+$  on mica to be of the order of seconds [48], relating to the complex energy landscape generated by inner- and outer-sphere adsorption, as shown alongside a schematic representation in Fig. 1.6(b). These results

correlated well with SFB measurements that demonstrated  $K^+$  condensation with exceedingly slow desorption relaxation times of  $\tau_r = 11 \pm 2$  min (equivalent to an energy barrier of  $33 \pm 4 k_B T$ ) [145]. Perhaps the most extreme example of damped interfacial kinetics was observed *via* second harmonic generation where moderate ( $> 50$  mM) concentrations of monovalent ions could “jam” pH changes by hours, in a manner that depended on the hydration of the charged species [126]. This impact of water-mediated interactions is emphasised by the direct comparison of adsorption strength of different ions. For instance, smaller ions such as  $Na^+$  bind tightly to the interface and resist desorption, even under extreme loads [28, 163], whereas caesium can easily be squeezed out from confined mica layers, presenting barely any hydration repulsion [28]. While these results reflect binding affinity, they nonetheless give an indication of the relative mobility of the ions once they arrive at the interface. It is this immobility of ions relative to the waters of their hydration shells that is proposed to give rise to hydration lubrication regimes [164], wherein strongly hydrated counterions prevent wear of surfaces and produce strikingly low coefficients of friction.

## 1.5 Conclusions

We have seen in this chapter how ions strongly modify the global and local properties of the water around them by interacting with their dipoles. On the continuum level, ionic effects at interfaces are very well described by the electrical double-layer and DLVO theories, despite their neglect of specific solvent-ion interactions and surface chemistry and heterogeneity. However, in systems with high ionic strength or surface charge, the specific hydration of ions and their affinity for chemical groups at the interface become increasingly important. The continuum breakdown evidenced by the structure of ions and water within the Stern layer has been demonstrated with X-rays, simulations and non-linear spectroscopy, as well as the perturbation caused by altering the charge-density of chemical species or their relative concentrations. Force based studies have allowed more direct interrogation of the energies associated with ion binding and dynamics, with AFM allowing molecular-level lateral resolution on top of this. While the equilibrium structure of ions mediated by water appears to be fairly well-defined, there remains controversies in the literature over the relevant timescales of the ions’ and waters’ dynamics at the interface. Most simulations and scattering experiments identify timescales reduced from that of bulk but certainly still at the ns- $\mu$ s level. The assimilation of this with results which clearly show some level of relaxation occurring on the millisecond-second-minute time scales (discrepancies of up to ten orders of magnitude!) is as yet unresolved and likely relies on the collective dynamics and jamming of many hundreds of molecules at once.

# REFERENCES: CHAPTER 1

- [1] G. Jones, M. Dole, “The viscosity of aqueous solutions of strong electrolytes with special reference to barium chloride”, *J. Am. Chem. Soc.* **1929**, *51*, 2950–2964.
- [2] L. Onsager, N. N. Samaras, “The surface tension of debye-hückel electrolytes”, *J. Chem. Phys.* **1934**, *2*, 528–536.
- [3] Y. Marcus, “Effect of ions on the structure of water: Structure making and breaking”, *Chem. Rev.* **2009**, *109*, 1346–1370.
- [4] H. Ohtaki, T. Radnai, “Structure and Dynamics of Hydrated Ions”, *Chem. Rev.* **1993**, *93*, 1157–1204.
- [5] H. J. Bakker, “Structural dynamics of aqueous salt solutions”, *Chem. Rev.* **2008**, *108*, 1456–1473.
- [6] U. Kaatze, “The dielectric properties of water in its different states of interaction”, *J. Solution Chem.* **1997**, *26*, 1049–1112.
- [7] Y. Zhang, P. S. Cremer, “Interactions between macromolecules and ions: the Hofmeister series”, *Curr. Opin. Chem. Biol.* **2006**, *10*, 658–663.
- [8] P. Jungwirth, P. S. Cremer, “Beyond hofmeister”, *Nat. Chem.* **2014**, *6*, 261–263.
- [9] J. Song, T. H. Kang, M. W. Kim, S. Han, “Ion specific effects: decoupling ion–ion and ion–water interactions”, *Phys. Chem. Chem. Phys.* **2015**, *17*, 8306–8322.
- [10] A. W. Omta, M. F. Kropman, S. Woutersen, H. J. Bakker, “Negligible effect of ions on the hydrogen-bond structure in liquid water.”, *Science* **2003**, *301*, 347–9.
- [11] Y. Chen, H. I. Okur, N. Gomopoulos, C. Macias-Romero, P. S. Cremer, P. B. Petersen, G. Tocci, D. M. Wilkins, C. Liang, M. Ceriotti, S. Roke, “Electrolytes induce long-range orientational order and free energy changes in the H-bond network of bulk water”, *Sci. Adv.* **2016**, *2*, e1501891–e1501891.
- [12] R. Mancinelli, A. Botti, F. Bruni, M. A. Ricci, A. K. Soper, “Perturbation of water structure due to monovalent ions in solution”, *Phys. Chem. Chem. Phys.* **2007**, *9*, 2959.
- [13] P. Schienbein, G. Schwaab, H. Forbert, M. Havenith, D. Marx, “Correlations in the Solute–Solvent Dynamics Reach Beyond the First Hydration Shell of Ions”, *J. Phys. Chem. Lett.* **2017**, *8*, 2373–2380.
- [14] K. J. Tielrooij, N. Garcia-Araez, M. Bonn, H. J. Bakker, “Cooperativity in ion hydration”, *Science (80-. )*. **2010**, *328*, 1006–1009.
- [15] N. F. A. van der Vegt, K. Haldrup, S. Roke, J. Zheng, M. Lund, H. J. Bakker, “Water-Mediated Ion Pairing: Occurrence and Relevance”, *Chem. Rev.* **2016**, *116*, 7626–7641.
- [16] N. Schwierz, D. Horinek, R. R. Netz, “Anionic and Cationic Hofmeister Effects on Hydrophobic and Hydrophilic Surfaces”, *Langmuir* **2013**, *29*, 2602–2614.
- [17] N. Schwierz, D. Horinek, U. Sivan, R. R. Netz, “Reversed Hofmeister series—The rule rather than the exception”, *Curr. Opin. Colloid Interface Sci.* **2016**, *23*, 10–18.
- [18] O. Björneholm, M. H. Hansen, A. Hodgson, L.-M. Liu, D. T. Limmer, A. Michaelides, P. Pedevilla, J. Rossmeis, H. Shen, G. Tocci, E. Tyrode, M.-M. Walz, J. Werner, H. Bluhm, “Water at Interfaces”, *Chem. Rev.* **2016**, *116*, 7698–7726.
- [19] J. N. Israelachvili, *Intermolecular and Surface Forces*, Third, Elsevier, **2011**.

- [20] A. P. Gaiduk, G. Galli, “Local and Global Effects of Dissolved Sodium Chloride on the Structure of Water”, *J. Phys. Chem. Lett.* **2017**, *8*, 1496–1502.
- [21] R. Hartkamp, B. Coasne, “Structure and transport of aqueous electrolytes: From simple halides to radionuclide ions”, *J. Chem. Phys.* **2014**, *141*, 124508.
- [22] D. J. Bonthuis, R. R. Netz, “Beyond the Continuum: How Molecular Solvent Structure Affects Electrostatics and Hydrodynamics at Solid–Electrolyte Interfaces”, *J. Phys. Chem. B* **2013**, *117*, 11397–11413.
- [23] H.-J. Butt, K. Graf, M. Kappl, *Physics and Chemistry of Interfaces*, Wiley-VCH, **2003**.
- [24] M. L. Berkowitz, D. L. Bostick, S. Pandit, “Aqueous Solutions next to Phospholipid Membrane Surfaces: Insights from Simulations”, *Chem. Rev.* **2006**, *106*, 1527–1539.
- [25] G. Trefalt, S. H. Behrens, M. Borkovec, “Charge Regulation in the Electrical Double Layer: Ion Adsorption and Surface Interactions”, *Langmuir* **2016**, *32*, 380–400.
- [26] C. Zhao, D. Ebeling, I. Siretanu, D. van den Ende, F. Mugele, “Extracting local surface charges and charge regulation behavior from atomic force microscopy measurements at heterogeneous solid-electrolyte interfaces”, *Nanoscale* **2015**, *7*, 16298–16311.
- [27] R. Tivony, D. B. Yaakov, G. Silbert, J. Klein, “Direct Observation of Confinement-Induced Charge Inversion at a Metal Surface”, *Langmuir* **2015**, *31*, 12845–12849.
- [28] S. Perkin, R. Goldberg, L. Chai, N. Kampf, J. Klein, “Dynamic properties of confined hydration layers”, *Faraday Discuss.* **2009**, *141*, 399–413.
- [29] C. Labbez, B. Jonsson, M. Skarba, M. Borkovec, “Ion-ion correlation and charge reversal at titrating solid interfaces”, *Langmuir* **2009**, *25*, 7209–7213.
- [30] R. B. Schoch, J. Han, P. Renaud, “Transport phenomena in nanofluidics”, *Rev. Mod. Phys.* **2008**, *80*, 839–883.
- [31] A. V. Delgado, F. González-Caballero, R. J. Hunter, L. K. Koopal, J. Lyklema, “Measurement and interpretation of electrokinetic phenomena”, *J. Colloid Interface Sci.* **2007**, *309*, 194–224.
- [32] F. H. J. van der Heyden, D. Stein, C. Dekker, “Streaming Currents in a Single Nanofluidic Channel”, *Phys. Rev. Lett.* **2005**, *95*, 116104.
- [33] J. C. Berg, *An Introduction to Interfaces and Colloids: The Bridge to Nanoscience*, 1st ed., World Scientific Publishing Co., **2009**.
- [34] I. Siretanu, D. Ebeling, M. P. Andersson, S. L. S. Stipp, A. Philipse, M. C. Stuart, D. van den Ende, F. Mugele, “Direct observation of ionic structure at solid-liquid interfaces: a deep look into the Stern Layer.”, *Sci. Rep.* **2014**, *4*, 4956.
- [35] P. Fenter, N. C. Sturchio, “Mineral-water interfacial structures revealed by synchrotron X-ray scattering”, *Prog. Surf. Sci.* **2005**, *77*, 171–258.
- [36] L. Cheng, P. Fenter, K. L. Nagy, M. L. Schlegel, N. C. Sturchio, “Molecular-Scale Density Oscillations in Water Adjacent to a Mica Surface”, *Phys. Rev. Lett.* **2001**, *87*, 156103.
- [37] P. Geissbühler, P. Fenter, E. DiMasi, G. Srajer, L. Sorensen, N. Sturchio, “Three-dimensional structure of the calcite–water interface by surface X-ray scattering”, *Surf. Sci.* **2004**, *573*, 191–203.
- [38] C. Park, P. Fenter, K. Nagy, N. Sturchio, “Hydration and Distribution of Ions at the Mica-Water Interface”, *Phys. Rev. Lett.* **2006**, *97*, 016101.
- [39] C. Park, P. a. Fenter, N. C. Sturchio, K. L. Nagy, “Thermodynamics, interfacial structure, and pH hysteresis of Rb<sup>+</sup> and Sr<sup>2+</sup> adsorption at the muscovite (001)-solution interface”, *Langmuir* **2008**, *24*, 13993–14004.
- [40] S. S. Lee, P. Fenter, C. Park, N. C. Sturchio, K. L. Nagy, “Hydrated cation speciation at the muscovite (001)-water interface”, *Langmuir* **2010**, *26*, 16647–16651.
- [41] O. Teschke, G. Ceotto, E. F. de Souza, “Interfacial water dielectric-permittivity-profile measurements using atomic force microscopy”, *Phys. Rev. E* **2001**, *64*, 011605.
- [42] D. J. Bonthuis, S. Gekle, R. R. Netz, “Dielectric profile of interfacial water and its effect on double-layer capacitance”, *Phys. Rev. Lett.* **2011**, *107*, 1–5.

- [43] A. Schlaich, E. W. Knapp, R. R. Netz, “Water Dielectric Effects in Planar Confinement”, *Phys. Rev. Lett.* **2016**, *117*, 048001.
- [44] S. S. Lee, P. Fenter, K. L. Nagy, N. C. Sturchio, “Monovalent Ion Adsorption at the Muscovite (001)-Solution Interface: Relationships among Ion Coverage and Speciation, Interfacial Water Structure, and Substrate Relaxation”, *Langmuir* **2012**, *28*, 8637–8650.
- [45] I. C. Bourg, S. S. Lee, P. Fenter, C. Tournassat, “Stern Layer Structure and Energetics at Mica–Water Interfaces”, *J. Phys. Chem. C* **2017**, *121*, 9402–9412.
- [46] S. Nemsák, A. Shavorskiy, O. Karslioglu, I. Zegkinoglou, A. Rattanachata, C. S. Conlon, A. Keqi, P. K. Greene, E. C. Burks, F. Salmassi, E. M. Gullikson, S.-H. Yang, K. Liu, H. Bluhm, C. S. Fadley, “Concentration and chemical-state profiles at heterogeneous interfaces with sub-nm accuracy from standing-wave ambient-pressure photoemission”, *Nat. Commun.* **2014**, *5*, 5441.
- [47] S. ben Jabrallah, F. Malloggi, L. Belloni, L. Girard, D. Novikov, C. Mocuta, D. Thiaudière, J. Daillant, “Electrolytes at interfaces: accessing the first nanometers using X-ray standing waves”, *Phys. Chem. Chem. Phys.* **2017**, *19*, 167–174.
- [48] S. S. Lee, P. Fenter, K. L. Nagy, N. C. Sturchio, “Real-time observation of cation exchange kinetics and dynamics at the muscovite-water interface”, *Nat. Commun.* **2017**, *8*, 15826.
- [49] J. Pittler, W. Bu, D. Vaknin, A. Travesset, D. J. McGillivray, M. Lösche, “Charge Inversion at Minute Electrolyte Concentrations”, *Phys. Rev. Lett.* **2006**, *97*, 046102.
- [50] W. Wang, N. a. Anderson, A. Travesset, D. Vaknin, “Regulation of the Electric Charge in Phosphatidic Acid Domains”, *J. Phys. Chem. B* **2012**, *116*, 7213–7220.
- [51] W. Wang, R. Y. Park, A. Travesset, D. Vaknin, “Ion-Specific Induced Charges at Aqueous Soft Interfaces”, *Phys. Rev. Lett.* **2011**, *106*, 056102.
- [52] M. Miller, M. Chu, B. Lin, M. Meron, P. Dutta, “Observation of Ordered Structures in Counterion Layers near Wet Charged Surfaces: A Potential Mechanism for Charge Inversion”, *Langmuir* **2016**, *32*, 73–77.
- [53] R. J. Alsop, R. Maria Schober, M. C. Rheinstädter, “Swelling of phospholipid membranes by divalent metal ions depends on the location of the ions in the bilayers”, *Soft Matter* **2016**, *12*, 6737–6748.
- [54] S. Ong, X. Zhao, K. B. Eisenthal, “Polarization of water molecules at a charged interface: second harmonic studies of the silica/water interface”, *Chem. Phys. Lett.* **1992**, *191*, 327–335.
- [55] Q. Du, E. Freysz, Y. R. Shen, “Vibrational spectra of water molecules at quartz/water interfaces”, *Phys. Rev. Lett.* **1994**, *72*, 238–241.
- [56] M. S. Yeganeh, S. M. Dougal, H. S. Pink, “Vibrational Spectroscopy of Water at Liquid/Solid Interfaces: Crossing the Isoelectric Point of a Solid Surface”, *Phys. Rev. Lett.* **1999**, *83*, 1179–1182.
- [57] S. C. Flores, J. Kherb, N. Konek, X. Chen, P. S. Cremer, “The Effects of Hofmeister Cations at Negatively Charged Hydrophilic Surfaces”, *J. Phys. Chem. C* **2012**, *116*, 5730–5734.
- [58] K. C. Jena, P. A. Covert, D. K. Hore, “The effect of salt on the water structure at a charged solid surface: Differentiating second- and third-order nonlinear contributions”, *J. Phys. Chem. Lett.* **2011**, *2*, 1056–1061.
- [59] A. A. Shahir, K. Khristov, K. T. Nguyen, A. V. Nguyen, E. Mileva, “Combined Sum Frequency Generation and Thin Liquid Film Study of the Specific Effect of Monovalent Cations on the Interfacial Water Structure”, *Langmuir* **2018**, *34*, 6844–6855.
- [60] Y.-C. Wen, S. Zha, X. Liu, S. Yang, P. Guo, G. Shi, H. Fang, Y. R. Shen, C. Tian, “Unveiling Microscopic Structures of Charged Water Interfaces by Surface-Specific Vibrational Spectroscopy”, *Phys. Rev. Lett.* **2016**, *116*, 016101.
- [61] L. B. Dreier, Y. Nagata, H. Lutz, G. Gonella, J. Hunger, E. H. Backus, M. Bonn, “Saturation of charge-induced water alignment at model membrane surfaces”, *Sci. Adv.* **2018**, *4*, 1–9.
- [62] R. Lenk, M. Bonzon, H. Greppin, “Dynamically oriented biological water as studied by NMR”, *Chem. Phys. Lett.* **1980**, *76*, 175–177.
- [63] G. M. Bowers, D. L. Bish, R. J. Kirkpatrick, “Cation exchange at the mineral-water interface: H<sub>3</sub>O<sup>+</sup>/K<sup>+</sup> competition at the surface of nano-muscovite”, *Langmuir* **2008**, *24*, 10240–10244.

- [64] R. A. Hillman, K. S. Ryder, E. Madrid, A. W. Burley, R. J. Wiltshire, J. Merotra, M. Grau, S. L. Horswell, A. Glidle, R. M. Dalgliesh, A. Hughes, R. Cubitte, A. Wildes, A. Hillman, K. S. Ryder, E. Madrid, A. W. Burley, R. J. Wiltshire, J. Merotra, M. Grau, S. L. Horswell, A. Glidle, R. M. Dalgliesh, A. Hughes, R. Cubitt, A. Wildes, "Structure and dynamics of phospholipid bilayer films under electrochemical control", *Faraday Discuss.* **2010**, *145*, 9.
- [65] M. Bai, A. Miskowicz, F. Y. Hansen, H. Taub, T. Jenkins, M. Tyagi, S. O. Diallo, E. Mamontov, K. W. Herwig, S.-K. Wang, "Study of water diffusion on single-supported bilayer lipid membranes by quasielastic neutron scattering", *EPL (Europhysics Lett.)* **2012**, *98*, 48006.
- [66] F. Zaera, "Probing Liquid/Solid Interfaces at the Molecular Level", *Chem. Rev.* **2012**, *112*, 2920–2986.
- [67] S. H. Park, G. Sposito, "Structure of Water Adsorbed on a Mica Surface", *Phys. Rev. Lett.* **2002**, *89*, 085501.
- [68] Y. Leng, P. T. Cummings, "Hydration structure of water confined between mica surfaces", *J. Chem. Phys.* **2006**, *124*, 074711.
- [69] H. Sakuma, K. Kawamura, "Structure and dynamics of water on Li<sup>+</sup>, Na<sup>+</sup>, K<sup>+</sup>, Cs<sup>+</sup>, H<sub>3</sub>O<sup>+</sup>-exchanged muscovite surfaces: A molecular dynamics study", *Geochim. Cosmochim. Acta* **2011**, *75*, 63–81.
- [70] K. Kobayashi, Y. Liang, S. Murata, T. Matsuoka, S. Takahashi, N. Nishi, T. Sakka, "Ion Distribution and Hydration Structure in the Stern Layer on Muscovite Surface", *Langmuir* **2017**, *33*, 3892–3899.
- [71] M. Fitzner, G. C. Sosso, S. J. Cox, A. Michaelides, "The Many Faces of Heterogeneous Ice Nucleation: Interplay Between Surface Morphology and Hydrophobicity", *J. Am. Chem. Soc.* **2015**, *137*, 13658–13669.
- [72] J. Faraudo, A. Travesset, "Phosphatidic Acid Domains in Membranes: Effect of Divalent Counterions", *Biophys. J.* **2007**, *92*, 2806–2818.
- [73] R. A. Böckmann, A. Hac, T. Heimburg, H. Grubmüller, "Effect of sodium chloride on a lipid bilayer", *Biophys. J.* **2003**, *85*, 1647–1655.
- [74] A. Martín-Molina, C. Rodríguez-Beas, J. Faraudo, "Charge Reversal in Anionic Liposomes: Experimental Demonstration and Molecular Origin", *Phys. Rev. Lett.* **2010**, *104*, 168103.
- [75] A. Martín-Molina, C. Rodríguez-Beas, J. Faraudo, "Effect of Calcium and Magnesium on Phosphatidylserine Membranes: Experiments and All-Atomic Simulations", *Biophys. J.* **2012**, *102*, 2095–2103.
- [76] R. Tivony, J. Klein, "Probing the Surface Properties of Gold at Low Electrolyte Concentration", *Langmuir* **2016**, *32*, 7346–7355.
- [77] J. N. Israelachvili, R. M. Pashley, "Molecular layering of water at surfaces and origin of repulsive hydration forces", *Nature* **1983**, *306*, 249–250.
- [78] R. M. Pashley, "DLVO and hydration forces between mica surfaces in Li<sup>+</sup>, Na<sup>+</sup>, K<sup>+</sup>, and Cs<sup>+</sup>electrolyte solutions: A correlation of double-layer and hydration forces with surface cation exchange properties", *J. Colloid Interface Sci.* **1981**, *83*, 531–546.
- [79] R. Pashley, "Hydration forces between mica surfaces in aqueous electrolyte solutions", *J. Colloid Interface Sci.* **1981**, *80*, 153–162.
- [80] J. Klein, E. Kumacheva, "Simple liquids confined to molecularly thin layers. I. Confinement-induced liquid-to-solid phase transitions", *J. Chem. Phys.* **1998**, *108*, 6996–7009.
- [81] J. N. Israelachvili, P. M. McGuiggan, "Forces Between Surfaces in Liquids", *Science (80-. )*. **1988**, *241*, 795–800.
- [82] V. Parsegian, T. Zemb, "Hydration forces: Observations, explanations, expectations, questions", *Curr. Opin. Colloid Interface Sci.* **2011**, *16*, 618–624.
- [83] G. Vigil, Z. Xu, S. Steinberg, J. Israelachvili, "Interactions of Silica Surfaces", *J. Colloid Interface Sci.* **1994**, *165*, 367–385.
- [84] J. Britton, N. E. A. Cousens, S. W. Coles, C. D. van Engers, V. Babenko, A. T. Murdock, A. Koós, S. Perkin, N. Grobert, "A Graphene Surface Force Balance", *Langmuir* **2014**, *30*, 11485–11492.

- [85] Q. Tan, G. Zhao, Y. Qiu, Y. Kan, Z. Ni, Y. Chen, “Experimental Observation of the Ion–Ion Correlation Effects on Charge Inversion and Strong Adhesion between Mica Surfaces in Aqueous Electrolyte Solutions”, *Langmuir* **2014**, *30*, 10845–10854.
- [86] R. García, R. Pérez, “Dynamic atomic force microscopy methods”, *Surf. Sci. Rep.* **2002**, *47*, 197–301.
- [87] Y. F. Dufrêne, T. Ando, R. Garcia, D. Alsteens, D. Martinez-Martin, A. Engel, C. Gerber, D. J. Müller, “Imaging modes of atomic force microscopy for application in molecular and cell biology”, *Nat. Nanotechnol.* **2017**, *12*, 295–307.
- [88] Y. Diao, R. M. Espinosa-Marzal, “Molecular insight into the nanoconfined calcite–solution interface”, *Proc. Natl. Acad. Sci.* **2016**, *113*, 12047–12052.
- [89] J. Valle-Delgado, J. Molina-Bolívar, F. Galisteo-González, M. Gálvez-Ruiz, “Evidence of hydration forces between proteins”, *Curr. Opin. Colloid Interface Sci.* **2011**, *16*, 572–578.
- [90] G. Gramse, M. A. Edwards, L. Fumagalli, G. Gomila, “Theory of amplitude modulated electrostatic force microscopy for dielectric measurements in liquids at MHz frequencies”, *Nanotechnology* **2013**, *24*, DOI [10.1088/0957-4484/24/41/415709](https://doi.org/10.1088/0957-4484/24/41/415709).
- [91] G. Gramse, A. Dols-Perez, M. Edwards, L. Fumagalli, G. Gomila, “Nanoscale Measurement of the Dielectric Constant of Supported Lipid Bilayers in Aqueous Solutions with Electrostatic Force Microscopy”, *Biophys. J.* **2013**, *104*, 1257–1262.
- [92] J. I. Kilpatrick, S.-H. Loh, S. P. Jarvis, “Directly Probing the Effects of Ions on Hydration Forces at Interfaces”, *J. Am. Chem. Soc.* **2013**, *135*, 2628–2634.
- [93] T. Fukuma, M. J. Higgins, S. P. Jarvis, “Direct Imaging of Individual Intrinsic Hydration Layers on Lipid Bilayers at Ångstrom Resolution”, *Biophys. J.* **2007**, *92*, 3603–3609.
- [94] M. J. Higgins, M. Polcik, T. Fukuma, J. E. Sader, Y. Nakayama, S. P. Jarvis, “Structured water layers adjacent to biological membranes.”, *Biophys. J.* **2006**, *91*, 2532–42.
- [95] T. Fukuma, K. Kobayashi, K. Matsushige, H. Yamada, “True atomic resolution in liquid by frequency-modulation atomic force microscopy”, *Appl. Phys. Lett.* **2005**, *87*, 034101.
- [96] T. Fukuma, M. Higgins, S. Jarvis, “Direct Imaging of Lipid-Ion Network Formation under Physiological Conditions by Frequency Modulation Atomic Force Microscopy”, *Phys. Rev. Lett.* **2007**, *98*, 106101.
- [97] B. W. Hoogenboom, H. J. Hug, Y. Pellmont, S. Martin, P. L. T. M. Frederix, D. Fotiadis, A. Engel, “Quantitative dynamic-mode scanning force microscopy in liquid”, *Appl. Phys. Lett.* **2006**, *88*, 193109.
- [98] C. Leung, A. Bestembayeva, R. Thorogate, J. Stinson, A. Pyne, C. Marcovich, J. Yang, U. Drechsler, M. Despont, T. Jankowski, M. Tschöpe, B. W. Hoogenboom, “Atomic Force Microscopy with Nanoscale Cantilevers Resolves Different Structural Conformations of the DNA Double Helix”, *Nano Lett.* **2012**, *12*, 3846–3850.
- [99] K. H. Sheikh, C. Giordani, J. I. Kilpatrick, S. P. Jarvis, “Direct Submolecular Scale Imaging of Mesoscale Molecular Order in Supported Dipalmitoylphosphatidylcholine Bilayers”, *Langmuir* **2011**, *27*, 3749–3753.
- [100] K. H. Sheikh, S. P. Jarvis, “Crystalline hydration structure at the membrane-fluid interface of model lipid rafts indicates a highly reactive boundary region.”, *J. Am. Chem. Soc.* **2011**, *133*, 18296–303.
- [101] S. H. Loh, S. P. Jarvis, “Visualization of ion distribution at the mica-electrolyte interface”, *Langmuir* **2010**, *26*, 9176–9178.
- [102] U. M. Ferber, G. Kaggwa, S. P. Jarvis, “Direct imaging of salt effects on lipid bilayer ordering at sub-molecular resolution”, *Eur. Biophys. J.* **2011**, *40*, 329–338.
- [103] M. Ricci, P. Spijker, K. Voitchovsky, “Water-induced correlation between single ions imaged at the solid-liquid interface.”, *Nat. Commun.* **2014**, *5*, 4400.
- [104] K. Voitchovsky, J. J. Kuna, S. A. Contera, E. Tosatti, F. Stellacci, “Direct mapping of the solid-liquid adhesion energy with subnanometre resolution.”, *Nat. Nanotechnol.* **2010**, *5*, 401–405.
- [105] K. Voitchovsky, “Anharmonicity, solvation forces, and resolution in atomic force microscopy at the solid-liquid interface”, *Phys. Rev. E* **2013**, *88*, 022407.

- [106] M. Ricci, P. Spijker, F. Stellacci, J.-F. Molinari, K. Voitchovsky, “Direct Visualization of Single Ions in the Stern Layer of Calcite”, *Langmuir* **2013**, *29*, 2207–2216.
- [107] I. Siretanu, D. van den Ende, F. Mugele, “Atomic structure and surface defects at mineral-water interfaces probed by in situ atomic force microscopy”, *Nanoscale* **2016**, *8*, 8220–8227.
- [108] H. Hölscher, S. M. Langkat, A. Schwarz, R. Wiesendanger, “Measurement of three-dimensional force fields with atomic resolution using dynamic force spectroscopy”, *Appl. Phys. Lett.* **2002**, *81*, 4428–4430.
- [109] T. Fukuma, Y. Ueda, S. Yoshioka, H. Asakawa, “Atomic-Scale Distribution of Water Molecules at the Mica-Water Interface Visualized by Three-Dimensional Scanning Force Microscopy”, *Phys. Rev. Lett.* **2010**, *104*, 016101.
- [110] K. Kobayashi, N. Oyabu, K. Kimura, S. Ido, K. Suzuki, T. Imai, K. Tagami, M. Tsukada, H. Yamada, “Visualization of hydration layers on muscovite mica in aqueous solution by frequency-modulation atomic force microscopy”, *J. Chem. Phys.* **2013**, *138*, 184704.
- [111] H. Asakawa, S. Yoshioka, K. I. Nishimura, T. Fukuma, “Spatial distribution of lipid headgroups and water molecules at membrane/water interfaces visualized by three-dimensional scanning force microscopy”, *ACS Nano* **2012**, *6*, 9013–9020.
- [112] H. Söngen, C. Marutschke, P. Spijker, E. Holmgren, I. Hermes, R. Bechstein, S. Klassen, J. Tracey, A. S. Foster, A. Kühnle, “Chemical Identification at the Solid–Liquid Interface”, *Langmuir* **2017**, *33*, 125–129.
- [113] K. Miyazawa, N. Kobayashi, M. Watkins, A. L. Shluger, K.-i. Amano, T. Fukuma, “A relationship between three-dimensional surface hydration structures and force distribution measured by atomic force microscopy”, *Nanoscale* **2016**, *8*, 7334–42.
- [114] K. Miyazawa, M. Watkins, A. L. Shluger, T. Fukuma, “Influence of ions on two-dimensional and three-dimensional atomic force microscopy at fluorite–water interfaces”, *Nanotechnology* **2017**, *28*, 245701.
- [115] T. Fukuma, B. Reischl, N. Kobayashi, P. Spijker, F. F. Canova, K. Miyazawa, A. S. Foster, “Mechanism of atomic force microscopy imaging of three-dimensional hydration structures at a solid-liquid interface”, *Phys. Rev. B* **2015**, *92*, 155412.
- [116] J. E. Sader, S. P. Jarvis, “Accurate formulas for interaction force and energy in frequency modulation force spectroscopy”, *Appl. Phys. Lett.* **2004**, *84*, 1801–1803.
- [117] D. Martin-Jimenez, E. Chacon, P. Tarazona, R. Garcia, “Atomically resolved three-dimensional structures of electrolyte aqueous solutions near a solid surface”, *Nat. Commun.* **2016**, *7*, 12164.
- [118] D. Martin-Jimenez, R. Garcia, “Identification of Single Adsorbed Cations on Mica–Liquid Interfaces by 3D Force Microscopy”, *J. Phys. Chem. Lett.* **2017**, *8*, 5707–5711.
- [119] E. T. Herruzo, H. Asakawa, T. Fukuma, R. Garcia, “Three-dimensional quantitative force maps in liquid with 10 piconewton, angstrom and sub-minute resolutions”, *Nanoscale* **2013**, *5*, 2678–2685.
- [120] K. Umeda, L. Zivanovic, K. Kobayashi, J. Ritala, H. Kominami, P. Spijker, A. S. Foster, H. Yamada, “Atomic-resolution three-dimensional hydration structures on a heterogeneously charged surface”, *Nat. Commun.* **2017**, *8*, 2111.
- [121] K. Kuchuk, U. Sivan, “Hydration Structure of a Single DNA Molecule Revealed by Frequency-Modulation Atomic Force Microscopy”, *Nano Lett.* **2018**, *18*, 2733–2737.
- [122] C. Peter, G. Hummer, “Ion Transport through Membrane-Spanning Nanopores Studied by Molecular Dynamics Simulations and Continuum Electrostatics Calculations”, *Biophys. J.* **2005**, *89*, 2222–2234.
- [123] A. Phan, D. R. Cole, R. G. Weiß, J. Dzubiella, A. Striolo, “Confined Water Determines Transport Properties of Guest Molecules in Narrow Pores”, *ACS Nano* **2016**, *10*, 7646–7656.
- [124] S. Antoranz Contera, K. Voitchovsky, J. F. Ryan, “Controlled ionic condensation at the surface of a native extremophile membrane.”, *Nanoscale* **2010**, *2*, 222–9.
- [125] A. Springer, V. Hagen, D. a. Cherepanov, Y. N. Antonenko, P. Pohl, “Protons migrate along interfacial water without significant contributions from jumps between ionizable groups on the membrane surface.”, *Proc. Natl. Acad. Sci. U. S. A.* **2011**, *108*, 14461–14466.

- [126] J. M. Gibbs-Davis, J. J. Kruk, C. T. Konek, K. A. Scheidt, F. M. Geiger, “Jammed Acid-Base Reactions at Interfaces”, *J. Am. Chem. Soc.* **2008**, *130*, 15444–15447.
- [127] D. T. Limmer, A. P. Willard, P. Madden, D. Chandler, “Hydration of metal surfaces can be dynamically heterogeneous and hydrophobic”, *Proc. Natl. Acad. Sci.* **2013**, *110*, 4200–4205.
- [128] D. T. Limmer, A. P. Willard, “Nanoscale heterogeneity at the aqueous electrolyte–electrode interface”, *Chem. Phys. Lett.* **2015**, *620*, 144–150.
- [129] D. Argyris, D. R. Cole, A. Striolo, “Ion-specific effects under confinement: The role of interfacial water”, *ACS Nano* **2010**, *4*, 2035–2042.
- [130] E. Mamontov, D. J. Wesolowski, L. Vlcek, P. T. Cummings, J. Rosenqvist, W. Wang, D. R. Cole, “Dynamics of Hydration Water on Rutile Studied by Backscattering Neutron Spectroscopy and Molecular Dynamics Simulation”, *J. Phys. Chem. C* **2008**, *112*, 12334–12341.
- [131] I. C. Bourg, G. Sposito, “Molecular dynamics simulations of the electrical double layer on smectite surfaces contacting concentrated mixed electrolyte (NaCl–CaCl<sub>2</sub>) solutions”, *J. Colloid Interface Sci.* **2011**, *360*, 701–715.
- [132] M. D. Fayer, “Dynamics of water interacting with interfaces, molecules, and ions.”, *Acc. Chem. Res.* **2012**, *45*, 3–14.
- [133] J. Song, J. Franck, P. Pincus, M. W. Kim, S. Han, “Specific Ions Modulate Diffusion Dynamics of Hydration Water on Lipid Membrane Surfaces”, *J. Am. Chem. Soc.* **2014**, *136*, 2642–2649.
- [134] S. Hocine, R. Hartkamp, B. Siboulet, M. Duvail, B. Coasne, P. Turq, J.-F. Dufrêche, “How Ion Condensation Occurs at a Charged Surface: A Molecular Dynamics Investigation of the Stern Layer for Water–Silica Interfaces”, *J. Phys. Chem. C* **2016**, *120*, 963–973.
- [135] H. Zhang, A. A. Hassanali, Y. K. Shin, C. Knight, S. J. Singer, “The water–amorphous silica interface: Analysis of the Stern layer and surface conduction”, *J. Chem. Phys.* **2011**, *134*, 024705.
- [136] D. E. Moilanen, N. E. Levinger, D. B. Spry, M. D. Fayer, “Confinement or the nature of the interface? Dynamics of nanoscopic water”, *J. Am. Chem. Soc.* **2007**, *129*, 14311–14318.
- [137] W. H. Briscoe, “Aqueous boundary lubrication: Molecular mechanisms, design strategy, and terra incognita”, *Curr. Opin. Colloid Interface Sci.* **2017**, *27*, 1–8.
- [138] J. Sotres, T. Arnebrant, “Experimental Investigations of Biological Lubrication at the Nanoscale: The Cases of Synovial Joints and the Oral Cavity”, *Lubricants* **2013**, *1*, 102–131.
- [139] L. Bocquet, P. Tabeling, “Physics and technological aspects of nanofluidics”, *Lab Chip* **2014**, *14*, 3143–3158.
- [140] N. Kastelowitz, V. Molinero, “Ice–Liquid Oscillations in Nanoconfined Water”, *ACS Nano* **2018**, *12*, 8234–8239.
- [141] S. Granick, S. Bae, S. Kumar, C. Yu, “Confined liquid controversies near closure?”, *Physics (College. Park. Md.)* **2010**, *3*, 73.
- [142] P. J. Feibelman, “Viscosity of Ultrathin Water Films Confined between Alumina Surfaces of Kaolinite: Ab Initio Simulations”, *J. Phys. Chem. C* **2013**, *117*, 6088–6095.
- [143] Y. Zhu, S. Granick, “Viscosity of Interfacial Water”, *Phys. Rev. Lett.* **2001**, *87*, 096104.
- [144] U. Raviv, P. Laurat, J. Klein, “Fluidity of water confined to subnanometre films”, *Nature* **2001**, *413*, 51–54.
- [145] U. Raviv, P. Laurat, J. Klein, “Time dependence of forces between mica surfaces in water and its relation to the release of surface ions”, *J. Chem. Phys.* **2002**, *116*, 5167.
- [146] U. Raviv, S. Perkin, P. Laurat, J. Klein, “Fluidity of Water Confined Down to Subnanometer Films”, *Langmuir* **2004**, *20*, 5322–5332.
- [147] G. H. Findenegg, S. Jähnert, D. Akcakayiran, A. Schreiber, “Freezing and Melting of Water Confined in Silica Nanopores”, *ChemPhysChem* **2008**, *9*, 2651–2659.

- [148] L. Fumagalli, A. Esfandiar, R. Fabregas, S. Hu, P. Ares, A. Janardanan, Q. Yang, B. Radha, T. Taniguchi, K. Watanabe, G. Gomila, K. S. Novoselov, A. K. Geim, “Anomalously low dielectric constant of confined water”, *Science (80-. )*. **2018**, *360*, 1339–1342.
- [149] K. Kapoor, V. Kanawade, V. Shukla, S. Patil, “A new tuning fork-based instrument for oscillatory shear rheology of nano-confined liquids”, *Rev. Sci. Instrum.* **2013**, *84*, 025101.
- [150] B. Kim, S. Kwon, M. Lee, Q. Kim, S. An, W. Jhe, “Probing nonlinear rheology layer-by-layer in interfacial hydration water”, *Proc. Natl. Acad. Sci.* **2015**, *112*, 201515033.
- [151] M. Antognozzi, A. D. L. Humphris, M. J. Miles, “Observation of molecular layering in a confined water film and study of the layers viscoelastic properties”, *Appl. Phys. Lett.* **2001**, *78*, 300.
- [152] D. Ortiz-Young, H.-C. Chiu, S. Kim, K. Voitchovsky, E. Riedo, “The interplay between apparent viscosity and wettability in nanoconfined water”, *Nat. Commun.* **2013**, *4*, 2482.
- [153] S. H. Khan, G. Matei, S. Patil, P. M. Hoffmann, “Dynamic Solidification in Nanoconfined Water Films”, *Phys. Rev. Lett.* **2010**, *105*, 106101.
- [154] S. H. Khan, P. M. Hoffmann, “Squeeze-out dynamics of nanoconfined water: A detailed nanomechanical study”, *Phys. Rev. E* **2015**, *92*, 042403.
- [155] S. H. Khan, E. L. Kramkowski, P. M. Hoffmann, “NaCl-Dependent Ordering and Dynamic Mechanical Response in Nanoconfined Water”, *Langmuir* **2016**, *32*, 10802–10807.
- [156] A. Ulcinas, G. Valdre, V. Snitka, M. J. Miles, P. M. Claesson, M. Antognozzi, “Shear Response of Nanoconfined Water on Muscovite Mica: Role of Cations”, *Langmuir* **2011**, *27*, 10351–10355.
- [157] T.-D. Li, H.-C. Chiu, D. Ortiz-Young, E. Riedo, “Nanorheology by atomic force microscopy”, *Rev. Sci. Instrum.* **2014**, *85*, 123707.
- [158] C. Cafolla, K. Voitchovsky, “Lubricating properties of single metal ions at interfaces”, *Nanoscale* **2018**, *10*, 11831–11840.
- [159] T.-D. Li, J. Gao, R. Szoszkiewicz, U. Landman, E. Riedo, “Structured and viscous water in subnanometer gaps”, *Phys. Rev. B* **2007**, *75*, 115415.
- [160] M. P. Goertz, J. E. Houston, X.-Y. Y. Zhu, “Hydrophilicity and the Viscosity of Interfacial Water”, *Langmuir* **2007**, *23*, 5491–5497.
- [161] S. Jeffery, P. M. Hoffmann, J. B. Pethica, C. Ramanujan, H. Ö. Özer, A. Oral, “Direct measurement of molecular stiffness and damping in confined water layers”, *Phys. Rev. B - Condens. Matter Mater. Phys.* **2004**, *70*, 054114.
- [162] T.-D. Li, E. Riedo, “Nonlinear Viscoelastic Dynamics of Nanoconfined Wetting Liquids”, *Phys. Rev. Lett.* **2008**, *100*, 106102.
- [163] A. Gaisinskaya-Kipnis, L. Ma, N. Kampf, J. Klein, “Frictional Dissipation Pathways Mediated by Hydrated Alkali Metal Ions”, *Langmuir* **2016**, *32*, 4755–4764.
- [164] L. Ma, A. Gaisinskaya-Kipnis, N. Kampf, J. Klein, “Origins of hydration lubrication”, *Nat. Commun.* **2015**, *6*, 6060.

## 2.0 DYNAMIC AFM: TECHNIQUES AND CANTILEVER CALIBRATION

The previous chapter outlined the many techniques which are available to characterise and investigate the structure of solid-liquid interfaces. Of these, only atomic force microscopy is able to operate on a wide variety of substrates fully immersed in liquid, extract physical properties from the interface *and* produce maps with lateral and vertical resolution on the sub-nanometre scale. These measurements shall prove crucial in this thesis' work in probing the nanoscale structure and dynamics on model crystals and biomembranes, and we shall therefore explore this technique in greater detail, covering the basic principles of operation, models of the cantilever's motion in fluids, and various application examples.

This chapter will briefly give an overview of the motivations to develop AFM beyond its initial "contact mode" origins to the (now standard) dynamic modes that regularly enable a sample's atomic-scale features to be resolved in ambient conditions in liquid. We shall discuss the operation techniques that allow not just topographic information but also material properties to be extracted from a sample. Finally, we shall demonstrate a novel method to calibrate the cantilever's flexural spring constant using just its thermal spectrum and with no assumptions made about its shape. Accurate knowledge of the spring constant is required if any quantitative information is to be gained from an AFM experiment, and our technique avoids many issues with common models, including dependence on cantilever shape and  $Q$ -factor.

### 2.1 Features, observables and modes of AFM operation

We first begin with a brief introduction to the practical aspects of AFM operation. Like other forms of scanning probe microscopies, it relies on a sharp tip being brought into close proximity to a sample, and then monitoring an interaction between the tip and sample as the tip is raster-scanned over a given area. By using a feedback system to keep the interaction of choice constant, information on the sample's topography, chemistry, physical and electrostatic properties can all potentially be extracted, with a resolution

that essentially only depends upon the tip size and the interaction's spatial gradient.

### 2.1.1 Contact mode AFM

AFM relies upon monitoring a generic interaction force between tip and sample while it scans, which allows a diverse range of samples to be studied in an equally broad span of environments. The original design for the atomic force microscope [1] involved monitoring the change in deflection,  $\Delta D$ , of a gold cantilever with an ultrasharp diamond tip as it was moved across an  $\text{Al}_2\text{O}_3$  surface. When the cantilever's normal displacement is kept relatively small, the tip-sample force exerted on the surface,  $F_{\text{ts}}$ , can be considered as a Hookean spring such that  $F_{\text{ts}} = k_1 \Delta D$ , with  $k_1$  the flexural spring constant of the lever. Thus, if the deflection is held constant by a feedback loop while the cantilever scans across a sample (in what is known as contact mode imaging) maps of the topography can be built up at constant force.

In that first instance, the cantilever's deflection was monitored using a scanning tunnelling microscope (STM), with the associated complexity that that entailed. Much more common in commercial machines now is the use of a laser focussed on the cantilever's reverse, with a four-quadrant photodiode (PD) used to detect the reflected signal (illustrated in Fig. 2.1). In this way, sub-nanometre changes in the cantilever's static deflection in  $z$  are translated into easily-detectable (vertical) movements of the laser on the PD. The varying geometry of the detector laser, cantilever and PD among AFMs means that there is no universal calibration from deflection (in nanometres) to laser displacement on the PD (in volts). Instead the so-called inverse optical lever sensitivity (invOLS,  $S_l^{-1}$ , in  $\text{nm V}^{-1}$ ) must be calibrated independently in each experiment (this will be discussed later in section 2.4).

The sensitivity of the cantilever to forces of  $\mathcal{O}(0.1 \text{ nN})$  means that in ambient conditions, van der Waals, electrostatic and capillary interactions can all conspire to make the net tip-sample interaction long-ranged and non-monotonic in  $z$  [2], with additional contributions from the thermal noise. These factors make feeding back solely on the force troublesome, especially when the interaction force gradient,  $k_{\text{ts}} = \text{d}F_{\text{ts}}/\text{d}z$ , is greater than the cantilever stiffness, as this will cause the tip to “snap” to contact with the sample, degrading the force sensitivity [3]. Further, the constant normal and lateral forces exerted by the cantilever while scanning can degrade both sample and tip in ways that are impossible to track *in situ*, which can especially be a problem when it comes to softer, biological specimens.

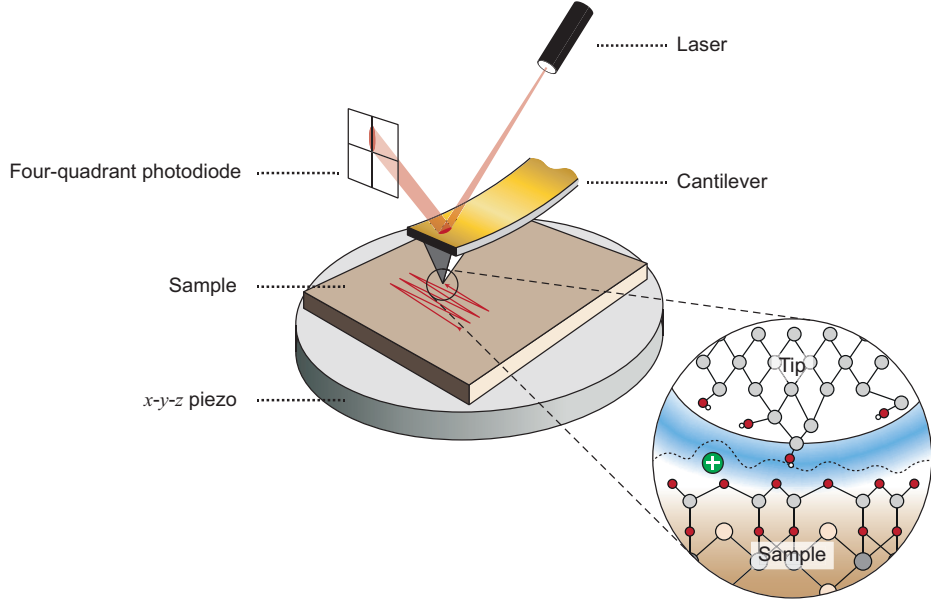


Fig. 2.1: Basic components of a commercial AFM. Changes in the cantilever’s static deflection (contact mode) or dynamic motion (FM or AM mode) while imaging are monitored by the motion of the laser spot in the four-quadrant photodiode. These are used as part of a feedback mechanism, which adjusts the  $z$  position of the sample to keep the imaging parameter constant, allowing topography maps to be built up as the tip is raster scanned across a sample (red zig-zag). (zoomed inset) In dynamic mode, monitored interactions tend to be shorter-ranged, meaning that just the outermost tip atoms (grey, upper) interact with the sample, enabling atomic-scale resolution in some cases (dashed line), despite the tip’s nanometre radius of curvature.

### 2.1.2 Frequency modulation AFM

Many of the problems associated with contact mode imaging can be overcome by driving the cantilever sinusoidally at one of its resonant frequencies,  $\omega_0$  and altering the focus of the feedback loops. Earlier examples of this technique measured the change of resonance frequency,  $\Delta\omega$ , due to interaction between the tip and sample [4, 5],

$$\frac{\Delta\omega}{\omega_0} = \frac{k_{ts}}{2k_1}, \quad (2.1)$$

valid for  $k_{ts} \ll k_1$  and a constant force gradient over the oscillation range. In what became known as frequency-modulation (FM) AFM,  $\Delta\omega$  and the oscillation amplitude,  $A$ , are kept constant while scanning and so the tip tracks contours of force gradient, essentially providing the same information as in contact mode. However, there are considerable advantages to operating the AFM dynamically. The measured interaction is the force *gradient*, which is typically more short-ranged than the net force. This dramatically increases the maximum achievable resolution, as it allows just the last few atoms of the tip to participate in the interaction, rather than the “macroscopic” body of the tip itself, as illustrated in the zoomed inset to Fig. 2.1. Further, operating in FM mode allows for non-contact interro-

gation of a sample, and minimises the  $1/\omega$  cantilever deflection noise by operating at high frequencies [2].

The first true atomic resolution FM-AFM experiments on silicon [5] were conducted in ultrahigh vacuum and with surprisingly large amplitudes,  $A$ , ( $\sim 68$  nm), relative to the chemical bond length. This inevitably meant that  $k_{ts}$  changed significantly during the tip's period, but it was found that these amplitudes were required so that the product  $k_1 A$  (equivalent to the maximum force) was great enough to overcome the attractive tip-sample interaction. Since then, high resolution has been shown to be possible with a great range of cantilever and operational parameters [6].

The above considerations are general for FM-AFM, but developments tended to focus on imaging in ultra-high vacuums that allowed precise control over the cantilever and tip environment. However, this misses out the great potential for AFM to operate in liquid environments on inert samples, which are clearly more relevant for this thesis. Operation in liquid comes with many problems, not least the added damping on the cantilever's motion (discussed in section 2.2), which reduces the quality factor,  $Q$ , and alters the associated feedback response [7]. Nevertheless, technological advancements that allowed reductions in deflection sensor noise to just  $17$  fm/ $\sqrt{\text{Hz}}$  [8, 9] allowed true molecular [10] and atomic-level [11] resolution in liquid to be attained by FM-AFM in 2005. This paved the way for the explosion in FM-AFM studies of the behaviour of water and solvated species at the fluid interface (see subsection 1.3.5), especially the imaging [12–16] and spectroscopy [17–20] of hydration layers.

Frequency modulation AFM has proven its ability to achieve resolution comparable to that of traditional STM, but immersed in fluid and on a great variety of samples. A key benefit is the ability to fairly straightforwardly reconstruct the tip-sample force from the recorded frequency shift [21–23]. This means that, with appropriate models for the sample's deformation, mechanical properties can be acquired, with the same resolution and rate as for imaging. There has been great success in recent years by applying this treatment to higher frequency oscillation modes of the cantilever, so that imaging and mechanical mapping can be carried out simultaneously [24–27].

### 2.1.3 Amplitude modulation AFM

Fig. 2.2(a) shows the amplitude spectrum of the flexural vibrations of the cantilever due solely to thermal motion in water at two different tip-sample separations (grey and black). It's clear that interactions with the sample and environment not only reduce the resonant

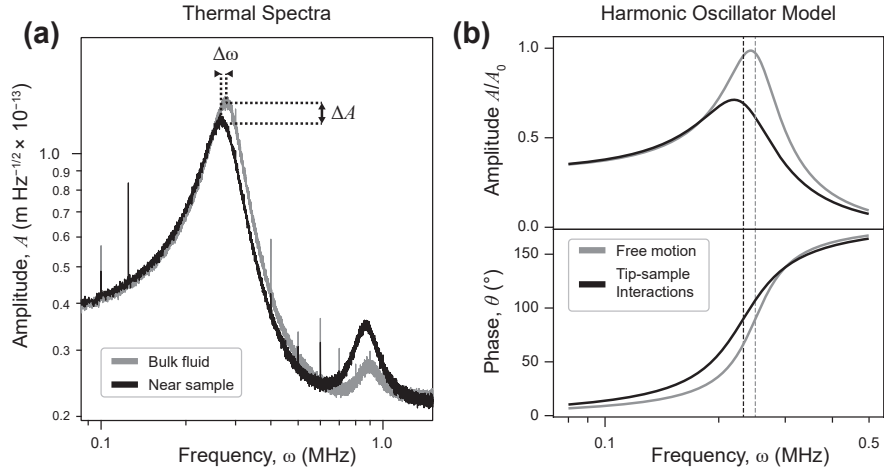


Fig. 2.2: Modelling the frequency-dependence of cantilever motion. (a) Flexural cantilever vibrations due to thermal motion recorded in water in bulk fluid (grey) and closer to the sample (black). The added hydrodynamic damping as well as tip-sample interactions in the latter situation cause a reduction in resonant frequency and amplitude (by  $\Delta\omega$  and  $\Delta A$ , respectively) of the first mode, as well as energy transfer to the second (peak increase at  $\sim 0.9$  MHz). (b) Treating the tip as a harmonic oscillator provides a useful description of its amplitude and phase variation with frequency (equation 2.7 and 2.8). Here a cantilever with  $\omega_0 = 0.25$  MHz and  $Q = 3$  is shown, both in the absence (grey) and presence (black) of conservative and dissipative tip-sample interactions that modify the effective stiffness and damping.

frequency of the first mode, but also its amplitude,  $A$ . This reduction in amplitude by  $\Delta A$  is key to the amplitude modulation (AM) AFM mode; the feedback loops adjust the  $z$ -piezo height so as to keep the oscillation amplitude constant while scanning across the sample. The excitation power and driving frequency are kept constant and the phase difference,  $\theta$ , between the driving signal and tip is allowed to vary. This in general allows for simpler and faster control electronics than for FM mode; there is no need to alter the driving frequency and monitor  $\Delta\omega$  in tandem because it is not necessary to keep the cantilever at resonance [28, 29]. As the amplitude and frequency signals relate to the variation of cantilever dynamics with separation from a surface, they both have similar  $z$ -dependencies and so can achieve similar levels of resolution, for a given free amplitude.

In early experiments, AM-AFM was avoided as a technique because of the mode's response time, which behaves as  $\tau = 2Q/\nu_0$  [4]. In air or vacuum,  $Q$  could be on the scale of tens of thousands, which clearly limits the bandwidth for feedback, even for high resonant frequencies. However, in liquid and with soft cantilevers,  $Q$  factors are reduced to  $\mathcal{O}(1)$ , effectively removing this obstacle. The main disadvantage of AM-AFM is that extracting or maintaining quantitative tip-sample interaction forces is much less straightforward than for FM-AFM and a complete inversion method is the subject of continued research [30–32]. That being said, there are still many approximate tools to extract information that goes

beyond sample topography by monitoring just the amplitude and phase of the cantilever's motion.

## 2.2 Approximating dynamic cantilever motion: harmonic oscillators and beyond

In contrast with contact mode, AM-AFM provides no direct way to measure the tip-sample interaction forces. Instead, these must be inferred from the dynamic properties such as cantilever amplitude and phase difference (relative to the driving excitation). Thus, any quantitative expression about the interaction implicitly requires knowledge of the cantilever motion. As cantilevers can be mechanically inhomogeneous with ill-defined dimensions, and oscillate in viscous media, an exact description of cantilever dynamics is usually beyond our grasp, but remarkable progress can be made with rather simple models. One of these – the harmonic oscillator formalism – is discussed below.

We begin by assuming that the cantilever is a cuboid of dimensions  $L$  (length),  $b$  (width),  $h$  (thickness) and can be described by the Euler-Bernoulli beam equation [28]:

$$EI \frac{\partial^4}{\partial x^4} W(x, t) + \rho_c b h \frac{\partial^2}{\partial t^2} W(x, t) = F_{\text{exc}} + F_{\text{int}}, \quad (2.2)$$

where  $E$ ,  $I$  and  $\rho_c$  are the lever's Young's modulus, rotary inertia and density respectively. The excitation force is  $F_{\text{exc}}$  and  $W(x, t)$  is the displacement of a thin section of the cantilever at position  $x$  along its length at time  $t$ . A generalised “interaction” force is given by  $F_{\text{int}}$ , which contains contributions from the surrounding fluid, as well as direct tip-sample forces. With the boundary conditions given by the tip being clamped at one end ( $W(0, t) = 0$ ), and the assumption that only the fundamental Eigenmode dominates cantilever motion, the description of the tip (i.e.  $W(L, t)$ ) as a damped simple harmonic oscillator can be recovered [30]:

$$m\ddot{\xi} + \mu\dot{\xi} + k_1\xi = F \cos(\omega t) + F_{\text{int}}. \quad (2.3)$$

The probe's instantaneous position is given by  $\xi$ , the effective tip mass is  $m$ , the damping coefficient is  $\mu$  and  $k_1$  is the flexural stiffness, as before. We have assumed the excitation force is sinusoidal so that  $F_{\text{exc}} = F \cos(\omega t)$ , with angular frequency  $\omega = 2\pi\nu$ . The quantities here can all be related to experimental observables by  $m = k_1/\omega_0^2$ ,  $\mu = k_1/(Q\omega_0)$  and  $F = k_1 A_0/Q$ , for angular resonance frequency  $\omega_0$  and free (non-interacting) amplitude  $A_0$ . This implies harmonic tip motion of the form

$$\xi(z, t) = \xi_0(z) + A(z) \sin(\omega t + \theta(z)), \quad (2.4)$$

where  $A(z)$  and  $\theta(z)$  are the amplitude and phase of the cantilever end; precisely the variables accessible during amplitude-modulation operation.

### 2.2.1 Phase-contrast imaging; extracting mechanical and energetic properties with high lateral resolution

In general, the tip-sample interaction force is composed of a non-linear combination of conservative,  $F_c$ , and non-conservative,  $F_{nc}$ , forces. However, use of the harmonic approximation simplifies the form of the average energy dissipated by the tip over a cycle,  $E_{dis}$ ; it can be found by integrating  $\dot{\xi}F_{nc}$  over one oscillation period, leading to the expression [30, 33, 34]

$$E_{dis} = -\pi \frac{k_1 A^2}{Q} \left( \frac{A_0}{A} \cos \theta - \frac{\omega}{\omega_0} \right), \quad (2.5)$$

which is valid regardless of the form of  $F_{nc}$ , as long as the motion is totally harmonic. The references of [33, 34] produce slightly different, but equivalent forms of equation 2.5. This is key for AM-AFM imaging; the amplitude is (nominally) kept constant over a scan, and any changes in the tip's phase are thus entirely due to lateral variation in  $E_{dis}$  through interaction with either the interface or the sample itself. The ability of phase imaging to directly resolve sample areas with different mechanical properties has been explored to great extent for over two decades [35], with success on polymers [36, 37], fabricated monolayers [38] and entire bacteria [39], as well as more advanced high resolution imaging of membrane proteins [40] and molecular details of the electrolyte-crystal interface [41–43].

The contrast in phase scans is sensitive to the AM-AFM imaging parameters such as set-point amplitude (relative to  $A_0$ ), because these determine the maximum force exerted by the tip and thus the energy dissipated per cycle [36]. Quantifying the factors contributing to  $E_{dis}$  is usually impractical, not least because of anomalous energy transfers between cantilever modes<sup>1</sup> [44–47], but for large  $A_0$  and significant tip-sample interactions (i.e. physically tapping on the surface), it is still possible to relate the phase signal to well-understood continuum mechanical properties such as stiffness [36]. The same cannot necessarily be said of small-amplitude AFM in liquid with  $A_0 \lesssim 2$  nm. In these situations, depending on the molecular dimensions of the solvent, the tip will oscillate between only a few discrete layers of fluid at the interface. Hence a significant proportion

<sup>1</sup> See e.g. the increase in amplitude at  $\nu \sim 0.9$  MHz in Fig. 2.2(a) when the cantilever is oscillating closer to the sample.

of energy will be dissipated into the fluid layers itself [48–53], often manifesting itself in oscillatory tip damping profiles. This dissipation on a molecular length-scale is often ascribed to the energy required to continuously perturb and reform layers of solvent, and thus gives information on how easy it is for fluid to slip across a solid or soft surface. In fact, Voitchovsky *et al.* extended this analogy to formally relate the macroscopic concept of “wetting”, measured *via* the contact angle of a droplet on a surface, to the microscopic energy dissipation of an AFM tip oscillating in the interfacial fluid [41]. The work of adhesion of a liquid to a solid,  $W_{sl}$ , a thermodynamic concept expressing the energy required to “create” a unit area of solid-liquid interface, was found to relate to the tip dissipation by the equation:

$$\lambda E_{\text{dis}} = \frac{8\pi R}{\alpha} \sqrt{W_{sl}W_{tl}} \left( e^{-\alpha\sigma/2} - e^{-\alpha(A+\sigma)/2} \right). \quad (2.6)$$

Here, the fluid’s molecular size and decay length of the interfacial layer are given by  $\sigma$  and  $\alpha$  respectively,  $W_{tl}$  is the work of adhesion for the liquid and the tip (determined independently) and the effective radius of curvature of the tip is  $R$ . Thus, the measured phase difference,  $\theta$  can be used, in combination with equation 2.5 and 2.6 to relatively straightforwardly extract the nanoscale work of adhesion of a liquid for a solid, as long as the tip spends the majority of its time oscillating within the interfacial fluid. Equation 2.6 was demonstrated to agree very well with the  $W_{sl}$  extracted from contact angle measurements, although a calibration factor,  $\lambda$ , is required, likely due to simplifications inherent in the model’s calculation of the pressure, the shape of the tip, or the thermodynamic nature of the oscillation.

### 2.2.2 Alternative descriptions of cantilever dynamics

While the simple harmonic oscillator formalism has allowed a great deal of insight to be gained from AM-AFM experiments, it is certainly rather simplistic in its assumption of the tip being a point mass with totally independent excitation modes and linear interactions. The properties of the cantilever’s fluid environment are also neglected in the majority of models, except *via* perturbations that introduce an effective interaction stiffness,  $k_{\text{eff}} = k + k_{\text{int}}$ , and damping,  $\mu_{\text{eff}} = \mu + \mu_{\text{int}}$ . These alter the oscillator’s resonance and quality factor such that  $\omega_{\text{eff}} = \sqrt{k_{\text{eff}}/m}$  and  $Q_{\text{eff}} = m\omega_{\text{eff}}/\mu_{\text{eff}}$ . Finally, we arrive at the well-known expressions for the frequency dependence of the perturbed oscillator’s amplitude and phase:

$$A(\omega) = \frac{F/m}{\left((\omega_{\text{eff}}^2 - \omega^2)^2 + (\omega\omega_{\text{eff}}/Q_{\text{eff}})^2\right)^{1/2}}; \quad (2.7)$$

$$\tan(\theta(\omega)) = \frac{\omega\omega_{\text{eff}}/Q_{\text{eff}}}{\omega_{\text{eff}}^2 - \omega^2}; \quad (2.8)$$

both of which are illustrated in Fig. 2.2(b), for an unperturbed (grey,  $k_{\text{int}} = \mu_{\text{int}} = 0$ ) and perturbed oscillator (black).

Work by Sader [54], which modelled the frequency response of cantilevers with arbitrary cross-sections, showed that for typical cantilever dimensions and resonant frequencies, the harmonic approximation is invalid due to its assumption of inviscid fluids. Instead, equation 2.2 can be explicitly solved while accommodating the Navier-Stokes behaviour of the fluid, leading to the dimensionless, complex quantity known as the hydrodynamic function,  $\Gamma(\omega)$ . The function effectively describes the frequency-dependence of the cantilever's energy dissipation as it oscillates in a viscous fluid and can be analytically solved for a beam with a circular cross-section:

$$\Gamma_{\text{circ}}(\omega) = 1 + \frac{4iK_1(-i\sqrt{i\text{Re}})}{\sqrt{i\text{Re}}K_0(-i\sqrt{i\text{Re}})}. \quad (2.9)$$

Here, the Reynold's number for a fluid of density,  $\rho_f$ , and viscosity,  $\eta_f$ , is  $\text{Re} = \rho_f\omega b^2/4\eta_f$ , and  $K_0, K_1$  are modified Bessel functions of the fourth kind. However for any other cross-sectional form of cantilever, a numerical correction factor must be applied:

$$\Gamma(\omega) = \Omega(\omega)\Gamma_{\text{circ}}(\omega) \quad (2.10)$$

where the complex coefficients  $\Omega(\omega)$  for a rectangular beam can be found in equations 21(a) and (b) of ref. [54].

While the Sader approach has become a benchmark tool for describing the motion of cantilevers, as well as calibrating their mechanical properties (discussed further in section 2.4), it can rapidly lose accuracy in practice and does not easily capture non-linear dynamics. Sader *et al.* highlighted this in a study that modelled the hydrodynamic influence of a solid surface on a vibrating cantilever [55], finding a dramatically increased dissipation as the separation between the two decreased below the lever's width. However, even this analysis was based on the assumption that the cantilever's width was constant and much smaller than its length. These issues can be somewhat circumvented with explicit finite-element models [7] or numerical simulations [44, 56], but both methods are

rather involved when compared to the relative simplicity of the harmonic approximation, and the latter is still common in interfacial studies.

## 2.3 Approaches for obtaining high resolution in dynamic AFM

It is clear from the discussion thus far in this chapter, that a full description of the tip's behaviour when operating in liquid requires precise knowledge of cantilever properties, operating parameters, sample chemistry and fluid dynamics. This is unlikely to be possible and is certainly not practical in the vast majority of cases, especially in complex biological systems that are far from ideal. Instead, over thirty years of AFM experiments and simulations have shed light on the key parameters necessary to obtain sub-nanometre lateral resolution in liquid, and various rules of thumb have been proposed. These can be seen as minimum conditions that must be fulfilled if atomic-scale contrast to be acquired (but do not guarantee it!). As high-resolution imaging of ionic organisation in the Stern layer is key to many of the experiments presented in this thesis, the current best-practice in AM-AFM imaging will be discussed and a practical guide to obtaining similar results will be discussed.

### 2.3.1 Solvation forces and vertical resolution

Chapter 1 highlighted the manner in which solid and soft surfaces modify the density and dynamics of aqueous electrolyte solutions, especially in the first few nanometres adjacent to the interface. This is most clear in ideal, molecularly flat interfaces such as calcite, highly ordered pyrolytic graphite (HOPG) or mica, on which oscillatory forces due to molecular layering are routinely observed [50, 57–61]. However, even in the case of rougher or more flexible surfaces, for which such high levels of ordering are not found, strongly-bound ions or waters generate monotonic repulsive forces when separations between surfaces are small [62, 63]. These forces reflect the energy necessary to remove solvated species from the interface, and are well-modelled by an exponential decay in  $z$  [56, 64–66]. While such repulsive interactions are generally termed hydration forces due to their prevalence in biological, aqueous systems, the reality is that as long as there is significant fluid affinity for the solid (macroscopically equivalent to the fluid “wetting” the surface), such forces will be present [41].

Solvation forces and their strength relative to other, longer-ranged interactions, are significant because they determine the changes to the cantilever's dynamic motion that are detected and used as part of the feedback loops. Formally, the noise in the measured height for any scanning probe technique,  $\delta h$ , is described by [2]

$$\delta h = \frac{\delta A}{|dA/dz|}. \quad (2.11)$$

Here the example uses the noise in the oscillation amplitude, but  $\delta A$  can in principle be any physical observable associated with the tip-sample interaction. Hence the resolution fundamentally depends on the gradient of the interaction,  $|dA/dz|$ ; this can be seen from the high resolution of STM, which results from the electron tunnelling current having an exponential distance-dependence [2]. The hydration forces will modify the cantilever amplitude *via* conservative and dissipative interactions (in a similar manner to Fig. 2.2(b)), meaning that  $A(z)$  has a comparable exponential drop off to the hydration force, permitting  $z$ -resolution of  $\mathcal{O}(10\text{-}100 \text{ pm})$ .

Recent advances in MD simulation capabilities, as well as the development of novel AFM techniques (see subsection 1.3.5) have allowed the solvation structure and its effects on tip forces to be probed in three dimensions experimentally and *in silico*, in comparable systems with minimal assumptions [57, 58, 67–69]. The explicit simulation of a tip throughout its oscillation cycle in refs [57, 67] allowed the precise mechanism of dynamic AFM image formation from fluid density oscillations to be uncovered. The authors highlighted the importance of highly ordered hydration shells on both tip and sample, which produced constructive and destructive “interference” in the free energy of the tip, as it moves through the interfacial layer. Further, the repulsive force was seen to be generated entirely by the confinement of water between tip and sample (although no dissolved ions were considered in the MD simulations).

Thus, a crucial requirement when aiming for high resolution imaging is for both the tip and sample to significantly structure the solvent, relative to bulk. This generates a well-defined solvation landscape, with characteristic short-ranged variations in solvent density that improve both vertical and lateral imaging quality. To some extent, this relaxes the need for a truly atomically sharp tip; the short-ranged interactions allow just the final few atoms to participate in the imaging process (inset to Fig. 2.1). Hence, even tips with nominal radii of curvature of  $> 10 \text{ nm}$  can still achieve atomic-scale resolution. This is well-demonstrated for molecularly smooth surfaces, but as soon as a degree of roughness or curvature is introduced, one must consider the convolution between tip and sample shape. For example, if a surface displayed protrusions of idealised “spikes” (i.e. with a negligible lateral profile), the finite width of the tip would broaden the apparent size of the features, distorting the measured topography. This has been shown to be the case with DNA, which has a radius of curvature of  $\sim 1 \text{ nm}$  and thus is much less forgiving when trying to acquire accurate sub-nanometre topography maps [70]. That being said, a recent

3D-AFM study was able to successfully measure the hydration landscape of B-DNA, in good agreement with reference structural models [71].

For biological applications in water, the need for structured fluid adjacent to the tip and sample is not particularly hard to meet, as cantilever tips are commonly made of silicon or silicon nitride which, despite being amorphous, can still order hydration layers, especially if cleaned with e.g. UV plasma [72]. Biological samples are more heterogeneous, but still structure interfacial water, often in a manner unique to their function [73, 74] which allows AFM techniques to explore their hydration landscape with high resolution.

### 2.3.2 *Anharmonic cantilever motion: the importance of small amplitudes*

As discussed in subsection 2.1.2, the repercussions of the cantilever’s oscillation amplitude on imaging have been recognised since the earliest days of dynamic AFM. In fact, a key approximation of many theories in both FM and AM-AFM (e.g. equation 2.1 and 2.6) is that the force field encountered by the tip varies linearly over the course of one oscillation, which allows meaningful interpretation of measured interaction stiffnesses. Thus, an absolute scale for appropriate amplitude sizes is given by the length scale of the forces being probed. As this thesis is primarily concerned with ions’ interactions with water and hydrophilic surfaces, solvation forces are clearly the relevant interaction. Their length scale certainly varies, and occasionally a longer-ranged “secondary” hydration force is invoked, but 2-4 Å appears to be a good estimate for the primary hydration force decay rate [65].

To first approximation then, we should aim for free oscillation amplitudes of between 0.5-1.5 nm to exploit solvation forces and generate maps of the hydration landscape. In principle, smaller amplitudes of  $\mathcal{O}(\text{Å})$  are also appropriate [75], but these have thus far been restricted to specialised off-resonance spectroscopy experiments that require interferometric detection systems [44, 66, 76, 77]. Implementing such small amplitudes in commercial AM-AFM systems with optical detection (Fig. 2.1) would likely result in very low signal-to-noise ratios – especially in water and with soft cantilevers – and in practice, we have not found this to generate stable high resolution maps. Our upper limit of  $\sim 1.5$  nm appears rather high relative to the solvation force length scale, but we note that some solids perturb the bulk fluid structure easily up to 1 nm from their surface (see e.g. Fig. 1.6 [78]), and the tip will still spend a large proportion of its time oscillating within the Stern layer. Either way, the amplitude range appears to reflect the tolerance of the interactions that govern small-amplitude AFM.

Aside from stating that the tip-sample interaction should be close to linear over an oscillation, we have not yet offered a mechanism for why this should improve resolution. Recent focus on AFM techniques that excite (or monitor) multiple cantilever oscillation modes have offered insight onto this problem. By tracking the dynamics of a cantilever in different imaging conditions (free/setpoint amplitudes, sample etc.), it is possible to measure the relative excitation of cantilever oscillation modes and thus quantify the parameters that allow for the (admittedly subjective) “best” resolution. One important control parameter for AM-AFM is the amplitude used as a target for the feedback system – known as the amplitude setpoint. In order for stable imaging, the setpoint must be below the free amplitude in bulk fluid,  $A_0$ , because tip-sample interactions in general reduce  $A$  (see Fig. 2.2). The setpoint ratio;  $A/A_0$ , is therefore an important determinant of tip dynamics. Keeping this value close to 100% allows for gentle imaging conditions, where the tip behaves similarly as in bulk fluid. A value that is too high may, however, lead to instabilities where the tip does not adequately track the sample topography. Reducing the setpoint ratio to, say, below 50% reflects much harsher tip-sample interactions; to reduce the oscillation amplitude so dramatically, the feedback loop is forced to move the cantilever closer to the sample which can mean that the tip comes into destructive contact with the surface.

It was found that both the use of large free amplitudes and small amplitude setpoints (i.e. harsh imaging conditions) degrade the apparent resolution and lead to dramatic increases in the anharmonicity of the cantilever motion [46, 56]. This is a reflection of the tip physically tapping on the sample and stimulating higher Eigenmodes. In contrast, the conditions that lead to the best images were those that retained small amplitudes and did not apply harsh forces (i.e. retained a high setpoint ratio). These correspond to the tip oscillating primarily in the interfacial fluid, without making physical contact with the sample. In this regime, where the fluid is more ordered, the tip loses significantly more energy through non-conservative fluid dissipation than in the bulk [49, 66]. This reduces the stimulation of higher modes, which allows the tip to be more adequately described as a perturbed harmonic oscillator *via* equation 2.7 and 2.8. This harmonic motion has the advantage of being more easily controlled by feedback loops and less likely to damage the tip and/or sample with higher mode dynamics, which have much greater effective stiffnesses.

## 2.4 Calibrating the flexural stiffness of AFM cantilevers

As it is the interfacial interactions that allow for stable imaging, it is of paramount importance for high-resolution AFM (and for the field as a whole) that the forces at play are accurately quantified. These forces are measured indirectly, *via* the bending of the

cantilever, and so the flexural spring constant,  $k_1$ , must be calibrated before this can be achieved. The spring constant must also be known in order to quantitatively extract information about the cantilever dynamics (equation 2.3) and thus the stiffness and damping induced by the interfacial fluid.

We can in fact predict  $k_1$  from the cantilever dimensions and its elastic properties alone, which represents an idealised stiffness [79]:

$$k_1 = \frac{1}{4} \frac{Ebh^3}{L^3}, \quad (2.12)$$

where the cantilever Young's modulus is given by  $E$ . However, typical lever widths,  $b$ , and lengths,  $L$ , are on the micrometre scale, where manufacturing defects and variations are commonplace. This can generate significant errors, especially considering the cubic dependence on lever thickness,  $h$  ( $\mathcal{O}(100 \text{ nm})$ ). Further, cantilevers commonly have sputtered coatings to enhance their reflectivity or functionalise their surface which will influence their dynamics in a non-trivial manner [80]. Thus these purely geometric calibration methods can be unreliable, especially if cantilevers with non-ideal shapes are used (e.g. triangular or picket-shaped). We shall focus instead on more commonplace methods for finding the stiffness, often *in situ*, that can better accommodate variation between cantilevers. These methods take advantage of the fact that the cantilever's equation of motion and resonant frequency depend on  $k_1$  and use the dynamic motion of the lever to determine its stiffness. In subsection 2.4.3, we then derive and present novel equations to calculate  $k_1$ , which circumvent some of the key issues with current methods, notably their applicability to arbitrary cantilever shapes and environmental dependence.

### 2.4.1 The thermal method

The calculation of the thermal noise in cantilever vibrations was first derived and implemented by Butt and Jaschke [79] and begins with the equipartition theorem, which states that every independent quadratic degree of freedom in a system in thermal equilibrium contributes  $k_B T/2$  to the mean total energy. Thus for small cantilever deflections generated only by thermal noise (i.e. no driving excitations), we have

$$\frac{1}{2} k_B T = \frac{1}{2} k_1 \langle z^2 \rangle. \quad (2.13)$$

This refers to the lever end's absolute deflection,  $z$ , rather than the inclination in its long axis,  $dz/dx$ , which is the quantity measured by the optical beam method, although the conversion between the two is relatively straightforward.

The power spectral density,  $P(\omega)$ , of the reflected laser's motion on the photodiode is known as the thermal spectra (Fig. 2.2(a) shows the square root of this) and is recorded in units of  $V^2 \text{ Hz}^{-1}$ . A calibration factor is required to convert the PD voltage change,  $\Delta V$ , to a cantilever deflection,  $\Delta z$ , in metres ( $S_l^{-1}$ , as mentioned earlier), but once this is done, integrating  $P(\omega)$  over the entire frequency range gives a value for the mean squared deflection. If we assume that the first Eigenmode dominates the deflection and the cantilever moves under harmonic motion, then the noise can be written as a combination of that of a simple harmonic oscillator (SHO) and a baseline white noise with no frequency dependence:  $P(\omega) = P_{\text{SHO}}(\omega) + P_{\text{white}}$  [81]. Then:

$$\begin{aligned} \langle z^2 \rangle &= S_l^{-2} \int_0^\infty (P_{\text{SHO}}(\omega) + P_{\text{white}}) d\omega \\ &= S_l^{-2} \int_0^\infty \left( \frac{P_0}{(\omega_{\text{eff}}^2 - \omega^2)^2 + (\omega\omega_{\text{eff}}/Q_{\text{eff}})^2} + P_{\text{white}} \right) d\omega \\ &= S_l^{-2} \left( \frac{1}{2} \pi \omega_e f P_0 Q + K \right), \end{aligned} \quad (2.14)$$

where  $K$  is a constant that represents the noise floor. Combining equation 2.13 and 2.14 gives:

$$k_1 = \frac{2k_B T}{\pi \omega_{\text{eff}} P_0 Q S_l^{-2}}, \quad (2.15)$$

for the squared inverse sensitivity,  $S_l^{-2}$ , effective resonant frequency,  $\omega_{\text{eff}}$ , and maximum power,  $P_0$ .

Equation 2.15 thus provides a relatively simple way to measure the spring constant, requiring only the thermal spectrum of a cantilever and a fit of the form of equation 2.7 to extract  $P_0$  and  $Q$  from the first mode. It makes no assumptions about the cantilever's shape, and the harmonic approximation is generally a good one, as long as the cantilever is far from the sample and in a Newtonian medium (i.e. one with no frequency-dependent viscosity,  $\eta(\omega) = \eta_0$ ).

The thermal method is not without limits however. The measurement requires accurate fitting in order to extract the cantilever's quality factor. This is rather trivial for cantilevers in air;  $Q$  values can easily reach into the thousands, and the percentage error of the fit is relatively low. When performing AFM in water or more viscous fluids however,  $Q$  is generally less than 5, which means there can be significant variation in the extracted value, depending on the region used for the fit. This is compounded by the fact that a low  $Q$  environment makes it more likely that oscillation modes overlap somewhat, increasing the fitting uncertainties. The need for an accurate value for  $S_l^{-1}$  is a limiting factor also.  $S_l^{-1}$

is conventionally acquired by monitoring the static deflection (in volts) of the cantilever as the tip is moved into contact with a stiff substrate such as mica or glass. This results in a linear region where, for a given  $z$ -piezo movement,  $\Delta z$ , the deflection is found by  $\Delta V = S_l \Delta z$ . Hence, a first-order polynomial fit trivially extracts the invOLS,  $S_l^{-1}$ . This can be problematic, especially for high-resolution studies, because the procedure requires hard, physical contact with a substrate that may irreversibly distort or damage the tip apex. It can always be done retrospectively, but this results in uncertainty about the forces applied when carrying out the experiment.

### 2.4.2 The Sader method

Sader's method for calibrating the spring constant of a cantilever [82–85] derives from an expression relating  $k_1$  to the resonant frequency of a cantilever in a vacuum,  $\omega_{\text{vac}}$  [86]. Clearly, for operation of AFM in ambient conditions, this is not particularly practical and so the hydrodynamic function can be used to approximate the change in resonance to  $\omega_{\text{eff}}$  upon immersion into a viscous fluid. This leads to the relation (for a rectangular beam):

$$k_1 = 0.1906 \rho_f b^2 L Q \Gamma_i(\omega_{\text{eff}}) \omega_{\text{eff}}^2. \quad (2.16)$$

The fluid's density is given by  $\rho_f$  and  $\Gamma_i(\omega_{\text{eff}})$  is the imaginary part of the hydrodynamic function of equation 2.10. We note that the derivation of this equation assumes  $Q \gg 1$  [82], the aspect ratio,  $L/b > 3$  (ideally as large as possible), and still requires the cantilever length and width to be known (although, significantly, not the thickness).

The equation can be generalised somewhat for cantilevers of different shapes [85], with the caveat that  $\Gamma(\omega_{\text{eff}})$  can be determined, and the geometry-specific  $b$  and  $L$  can be obtained. Rather than aim for analytic solutions for the hydrodynamic function as in equation 2.9, Sader *et al.* provided practical fits of the  $\Gamma_i(\omega_{\text{eff}})$  vs.  $\text{Re}(\omega_{\text{eff}})$ , of the form  $\Gamma_i(\text{Re}) = a_0 \text{Re}^{a_1 + a_2 \log_{10} \text{Re}}$ , along with fitting parameters,  $a_0$ ,  $a_1$  and  $a_2$ , for a variety of different cantilever shapes. To do this, the cantilevers' thermal spectra were captured (using an interferometer so as to avoid requiring the conversion factor,  $S_l^{-1}$ ) at a range of  $\text{N}_2$  and  $\text{CO}_2$  gas pressures. Once the hydrodynamic coefficients have been found for a given cantilever,  $\Gamma_i(\text{Re})$  is then uniquely determined for any lever with the same plan view, as the function is dimensionless [85], allowing for straightforward calculation of  $k_1$  in the future.

This is a successful approach that leads to accurate stiffness measurements when compared to existing methods or manufacturer's values [82]. There are no constraints on the AFM geometry and it can in principle determine the stiffness for any thin lever, for which

the thermal spectra, hydrodynamic coefficients and plan dimensions are known. This latter requirement is not trivial however; the coefficients must be obtained by recording a thermal spectrum for a cantilever of *known* stiffness with the same plan as the lever of interest while varying the gas pressure in a controlled manner – a capability not present in the majority of AFMs. While Sader *et al.* provide the coefficients for a wide range of cantilevers, full calibration of a novel shape would be a lengthy process. Finally, the underlying dependence of equation 2.16 on the quality factor increases the uncertainty when such calibrations are performed *in situ* in viscous liquids.

### 2.4.3 A shape-independent method for calculating the cantilever stiffness

#### *Derivation of the primary, shape-independent calibration equation*

We now present our derivation of a novel set of equations to calibrate a cantilever's flexural stiffness. The calibration originates from the hydrodynamic approach incorporated into Sader's method but has no dependence on the lever's quality factor, no need for calibration of  $S_l^{-1}$  and can be used in air or viscous liquids with comparable results. The method makes no assumptions about the lever geometry and only requires two resonance frequencies to be measured, each in air and the fluid of choice.

The real and imaginary parts of the hydrodynamic function are first parametrised as [7, 87]:

$$\Gamma_r(\text{Re}) = a_1 + \frac{a_2}{\sqrt{\text{Re}}}, \quad (2.17)$$

$$\Gamma_i(\text{Re}) = \frac{b_1}{\sqrt{\text{Re}}} + \frac{b_2}{\text{Re}}. \quad (2.18)$$

We will make use of  $\Gamma_r$  and take the coefficients to be  $a_1 = 1.0553$ ;  $a_2 = 3.7997$  [87]. These can be used to relate the angular resonance frequencies of a cantilever in an arbitrary fluid,  $\omega_{fn}$ , to that in air,  $\omega_{an}$ , for any oscillation mode number  $n$  [88]:

$$\omega_{fn}^2 \left( \frac{\pi a_1 \rho_f b}{4 \rho_c h} + 1 \right) + \omega_{fn}^{3/2} \left( \frac{\pi a_2 \sqrt{\eta_f \rho_f}}{2 \rho_c h} \right) = \omega_{an}^2. \quad (2.19)$$

By measuring two resonance frequencies in the fluid and air environment the two unknown cantilever parameters of the areal mass density,  $\widehat{\rho_c h}$ , and width,  $\widehat{b}$ , can respectively be determined by

$$\widehat{\rho_c h} = \frac{\pi a_2 \sqrt{\rho_f \eta_f}}{2} \frac{\omega_{f1}^{3/2} \omega_{f2}^{3/2} (\sqrt{\omega_{f2}} - \sqrt{\omega_{f1}})}{(\omega_{a1}^2 - \omega_{f1}^2) \omega_{f2}^2 - (\omega_{a2}^2 - \omega_{f2}^2) \omega_{f1}^2}, \quad (2.20)$$

$$\hat{b} = \frac{2a_2 \sqrt{\eta_f}}{a_1 \sqrt{\rho_f \omega_{f1}}} \left( \frac{\omega_{f2}^{3/2} (\sqrt{\omega_{f2}} - \sqrt{\omega_{f1}}) (\omega_{a1}^2 - \omega_{f1}^2)}{(\omega_{a1}^2 - \omega_{f1}^2) \omega_{f2}^2 - (\omega_{a2}^2 - \omega_{f2}^2) \omega_{f1}^2} - 1 \right), \quad (2.21)$$

where we use the caret to denote calculated values. The geometric parameters can then be related to the flexural spring constant of the first mode by [89]

$$k_1 = m_1 \omega_{a1}^2 = 0.25 m_c \omega_{a1}^2 = 0.25 \widehat{\rho_c h} \hat{b} L \omega_{a1}^2. \quad (2.22)$$

Here, we have used  $m_1 = 0.25 m_c$  to relate the first Eigenmode's effective mass,  $m_1$ , to the cantilever mass  $m_c$  [89], which is then obtained through equation 2.20 and 2.21. Our approach relies on the fact that the hydrodynamic function of the cantilever is, for a given value of Reynold's number, defined by geometry alone. Thus, measurement of the cantilever dynamics in two environments allows us to effectively "calibrate" the geometry of the cantilever – that is, find that the appropriate lengthscales that define  $\Gamma(\text{Re})$ , with no explicit dependence on the shape or, importantly, the quality factor.

### *Experimentally evaluating the method*

To assess the accuracy of equation 2.22, we compare its predictions for the flexural stiffness of three differently-shaped cantilevers with those produced by the thermal method (equation 2.15) and by Sader's method. The cantilevers chosen have plan views that are rectangular (RC800 PSA, Olympus), V-shaped (TR-400 PB, Olympus) and arrow-like (Arrow UHF AuD, Nanoworld) (see Fig. 2.3(a)) and, to emphasise the other methods' dependence on the quality factor, we assess the predictions in both air and ultrapure water. To compute Sader's stiffness for the beam cantilever, we make use of equation 2.16, whereas for the V-shaped cantilever we use an adapted form;  $k_1 = \rho_f b^2 L \Lambda(\text{Re}) \omega_{\text{eff}}$ , where  $\Lambda(\text{Re})$  is a hydrodynamic function modified for the V-shaped cantilever [85]. The results are presented in Fig. 2.3(b).

The predictions obtained from our equation 2.22 broadly agree with the thermal method and are as accurate as the Sader method in most cases, with reference to the nominal stiffness value. We note that there is no independent measurement of  $k_1$  here – even manufacturer's values are typically given with large uncertainties – and so there is no formal method of accuracy for the model. The proximity of the thermal method and nominal values does however imply that our results are accurate. As mentioned previously,

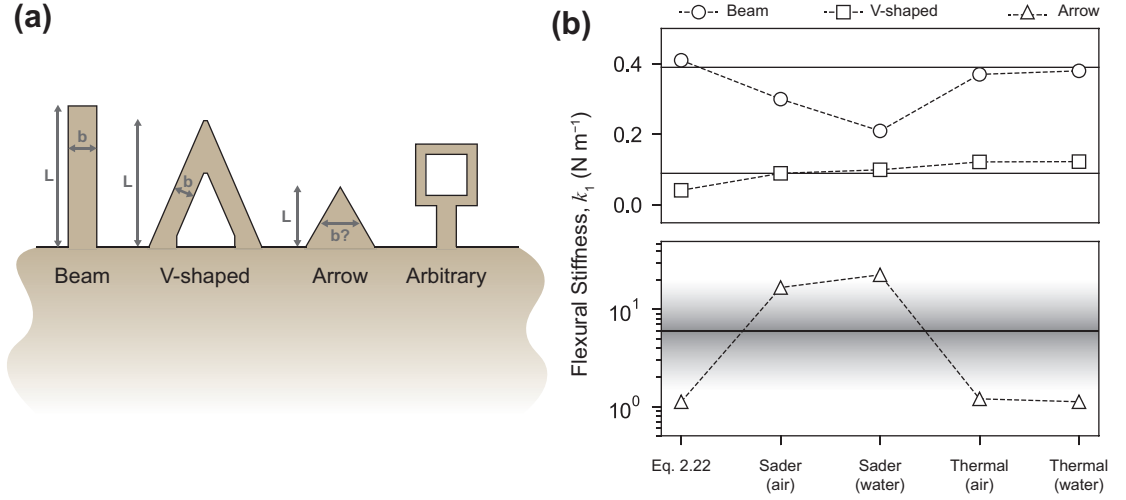


Fig. 2.3: Calibrating the flexural stiffness,  $k_1$  of cantilevers of various shapes. (a) plan-view geometries of the three cantilevers that were tested experimentally (left) and an representative shape that traditional methods would struggle with. Characteristic length scales are annotated; for the arrow, the aspect ratio is low and the small dimension is not well-defined. (b, upper) Spring constants predicted by equation 2.22, the Sader method and the thermal method for a beam and V-shaped levers in air and water. Manufacturer's values ( $0.39$  and  $0.09$  N m<sup>-1</sup>) are shown by horizontal lines. (b, lower) Predictions for arrow-shaped cantilevers; the nominal stiffness is poorly defined (note the logarithmic  $y$ -axis). Nominal stiffnesses are  $k_1 \sim 6$  N m<sup>-1</sup> with a range of  $1.5 < k_1 < 20.0$  N m<sup>-1</sup> highlighted by the gradient, but there is good agreement between the thermal results and those from our equation. Calculated errors are smaller than the data markers.

our equation does *not* require invOLS calibration, with potentially damaging tip-sample contact. Sader's equations are closer to the nominal value than both the thermal and our method for the V-shaped lever, but we emphasise that this is not a general formula, but made use of a specially-developed  $\Lambda(\text{Re})$ . For the arrow-shaped cantilever (b, lower), the agreement between the thermal method and our equation 2.22 is excellent (less than 7% deviation), demonstrating the validity of our approach. There is no adapted hydrodynamic function  $\Lambda(\text{Re})$  available for such geometries and they have a low aspect ratio, breaking many of the assumptions used in Sader's model. Indeed, the values obtained using equation 2.16 are completely offset from both our equation and the thermal results. There is a broad range of nominal values, indicated by the gradient, which is a result of the complex geometry; its trapezoidal cross-section means that manufacturing variability is common. The range ( $1.5 < k_1 < 20.0$  N m<sup>-1</sup>) emphasises the need for accurate calibration methods that are not based on nominal values.

#### Modification of the model for use in viscous fluids

We have already mentioned the importance of viscosity when considering such dynamic cantilever calibration techniques; the effect of the fluid on the cantilever's effective mass dramatically reduces  $Q$  and makes it harder to accurately determine the resonance char-

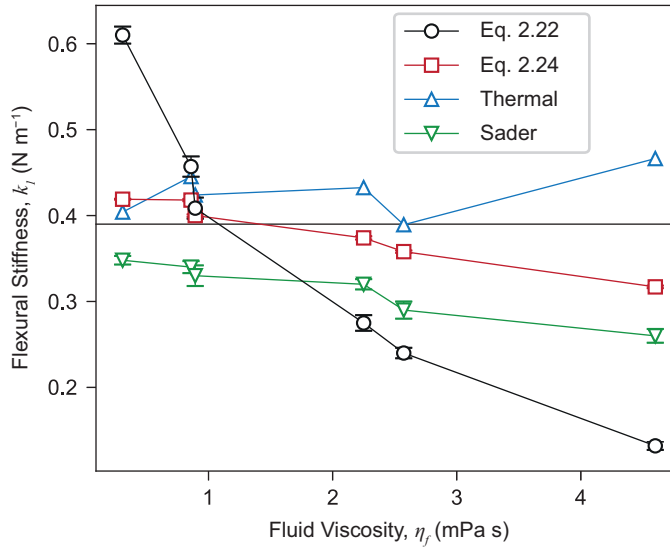


Fig. 2.4: Assessment of the impact of the surrounding fluid’s viscosity on the predicted spring constant of a beam cantilever. The thermal method is reasonably constant with viscosity as expected but deviates from the nominal manufacturer’s value (horizontal line) of  $0.39 \text{ N m}^{-1}$ . In contrast, both equation 2.22 and the Sader method vary, decreasing as the viscosity increases. Equation 2.24 performs much better, returning a more stable value for  $k_1$  that is consistent with the thermal method and has reduced errors at all but the highest viscosities.

acteristics. Equation 2.22 is no exception to this; the results of Fig. 2.3(b) are based on experiments performed in air and water; relatively low-viscosity environments. However, when working in more viscous liquids and especially with softer cantilevers, the quality of predictions progressively decreases. This is a problem for applications such as viscometry or biosensing, where cantilevers are used in viscous or non-Newtonian fluids. To this end, we adapted our equation to make it more accurate in the case of predicting  $k_1$ . This however requires an extra input parameter; the width,  $b$  (or an effective value for non-rectangular cantilevers). If  $b$  is known, the areal mass density can be written as:

$$\widehat{\rho c h} = \frac{\omega_{f1}^2 \pi a_1 \rho_f b + 2\omega_{f1}^{3/2} \pi a_2 \sqrt{\rho_f \eta_f}}{4(\omega_{a1}^2 - \omega_{f1}^2)}, \quad (2.23)$$

which yields the following expression for the cantilever flexural stiffness:

$$k_1 = \frac{\omega_{f1}^2 \pi a_1 \rho_f b + 2\omega_{f1}^{3/2} \pi a_2 \sqrt{\rho_f \eta_f}}{16(\omega_{a1}^2 - \omega_{f1}^2)} b L \omega_{a1}^2. \quad (2.24)$$

Although it requires an effective width for the cantilever, the above equation no longer needs a second resonant frequency, which may be an advantage if the second mode’s oscillation is too small to be detected in the viscous fluid. We investigated the validity of this equation in fluids of varying viscosity, making use of ultrapure water, isopropanol, acetone, butanol, decane and hexanol (all Sigma Aldrich, Dorset, purity > 99%). We conducted

the measurements with a rectangular cantilever (Olympus RC800 PSA, as before) and compared the predictions with the same methods as before.

The results are shown in Fig. 2.4, which shows that the stiffness as calculated via equation 2.24 is less sensitive to viscosity than the other methods, whereas equation 2.22 fails dramatically, with around 70% variation. The Sader method's results decrease with viscosity and are offset from both the thermal method and nominal values. This reflects the dependence of the method on the  $Q$ -factor, which tends to vary dramatically with the fluid viscosity. Together, these results validate equation 2.24 and show that it provides the most reliable model for calculating  $k_1$ , particularly when operating in highly viscous environments.

## 2.5 Conclusions

This chapter has discussed the development of AFM over the thirty years since its inception, from its initial capability to measure normal forces and topography in contact mode, to the myriad dynamic modes of operation which have enabled atomic-level resolution of the interface between liquids and solids to be obtained. The theory and mechanisms underlying such high resolution while immersed in liquid are still being revealed, but it is clear that the structure of the interfacial solvent, and the tip's motion within it are imperative. In the case of aqueous solutions, the hydration layers formed between the tip and sample increase the energy dissipated over each oscillation, resulting in a very short ranged interaction that increases resolution. As well as helping obtain insight into the molecular-level organisation of fluids at the interface, the motion of a vibrating cantilever can be used to infer mechanical properties, either about the sample (in the case of phase- or bimodal imaging) or about the cantilever itself (if the fluid properties are known). In the latter case, two common methods were discussed and a third, novel set of equations for calibrating the spring constant were developed. We showed that our equations were at least as good as the conventional approaches and could be applied to arbitrarily-shaped cantilevers, without the need for destructive calibration of  $S_l^{-1}$ . Further we showed that a similar equation, which took the additional input of an effective width, was successful at predicting  $k_1$  in viscous environments as well.



## REFERENCES: CHAPTER 2

- [1] G. Binnig, C. F. Quate, C. Gerber, “Atomic Force Microscope”, *Phys. Rev. Lett.* **1986**, *56*, 930–933.
- [2] F. J. Giessibl, *Advances in atomic force microscopy*, **2003**.
- [3] F. J. Giessibl, “AFM’s path to atomic resolution”, *Mater. Today* **2005**, *8*, 32–41.
- [4] T. R. Albrecht, P. Grütter, D. Horne, D. Rugar, “Frequency modulation detection using high-Q cantilevers for enhanced force microscope sensitivity”, *J. Appl. Phys.* **1991**, *69*, 668–673.
- [5] F. J. Giessibl, “Atomic Resolution of the Silicon (111)-(7x7) Surface by Atomic Force Microscopy”, *Science (80-. )*. **1995**, *267*, 68–71.
- [6] F. J. Giessibl, S. Hembacher, H. Bielefeldt, J. Mannhart, “Subatomic Features on the Silicon (111)-(7x7) Surface Observed by Atomic Force Microscopy”, *Science (80-. )*. **2000**, *289*, 422–425.
- [7] S. Basak, A. Raman, S. V. Garimella, “Hydrodynamic loading of microcantilevers vibrating in viscous fluids”, *J. Appl. Phys.* **2006**, *99*, 114906.
- [8] T. Fukuma, M. Kimura, K. Kobayashi, K. Matsushige, H. Yamada, “Development of low noise cantilever deflection sensor for multienvironment frequency-modulation atomic force microscopy”, *Rev. Sci. Instrum.* **2005**, *76*, 053704.
- [9] T. Fukuma, S. P. Jarvis, “Development of liquid-environment frequency modulation atomic force microscope with low noise deflection sensor for cantilevers of various dimensions”, *Rev. Sci. Instrum.* **2006**, *77*, 043701.
- [10] T. Fukuma, K. Kobayashi, K. Matsushige, H. Yamada, “True molecular resolution in liquid by frequency-modulation atomic force microscopy”, *Appl. Phys. Lett.* **2005**, *86*, 1–3.
- [11] T. Fukuma, K. Kobayashi, K. Matsushige, H. Yamada, “True atomic resolution in liquid by frequency-modulation atomic force microscopy”, *Appl. Phys. Lett.* **2005**, *87*, 034101.
- [12] T. Fukuma, M. Higgins, S. Jarvis, “Direct Imaging of Lipid-Ion Network Formation under Physiological Conditions by Frequency Modulation Atomic Force Microscopy”, *Phys. Rev. Lett.* **2007**, *98*, 106101.
- [13] T. Fukuma, M. J. Higgins, S. P. Jarvis, “Direct Imaging of Individual Intrinsic Hydration Layers on Lipid Bilayers at Ångstrom Resolution”, *Biophys. J.* **2007**, *92*, 3603–3609.
- [14] S. H. Loh, S. P. Jarvis, “Visualization of ion distribution at the mica-electrolyte interface”, *Langmuir* **2010**, *26*, 9176–9178.
- [15] U. M. Ferber, G. Kaggwa, S. P. Jarvis, “Direct imaging of salt effects on lipid bilayer ordering at sub-molecular resolution”, *Eur. Biophys. J.* **2011**, *40*, 329–338.
- [16] K. Suzuki, N. Oyabu, K. Kobayashi, K. Matsushige, H. Yamada, “Atomic-Resolution Imaging of Graphite–Water Interface by Frequency Modulation Atomic Force Microscopy”, *Appl. Phys. Express* **2011**, *4*, 125102.
- [17] T. Uchihashi, M. Higgins, Y. Nakayama, J. E. Sader, S. P. Jarvis, “Quantitative measurement of solvation shells using frequency modulated atomic force microscopy”, *Nanotechnology* **2005**, *16*, S49–S53.
- [18] M. J. Higgins, M. Polcik, T. Fukuma, J. E. Sader, Y. Nakayama, S. P. Jarvis, “Structured water layers adjacent to biological membranes.”, *Biophys. J.* **2006**, *91*, 2532–42.
- [19] A. Labuda, K. Kobayashi, K. Suzuki, H. Yamada, P. Grütter, “Monotonic Damping in Nanoscopic Hydration Experiments”, *Phys. Rev. Lett.* **2013**, *110*, 066102.

- [20] J. I. Kilpatrick, S.-H. Loh, S. P. Jarvis, “Directly Probing the Effects of Ions on Hydration Forces at Interfaces”, *J. Am. Chem. Soc.* **2013**, *135*, 2628–2634.
- [21] J. E. Sader, S. P. Jarvis, “Accurate formulas for interaction force and energy in frequency modulation force spectroscopy”, *Appl. Phys. Lett.* **2004**, *84*, 1801–1803.
- [22] J. E. Sader, T. Uchihashi, M. J. Higgins, A. Farrell, Y. Nakayama, S. P. Jarvis, “Quantitative force measurements using frequency modulation atomic force microscopy?theoretical foundations”, *Nanotechnology* **2005**, *16*, S94–S101.
- [23] B. W. Hoogenboom, H. J. Hug, Y. Pellmont, S. Martin, P. L. T. M. Frederix, D. Fotiadis, A. Engel, “Quantitative dynamic-mode scanning force microscopy in liquid”, *Appl. Phys. Lett.* **2006**, *88*, 193109.
- [24] E. T. Herruzo, A. P. Perrino, R. Garcia, “Fast nanomechanical spectroscopy of soft matter.”, *Nat. Commun.* **2014**, *5*, 3126.
- [25] M. Kocun, A. Labuda, W. Meinhold, I. Revenko, R. Proksch, “Fast, High Resolution, and Wide Modulus Range Nanomechanical Mapping with Bimodal Tapping Mode”, *ACS Nano* **2017**, *11*, 10097–10105.
- [26] C. A. Amo, A. P. Perrino, A. F. Payam, R. Garcia, “Mapping Elastic Properties of Heterogeneous Materials in Liquid with Angstrom-Scale Resolution”, *ACS Nano* **2017**, *11*, 8650–8659.
- [27] Z. Al-Rekabi, S. Contera, “Multifrequency AFM reveals lipid membrane mechanical properties and the effect of cholesterol in modulating viscoelasticity”, *Proc. Natl. Acad. Sci.* **2018**, *In Press*, 1–6.
- [28] R. García, R. Pérez, “Dynamic atomic force microscopy methods”, *Surf. Sci. Rep.* **2002**, *47*, 197–301.
- [29] R. García, *Amplitude Modulation Atomic Force Microscopy*, Wiley-VCH, **2010**.
- [30] M. Lee, W. Jhe, “General Theory of Amplitude-Modulation Atomic Force Microscopy”, *Phys. Rev. Lett.* **2006**, *97*, 036104.
- [31] A. J. Katan, M. H. van Es, T. H. Oosterkamp, “Quantitative force versus distance measurements in amplitude modulation AFM: a novel force inversion technique”, *Nanotechnology* **2009**, *20*, 165703.
- [32] A. F. Payam, D. Martin-Jimenez, R. Garcia, “Force reconstruction from tapping mode force microscopy experiments”, *Nanotechnology* **2015**, *26*, 185706.
- [33] J. P. Cleveland, B. Anczykowski, A. E. Schmid, V. B. Elings, “Energy dissipation in tapping-mode atomic force microscopy”, *Appl. Phys. Lett.* **1998**, *72*, 2613–2615.
- [34] B. Anczykowski, B. Gotsmann, H. Fuchs, J. P. Cleveland, V. B. Elings, “How to measure energy dissipation in dynamic mode atomic force microscopy”, *Appl. Surf. Sci.* **1999**, *140*, 376–382.
- [35] R. García, R. Magerle, R. Perez, “Nanoscale compositional mapping with gentle forces.”, *Nat. Mater.* **2007**, *6*, 405–11.
- [36] S. N. Magonov, V. Elings, M. H. Whangbo, “Phase imaging and stiffness in tapping-mode atomic force microscopy”, *Surf. Sci.* **1997**, *375*, L385–L391.
- [37] G. Reiter, G. Castelein, J.-U. Sommer, A. Röttele, T. Thurn-Albrecht, “Direct Visualization of Random Crystallization and Melting in Arrays of Nanometer-Size Polymer Crystals”, *Phys. Rev. Lett.* **2001**, *87*, 226101.
- [38] N. F. Martínez, R. García, “Measuring phase shifts and energy dissipation with amplitude modulation atomic force microscopy”, *Nanotechnology* **2006**, *17*, S167–S172.
- [39] Z. Suo, X. Yang, R. Avci, L. Kellerman, D. W. Pascual, M. Fries, A. Steele, “HEPES-stabilized encapsulation of Salmonella typhimurium”, *Langmuir* **2007**, *23*, 1365–1374.
- [40] M. Stark, C. Möller, D. J. Müller, R. Guckenberger, “From Images to Interactions: High-Resolution Phase Imaging in Tapping-Mode Atomic Force Microscopy”, *Biophys. J.* **2001**, *80*, 3009–3018.
- [41] K. Voitchovsky, J. J. Kuna, S. A. Contera, E. Tosatti, F. Stellacci, “Direct mapping of the solid-liquid adhesion energy with subnanometre resolution.”, *Nat. Nanotechnol.* **2010**, *5*, 401–405.
- [42] M. Ricci, P. Spijker, F. Stellacci, J.-F. Molinari, K. Voitchovsky, “Direct Visualization of Single Ions in the Stern Layer of Calcite”, *Langmuir* **2013**, *29*, 2207–2216.

- [43] M. Ricci, P. Spijker, K. Voïtchovsky, “Water-induced correlation between single ions imaged at the solid-liquid interface.”, *Nat. Commun.* **2014**, *5*, 4400.
- [44] S. Basak, A. Raman, “Dynamics of tapping mode atomic force microscopy in liquids: Theory and experiments”, *Appl. Phys. Lett.* **2007**, *91*, 064107.
- [45] J. Melcher, C. Carrasco, X. Xu, J. L. Carrascosa, J. Gomez-Herrero, P. Jose de Pablo, A. Raman, “Origins of phase contrast in the atomic force microscope in liquids”, *Proc. Natl. Acad. Sci.* **2009**, *106*, 13655–13660.
- [46] K. Voïtchovsky, “Anharmonicity, solvation forces, and resolution in atomic force microscopy at the solid-liquid interface”, *Phys. Rev. E* **2013**, *88*, 022407.
- [47] S. An, S. D. Solares, S. Santos, D. Ebeling, “Energy transfer between eigenmodes in multimodal atomic force microscopy”, *Nanotechnology* **2014**, *25*, 475701.
- [48] S. de Beer, D. van den Ende, F. Mugele, “Atomic force microscopy cantilever dynamics in liquid in the presence of tip sample interaction”, *Appl. Phys. Lett.* **2008**, *93*, 253106.
- [49] S. H. Khan, G. Matei, S. Patil, P. M. Hoffmann, “Dynamic Solidification in Nanoconfined Water Films”, *Phys. Rev. Lett.* **2010**, *105*, 106101.
- [50] S. de Beer, D. van den Ende, F. Mugele, “Dissipation and oscillatory solvation forces in confined liquids studied by small-amplitude atomic force spectroscopy.”, *Nanotechnology* **2010**, *21*, 325703.
- [51] A. Ulcinas, G. Valdre, V. Snitka, M. J. Miles, P. M. Claesson, M. Antognozzi, “Shear Response of Nanoconfined Water on Muscovite Mica: Role of Cations”, *Langmuir* **2011**, *27*, 10351–10355.
- [52] S. de Beer, W. K. den Otter, D. van den Ende, W. J. Briels, F. Mugele, “Can Confinement-Induced Variations in the Viscous Dissipation be Measured?”, *Tribol. Lett.* **2012**, *48*, 1–9.
- [53] S. H. Khan, P. M. Hoffmann, “Squeeze-out dynamics of nanoconfined water: A detailed nanomechanical study”, *Phys. Rev. E* **2015**, *92*, 042403.
- [54] J. E. Sader, “Frequency response of cantilever beams immersed in viscous fluids with applications to the atomic force microscope”, *J. Appl. Phys.* **1998**, *84*, 64–76.
- [55] C. P. Green, J. E. Sader, “Frequency response of cantilever beams immersed in viscous fluids near a solid surface with applications to the atomic force microscope”, *J. Appl. Phys.* **2005**, *98*, 114913.
- [56] D. Kiracofe, A. Raman, “Nonlinear dynamics of the atomic force microscope at the liquid-solid interface”, *Phys. Rev. B* **2012**, *86*, 205405.
- [57] T. Fukuma, B. Reischl, N. Kobayashi, P. Spijker, F. F. Canova, K. Miyazawa, A. S. Foster, “Mechanism of atomic force microscopy imaging of three-dimensional hydration structures at a solid-liquid interface”, *Phys. Rev. B* **2015**, *92*, 155412.
- [58] H. Söngen, C. Marutschke, P. Spijker, E. Holmgren, I. Hermes, R. Bechstein, S. Klassen, J. Tracey, A. S. Foster, A. Kühnle, “Chemical Identification at the Solid–Liquid Interface”, *Langmuir* **2017**, *33*, 125–129.
- [59] T.-D. Li, J. Gao, R. Szoszkiewicz, U. Landman, E. Riedo, “Structured and viscous water in subnanometer gaps”, *Phys. Rev. B* **2007**, *75*, 115415.
- [60] J. N. Israelachvili, R. M. Pashley, “Molecular layering of water at surfaces and origin of repulsive hydration forces”, *Nature* **1983**, *306*, 249–250.
- [61] D. Martin-Jimenez, E. Chacon, P. Tarazona, R. Garcia, “Atomically resolved three-dimensional structures of electrolyte aqueous solutions near a solid surface”, *Nat. Commun.* **2016**, *7*, 12164.
- [62] J. Valle-Delgado, J. Molina-Bolívar, F. Galisteo-González, M. Gálvez-Ruiz, “Evidence of hydration forces between proteins”, *Curr. Opin. Colloid Interface Sci.* **2011**, *16*, 572–578.
- [63] M. Kanduč, A. Schlaich, E. Schneck, R. R. Netz, “Water-Mediated Interactions between Hydrophilic and Hydrophobic Surfaces”, *Langmuir* **2016**, *32*, 8767–8782.
- [64] J. N. Israelachvili, P. M. McGuiggan, “Forces Between Surfaces in Liquids”, *Science (80-. )*. **1988**, *241*, 795–800.
- [65] V. Parsegian, T. Zemb, “Hydration forces: Observations, explanations, expectations, questions”, *Curr. Opin. Colloid Interface Sci.* **2011**, *16*, 618–624.

- [66] S. Jeffery, P. M. Hoffmann, J. B. Pethica, C. Ramanujan, H. Ö. Özer, A. Oral, “Direct measurement of molecular stiffness and damping in confined water layers”, *Phys. Rev. B - Condens. Matter Mater. Phys.* **2004**, *70*, 054114.
- [67] K. Miyazawa, N. Kobayashi, M. Watkins, A. L. Shluger, K.-i. Amano, T. Fukuma, “A relationship between three-dimensional surface hydration structures and force distribution measured by atomic force microscopy”, *Nanoscale* **2016**, *8*, 7334–42.
- [68] K. Miyazawa, M. Watkins, A. L. Shluger, T. Fukuma, “Influence of ions on two-dimensional and three-dimensional atomic force microscopy at fluorite–water interfaces”, *Nanotechnology* **2017**, *28*, 245701.
- [69] K. Umeda, L. Zivanovic, K. Kobayashi, J. Ritala, H. Kominami, P. Spijker, A. S. Foster, H. Yamada, “Atomic-resolution three-dimensional hydration structures on a heterogeneously charged surface”, *Nat. Commun.* **2017**, *8*, 2111.
- [70] A. Pyne, R. Thompson, C. Leung, D. Roy, B. W. Hoogenboom, “Single-molecule reconstruction of oligonucleotide secondary structure by atomic force microscopy”, *Small* **2014**, *10*, 3257–3261.
- [71] K. Kuchuk, U. Sivan, “Hydration Structure of a Single DNA Molecule Revealed by Frequency-Modulation Atomic Force Microscopy”, *Nano Lett.* **2018**, *18*, 2733–2737.
- [72] S. M. R. Akrami, H. Nakayachi, T. Watanabe-Nakayama, H. Asakawa, T. Fukuma, “Significant improvements in stability and reproducibility of atomic-scale atomic force microscopy in liquid.”, *Nanotechnology* **2014**, *25*, 455701.
- [73] S. Antoranz Contera, K. Voitchovsky, J. F. Ryan, “Controlled ionic condensation at the surface of a native extremophile membrane.”, *Nanoscale* **2010**, *2*, 222–9.
- [74] M. Ricci, R. A. Quinlan, K. Voitchovsky, “Sub-nanometre mapping of the aquaporin–water interface using multifrequency atomic force microscopy”, *Soft Matter* **2017**, *13*, 187–195.
- [75] S. V. Patil, P. M. Hoffmann, “Small-amplitude atomic force microscopy”, *Adv. Eng. Mater.* **2005**, *7*, 707–712.
- [76] S. H. Khan, E. L. Kramkowski, P. J. Ochs, D. M. Wilson, P. M. Hoffmann, “Viscosity of a nanoconfined liquid during compression”, *Appl. Phys. Lett.* **2014**, *104*, 023110.
- [77] S. H. Khan, E. L. Kramkowski, P. M. Hoffmann, “NaCl-Dependent Ordering and Dynamic Mechanical Response in Nanoconfined Water”, *Langmuir* **2016**, *32*, 10802–10807.
- [78] S. S. Lee, P. Fenter, K. L. Nagy, N. C. Sturchio, “Real-time observation of cation exchange kinetics and dynamics at the muscovite–water interface”, *Nat. Commun.* **2017**, *8*, 15826.
- [79] H. J. Butt, M. Jaschke, “Calculation of thermal noise in atomic force microscopy”, *Nanotechnology* **1995**, *6*, 1.
- [80] R. R. Grüter, Z. Khan, R. Paxman, J. W. Ndieyira, B. Dueck, B. A. Bircher, J. L. Yang, U. Drechsler, M. Despont, R. A. McKendry, B. W. Hoogenboom, “Disentangling mechanical and mass effects on nanomechanical resonators”, *Appl. Phys. Lett.* **2010**, *96*, 023113.
- [81] S. M. Cook, K. M. Lang, K. M. Chynoweth, M. Wigton, R. W. Simmonds, T. E. Schäffer, “Practical implementation of dynamic methods for measuring atomic force microscope cantilever spring constants”, *Nanotechnology* **2006**, *17*, 2135–2145.
- [82] J. E. Sader, J. W. Chon, P. Mulvaney, “Calibration of rectangular atomic force microscope cantilevers”, *Rev. Sci. Instrum.* **1999**, *70*, 3967–3969.
- [83] C. P. Green, H. Lioe, J. P. Cleveland, R. Proksch, P. Mulvaney, J. E. Sader, “Normal and torsional spring constants of atomic force microscope cantilevers”, *Rev. Sci. Instrum.* **2004**, *75*, 1988–1996.
- [84] J. E. Sader, J. Pacifico, C. P. Green, P. Mulvaney, “General scaling law for stiffness measurement of small bodies with applications to the atomic force microscope”, *J. Appl. Phys.* **2005**, *97*, 124903.
- [85] J. E. Sader, J. A. Sanelli, B. D. Adamson, J. P. Monty, X. Wei, S. A. Crawford, J. R. Friend, I. Marusic, P. Mulvaney, E. J. Bieske, “Spring constant calibration of atomic force microscope cantilevers of arbitrary shape”, *Rev. Sci. Instrum.* **2012**, *83*, 103705.

- 
- [86] J. E. Sader, I. Larson, P. Mulvaney, L. R. White, “Method for the calibration of atomic force microscope cantilevers”, *Rev. Sci. Instrum.* **1995**, *66*, 3789–3798.
- [87] A. Maali, C. Hurth, R. Boisgard, C. Jai, T. Cohen-Bouhacina, J.-P. Aimé, “Hydrodynamics of oscillating atomic force microscopy cantilevers in viscous fluids”, *J. Appl. Phys.* **2005**, *97*, 074907.
- [88] A. Farokh Payam, “Sensitivity of flexural vibration mode of the rectangular atomic force microscope micro cantilevers in liquid to the surface stiffness variations”, *Ultramicroscopy* **2013**, *135*, 84–88.
- [89] J. R. Lozano, R. Garcia, “Theory of phase spectroscopy in bimodal atomic force microscopy”, *Phys. Rev. B* **2009**, *79*, 014110.



## 3.0 DYNAMIC AFM: EXAMPLE APPLICATIONS

In this chapter, we will take the principles outlined in chapter 2 regarding dynamic AFM and apply them to two situations that are relevant for this thesis. Firstly, we will use the small-amplitude AFM approach to obtaining high-resolution discussed in section 2.3 to produce maps of the hydration landscape of mica when immersed in common buffering solutions. The effects of simpler ions on this system have been studied quite rigorously (see e.g. section 1.3 and 1.4) but there has been little quantitative comparison between buffering agents' interfacial effects at a molecular scale to date, despite their ubiquity in biological studies. We show that a range of buffers form distinct structures, templated by the mica and driven by their varying size and molecular structure. The inclusion of smaller salts (NaCl) mitigates the buffers' perturbation of the mica's hydration landscape to some extent, but we show that there are still discernable effects. We further show, using a model lipid membrane, that the observed phenomenon is likely to have consequences for biological systems.

The second study relies on the formalism for analysing cantilever dynamics that was developed in subsection 2.4.3, but in this case, it is used to probe the properties of the immersing fluid, namely its viscosity,  $\eta_f$ , and density,  $\rho_f$ . We derive a general method that requires two resonance frequencies of the cantilever in air and a reference fluid as a calibration before the measurement can be made. Our model requires only microlitre fluid volumes, needs no precise knowledge of cantilever geometry and we show, for a variety of fluids, that the calculated viscosity and density agree very well with accepted values. The method is reasonably robust to non-Newtonian fluids, but begins to break down as the frequency-dependence of the viscosity becomes more significant. On the face of it, the measurement of  $\eta_f$  and  $\rho_f$  is not directly relevant to the theme of aqueous interfaces, but the technique has potential application to complex, crowded biological fluids. In these systems, the cantilever probes the bulk fluid, but in doing so, can shed light on the interactions between molecules in solution, thereby giving indirect interfacial information.

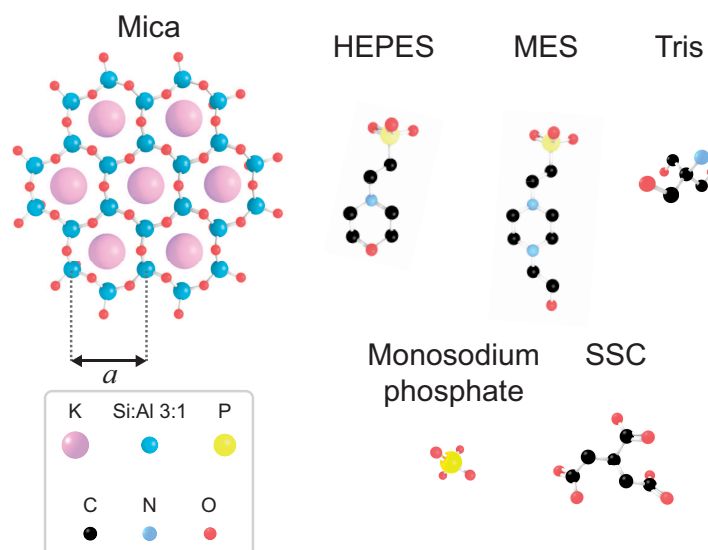


Fig. 3.1: Illustration of the scale and structure of the substrate (mica) and buffering compounds used in this study. The entire molecules are shown approximately to scale and the hexagonal lattice of mica's [100] surface has  $a = 5.2 \text{ \AA}$  [8]

### 3.1 Buffering agents at hydrophilic interfaces: a high resolution AFM study

Control over the electrostatic interactions within aqueous solutions is crucial in biological assays; the pH and charge densities are actively regulated *in vivo*, as they affect the stability of proteins as well as the mechanical and dynamic properties of biomimetic membranes [1–4] (discussed in much greater detail in chapter 5). In experiments, control over the concentration of protons and hydroxide ions is usually enforced with buffering agents [5]; macro-ions with dimensions of the order of nanometres that partially dissociate in aqueous solutions. There is no one molecular characteristic that determines whether a compound will be useful as a buffer – rather, their efficacy is judged on a set of criteria popularised by Norman Good [6, 7], resulting in the well-known family of “Good’s buffers”, many of which are in common use today. These criteria are not particularly strict; the compounds must be soluble in water, unable to cross biomembranes and have a  $pK_a$  between 6–8, among others. These minimal restrictions mean that buffers with a wide range of molecular sizes and degrees of charge/hydrophilicity are in common use (see Fig. 3.1 for the molecules studied here).

It is a basic assumption when using these buffer molecules that they do not affect any significant aspects of their biological assay. However, a buffer’s inertness tends not to be rigorously tested, especially not at the scale of single ions or molecules. Aside from

proteins, biological membranes are mostly composed of zwitterionic or negatively charged lipids, the organisation of which depend on specific electrostatic and hydration interactions. Therefore buffers, which are often zwitterionic themselves, can exert a great deal of influence on such biological systems. Indeed, they have been shown to induce buckling and clustering in neutral lipid membranes [9, 10], as well as perturbing the mechanics and structure of vesicles [11, 12] and altering protein-protein interactions [13]. The general mechanism underlying such effects is not yet clear, but undoubtedly is related to the specific manner each buffer perturbs the water around it.

High-resolution, small amplitude AFM can shed light on this problem by allowing the systematic comparison of the impact of various common buffers on the hydration landscape of a negatively-charged mineral (mica, structure in Fig. 3.1). The sub-nanometre lateral resolution of this AFM technique, as well as its sensitivity to the structure of the interfacial solution means that we can directly probe the aggregation and layering of the buffers at a similar scale to the molecules themselves. The use of mica is important because it provides a reproducible, atomically flat structure with well-defined dimensions as a canvas on which the buffers' perturbation is easily identifiable. It is also negatively charged, in common with most biological membranes, and its unit cell is of a similar area to the lipids molecules that compose them [14].

The buffers we investigated in this study, along with their nominal  $pK_a$ s [15] are listed in Table 3.1, along with illustrations of their structures in Fig. 3.1. We omit PBS buffer from the figure, as it is identical to the monosodium phosphate buffer, but with additional monovalent salts. In order to systematically compare the effects of the buffers, we made up 10 mM solutions of each and titrated them to pH 7.0. The different  $pK_a$ s of each molecule will result in a distinct charge state when the pH is adjusted to 7.0. The extent of this can be quantified using the well-known Henderson-Hasselbalch equation:

$$pK_a = pH + \log_{10} \frac{[B]}{[HB]}. \quad (3.1)$$

The above equation relates the  $pK_a$  of a buffer,  $B$ , to the relative concentration of species that are dissociated ( $[B]$ ) and associated ( $[HB]$ ) with protons,  $H$ . At a given pH, the ratio  $[B]/[HB]$  therefore denotes an effective charge state for the buffer in solution, which can be considered the buffering compounds' "valency",  $Z_B$ .  $Z_B$  can be used, along with equation 1.3, to calculate an effective Debye length,  $\kappa^{-1}$ . We document the  $pK_a$  of each buffer in this study, as well as polarity of the charged species and the calculated  $\kappa^{-1}$  in Table 3.1 It can be seen that the polarity of the charged species and the  $pK_a$  dramatically influence the electrostatic screening of the buffers. For example, at pH 7.0, HEPES

Buffering compound	Charged species polarity	$pK_a$	Debye length, $\kappa^{-1}$ (nm)
MES	–	6.27	4.90
HEPES	–	7.56	18.84
Monosodium phosphate	–	7.20	11.01
SSC	–	3.13	4.29
Tris	+	8.07	4.66
PBS	–	7.20	0.78

Tab. 3.1: Buffering agents investigated in the following study. Specific chemical species are: 2-(N-morpholino)ethanesulfonic acid hydrate (MES); 4-(2-hydroxyethyl)piperazine-1-ethanesulfonic acid (HEPES); monosodium phosphate ( $\text{NaH}_2\text{PO}_4$ ); saline-sodium citrate ( $\text{Na}_3\text{C}_6\text{H}_5\text{O}_7$ , SSC); trizma base (2-amino-2-(hydroxymethyl)-1,2-propanediol) (tris); phosphate buffered saline (PBS). The latter makes use of the same buffering molecule as monosodium phosphate, but includes  $\mathcal{O}(100 \text{ mM})$  monovalent salt, reflected in the minuscule Debye length.  $\kappa^{-1}$  was estimated from the relative concentration of the charged buffer species and equation 1.3. For reference, in pure water,  $\kappa^{-1} \sim 1 \text{ }\mu\text{m}$ .

is predominantly neutral in solution and thus has a large  $\kappa^{-1} \sim 20 \text{ nm}$ , despite having similar structure to MES, which has  $\kappa^{-1} \sim 5 \text{ nm}$ .

We then imaged a freshly-cleaved mica surface using AM-AFM while immersed in each buffer solution. As discussed in section 2.3, the free amplitude of oscillation was kept below about 1.6 nm and care was taken to keep the setpoint amplitude above  $\sim 70\%$  in order to probe the interfacial layer of water and buffers, without directly interacting with the mica itself [16].

### 3.1.1 Buffer organisation on mesoscopic length scales

Fig. 3.2 shows the apparent topography (purple/yellow, upper) and phase traces (blue/black, lower) of the mica in each buffering solution, as well as with ultrapure water as a control. The images all represent the impact of buffers on the hydration landscape on a scale of  $\sim 100 \text{ nm}$  – much larger than that of individual molecules. It is immediately obvious that, despite the substrate being identical in each case, each buffer alters the interface in a characteristic manner. This is due to the macroions in solution screening the mica’s surface potential to different extents (c.f. Table 3.1), and their size and geometry forcing them into species-specific configurations. These epitaxial arrangements can be resolved by the AFM tip, and their modification of the local fluid density generates similar contrast in the phase trace.

Both MES and HEPES (Fig. 3.2(a),(b)) produce periodic rows visible in both topography and phase, with a Fourier analysis giving their periodicity as  $3 \pm 1 \text{ nm}$ . The two buffers’ similar organisation at this scale is to be expected, given their similar structure (Fig. 3.1). Indeed, it may be the molecules’ relatively high aspect ratio that promotes

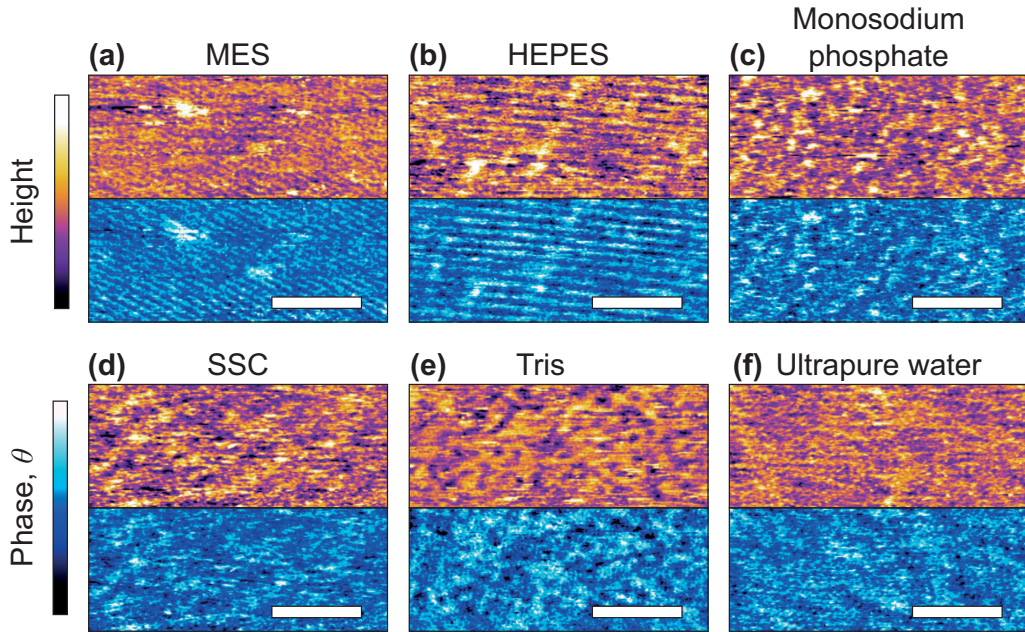


Fig. 3.2: Larger-scale AFM images of mica topography (purple/yellow, upper) and phase contrast (blue, lower) in buffer solutions. In MES (a) and HEPES (b) rows are clearly visible in topography and in phase. No regular structure is visible in monosodium phosphate (c), SSC (d) and Tris (e). Ultrapure water (f) was imaged as a control. Rows related to the mica lattice are hardly visible at that scale. In all images, the scale bar represents 30 nm. The topographic colour scale represents relative height variations ranging over 150 pm. The phase colour scale corresponds to variations of  $10^\circ$ .

supramolecular organisation of this regularity (the rows are about six times greater than mica's lattice parameter). The similarity in apparent topography, despite the distinct screening lengths of 4.90 and 18.84 nm respectively, emphasises the importance of steric and hydration interactions at the interface, which appear to dominate over mean-field concepts such as  $\kappa^{-1}$  here. In contrast, monosodium phosphate, SSC and Tris (Fig. 3.2(c)-(e)) present a much more amorphous landscape. The structures generated have a characteristic size of approximately 10 nm, but the lack of symmetry associated with the images indicates the inability of these buffers to organise themselves in a commensurate manner with the underlying mica lattice. The mica surface imaged in ultrapure water (Fig. 3.2(f)) shows features relating to the underlying mica lattice (likely due to Moiré effects) but no large height variations or aggregates, confirming that the variation observed previously is due to the action of buffer organisation at the interface.

### 3.1.2 Buffer organisation on molecular length scales

In order to investigate the nature of the adsorbed buffer layers with greater resolution, we took additional scans on a 20 nm scale. The results are shown in Fig. 3.3 and display molecular details of the mica lattice, but with superimposed features that reflected the

larger-scale structures observed earlier. In MES and SSC (Fig. 3.3(a), (d)), atomic-level resolution images were obtained but their quality was often inconsistent, with horizontal discontinuities and instabilities. HEPES (Fig. 3.3(b)) produced very stable and reproducible images, showing a mesh-like network developing epitaxially on the surface of mica. Of the five buffers used, HEPES demonstrates the greatest height variations whilst retaining stable atomic-level detail (see Fig. 3.4); HEPES has a roughness of 50 pm at the  $(20 \times 20)$  nm<sup>2</sup> scale, second only to monosodium phosphate (which did not allow the same imaging stability). We tentatively relate this enhanced layering to HEPES' larger Debye length (Table 3.1); its small effective charge results in short-ranged steric interactions dominating the interfacial structure, allowing for complex networks to form such as those observed here. The lack of atomic-level features in the topography when imaging in monosodium phosphate (Fig. 3.3(c)), is likely due to the small size of this buffer, which allows it to be more mobile at the interface due to a lack of steric hindrance upon adsorption. Interestingly, despite the lack of resolution in topography, the phase signal could resolve details of the mica lattice which indicates that there may be some underlying structuring of the solution, perhaps driven by Na<sup>+</sup> that dissociates from the powdered form of the buffer. The instability of imaging is reflected in the extremely high roughness values of the images (Fig. 3.4). Finally, the Tris-buffered solution (Fig. 3.3(e)) tended to induce some bi-stability while imaging, with regions revealing atomic-level details while other showed some aggregates adsorbed on the surface (dashed lines, lower half of (e)). These indicate that Tris forms at least two stable structures in  $z$ , and the larger surface features are in good agreement with those observed at lower magnification.

Imaging in ultrapure water proved difficult for achieving atomic-level resolution images of the muscovite lattice and it was necessary to reduce the cantilever's free and working amplitudes by about 20% to obtain the images presented above. This reduction meant that oscillations better mimicked the decay length of the hydration forces, allowing for improved resolution. Although water forms multiple, well-defined hydration states on muscovite mica [17–19], these layers do not alter the AFM tip's motion as much as larger, ionic adsorbates [19, 20], presumably due to water's smaller volume and greater surface diffusivity. This limited the overall resolution and was detrimental for high resolution imaging [21]. However, there are still several domains on a scale of a few nanometres superimposed to the lattice structure visible in Fig. 3.3(f), which are likely induced by the tip probing different hydration states of the surface.

It is common knowledge in the AFM community that the addition of salt to aqueous solutions aids resolution, presumably through the formation of better-defined, more symmetrical hydration structures on both surfaces. The concentration and type of charges in

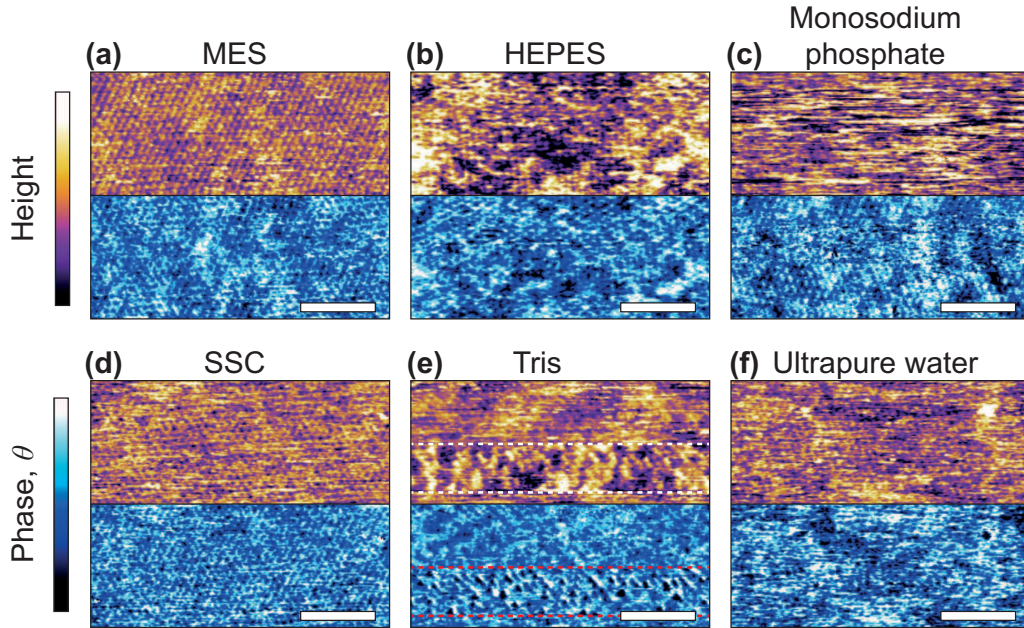


Fig. 3.3: High magnification AFM images of mica topography (upper) and phase (lower) in buffer solutions. In MES (a) the hexagonal symmetry of the lattice can be clearly resolved despite infrequent horizontal defects. Regular epitaxial modulations are visible in the phase. In HEPES (b) the symmetry is again clear, but convoluted with large variations in both topography and phase. The topography of monosodium phosphate (c) displays no atomic features but they can be occasionally resolved in the corresponding phase image. The mica lattice is perceptible in SSC (d) and appears similar to (a). In Tris (e), large features consistent with those in Fig. 2e are visible in the upper part of the image. Occasionally, the tip jumps (dashes) revealing a structured mesh. In ultrapure water (f) atomic-level features are visible alongside point-like deformities. The scale bar is 5 nm. Colour scales: the height is 150 pm and phase is  $10^\circ$

solution can strongly influence the electrical double-layer forces of submerged solids [22] (see also, subsection 1.2.1) and therefore play a significant role for AFM resolution [23]. However, the use of small oscillation amplitudes while imaging here leads to the resolution being dominated by short-range hydration effects, including those of adsorbed buffer ions. In practice, stock solutions typically contain a wide range and density of salts aside from the buffering agent. This salt can compete with the buffers at the charged interface and partially mitigate the effects observed in Fig. 3.2 and 3.3. We therefore investigated the impact of increasing ionic content by comparing three solutions; ultrapure water, a monosodium phosphate buffer and a phosphate-buffered saline (PBS) solution. The PBS solution is routinely used in biology to mimic physiological conditions and its buffering effect comes from the same phosphate molecule as that presented in Fig. 3.1, but with the addition of 140 mM NaCl. The high-resolution scan results are presented in Fig. 3.5.

The image in ultrapure water, Fig. 3.5(a), is consistent with Fig. 3.2 and 3.3; the underlying lattice of mica is visible but the imaging is at times unstable. In monosodium

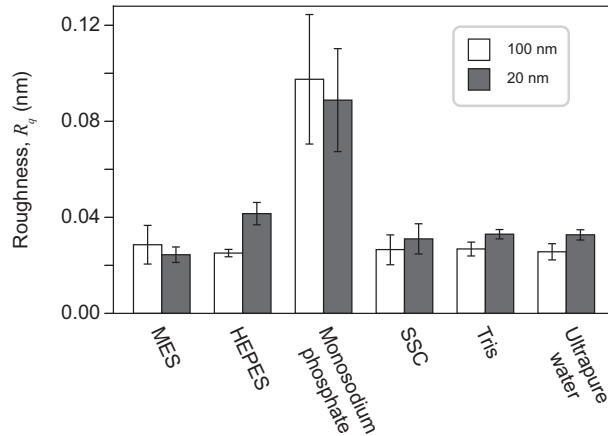


Fig. 3.4: Comparison of the root-mean squared roughness,  $R_q$ , of the buffer/mica interface as imaged by the AFM. The effect of monosodium phosphate upon the AFM imaging process is clearly elucidated by its large roughness. HEPES demonstrates an anomalous increase in roughness from 25.1 pm to 41.6 pm at  $(100 \times 100)$  nm<sup>2</sup> and  $(20 \times 20)$  nm<sup>2</sup> scans respectively. This is contrasted with the other buffers, where the 100 nm roughness is equal to that at 20 nm. It is likely related to the increase in resolution at this lengthscale that leads to the mesh being observed in Fig. 3.3(b). Error bars represent standard deviation of 5 consecutive scans in each buffer.

phosphate (Fig. 3.5(b)), the image quality is noticeably reduced and evidence of interfacial structure is only resolved through the phase trace (i.e. the modification of tip energetics, see section 2.2). The low resolution is in part due to buffer molecules loosely adsorbed on the surface that interfere with the imaging process but also may be a result of non-specific adsorption to the tip itself. In contrast, PBS generates the clearest images (Fig. 3.5(c)), demonstrating atomic-level resolution over the entire image. The overall imaging stability was confirmed by the roughness measurement of  $0.018 \pm 0.002$  nm, smaller than every previous buffer measured (Fig. 3.4). However, despite its regularity, the surface is not entirely homogeneous, with the lower portion of the phase image exhibiting individuated lattice sites (red dots), while the upper half only rows can be discerned (dashed lines). This is another indication that, although the resolution is improved, the buffer molecules are still interfering with the solid-liquid boundary, but in competition with  $\text{Na}^+$  ions.

### 3.1.3 Impact on biomimetic membranes

The discussion thus far has revolved around the potential impacts of buffers on *biological* systems. While mica is a vital tool in quantitatively comparing the nanoscale structuring of buffers given its hydrophilicity and uniformity, it clearly does not possess any surface groups that could be said to be biologically relevant. To emphasise the generality of our results, and their application to the life sciences, we performed AM-AFM experiments investigating the effect of the buffering solutions upon a silica-supported lipid bilayer

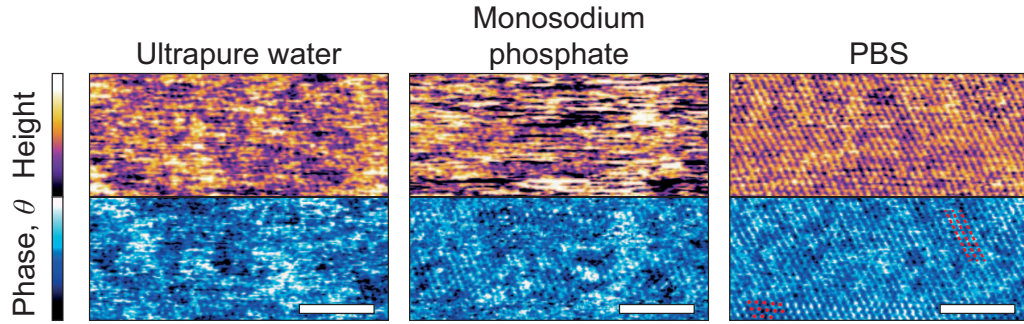


Fig. 3.5: Ionic content and strength affects the image quality in buffered solutions. Topographic images are presented in the upper portion and phase in the lower. (a) Ultrapure water, (b) monosodium phosphate buffer; again no atomic-scale features are observable in the topography. (c) Phosphate-buffered saline solution; the addition of 140 mM NaCl to the buffer results in a dramatic increase in image quality. However, variability in imaging conditions remains; from individual lattice points (dots) to row-like formations (dashed lines). Each image's scale bar is 5 nm and the colour scales are 150 pm for the height and  $10^\circ$  for the topography.

(SLB) composed of purified 1,2-dipalmitoyl-*sn*-glycero-3-phosphate (DPPA, Avanti Polar Lipids, Al, USA). The use of a silicon/silicon dioxide substrate had two motivations. The first was that it introduced a larger degree of roughness to the lipid bilayer, which better-approximated complex biological systems that do not show the uniformity of mica. Second, it enabled complimentary ellipsometry measurements to be carried out. These provide a label-free, non-perturbative method of investigating the solid-electrolyte interface, based on the surface-specific polarisation of light [24]. If we used a mica substrate, the measurement would otherwise have been hindered by the interference between its upper and lower crystallographic planes [25] and required either advanced averaging techniques or assumptions about the refractive index to be made [26].

### AM-AFM Imaging

A selection of representative ( $100 \times 100$ ) nm<sup>2</sup> images of the SLB in different buffer solutions is presented in Fig. 3.6. The height variations are much larger than that of mica ( $z$ -scale ranges over 500 pm) due to the intrinsic roughness of the silica support. This roughness inhibited high-resolution comparisons between the different buffer solutions and for this reason, only three of the previously-investigated buffers were compared; HEPES, Tris and monosodium phosphate (Fig. 3.6(b)-(d) respectively) as these produced the most characteristic changes in topography previously. They were compared to the SLB in 150 mM NaCl – that is, the solution it was formed in. Distinctive changes in topography upon the exchanging of buffers are still evident.

The image in 150 mM NaCl, demonstrates a smoothly-varying topography over a lengthscale similar to that of the bare silica, with  $R_q = 107$  pm. This is smaller than

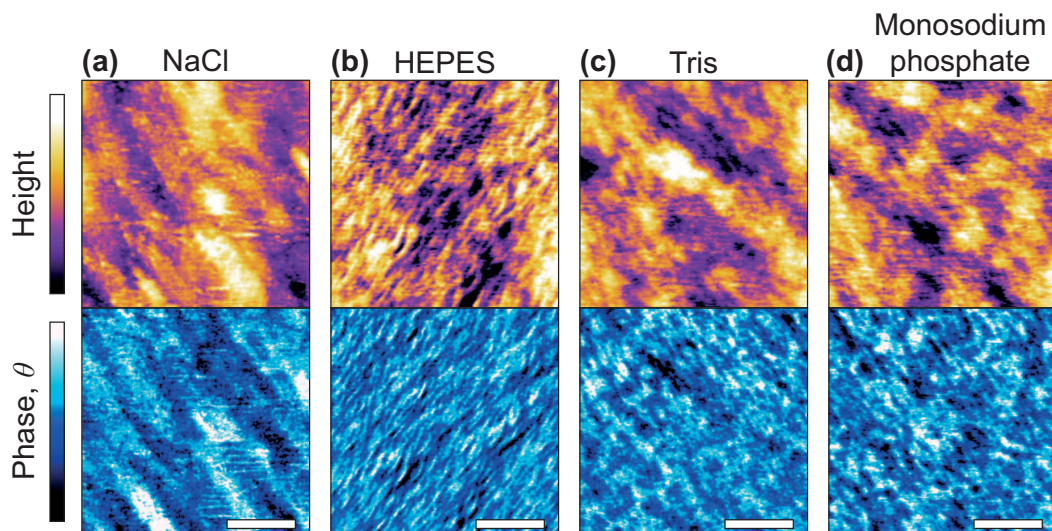


Fig. 3.6: Comparison of the impact of buffering agents on a silica-SLB with that of a monovalent salt. In 150 mM NaCl (a), the surface demonstrates similar features to that of the bare silica surface, indicating that the bilayer follows the support straightforwardly. Replacing this with 10 mM HEPES (b) induces clear wrinkling with a coherent direction (bottom-left to top-right) and approximate width of 7 nm. (c) In 10 mM Tris, the apparent topography is rather unremarkable, but the phase displays non-uniform mesh-like structures across the surface of  $\sim 15$  nm size, in a similar manner to its behaviour on mica. (d) The SLB in 10 mM monosodium phosphate demonstrates similar features to those when immersed in Tris; a homogeneous network-like structure is found in the phase trace, but the topography more closely resembles that of the SLB in NaCl. Topography is shown in orange/purple (colour scale range = 500 pm in all), with the corresponding phase shown below in blue (colour scale range =  $10^\circ$  in all) and scale bars represent 30 nm.

the roughness observed on the bare silicon/silicon dioxide surface (137 pm), reflecting the bilayer’s “smoothing out” out some of the rougher features. Other than this, the bilayer follows the topography of the support well, with no anomalous surface features. After exchanging the solution for HEPES, the bilayer was imaged again. In this case (Fig. 3.6(b)), strong modifications to the surface topography are observed; the SLB is wrinkled (on a lengthscale of 5-10 nm) and has  $R_q = 158$  pm, likely induced by electrostatic interactions between the charged lipid headgroups. Specifically, HEPES is much less able to screen the repulsive headgroups when compared to the high concentration of sodium ions, possibly resulting in a non-zero spontaneous curvature, in a similar manner to electrostatic ripple formation in lipid bilayers supported on an electrode [27]. The effects of Tris and monosodium phosphate ((c), (d)) demonstrate qualitatively similar topographies, but are distinct from that of HEPES. The reason for the discrepancy between HEPES and the other buffers is not clear, but could well be related to HEPES’ zwitterionic form, rather than the ionic phosphate, or the rather charged tris ( $pK_a = 8.07$ ). The latter buffers each induce small ( $\sim 15$  nm) features in the phase trace which mimic those observed their impact on mica (Fig. 3.2(c) and (e)). These similarities indicate an equivalent templating process of the buffering ions occurring at the membrane as occurred on mica.

### *Ellipsometry*

To confirm that the results presented thus far are driven by the presence of buffering agents and not influenced by the action of the tip, ellipsometry was performed on a DPPA/silica system (prepared identically as before), and the characteristic angles,  $\psi$  and  $\Delta$  (see subsection 3.1.5), presented in Fig. 3.7. Typically, these would be analysed over a range of wavelengths and fitted to a model to gain information about the adsorbed film thickness and optical properties of the layer but given the uncertainty about the true nature of the adlayer and complexity of the lipid layer itself, this is somewhat beyond the scope of this study. Instead, the extent to which the angles depended on the buffering agent was measured at a single wavelength (589 nm). The data show a clear difference in both  $\psi$  and  $\Delta$  between the solutions with buffer in and that with solely NaCl. The buffered solutions are of comparable magnitude, which is somewhat intriguing given that the topography scans of Fig. 3.6(a), (c) and (d) are qualitatively very similar. Although the  $\psi$  values with buffer molecules are not equal within errors they are much better grouped than that of NaCl. The  $\Delta$  data points are not so distinct, but the values for Tris and monosodium phosphate are much closer together than they are to HEPES or NaCl, which could explain the similar templating effect seen in the phases of Fig. 3.6(c) and (d). Ellipsometric measurements on similar systems such as a lipid monolayer-coated silicon dioxide wafer [28] or a phosphoryl choline-modified polymer on silica [29] do not agree with our values of  $\psi$  or  $\Delta$  – it was assumed that this was due in part to the different nature of their samples – but their results indicate that changes in the ellipsometric angles of  $\sim 0.5^\circ$  are significant in relation to the formation of thin films. This indicates that the difference in phase scans observed in the same images did indeed represent a layering of buffer molecules on the bilayer surface. However, without further models or analysis, no stronger conclusions can be drawn.

### *3.1.4 Conclusions: buffers at hydrophilic interfaces*

We have used small amplitude AFM, as described in chapter 2, to investigate the interfacial behaviour of five common buffering agents with molecular-level resolution. The buffers produce cohesive aggregates on mica's charged substrate that affect the apparent structure of the Stern layer. MES and HEPES can form epitaxial lattice-like arrangements commensurate with the underlying mica structure, suggesting that they offer the most suitable solution for high-resolution studies. SSC, Tris and monosodium phosphate conversely formed an amorphous mesh layer with no preferential ordering. In particular, the latter interferes with the imaging process to such an extent that no atomic-level details is visible in the topography. The effects of the buffering agents are however mitigated by the adjunction of salt which can displace them from the interface. We have also shown,

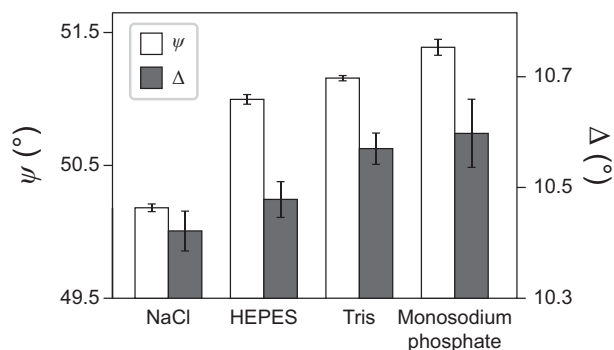


Fig. 3.7: The effect of buffering agents on the interfacial properties of a silica-supported lipid bilayer as probed by ellipsometry. The angles  $\psi$  and  $\Delta$  are defined such that the ratio of polarised light,  $R_p/R_s = \tan \psi \exp(i\Delta)$ . There is a clear discrepancy in the  $\psi$  values between the sample immersed in a NaCl solution and those immersed in buffers, which have much smaller separations. This suggests a distinct interfacial modification in agreement with Fig. 3.6. The  $\Delta$  values' trend is less clear, but Tris and monosodium phosphate are equal within errors, which correlates with the AFM images produced.

using ellipsometry as well as AM-AFM, that this behaviour is observed in biomimetic membranes; buffer molecules can actively assemble at their surface, forming cohesive layers over hundreds of nanometres. The results hold significance for future biological assays, as the buffers' modification of the interfacial organisation may impact upon adsorption or binding of key molecules in solution.

### 3.1.5 Materials and methods: section 3.1

All buffers were purchased from Sigma-Aldrich (St. Louis, MO, USA) at purity of at least 99.95%. The  $pK_a$ s quoted above are from ref. [15] and are valid at 25°C. Buffers were made up to a concentration of 10 mM and titrated to a pH of 7.0 at 25 °C with 0.17 M KOH and 0.5 M HCl. The solutions were then sonicated for 10 minutes in order to ensure complete solution of the buffering molecules and removal of any dissolved gases. Approximately 50  $\mu$ l of the buffer solution was deposited on the mica and a similar quantity on the cantilever tip using a pipette. A capillary bridge was then formed between the mica and cantilever by bringing the two into close proximity.

#### Atomic force microscopy

A commercial Cypher ES AFM (Asylum Research, Santa Barbara, USA) equipped with photothermal excitation (blueDrive) and thermal control was used for all experiments. The blueDrive and temperature control result in highly stable imaging parameters, making direct comparison between buffers more meaningful. We also improved comparability by using the same cantilever model (Arrow UHF AuD, NanoWorld, Neuchâtel) for the duration of the experiment. It had a stiffness of  $k_1 = 1.8 \text{ N m}^{-1}$  calculated from its thermal

spectrum and calibration of  $S_f^{-1}$  [30] (see subsection 2.4.1 and equation 2.15), and was driven at its fundamental resonance frequency of  $\sim 390$  kHz in liquid. The measurements on mica were conducted sequentially over one day. Prior to imaging, the cantilever was immersed in a bath of ultrapure water (18.2 M $\Omega$ ,  $< 5$  ppm organics, Merck Millipore, Watford, UK), followed by isopropyl alcohol (Sigma-Aldrich, 99.7% purity), followed by ultrapure water again for a total of 30 minutes to remove as much organic matter from the tip as possible, while minimising physical tip alterations. Grade I Muscovite mica (SPI supplies, USA) was used and freshly cleaved with adhesive tape before all measurements. The AFM was operated in amplitude-modulation mode with the cantilever and tip fully immersed in the liquid. The working amplitude was adjusted to gain the best image quality possible between 1.0 nm and 1.5 nm while the free oscillation amplitude was kept constant at 1.6 nm. In Fig. 3.2, 3.3, 3.5 and 3.6, original scan sizes were  $(100 \times 100)$  nm<sup>2</sup>,  $(20 \times 20)$  nm<sup>2</sup>,  $(20 \times 20)$  nm<sup>2</sup> and  $(100 \times 100)$  nm<sup>2</sup>, respectively. All images were taken at a constant scan rate (lines-per-second) of 4.88 Hz.

### *Image analysis*

The AFM images were produced by Asylum Research software package (ver. 13.17.101) (Asylum Research, Santa Barbara, USA) for Igor (ver. 6.3.7.2, Wavemetrics, Lake Oswego, USA), before being flattened line-by-line with a first-order polynomial. The root-mean squared roughness,  $R_q$ , values were calculated according to:

$$R_q = \sqrt{\frac{1}{MN} \sum_{k=0}^{M-1} \sum_{l=0}^{N-1} z(x_k, y_l)^2}, \quad (3.2)$$

where  $z(x_k, y_l)$  is the measured height at point  $(x_k, y_l)$  and  $k$  and  $l$  sum over the points and lines of each image (here,  $M = N = 256$ ). Each data point in Fig. 3.4 was taken as the average of 5 images, with the error bars representing the standard deviation of that set. The presented figures were slightly low-pass filtered using FFT-based analysis to remove unwanted high-frequency noise.

### *Silica-supported lipid bilayer formation*

Supported lipid bilayers (SLBs) of the anionic lipid 1,2-dipalmitoyl-*sn*-glycero-3-phosphate (DPPA) (Avanti Polar Lipids Inc., AL, USA) were formed via the vesicle fusion method [31, 32] Briefly, a chloroform solution containing DPPA at 1 mg ml<sup>-1</sup> was pipetted into a 10 ml vial and dried under nitrogen until there was no visible fluid remaining. It was then placed under vacuum for  $> 4$  hours to ensure complete evaporation. The lipid film was rehydrated with Milli-Q ultrapure water to a concentration of 3 mg ml<sup>-1</sup> and bath sonicated. The solution was then extruded at least 19 (but always an odd number) times using a Mini-

Extruder kit (Avanti Polar Lipids Inc., AL, USA) with a 100 nm filter (Whatman, GE Healthcare Life Sciences, Buckinghamshire, UK) to form small, unilamellar vesicles (SUVs) above the transition temperature of the lipids (for DPPA, this is approximately 67°C [14]). The solution was then diluted with 150 mM NaCl to a concentration of 0.1 mg ml<sup>-1</sup>. This resulted in a salt concentration of  $\sim 145$  mM which would encourage the SUVs to fuse and spread onto the silica substrate. All glassware and components had been cleaned thoroughly by sonication with ultrapure water, then isopropyl alcohol, and water again for ten minutes each before coming into contact with the lipids.

A silicon wafer with a native silicon dioxide layer was cleaned thoroughly by sonication in diluted Deacon-90 (Deacon Laboratories, Sussex, UK) detergent for ten minutes, followed by a similar treatment with ultrapure water, isopropyl alcohol and then ultrapure water once more. The silica was then made hydrophilic via exposure to an argon plasma at 1 mbar for 30 s. Immediately afterwards,  $\sim 80$   $\mu$ l of the SUV/NaCl solution was pipetted onto the wafer before being sealed in a petri-dish, heated to 77°C for 1 hour and cooling to room temperature at a rate of 10°C h<sup>-1</sup>. When exchanging the buffering fluid, the bilayer was copiously rinsed, with at least ten times the initial volume ( $\sim 100$   $\mu$ l) covering the silicon wafer.

### *Ellipsometry*

As discussed previously in the chapter, ellipsometry provides a label-free, non-perturbative method of investigating thin films forming interfaces [24] It works on the principle that the parallel and perpendicular coefficients of reflection of monochromatic light ( $R_p$  and  $R_s$  respectively) are extremely sensitive to the presence of chemical layers formed at a reflective surface. Ellipsometric measurements typically probe the ratio between these complex reflectivities,  $\rho$ , such that  $\rho \equiv R_p/R_s = \tan \psi \exp(i\Delta)$ , where the ellipsometric angles  $\psi$  and  $\Delta$  give an indication of the extent to which a surface is modified. Measurements were carried out on a picometer phase-modulated ellipsometer (Beaglehole Instruments) using a He-Ne laser ( $\lambda = 589$  nm), with an incident angle of 70°. After the SLB was formed on the silica surface (see above), the wafer was gently rinsed with 150 mM NaCl solution to remove any unfused vesicles. It was then entirely submerged in the NaCl solution in a Petri dish so as to remove aberration that would be produced by a curved droplet surface. Each data-point presented is the average of five sets (each at different points on the silica) of ten ellipsometric measurements. When altering buffering agents, care was taken not to expose the sample to air (and potentially destroy the SLB) by exchanging fluids using a pipette tip. At least twice the volume of the Petri dish was used when rinsing the bilayer, to ensure no residual salt or buffer remained at its surface. The sample was then left to equilibrate for 30 minutes before continuing the measurement.

## 3.2 Viscometry and density sensing of fluids using a vibrating lever

We now focus briefly on how AFM (more precisely, its oscillating cantilever) can be used to measure properties of bulk liquids. Thorough characterisation of both the viscosity,  $\eta_f$ , and density,  $\rho_f$ , of complex fluids is a pertinent topic in many fields ranging from the petroleum industry, chemical engineering, the food and beverage industry and biomedical diagnosis of bodily fluids [33–37]. The latter case is of particular interest due to our increasing understanding of the significance of exosomes – extracellular vesicles with diameters of  $\mathcal{O}(10\text{-}100\text{ nm})$  – as biomarkers of disease [38]. The interaction of such exosomes with each other and the surrounding fluid will inevitably affect global dynamic properties such as the viscosity and may well depend on the specific interfacial properties of the vesicles, especially their charge and protein content. Thus our development of an AFM-based calibration for the viscosity and density of simple fluids represents a first step towards understanding the interfacial interactions between biological macromolecular assemblies in solution.

Standard devices for measuring viscosity, such as rheometers [39], typically require large samples of several millilitres or more. One way around this problem is to use micro-cantilevers – of similar dimensions to those used in AFM – as sensors to probe their local fluid environment [40–44]. The levers’ size means that only microlitres of the fluid are needed, and interrogation of their dynamic behaviour allows the simultaneous extraction of their viscosity and density (clear in the dependency of e.g. equation 2.16 on  $\Gamma$ , itself a function of  $\text{Re} = \rho_f \omega b^2 / 4\eta_f$ ), making them an attractive target for novel lab-on-chip-style devices. However, the indirect method of measuring the levers’ motion (commonly a reflected laser signal, as with AFM) means that developing appropriate and easily-applicable models is not trivial. Many methods begin with the approach of Sader which, for given cantilever dimensions and the measurement of a thermal spectrum, allows the hydrodynamic function,  $\Gamma(\text{Re})$ , to be computed. This is then inverted to extract  $\eta_f$  and  $\rho_f$ . Key here is the implicit knowledge of the geometry wrapped up in  $\Gamma(\text{Re})$ ; at the scale of these levers, characterisation is lengthy and requires electron microscopy to achieve the necessary precision. As such, these methods are successful, but can often have errors of  $\sim 20\%$  [43].

We tackle this problem by deriving novel equations that allow the viscosity and density of a solution to be calculated using just the measurement of a cantilever’s first two resonance frequencies in air and the fluid. At this stage however, knowledge of the cantilever’s

density and thickness is required, which is not ideal, as mentioned above. We circumvent this *via* a “calibration” procedure that takes as input the first two resonance frequencies of the cantilever in another liquid of known density and viscosity (here, we suggest water). Following this, the viscosity and density can be found for any fluid the cantilever is immersed in, provided that a well-defined thermal spectrum can be acquired (in effect this places soft limits on the opacity and absolute viscosity of the samples that can be studied). Significantly, our calibration process takes cantilever geometry into account and so no approximations must be made in the case of non-ideal shapes or manufacturing defects.

### 3.2.1 Development of analytic equations for viscosity and density

We begin from the same formalism of equation 2.17-2.19 – that is, assuming a hydrodynamic function characterised by two real ( $a_1, a_2$ ) and two imaginary ( $b_1, b_2$ ) coefficients. From equation 2.19, if the first two resonance frequencies of the cantilever in air ( $\omega_{a1}, \omega_{a2}$ ) and a fluid ( $\omega_{f1}, \omega_{f2}$ ) are measured, the expression can be solved for the two unknowns of viscosity and density of the fluid:

$$\rho_f = \frac{4\rho_c h}{\pi a_1 b (\sqrt{\omega_{f2}} - \sqrt{\omega_{f1}})} \left( \frac{\omega_{f1}^{3/2} (\omega_{a2}^2 - \omega_{f2}^2) - \omega_{f2}^{3/2} (\omega_{a1}^2 - \omega_{f1}^2)}{\omega_{f2}^{3/2} \omega_{f1}^{3/2}} \right), \quad (3.3)$$

$$\eta_f = \frac{4(\rho_c h)^2}{\pi^2 a_2^2 \rho_f \omega_{f1}^3} \left( \omega_{a1}^2 - \omega_{f1}^2 - \frac{\pi a_1 \rho_f b}{4\rho_c h} \omega_{f1}^2 \right)^2. \quad (3.4)$$

Clearly, these expressions are still dependent on the cantilever’s width, thickness and density ( $b, h$  and  $\rho_c$ ), not to mention the (as yet unknown) hydrodynamic coefficients  $a_1, a_2$ . The former parameters are decidedly non-trivial to measure, especially for composite cantilevers made from different materials [42]. We therefore measure a further two resonance frequencies ( $\omega_{w1}, \omega_{w2}$ ) of the cantilever immersed in water, which has a well-defined viscosity,  $\eta_w$ , and density,  $\rho_w$ , for a given temperature and pressure. Incorporation of these values into the above formulae removes any dependency on geometrical parameters or hydrodynamic coefficients, allowing for rather general expressions that can be easily applied to any vibrating lever. For the sake of clarity, we define

$$X(j, k, l, m) \equiv \frac{j^{3/2}(m^2 - k^2) - k^{3/2}(l^2 - j^2)}{(jk)^{3/2}}, \quad (3.5)$$

where  $j, k, l, m$  are dummy variables representing the various resonant frequencies. This results in the expressions:

$$\frac{\rho_f}{\rho_w} = \left( \frac{\sqrt{\omega_{w2}} - \sqrt{\omega_{w1}}}{\sqrt{\omega_{f2}} - \sqrt{\omega_{f1}}} \right) \frac{X(\omega_{f1}, \omega_{f2}, \omega_{a1}, \omega_{a2})}{X(\omega_{w1}, \omega_{w2}, \omega_{a1}, \omega_{a2})}, \quad (3.6)$$

$$\frac{\eta_f}{\eta_w} = \frac{\rho_w \omega_{w1}^3}{\rho_f \omega_{f1}^3} \left( \frac{\omega_{a1}^2 - \omega_{f1}^2 - \omega_{f1}^2 (\sqrt{\omega_{f2}} - \sqrt{\omega_{f1}})^{-1} X(\omega_{f1}, \omega_{f2}, \omega_{a1}, \omega_{a2})}{\omega_{a1}^2 - \omega_{w1}^2 - \omega_{w1}^2 (\sqrt{\omega_{w2}} - \sqrt{\omega_{w1}})^{-1} X(\omega_{w1}, \omega_{w2}, \omega_{a1}, \omega_{a2})} \right)^2. \quad (3.7)$$

To re-iterate, the subscripts  $a, w, f, 1$  and  $2$  represent the measurements in air, water and the fluid of interest, and the first and second resonant frequency respectively. These expressions only require six resonant frequencies, without any dependence on the choice of cantilever or indeed hydrodynamic coefficients in the calculation. In principle, this formalism can also be used to calculate the added mass and damping of the cantilever in various fluids, but we do not investigate this here.

### 3.2.2 Experimental verification of the method

We now verify the accuracy of equation 3.6 and 3.7 by using them to measure the density and viscosity of six common fluids: isopropanol, acetone, butanol, decane, bromoform and hexanol (all purchased from Sigma-Aldrich with purity  $> 99\%$  and used without further purification). Our reference liquid was ultrapure water (18.2 M $\Omega$ , Merck-Millipore, Dorset, UK), with  $\rho_w = 997 \text{ kg m}^{-3}$  and  $\eta_w = 8.94 \times 10^{-4} \text{ kg m}^{-1} \text{ s}^{-1}$  [45]. To emphasise the generality of this expression, we conducted our experiments using four different (rectangular) cantilevers of varying dimensions and stiffnesses (all RC800 PSA, Olympus, Japan, see Table 3.2). In all cases, the thermal spectra were acquired by an MFP-3D Infinity AFM (Asylum Research, Santa Barbara, CA, USA), with the deflection monitored *via* the AFM's laser.

Cantilever	Width ( $\mu\text{m}$ )	Length ( $\mu\text{m}$ )	Thickness ( $\mu\text{m}$ )	Stiffness, $k_1$ ( $\text{N m}^{-1}$ )
C1	40	100	0.8	0.76
C2	20	100	0.8	0.39
C3	40	200	0.8	0.10
C4	20	200	0.8	0.05

Tab. 3.2: Nominal physical characteristics of the cantilevers used to verify our equations. The cantilevers have a 3  $\mu\text{m}$ -high tip mounted at one extremity, but this is not expected to influence the measurement.

The measurements of resonant frequency extracted from the cantilevers' thermal spectra are shown in Fig. 3.8, as a function of the fluids' accepted viscosity and density [45–48]. It is clear that, for a given cantilever and mode, the resonance frequency generally decreases as the liquid becomes more viscous or more dense. This is to be expected, from

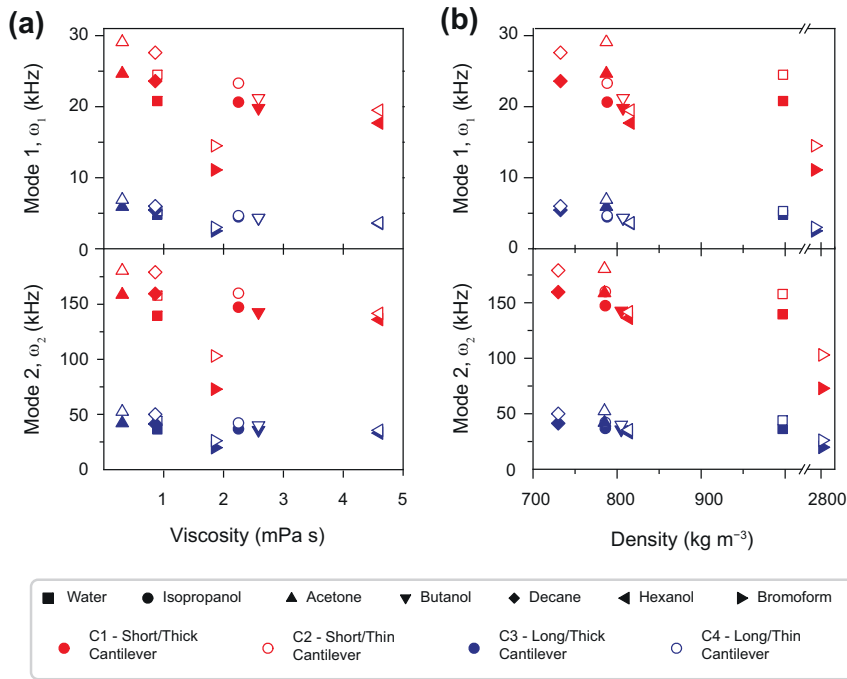


Fig. 3.8: Measured resonance frequencies of the four different cantilevers plotted against the liquids' viscosities (a) and densities (b). In general, increasing the liquid's density and viscosity leads to a decrease in resonance frequency, regardless of cantilever or mode. This is however non-monotonic and its extent depends on the geometry of the cantilever used for the measurement.

the added damping and effective mass that results from a greater coupling between the lever and its environment (compare with, e.g. Fig. 2.2). However, the extent of this change varies depending on the lever stiffness and dimensions, and is not always consistent (note the bromoform measurement in (a), which may deviate due to its much greater mass than the other fluids (b)).

From the measurements of resonant frequencies in Fig. 3.8, as well as the two in air,  $\omega_{a1}, \omega_{a2}$ , equation 3.6 and 3.7 can then be used to find predicted values for the viscosity and density of the fluids. The results are presented in Fig. 3.9, compared against the predicted values at 25°C [45–48]. The dashed line is a guide for the eye and has a gradient of unity. The results agree excellently for the range of fluids studied here, with deviation from the accepted viscosity values less than 10% for those fluids with low  $\eta_f$ . The error for high viscosity fluids is increased, regardless of the cantilever used (see the data points for hexanol), which is to be expected given the approximation of the hydrodynamic function is optimised for lower viscosities [49]. The density has a rather larger spread (see inset in (b)) but the relative error remains low.

The main issue with our method when dealing with highly viscous liquids comes from

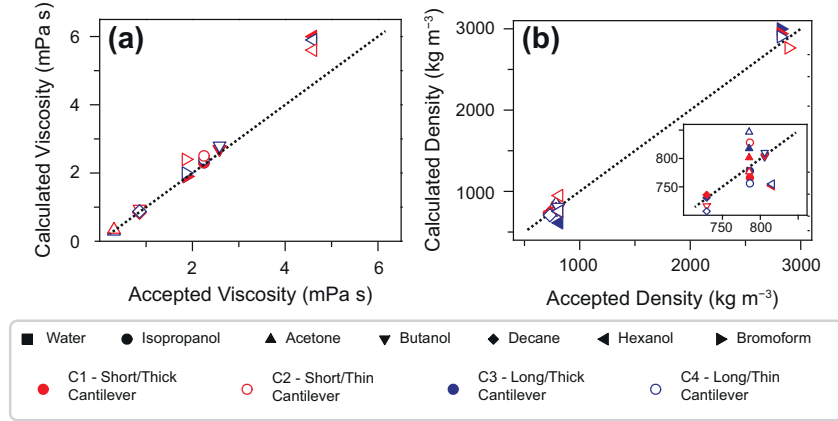


Fig. 3.9: Comparison between the accepted and calculated viscosities (a) and densities (b) of the probed fluids. The values of  $\eta_f$  and  $\rho_f$  derived from the measurements compare well with the accepted values, as evidenced by their collapse onto the line of unity gradient. The inset in (b) highlights the data points at lower densities.

Fluid	Error in $\rho_{12}$ (%)	Error in $\rho_{23}$ (%)	Error in $\eta_{12}$ (%)	Error in $\eta_{23}$ (%)
Isopropanol	3.8	1	10	8
Butanol	0.62	5	8.4	5.8
Hexanol	7.3	4.5	28.2	5

Tab. 3.3: Percentage errors between the calculated and accepted values of  $\rho$  and  $\eta$  for the more viscous liquids using the 1<sup>st</sup>/2<sup>nd</sup> and 2<sup>nd</sup>/3<sup>rd</sup> resonant frequencies. All cases refer to cantilever C4. The error is reduced by considering the 2<sup>nd</sup>/3<sup>rd</sup> resonance frequencies except for the density of butanol where the third resonance was difficult to identify.

the experimental uncertainty of locating the resonant frequency. We extracted the various  $\omega$  by fitting an function of the form of equation 2.7 to the thermal spectra, which required the manual choice of a fit region in each case. This can incur errors, especially when the oscillation amplitude peak is highly damped (common in viscous fluids). This effect can be minimised by choosing higher oscillation modes, if they can be resolved in the spectra, due to their higher effective stiffness and thus lower fluid damping. We therefore calculated the density and viscosity of hexanol from the second and third cantilever Eigenmodes, as shown in Table 3.3. Comparison with derivations using respectively the 1<sup>st</sup>/2<sup>nd</sup> ( $\rho_{12}$ ,  $\eta_{12}$ ) and 2<sup>nd</sup>/3<sup>rd</sup> ( $\rho_{23}$ ,  $\eta_{23}$ ) resonance frequencies shows that the latter perform better in more viscous fluids.

There is, however, an important point that has not been considered so far. Our model assumes that the viscosity is a scalar quantity and not a function of the probing frequency – i.e. the liquids probed are Newtonian. This assumption is mostly justified for the test liquids used to validate our model, but this may not hold, for example, for bodily fluids [35, 37] or lubricants [33]. A deviation from Newtonian behaviour will induce some error in our predictions since the liquid is probed simultaneously at different frequencies, with the

second frequency typically 5-6 times higher than the first. This could partially explain the poorer results obtained in the more viscous hexanol.

In order to tackle this issue up front, we tested the model in ultrapure water solutions containing increasing concentrations of poly(ethylene) oxide (PEO), a simple uncross-linked polymer that has been shown to exhibit non-Newtonian properties in aqueous solutions [50, 51]. We used varying concentrations of  $300\,000\text{ g mol}^{-1}$  PEO (Sigma-Aldrich, Dorset, UK) in water. It was immersed in ultrapure water to a concentration of 3 wt% and dissolved using a magnetic stirrer at 700 RPM for 24 hours until a uniform milky solution was obtained. The solution was then centrifuged at 2500 RPM for 10 minutes to separate the PEO solution from the insoluble butylated hydroxytoluene (BHT) that the initial powder contained. The then-clear fluid was removed with a pipette and bath-sonicated for 10 minutes to remove any dissolved air. The PEO solution was diluted to the required concentration with ultrapure water and the resulting mixture was bath-sonicated for 10 minutes. These solutions are shear thinning across a broad range of molecular weights and concentrations [52], similarly to most bodily fluids, which means the cantilevers of different lengths will experience different rheological environments.

Fig. 3.10 shows the density and viscosity of various dilutions of PEO in ultrapure water, as calculated using our model, with two cantilevers of different lengths (C1 and C3; subscripts “short” and “long” respectively). In practice, the first resonance peak,  $\omega_1$  was not observed in the more concentrated PEO solutions for C3 (the longer cantilever), and so we calculated  $\eta_{23}$  and  $\rho_{23}$  (as in Table 3.3). This meant that the longer cantilever effectively probed the solution at higher frequencies than the short. As the concentration of PEO increases, the viscosity and density derived from both cantilevers increases and decreases, respectively. For relatively low PEO concentrations ( $< 1.0\text{ wt}\%$ ),  $\rho$  and  $\eta$  as measured by each cantilever are similar, but at greater concentrations, the discrepancy increases dramatically. This indicates a strong dependence of the calculated values on the cantilever geometry and therefore the resonance frequency, as expected for non-Newtonian fluids. The fact that the observed discrepancy increases with PEO concentration is to be expected given that cantilevers are of different lengths (see Table 3.2) and therefore resonate at quite different frequencies – for example in ultrapure water, the resonance frequency of the first mode of the short cantilever is more than four times that of the long one. Our model is hence particularly sensitive to viscosity and density variations in non-Newtonian liquids.

For the shorter cantilever, the derived viscosity agrees very well with the standard

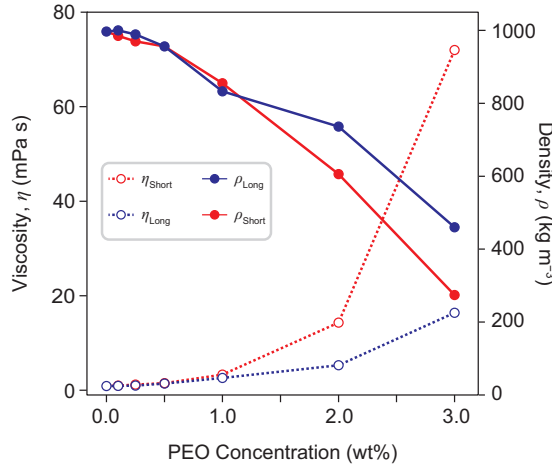


Fig. 3.10: The calculated density,  $\rho$ , and viscosity,  $\eta$ , of different concentrations of PEO in ultrapure water as measured by two different cantilevers. Both  $\eta_{\text{short}}$  and  $\eta_{\text{long}}$  increase with increasing PEO concentration, but the effective viscosity measured by the shorter lever is always higher. The discrepancy between the two cantilevers increases with the PEO concentration due to a frequency dependence of the actual viscosity that is not accounted for by our model. However,  $\eta_{\text{short}}$  agrees with standard rheometer measurements even for the highest PEO concentration measured. This demonstrates the validity of microcantilever measurements for non-Newtonian liquids, provided there is a suitable choice of a cantilever. The calculated density decreases as the concentration of PEO increases, and the discrepancy between the two cantilevers, increases in a similar manner to the viscosity. The dramatic reduction in  $\rho_{\text{short}}, \rho_{\text{long}}$  for a relatively small wt% of PEO implies that the model’s calculated densities are less robust than its viscosities (see also inset to Fig. 3.9(b)).

rheometer measurements of PEO in fluid at concentrations of 2 and 3 wt%<sup>1</sup>, while for the longer cantilever the calculated viscosity values are significantly lower. The viscosity as measured by the shorter cantilever is always greater than that obtained from the longer cantilever, for solutions containing PEO. This reflects the fact that for longer cantilevers, the second and third modes of vibration were used as part of our model, due to the first mode being not measureable at high PEO concentration. This is in line with PEO’s shear-thinning behaviour [52], since the frequencies used for the longer cantilever are in fact higher than those used for the short cantilever. We therefore expect to find  $\eta_{\text{long}} < \eta_{\text{short}}$  as observed.

The measured density decreases monotonically with PEO concentration for both cantilevers, but the relationship between the two measurements is less straightforward than for viscosity. At PEO concentrations of nearly 0.5 wt% and 1.1 wt%, the density measured by both cantilevers coincides. These concentrations are greater than the so-called overlap concentration i.e. the concentration above which the polymer coils are dense enough to form transient meshes [50]. This suggests that the agreement may be due to non-linearities in our model or possibly errors in determining the resonant frequency, rather

<sup>1</sup> R. Thompson, private communication, 2017

than reflecting the intrinsic properties of the polymer solution. At higher concentrations, the apparent reduction in density by a factor of over 3.5 ( $\rho_{\text{short}}$ ) or over 2 ( $\rho_{\text{long}}$ ) cannot be correct given the inclusion of only a few weight percent of the polymer. This suggests our model's calculated viscosity to be more reliable than the derived density, the latter becoming unphysical when probing non-Newtonian fluids.

### 3.2.3 *Conclusions: dynamic cantilevers as viscometers*

Our developed method is able to quantitatively determine the viscosity and density of different liquids from interrogation of the thermal vibrations of an immersed microcantilever. We derive analytical expressions based on the Euler-Bernoulli beam theory to quantify the hydrodynamic influence of various fluids and deduce their viscosity and density. It requires only measurement of the first two resonance frequencies of the immersed cantilever after calibration in air and in a reference liquid, here water and provides analytical expressions for the viscosity and density that are completely independent of the cantilever's characteristics. Experimental validation of the method over an extensive range of liquids yields errors of less than 10% with accepted values. The validity of the model in fluids with frequency-dependent viscosities,  $\eta = \eta(\omega)$ , was also investigated using PEO in different concentrations as a model non-Newtonian shear-thinning fluid. As expected, the method becomes progressively dependent on the cantilever geometry as the concentration of PEO increases. This is due to the fluid's viscosity becoming more dependent on the frequency as the density of the polymer chains increases. The method could also be used in the field of AFM in liquid, in particular in the analysis of surface-coupled effects on the cantilever vibrations and for the investigation of liquid flow near liquid-solid interfaces.

## REFERENCES: CHAPTER 3

- [1] E. Lacroix, A. R. Viguera, L. Serrano, “Elucidating the folding problem of alpha-helices: local motifs, long-range electrostatics, ionic-strength dependence and prediction of NMR parameters.”, *J. Mol. Biol.* **1998**, *284*, 173–91.
- [2] R. A. Böckmann, A. Hac, T. Heimburg, H. Grubmüller, “Effect of sodium chloride on a lipid bilayer”, *Biophys. J.* **2003**, *85*, 1647–1655.
- [3] Y. A. Ermakov, K. Kamaraju, K. Sengupta, S. Sukharev, “Gadolinium Ions Block Mechanosensitive Channels by Altering the Packing and Lateral Pressure of Anionic Lipids”, *Biophys. J.* **2010**, *98*, 1018–1027.
- [4] B. P. Young, J. J. H. Shin, R. Orij, J. T. Chao, S. C. Li, X. L. Guan, A. Khong, E. Jan, M. R. Wenk, W. A. Prinz, G. J. Smits, C. J. R. Loewen, “Phosphatidic Acid Is a pH Biosensor That Links Membrane Biogenesis to Metabolism”, *Science (80-. )*. **2010**, *329*, 1085–1088.
- [5] R. Beynon, J. Easterby, *Buffer Solutions: The Basics*, 1st ed., Oxford University Press, **1996**.
- [6] N. E. Good, G. D. Winget, W. Winter, T. N. Connolly, S. Izawa, R. M. M. Singh, “Hydrogen Ion Buffers for Biological Research”, *Biochemistry* **1966**, *5*, 467–477.
- [7] W. J. Ferguson, K. Braunschweiger, W. Braunschweiger, J. R. Smith, J. McCormick, C. C. Wasmann, N. P. Jarvis, D. H. Bell, N. E. Good, “Hydrogen ion buffers for biological research”, *Anal. Biochem.* **1980**, *104*, 300–310.
- [8] J. Fraxedas, *Water at Interfaces: a Molecular Approach*, CRC Press, **2014**.
- [9] J. Mou, J. Yang, Z. Shao, “Tris(hydroxymethyl)aminomethane (C<sub>4</sub>H<sub>11</sub>NO<sub>3</sub>) Induced a Ripple Phase in Supported Unilamellar Phospholipid Bilayers”, *Biochemistry* **1994**, *33*, 4439–4443.
- [10] L. Piantanida, H. L. Bolt, N. Rozatian, S. L. Cobb, K. Voitchovsky, “Ions Modulate Stress-Induced Nanotexture in Supported Fluid Lipid Bilayers”, *Biophys. J.* **2017**, *113*, 426–439.
- [11] M. M. Koerner, L. A. Palacio, J. W. Wright, K. S. Schweitzer, B. D. Ray, H. I. Petrache, “Electrodynamics of Lipid Membrane Interactions in the Presence of Zwitterionic Buffers”, *Biophys. J.* **2011**, *101*, 362–369.
- [12] H. Bouvrais, L. Duelund, J. H. Ipsen, “Buffers Affect the Bending Rigidity of Model Lipid Membranes”, *Langmuir* **2014**, *30*, 13–16.
- [13] D. Roberts, R. Keeling, M. Tracka, C. F. van der Walle, S. Uddin, J. Warwicker, R. Curtis, “Specific Ion and Buffer Effects on Protein–Protein Interactions of a Monoclonal Antibody”, *Mol. Pharm.* **2015**, *12*, 179–193.
- [14] D. Marsh, *CRC Handbook of Lipid Bilayers*, Second, CRC Press, **2013**.
- [15] *CRC Handbook of Chemistry and Physics*, 97th ed., CRC Press, **2016**.
- [16] K. Voitchovsky, “Anharmonicity, solvation forces, and resolution in atomic force microscopy at the solid-liquid interface”, *Phys. Rev. E* **2013**, *88*, 022407.
- [17] L. Cheng, P. Fenter, K. L. Nagy, M. L. Schlegel, N. C. Sturchio, “Molecular-Scale Density Oscillations in Water Adjacent to a Mica Surface”, *Phys. Rev. Lett.* **2001**, *87*, 156103.
- [18] C. Park, P. Fenter, K. Nagy, N. Sturchio, “Hydration and Distribution of Ions at the Mica-Water Interface”, *Phys. Rev. Lett.* **2006**, *97*, 016101.

- [19] J. I. Kilpatrick, S.-H. Loh, S. P. Jarvis, “Directly Probing the Effects of Ions on Hydration Forces at Interfaces”, *J. Am. Chem. Soc.* **2013**, *135*, 2628–2634.
- [20] M. Ricci, P. Spijker, F. Stellacci, J.-F. Molinari, K. Voitchovsky, “Direct Visualization of Single Ions in the Stern Layer of Calcite”, *Langmuir* **2013**, *29*, 2207–2216.
- [21] F. J. Giessibl, *Advances in atomic force microscopy*, **2003**.
- [22] J. N. Israelachvili, *Intermolecular and Surface Forces*, Third, Elsevier, **2011**.
- [23] D. J. Müller, D. Fotiadis, S. Scheuring, S. a. Müller, A. Engel, “Electrostatically balanced subnanometer imaging of biological specimens by atomic force microscope.”, *Biophys. J.* **1999**, *76*, 1101–1111.
- [24] K. Vedam, “Spectroscopic ellipsometry: a historical overview”, *Thin Solid Films* **1998**, *313-314*, 1–9.
- [25] A. Naderi, J. Iruthayaraaj, A. Vareikis, R. Makuška, P. M. Claesson, “Surface Properties of Bottle-Brush Polyelectrolytes on Mica: Effects of Side Chain and Charge Densities”, *Langmuir* **2007**, *23*, 12222–12232.
- [26] D. Beaglehole, H. K. Christenson, “Vapor adsorption on mica and silicon: entropy effects, layering, and surface forces”, *J. Phys. Chem.* **1992**, *96*, 3395–3403.
- [27] M. Li, M. Chen, E. Sheepwash, C. L. Brosseau, H. Li, B. Pettinger, H. Gruler, J. Lipkowski, “AFM studies of solid-supported lipid bilayers formed at a Au(111) electrode surface using vesicle fusion and a combination of Langmuir-Blodgett and Langmuir-Schaefer techniques”, *Langmuir* **2008**, *24*, 10313–10323.
- [28] T.-L. Phang, E. I. Franses, “Physically Self-Assembled Monolayers (PSAMs) of Lecithin Lipids at Hydrophilic Silicon Oxide Interfaces”, *Langmuir* **2006**, *22*, 1609–1618.
- [29] E. F. Murphy, J. R. Lu, J. Brewer, J. Russell, J. Penfold, “The reduced adsorption of proteins at the phosphoryl choline incorporated polymer-water interface”, *Langmuir* **1999**, *15*, 1313–1322.
- [30] H. J. Butt, M. Jaschke, “Calculation of thermal noise in atomic force microscopy”, *Nanotechnology* **1995**, *6*, 1.
- [31] M.-P. Mingeot-Leclercq, M. Deleu, R. Brasseur, Y. F. Dufrène, “Atomic force microscopy of supported lipid bilayers”, *Nat. Protoc.* **2008**, *3*, 1654–1659.
- [32] I. Reviakine, A. Brisson, “Formation of supported phospholipid bilayers from unilamellar vesicles investigated by atomic force microscopy”, *Langmuir* **2000**, *16*, 1806–1815.
- [33] O. Amund, A. Adebisi, “Effect of viscosity on the biodegradability of automotive lubricating oils”, *Tribol. Int.* **1991**, *24*, 235–237.
- [34] Y. Xie, H. Dong, S. Zhang, X. Lu, X. Ji, “Effect of Water on the Density, Viscosity, and CO<sub>2</sub> Solubility in Choline Chloride/Urea”, *J. Chem. Eng. Data* **2014**, *59*, 3344–3352.
- [35] M. J. Simmonds, H. J. Meiselman, O. K. Baskurt, “Blood rheology and aging”, *J. Geriatr. Cardiol.* **2013**, *10*, 291–301.
- [36] R. Paxman, J. Stinson, A. Dejardin, R. A. McKendry, B. W. Hoogenboom, “Using Micromechanical Resonators to Measure Rheological Properties and Alcohol Content of Model Solutions and Commercial Beverages”, *Sensors* **2012**, *12*, 6497–6507.
- [37] G. Young, B. Sorensen, Y. Dargaud, C. Negrier, K. Brummel-Ziedins, N. S. Key, “Thrombin generation and whole blood viscoelastic assays in the management of hemophilia: current state of art and future perspectives”, *Blood* **2013**, *121*, 1944–1950.
- [38] B. György, T. G. Szabó, M. Pásztói, Z. Pál, P. Misják, B. Aradi, V. László, É. Pállinger, E. Pap, Á. Kittel, G. Nagy, A. Falus, E. I. Buzás, “Membrane vesicles, current state-of-the-art: emerging role of extracellular vesicles”, *Cell. Mol. Life Sci.* **2011**, *68*, 2667–2688.
- [39] *Springer Handbook of Experimental Fluid Mechanics*, First, (Eds.: C. Tropea, A. Yarin, J. F. Foss), Springer-Verlag, Berlin, **2007**.
- [40] W. Y. Shih, X. Li, H. Gu, W.-H. Shih, I. A. Aksay, “Simultaneous liquid viscosity and density determination with piezoelectric unimorph cantilevers”, *J. Appl. Phys.* **2001**, *89*, 1497–1505.
- [41] M. Papi, G. Arcovito, M. De Spirito, M. Vassalli, B. Tiribilli, “Fluid viscosity determination by means of uncalibrated atomic force microscopy cantilevers”, *Appl. Phys. Lett.* **2006**, *88*, 194102.

- [42] R. R. Grüter, Z. Khan, R. Paxman, J. W. Ndieyira, B. Dueck, B. A. Bircher, J. L. Yang, U. Drechsler, M. Despont, R. A. McKendry, B. W. Hoogenboom, “Disentangling mechanical and mass effects on nanomechanical resonators”, *Appl. Phys. Lett.* **2010**, *96*, 023113.
- [43] M. Youssry, N. Belmiloud, B. Caillard, C. Ayela, C. Pellet, I. Dufour, “A straightforward determination of fluid viscosity and density using microcantilevers: From experimental data to analytical expressions”, *Sensors Actuators A Phys.* **2011**, *172*, 40–46.
- [44] B. A. Bircher, L. Duempelmann, K. Renggli, H. P. Lang, C. Gerber, N. Bruns, T. Braun, “Real-Time Viscosity and Mass Density Sensors Requiring Microliter Sample Volume Based on Nanomechanical Resonators”, *Anal. Chem.* **2013**, *85*, 8676–8683.
- [45] J. Kestin, M. Sokolov, W. A. Wakeham, “Viscosity of liquid water in the range -8 °C to 150 °C”, *J. Phys. Chem. Ref. Data* **1978**, *7*, 941–948.
- [46] F.-J. Elmer, M. Dreier, “Eigenfrequencies of a rectangular atomic force microscope cantilever in a medium”, *J. Appl. Phys.* **1997**, *81*, 7709–7714.
- [47] S. Basak, A. Raman, S. V. Garimella, “Hydrodynamic loading of microcantilevers vibrating in viscous fluids”, *J. Appl. Phys.* **2006**, *99*, 114906.
- [48] B. García, R. Alcalde, S. Aparicio, J. M. Leal, “Volumetric properties, viscosities and refractive indices of binary mixed solvents containing methyl benzoate”, *Phys. Chem. Chem. Phys.* **2002**, *4*, 5833–5840.
- [49] A. Maali, C. Hurth, R. Boisgard, C. Jai, T. Cohen-Bouhacina, J.-P. Aimé, “Hydrodynamics of oscillating atomic force microscopy cantilevers in viscous fluids”, *J. Appl. Phys.* **2005**, *97*, 074907.
- [50] E. Cooper, P. Johnson, A. Donald, “Probe diffusion in polymer solutions in the dilute/semi-dilute crossover regime: 1. Poly(ethylene oxide)”, *Polymer (Guildf)*. **1991**, *32*, 2815–2822.
- [51] J. H. van Zanten, S. Amin, A. A. Abdala, “Brownian Motion of Colloidal Spheres in Aqueous PEO Solutions”, *Macromolecules* **2004**, *37*, 3874–3880.
- [52] K. W. Ebaginin, A. Benchabane, K. Bekkour, “Rheological characterization of poly(ethylene oxide) solutions of different molecular weights”, *J. Colloid Interface Sci.* **2009**, *336*, 360–367.



## 4.0 DIFFUSION, FRICTION AND VISCOELASTICITY OF IONS AT SOLID-LIQUID INTERFACES

Moving on from the structuring of complex molecules at interfaces, this chapter will delve further into the dynamics of simple ions and interfacial water that was introduced in section 1.4. We focus on how AFM can provide a unique perspective on the altered energetics of these systems; specifically how small-amplitude operation (section 2.3) can be used to measure the relaxation timescales of single ions adsorbed onto the surface of mica. Despite our instrument's limitation to a time resolution of  $\sim 25$  ms, individual diffusion events can clearly be resolved by their alteration of the interface's apparent height, pointing towards a much slower kinetic behaviour than is traditionally assumed. Indeed, such events have two characteristic timescales which are generated by the adsorbed ions and the interfacial water respectively. These lifetimes are much longer than those typically expected of aqueous species, and are not usually probed experimentally. The results thus have considerable implications for surface-based dynamic events such as heterogeneous nucleation or the diffusion of charges along biological membranes.

Next, we present an in-depth study of the collective dynamics of *confined* electrolytes. This thesis has so far highlighted how interfaces perturb fluids by breaking the spherical interaction symmetry of the bulk with long- and short-ranged forces. This perturbation is even further enhanced by the introduction of a second, confining surface. As the fluid thickness is reduced to just a few molecular layers, the energetic cost of rearrangement – and thus diffusion – soars. This skews the behaviour of confined fluids, which in turn has ramifications for our understanding of the origins of friction and lubrication in liquids. We probe the dynamic behaviour of pure water and solutions of KCl using so-called shear force spectroscopy. We show that both solutions behave in distinctly non-Newtonian manner, with a friction and viscoelasticity that depends strongly on the time- and lengthscale of the interaction. Ions mitigate the frictional coupling between the layers but show similar time-dependent characteristics. Interestingly, many discussions of the nanoscale origins of

friction focus solely on velocity, but we show that crystal features of the surface define an absolute lengthscale that is crucial for the system's behaviour.

## 4.1 Lateral diffusion of individual $\text{Rb}^+$ ions within the Stern layer

Understanding the motion and energetics of water and ions is key to explaining countless interfacial phenomena in nature and industry, including crystal growth and dissolution [1, 2], transport in nano-channels [3, 4] and energy storage [5]. The global motion of ions within large channels is rather straightforward to measure from the conductance of a fluid, given an external pressure, electric field or concentration gradient. In contrast, the specific in-plane kinetics of molecules or ions close to a charged surface (such as an electrode, or pore walls) are much harder to extract, and often require indirect models based on the electric double layer to estimate. Electrokinetic studies have long understood the importance of accounting for a distinct diffusion behaviour for surface-mediated ions, with a total conductance,  $K^\sigma = K_s^\sigma + K_d^\sigma$ , accounting for the Stern and diffuse layer, (subscripts  $s$ , and  $d$  respectively) [6]. These models are generally based upon amended versions of the 1D Gouy-Chapman description of the interface and break down in a similar fashion when the lengthscales or electric fields are such that ion-ion interactions become significant [7]. Further, while they provide powerful models far away from the surface, they should not be taken as literal descriptors of the microscopic behaviour of the interface, requiring (as they do) that Stern layer ions exhibit *conductive*, but not *convective* flux [8].

More direct, surface sensitive experimental methods are required if the kinetics of the Stern layer are to be unequivocally understood. This is because effects such as charge overscreening generated by ion-ion correlations are not observed in mean-field theories, even recent, adapted versions [9]. Important progress in direct measurement of ionic kinetics has been made by scanning electrochemical microscopy (SECM), which revealed that the lateral diffusion coefficients of protons at the interface with Langmuir monolayers are at most 15% that of their bulk value [10, 11]. Further, the coming-of-age of scanning ion conductance microscopy (SICM), which does not rely on *in situ* redox reactions, has enabled a broad range of electrochemical events to be mapped with spatial resolutions of  $\mathcal{O}(10\text{-}100\text{ nm})$  [12, 13]. SICM has allowed the independent mapping of topography, surface charge and ion flux at pores and reaction sites [12], but is limited to a probe diameter of  $\gtrsim 100\text{ nm}$  and the need for a constant charge flux. Thus, despite the power and versatility of the technique, it cannot access the steady-state energetics of single ions at the solid-liquid interface.

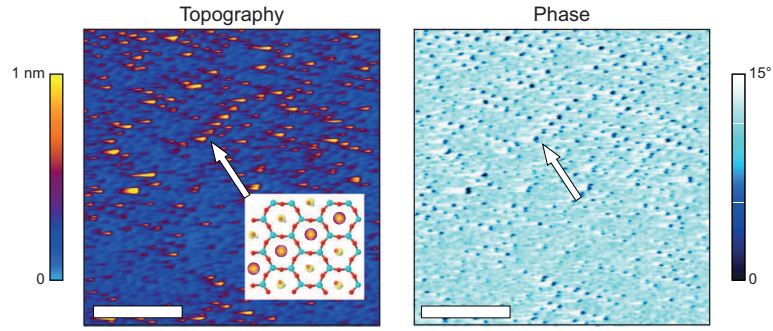


Fig. 4.1: AM-AFM scans of mica in 3 mM RbCl solutions showing the technique’s ability to discriminate singly-adsorbed ions at the solid-liquid interface. The ions are represented as sharp peaks in topography (left) and troughs in phase (right, arrows) due to their perturbation of the local hydration structure. Their stability while scanning (each peak represents multiple horizontal tip scan lines) implies relatively long residence times for the ions. Length scale bars represent 3 nm; figure adapted from ref. [19].

Section 1.4 highlighted some key disparities in our understanding of interfacial dynamics; particularly the lack of overlap between techniques such as MD, SICM and NMR, which broadly find interfacial diffusion coefficients of  $\sim 10^{-7}$ - $10^{-5}$   $\text{cm}^2 \text{s}^{-1}$  [11, 14, 15] and surface probe-based experiments, which have observed relaxation times of milliseconds to minutes [16–18]. The former diffusion coefficients are equivalent to an ion having an RMS displacement of  $\langle x^2 \rangle^{1/2} \sim 10^3$ - $10^4$  nm every second, which was assumed to mean that high-resolution scanning probe studies (that typically explore much smaller lengthscales over longer times) could not access dynamical aspects of the Stern layer. However, Ricci *et al.* showed that it was possible to image single rubidium ions adsorbed to mica with AM-AFM [19] (Fig. 4.1) and further, the stability of the ions over multiple scan lines suggests their residence on the crystal is greater than the  $\mathcal{O}(50 \text{ ms})$  scan rate. Thus AFM can, in principle, access the interfacial dynamics of individual ions within the Stern layer, without relying on indirect or large-scale average measures of the charges’ dynamics. However, this ability is certainly system-dependent and in the case of Fig. 4.1, relies on the well-defined symmetry of the mica and large (hydrated) size of  $\text{Rb}^+$  ions to provide a clear signal when the latter is adsorbed.

In order to investigate the ions’ dynamics with greater time resolution and better statistics, the 2D AFM raster-scanning (red zig-zag in Fig. 2.1) can be replaced by a repeated 1D line scan over a single crystalline row. This improves imaging stability and thus enables much faster acquisition, with our commercial Cypher ES AFM scanner demonstrating a time delay of just 25 ms before the tip returns to a position on the sample<sup>1</sup>. Imaging in this way, and representing the data as in Fig. 4.2, the vertical dimension has units of

<sup>1</sup> This is by no means a hard resolution limit, and more specialised high-speed AFMs will likely be able to increase the stable scan rate by orders of magnitude

length and the horizontal dimension represents the interface’s evolution over time. Upon inspection of Fig. 4.2(a), it is clear that this technique can stably image the Stern layer over many seconds, providing a unique combination of time-resolved information over a “macroscopic” period while retaining Ångström-level spatial features. Further, the rubidium ions’ modulation of the apparent height of the interface generates three distinct height levels (coloured arrows), the existence of which is confirmed by analysis of a Gaussian fit to a histogram of the scanning height distribution (Fig. 4.2(b)). The residuals of this fit (c) show that the heights do not follow a normal distribution but instead have distinct peaks corresponding to the three levels. Using these peaks to categorise the scans (d) results in qualitatively similar images. We interpret the highest features on the surface (yellow arrow in (a)) as hydrated  $\text{Rb}^+$  ions adsorbed above the ditrigonal cavity of the mica lattice [19–21]. The lower two levels (orange and purple arrows) are related to the specific hydration of the interface and  $\text{H}_3\text{O}^+$  adsorption and shall be discussed later.

#### 4.1.1 Residence timescale of adsorbed rubidium

To quantitatively measure the residence times of the adsorbed ions, we take a time profile over a site temporarily occupied by an  $\text{Rb}^+$  ion, as shown in Fig. 4.2(a) and 4.3(b). A homemade algorithm used line-by-line fast Fourier transforms to track each lattice site of the mica and account for lateral drift in the piezo scanner. The impact of scanning noise was reduced by a procedure that, for each scan line, averaged the height of the pixels associated with each mica lattice site: the output of this procedure is illustrated in Fig. 4.3(a). A height profile taken along one site (Fig. 4.3(b)) can then be analysed using a threshold value carefully selected to be between the heights respectively associated with the different surface states, that is, the rightmost peaks in Fig. 4.2(c). The time interval during which the height of the kinetic trace is continuously above the threshold is interpreted as a single residence event. Our technique cannot distinguish between in-plane (lateral) or vertical diffusion (desorption), which are likely to have distinct underlying mechanisms, but when considering the entire data set – over 30 min · site in total – the ions’ dynamics are well-described by a triple exponential (Fig. 4.3(c)).

The first timescale is  $\tau_0 = 25$  ms and is simply related to the measurement frequency (which is thus imposed when fitting). The second timescale is  $\tau_1 = 104 \pm 5$  ms and is due to the motion of adsorbed rubidium ions. The third timescale is associated with the specific hydration of the mica – that is, the organisation of oriented waters and  $\text{H}_3\text{O}^+$  ions on the crystal – and was found to be  $\tau_2 = 608 \pm 30$  ms. The link between  $\tau_1$  and adsorbed ions’ motion arises from the observation that if the height threshold,  $h$ , is increased past 0.1 nm (the limit in Fig. 4.3(d)),  $\tau_2$  converges to the value of  $\tau_1$ . Further, choosing lower

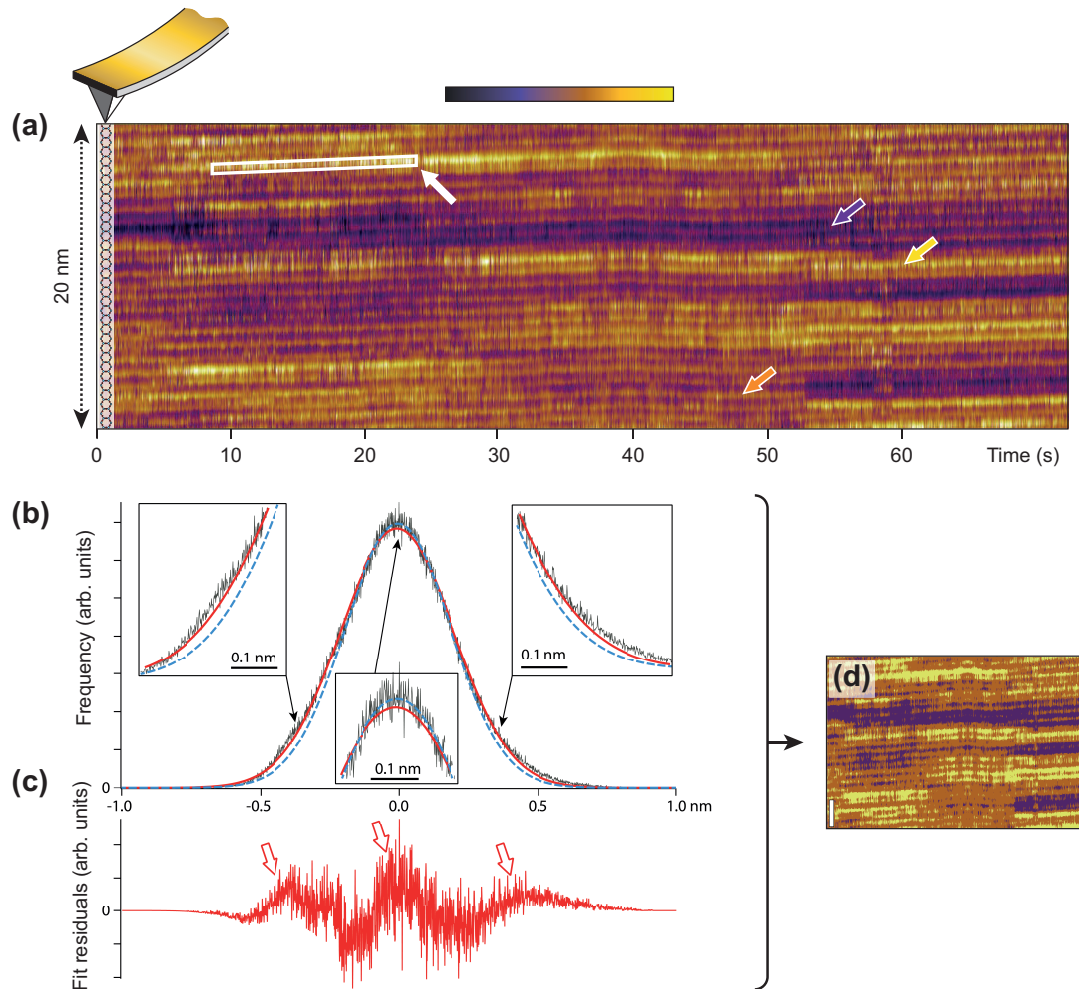


*Fig. 4.2:* Time evolution of cations at the mica-electrolyte interface. (a) Scanning the mica uniaxially in a solution of 1 mM RbCl allows maps of height as a function of distance (vertical) and time (horizontal) to be built up over long timescales with 25 ms resolution. A scaled schematic of the lattice is shown (left) for comparison. The topography demonstrates three distinct levels; an upper feature (yellow arrow) that is related to the adsorption of hydrated rubidium ions and two lower levels (orange and purple) that relate to the mica's hydration and adsorption of  $\text{H}_3\text{O}^+$ . The mica sites vary slowly between each adsorption state relative to the experimental timescale. A height section taken at the white box is shown in Fig. 4.3(b). (b) The designation of three separate levels is confirmed by fitting a histogram of the scan heights (black) with a Gaussian function (red), which demonstrates an excess at three points (zoomed insets). This is exaggerated if only the central region is used for the fit (blue dashes). (c) The residuals demonstrate clearly the three excesses (arrows) that correspond to the height levels qualitatively marked in (a). These can be used to categorise the sites from the raw data (d). Colour scale in (a) covers 1.5 nm.

height thresholds results in longer timescales, emphasising that the higher level (adsorbed  $\text{Rb}^+$ ) is linked to  $\tau_1$ . This exponential decay in residence times is consistent with previous studies of the analysis of the residence time of water molecules in the solvation shell of ions [22, 23].  $\tau_2$  is therefore related to the dynamic transitions between the lower topographic levels (orange and purple arrows in Fig. 4.2(a)), which is confirmed by the pH experiments discussed later (Fig. 4.4). Since the transitions are relatively slow – typically several seconds in Fig. 4.3(b) – fewer events are counted in the statistics, despite representing a significant part of the measurements.

A residence time of hundreds of milliseconds is well above the measurement resolution and extremely large considering rubidium’s bulk diffusion coefficient of  $D_b \sim 10^{-5} \text{ cm}^2 \text{ s}^{-1}$  [24]. However, it is clear that surface hydration plays a central role in cation adsorption and interfacial dynamics [19, 25, 26], and the motion of ions specifically adsorbed to a crystal binding site is unlikely to adhere to the same diffusion mechanisms as those in bulk. At present, there is no model which can successfully accommodate hydration effects, substrate geometry and interactions with the bulk to predict the behaviour of hydrated cations at interfaces, but we can adapt developments in Transition State Theory to describe our results, at least to first approximation. Our approach assumes that the free energy associated with ion adsorption,  $\Delta G_{\text{Rb}^+}$ , dominates the reduction in ion dynamics that we directly observe *via* AFM and thus allows the casting of the interfacial diffusion coefficient,  $D_i$ , as [27]

$$D_i \sim D_b \exp\left(\frac{\Delta G_{\text{Rb}^+}}{k_B T}\right). \quad (4.1)$$

Here,  $\Delta G_{\text{Rb}^+}$  is taken as  $-23.5 \pm 4.5 \text{ kJ mol}^{-1}$  [19, 28] and accounts for (albeit indirectly) the energy required to modify the hydration landscape of the mica by an adsorbing ion. Thus, while not accommodating any directional effects, this relation can somewhat acknowledge the complex interplay between cation charge, hydration shells and specific interaction with the crystal lattice. The Arrhenius factor will vary between  $4 \times 10^{-5}$  (at  $5^\circ\text{C}$ ) and  $2.3 \times 10^{-4}$  (at  $65^\circ\text{C}$ )<sup>2</sup>, which leads to interfacial diffusion coefficients of the order of  $D_i \sim 10^{-10}$ - $10^{-9} \text{ cm}^2 \text{ s}^{-1}$ . This value of  $D_i$  allows for timescales of the order of tens of milliseconds to seconds for an ion to move between adjacent crystal sites, in line with our experimental results.

---

<sup>2</sup> Further experiments were performed while varying the temperature in this range (detailed in ref. [29]), which revealed remarkably little dependence of the timescales  $\tau_1$ ,  $\tau_2$ , on the Arrhenius factor, within experimental error. The data suggested instead that a temperature increase reduced the apparent surface roughness, due to the water becoming less “glassy”. However, the data were not collected by the author and do not significantly affect the conclusions presented here, and so shall not be reported.

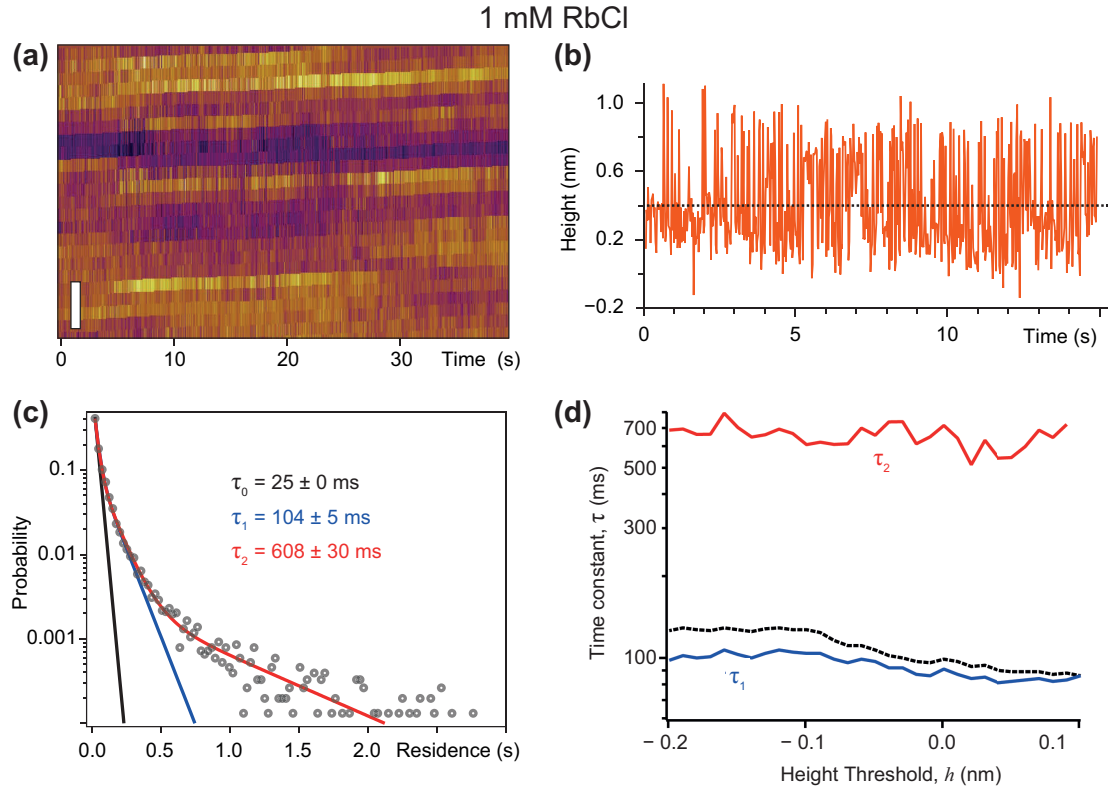


*Fig. 4.3:* Quantifying the ions' residence dynamics from time series scans. (a) The data is first averaged over individual unit cells at each time point on the horizontal axis to reduce imaging noise and the impact of the mica corrugation. (b) A height section taken from white box in Fig. 4.2(a) with the threshold (dashes) indicating the height above which an adsorbed ion is considered to be present. The time spent above the threshold is used to create a histogram of adsorption times (c). Semi-automated analysis of the Rb<sup>+</sup> ions' residence over the entire data set (over 30 min · site) unveils three distinct timescales. The first ( $\tau_0 = 25$  ms) is associated with the scan frequency and is imposed when fitting; the second and third have  $\tau_1 = 104 \pm 5$  ms and  $\tau_2 = 608 \pm 30$  ms respectively and represent physical timescales of the system. (d) Systematically varying the threshold level shows the two timescales to be robust over the range  $-0.2 < h < 0.1$  nm, above which  $\tau_2$  (red) collapses to the value of  $\tau_1$  (blue), emphasising that shorter time constants are associated with the higher topographic levels. The dashed line shows the results of a single exponential fit. Scale bar in (a) is 3 nm and data in (b) were analysed using a height threshold of  $h = -0.1$  nm.

### 4.1.2 *Dynamic hydration behaviour at the mica surface*

Due to the large size of the rubidium cation relative to water (Fig. 1.2), and thus significant perturbation of the Stern layer, we assume that the lower levels of Fig. 4.2(a) are dominated by the structuring of water and hydronium,  $\text{H}_3\text{O}^+$ , at the mica lattice. The latter's permanent negative charge of  $-1 e$  per unit cell is generated from the removal of native  $\text{K}^+$  ions that neutralise the crystal in solid state. At this concentration of  $\text{Rb}^+$  (1 mM), and under these imaging conditions, the cations do not fully cover the Stern layer (emphasised by e.g. Fig. 1.10) and thus the charge is partially screened by oriented water dipoles and  $\text{H}_3\text{O}^+$ . Hydronium is always present in aqueous electrolytes, especially in unbuffered solutions that we use here: the pH is typically around 5.5, indicating a proton concentration of  $3.2 \mu\text{M}$  (about 300 times smaller than that of rubidium). Hydronium therefore competes with dissolved metal cations for adsorption on the mica substrate [28, 30, 31], but it tends to adsorb deeper in mica's ditrigonal cavities than alkali ions due to its smaller size [21, 32]. Given the electrostatic affinity between  $\text{H}_3\text{O}^+$  and mica, it is likely that the former will preferentially form more condensed surface states than a neutral water molecule. We note that in principle the water ion can exist in higher- and lower-order clusters than hydronium (e.g.  $\text{H}_5\text{O}_2^+$  or the proton, respectively), but it is not possible for the AFM tip to distinguish between these in the current work.

The balance between an interface dominated by hydronium cations and structured water molecules is governed by the bulk pH, and we can thus investigate the dynamic behaviour of water alone at the interface by following the same experimental procedure as above, but using ultrapure water as the immersing fluid. By titrating the solution with HCl, we adjust the bulk pH in a range where the surface charge of mica changes significantly [33] but with limited impact on the silicon tip's negative potential [34, 35]. The results are shown in Fig. 4.4 and demonstrate that the height variations are much smaller than for solutions containing  $\text{Rb}^+$ . Two levels can still be observed, although objectively defining them is unreliable given the topography variations are close to the AFM's imaging noise level. The levels are highlighted by binarising the data (with a threshold halfway between the maximum and minimum height values) and comparing the area of the lower and upper levels (purple and yellow, respectively). Analysing the entire data set, we find that a pH of 5.56 generates a lower level coverage of  $55 \pm 3\%$  (i.e. approximate equilibrium between water and  $\text{H}_3\text{O}^+$ ), while at pH 4.49, the coverage increases to  $75.2 \pm 2\%$  (Fig. 4.4(c)-(d)). The latter result gives weight to our interpretation that the lower levels correspond to a condensed layer of hydronium ions that adsorb deeply into mica's ditrigonal cavities.

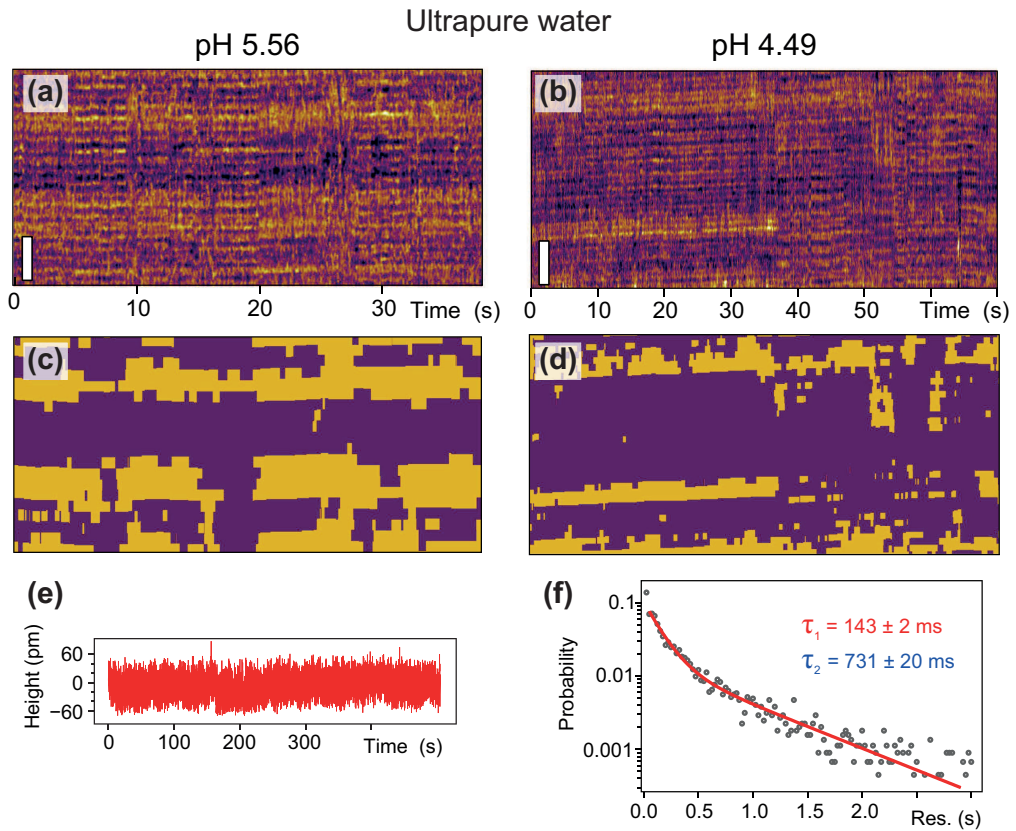


*Fig. 4.4:* The relative concentration of water and hydronium alter the dynamic behaviour of mica's Stern layer. Analysing the evolution of ultrapure water titrated to pH 5.56 ((a) and (c)) and pH 4.49 ((b) and (d)) allows the effect of  $\text{H}_3\text{O}^+$  to be discriminated. As expected, height variations are much smaller when compared to solutions with rubidium (e) and only two levels are observed. Their relative abundance can be found from binarising the data ((c)-(d), see text). The fractional coverage of hydronium (lower level) increases from  $55 \pm 3\%$  at pH 5.56 to  $75 \pm 2\%$  at pH 4.49. The fitting of timescales  $\tau_1$  and  $\tau_2$  is less robust in ultrapure water but in general results in slower dynamics (f). The colour scale for (a)-(b) covers 1.5 nm

Analysis of the kinetic data, as in Fig. 4.4(e)-(f), reveals slower timescales than in saline solutions, sometimes with  $\tau_2$  in excess of seconds, although there is a relatively strong dependence on the choice of threshold due to the greatly decreased signal-to-noise ratio when imaging in ultrapure water. The existence of longer timescales than for  $\text{Rb}^+$  ions is however a robust result. The exact hydration structure of the surface cannot be derived from our results alone, and a fully quantitative analysis of the pH-induced change of the apparent  $\text{H}_3\text{O}^+$ /water surface ratio is questionable given the influence of the AFM probe on the measurement [19, 36]. The results, however, are qualitatively in agreement with available literature [33] and the attribution of the different levels is compatible with X-ray reflectivity observations obtained at equilibrium [21, 32, 37]. The lifetime of a single hydrogen bond (typically  $\mathcal{O}(1-10\text{ ps})$  [38, 39]) is extremely fast compared to the timescale identified here, but water’s translational motion can be substantially slower due to the need for a collective rearrangement of the hydrogen bond network [40]. This is likely to be exacerbated at such a hydrophilic surface as mica, where water is templated by the crystal structure of the [001] surface [41] and exhibits dynamics more akin to a glass than a fluid [42].

These first few layers of water critically determine the structure and adsorption behaviour of dissolved ions [19, 43, 44] and thus are likely to play a key role in their dynamics as well. When analysing the transitions of  $\text{Rb}^+$  ions, we find that the vast majority of adsorption events ( $> 92\%$ ) occur on sites that are straightforwardly hydrated by water – that is, the mid-level features in Fig. 4.2(a) – rather than those occupied by hydronium. This implies that rubidium has a much lower affinity for mica when the latter’s charge is neutralised by  $\text{H}_3\text{O}^+$ . While this is perhaps not so surprising given simple electrostatic considerations, it also emphasises the manner in which “slow” waters can dictate the dynamics of  $\text{Rb}^+$  at the crystal surface. Our AFM experiments observe these waters to be immobilised on the millisecond timescale, but this refers only to the water’s location above the mica crystal: the molecule will undoubtedly still dissipate kinetic energy through librational and vibrational modes on the picosecond timescale. This mechanism would enable water to essentially retain many of its fast dynamic characteristics as observed in hydration shells [45], but demonstrate exceedingly slow in-plane diffusion.

To briefly summarise section 4.1, we have shown using uniaxial, small-amplitude AFM, that rubidium ions adsorbed to mica in solution are characterised by a  $\sim 100\text{ ms}$  timescale but also strongly depend on the surface hydration state which varies much more slowly, with  $\tau_2 > 600\text{ ms}$ . This latter timescale, which we ascribe to the adsorption of hydronium ions effectively modulates the availability of binding sites for rubidium. The difference between the two timescales is consistent with the fact that the binding constant for individual

ions on mica is about ten times larger for  $\text{H}_3\text{O}^+$  than for  $\text{Rb}^+$  at room temperature [30]. The ability of AFM to probe solid-liquid interfaces locally with sub-nanometre spatial resolution opens many possibilities for investigating molecular dynamics at interfaces, in particular for systems currently beyond the reach of computer simulations. As already touched upon, biological systems are of particular interest due to the heterogeneous hydration of many biomolecules, and the intrinsic link between water structure and protein function that is increasingly becoming apparent [45]. Indeed, we shall return to the concept of spatially and temporally resolved ionic evolution in a biological system in chapter 5.

## 4.2 Confined electrolytes: scale-dependent friction and viscoelasticity

In the previous section, the dynamics of rubidium and mica's hydration layer were investigated *via* AM-AFM with small amplitudes and, while the probe inevitably will influence the apparent topography [36, 46], the continual “test” of achieving lattice-level spatial resolution indicates that the portion of the tip conducting the imaging is sharp on a molecular scale [47–49]. Hence, while the water and ions imaged in this way will not be in a truly relaxed state (the ability of the tip to excite adsorbed ions will be considered in Fig. 5.6), they may be considered unconfined and free to diffuse. While the study of such unconstrained systems is undoubtedly important, there is also great relevance to the study of *strongly confined* fluids due to their significance in biology [50–55], chemical engineering [4, 56] and electrochemistry [57–59]. For instance, in biological systems, water is routinely forced through membrane-bound channels, confined in synovial joints between lipid structures or trapped as protein hydration water, where it shares properties with water held in silica nanopores [52].

As discussed in subsection 1.4.2, nanoconfined fluids behave in a distinct manner when compared with their bulk equivalents, due to the increasing influence of the interface at this scale. This manifests itself in altered thermodynamic properties such as isobaric heat capacity and melting point [60–62], as well as the molecular orientation and structure of the fluid [63, 64]. There is a limited consensus regarding the dynamic behaviour of aqueous solutions under confinement (the dynamic solidification of Hoffman *et al.* [65]) but little certainty about the extent to which this depends on experimental specifics such as interfacial chemistry and geometry rather than the confinement itself. Indeed, while some groups find that the dissipation of a fluid moving over a solid is dependent on the affinity between the two phases [66, 67], others ascribe much greater significance to the confinement curvature or other geometric factors [39, 68, 69].

The energy dissipated as molecules move through the interfacial fluid is analogous to an effective local viscosity [70] and determines the width of the stagnant layer – in other words, how far into the fluid one has to be before the solid’s relative motion is no longer detectable. If the plates confining the fluid are close enough that their respective stagnant layers overlap, the motion of one surface will elicit a response from its partner, which of course can be expressed as a friction between the two. Despite friction being universal and generally intuitive, there is still active debate about its molecular origins [71–74] and many of its laws, while startlingly successful, remain empirical [75]. It is thus necessary to discuss the theoretical foundations of friction and subsequent tribological models in dry and lubricated systems first, before applying some of these considerations to the dynamical properties of confined fluids.

### 4.2.1 Friction: origins and models

#### *Dry friction*

Friction inherently describes the transfer of kinetic energy from one body to another, with the converted energy being distributed in a random way between its molecules – i.e. as heat. However, long before a microscopic description of friction was ever explored, experiments begun by da Vinci in the 15<sup>th</sup> century concluded that friction obeyed three “laws”:

1. The frictional force,  $F_L$ , is directly proportional to the applied load,  $F_N$  (with the constant of proportionality often designated  $\mu$ ).
2. The frictional force is independent of the apparent contact area,  $A$ .
3. The kinetic friction is independent of the relative velocity of the two surfaces,  $v$ .

The original experiments consisted of simple wooden blocks moving on an incline, but these were relatively smooth, displayed little adhesion and did not account for much of the complexity of real-world friction. In general, real forces are not linear but follow power laws or exponential functions, which results in strong dependencies on the interaction timescale and relative velocities involved [76]. This means that the specific molecular structure of, say, two planes in relative motion is crucial in determining the lateral frictional forces. This is because the sliding of idealised surfaces requires dilation, even if only by a few Å, to overcome their molecular roughness, and this introduces a term proportional to the load on the surfaces. Sliding also requires adhesive molecular interactions to be continually broken as contact points are created and destroyed: this is the mechanism through which

friction dissipates energy and gives a term linear in the true contact area,  $A$ . This leads to a more realistic expression for the frictional force as [71]:

$$F_L = \mu F_N + \sigma A, \quad (4.2)$$

where  $\mu$  and  $\sigma$  are constants of proportionality. Equation 4.2 is compatible with the laws of friction in the case of negligible adhesion between the surfaces (i.e.  $\sigma \rightarrow 0$ , known as load-dominated friction). However, this is still a coarse description of static friction, and a great deal of complexity can be concealed within the innocent-looking empirical constants. The model also does not account for the energy built up when sliding at a constant velocity (so-called kinetic friction), which is typically lower.

Further insight was gained in the early 20<sup>th</sup> century by Prandtl's conceptual model of friction that described a point mass being mechanically moved by a harmonic force across a periodic potential, intended to mimic a crystal lattice (Fig. 4.5). Despite appearing rather simplistic in its considerations of a 1D potential and a single point of contact, the Prandtl-Tomlinson (PT) model has been able to capture phenomena such as slip-stick motion (Fig. 4.5(c)) and the difference between the static friction and kinetic friction, explained by the inertia built up by the mass as it travels; so much so that versions of it are still commonly used in modern research [77]. The advent of the AFM in the 1980s allowed for nano-tribological studies to directly explore the validity of the model with excellent control of the contact area and interaction chemistry. In particular, key progress was made when the atomically-resolved friction of a silicon probe against a crystal of NaCl was found to scale with the logarithm of the lateral velocity [78] (note this contradiction with the third law of friction). This was incorporated into a PT model that accounted for the finite temperature of the system, which aided the system in hopping over energy barriers. Specifically, Riedo *et al.* found that the mean friction force,  $F_L$ , on a mica crystal obeys the  $\ln(v)$  proportionality, but only for velocities low enough that the thermal energy can aid the transitions; beyond this point, the energy barriers for "hopping" become too great and  $F_L$  plateaus [79]. This is formally described by the relation:

$$\frac{1}{\beta k_B T} (F^* - F_L)^{3/2} = \ln \frac{v_0}{v} - \frac{1}{2} \ln \left( 1 - \frac{F_L}{F^*} \right), \quad (4.3)$$

where  $F^*$  is the effective frictional force at zero temperature, and  $\beta$  and  $v_0$  are constants that depend on the temperature, effective stiffness of the contact and microscopic attempt frequency for jumping over the energy barrier,  $f_0$ . Following this, studies that incorporate finite temperature and velocity into models of dry friction in different systems have become common [72, 80, 81], although an unambiguous way of scaling up such phenomena to explain cataclysmic geophysical events remains a challenge [82].

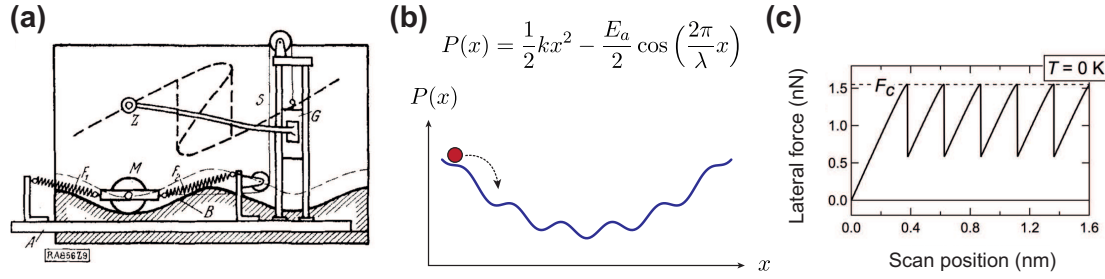


Fig. 4.5: Key features of the Prandtl-Tomlinson model for atomic-scale friction. (a) The original mechanical model designed by Prandtl in 1928 to illustrate the stick-slip motion of a mass,  $M$ , in a periodic potential set into motion by two springs,  $F_1$ ,  $F_2$ . The mass' motion is displayed by the dashed line. (b) The effective potential energy,  $P(x)$ , experienced by the mass is a combination of that generated by the springs (stiffness  $k$ ) and the underlying crystal potential (activation energy  $E_a$ , and lattice parameter  $\lambda$ ). If the springs drag the mass with velocity  $v$ , such that  $1/2kx^2 \rightarrow 1/2k(x - vt)^2$ , the energy landscape is tilted until the mass (red) has enough potential energy to overcome  $E_a$ , causing it to jump to the next local minimum. This leads to slip-stick motion similar to that exemplified (without thermal fluctuations) in (c). Panels (a) and (c) adapted from ref. [75].

### Fluid-mediated sliding and hydration lubrication

In the majority of mechanical systems, the aim is to reduce friction, as it introduces unnecessary energy losses and can result in potentially damaging wear. A simple method to minimise the damage to mechanically coupled systems is to prevent them coming into direct contact in the first place; in industry, this is achieved using lubricants – typically organic oils and greases that shift the shear plane so that energy is dissipated within their liquid layer. Biological systems such as synovial joints and the cornea's mucus layer, in contrast, tend to make use of aqueous suspensions of macromolecules for lubrication that are astoundingly successful, allowing long term, low-friction operation. For example, biomimetic systems incorporating lipids were found to produce friction coefficients as low as  $\mu \equiv F_L/F_N \sim 2 \times 10^{-5}$  [53]. While biology has made good use of water-based lubricants, a lack of understanding about the physical mechanism underpinning it has prevented the widespread uptake of these environmentally friendly and fire-resistant alternatives to oil-based lubrication in industry [83].

The complexity of lubricant-mediated sliding arises partly from the inherently non-linear nature of friction itself (discussed above), but also because the film properties are strongly dependent on the nature of the interaction between the solid surfaces. At high confining pressures, liquid tends to be squeezed out, resulting in just a few molecular layers on the boundary supporting the shearing motion, in what is known as boundary lubrication. This is associated with a relatively large coefficient of friction due to the instability of the fluid film which allows energy transfer between the surfaces. This is schematically outlined by the Stribeck curve in Fig. 4.6 (left), which relates  $\mu$  to a dimensionless param-

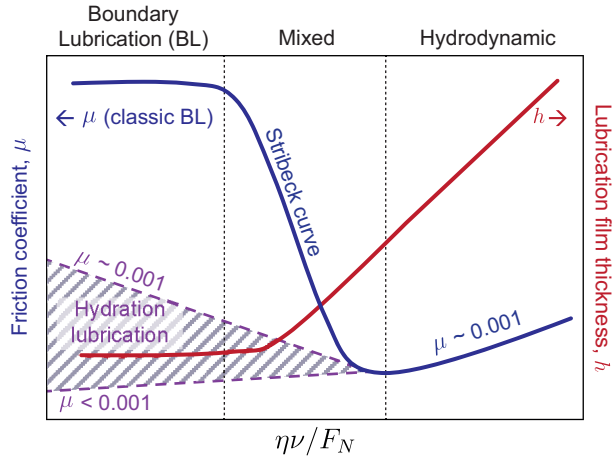


Fig. 4.6: The performance of fluid lubricating films in different dynamic regimes is captured by the so-called Stribeck curve (blue) that plots the friction coefficient versus the dimensionless parameter  $\eta\nu/F_N$ . For high normal forces or inviscid fluids, the solid surfaces squeeze out all but a few monolayers of lubricant, resulting in a relatively high coefficient of friction,  $\mu$  and thin separating layer,  $h$ , in what is known as boundary lubrication (left). Decreasing  $F_N$ , or using a fluid of higher viscosity allows thicker layers of fluid to exist and the frictional response is much lower, dominated as it is by the lubricant’s hydrodynamic properties (right). The inclusion of highly hydrated molecules similar to those found in nature have unveiled a new regime of hydration lubrication [84] (shaded area) in which strongly-bound water molecules cannot be simply forced from the interface, allowing for dramatically reduced friction. Figure adapted from ref. [50].

eter that accounts for the viscosity of the fluid,  $\eta$ , frequency of shear,  $\nu$ , and the normal force,  $F_N$ . If  $F_N$  is reduced, or if the relative velocity is increased the film is allowed to dilate, which leads to a greatly reduced frictional contact. These films allow for energy to be dissipated within the fluid by means of hydrodynamic damping, minimising wear on the surfaces.

In recent decades, a third regime, known as “hydration lubrication” has been uncovered in aqueous solutions (shaded region in Fig. 4.6) whereby highly hydrated molecules within the lubricating fluid allow for miniscule frictional coefficients of less than  $10^{-3}$  [50]. Underpinning this mode is the altered properties of the interfacial fluid that have been discussed throughout this thesis. The water at hydrophilic interfaces is strongly bound, structured and demonstrates damped kinetics that reflect an increased effective viscosity. This conspires to make aqueous interfacial layers tenacious and resistant to squeeze-out *via* hydration forces, preventing true solid-solid contact even under high pressures [18, 84, 85]. The molecularly thin film of water is a sink for energy generated by the sliding surfaces that minimises their wear or degradation. In fact, Klein argues that water is particularly suited for this due to the fact that its liquid phase is denser than ice; strongly confining  $H_2O$  would thus drive it towards a more fluid state [84] – although as discussed in subsection 1.4.2, this view is not uncontested in the literature!

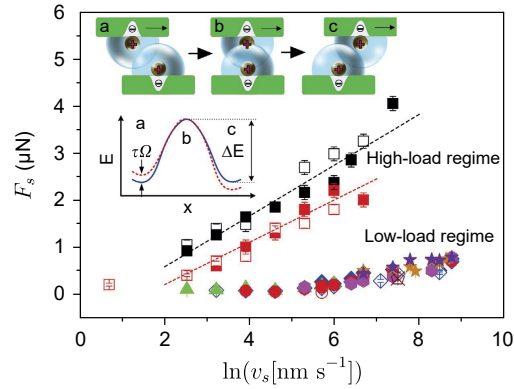


Fig. 4.7: SFB measurements demonstrate the ability of ions to mediate aqueous lubrication between hydrophilic surfaces. At low loads, there is a minimal friction as the ions and their hydration shells act as microscopic “ball-bearings” which ease the sliding of the two surfaces. At high loads, the friction is dominated by the activated process of overlapping hydration shells moving past one another (cartoon, top; a-c correspond to positions in energy landscape, centre-left). This reproduces the  $F_s \propto \ln(v_s)$  dependency found by Riedo *et al.* [79]. Figure adapted from ref. [85].

As well as requiring hydrophilic boundary surfaces, it appears that small cations of high charge density (kosmotropic, see Fig. 1.2) play a key role in facilitating this mode of lubrication [26, 85–88]. This mechanism is predominantly assumed to rely on two processes. The first is the adsorption of ions to the boundary surfaces which, at least in many biological and geological contexts, tend to be negatively charged. As detailed in section 1.3, ion adsorption is a complex process that can result in multiple binding states with varying degrees of hydration and coordination with the surface groups. The second process is the ions’ strong coupling to their neighbouring waters; typical hydration energies are  $\mathcal{O}(10\text{--}100 \text{ kJ mol}^{-1})$  [87], which ensures that each ion tightly retains a sheath of waters around it, increasing its steric size. These two effects work together to ensure that confining hydrophilic surfaces in electrolyte solutions have a strongly-lubricating ionic layer at their boundary (see schematic in Fig. 4.7), which prevents true contact and wear, even at pressures of hundreds of atmospheres [87]. Simple monovalent cations have been shown to dramatically reduce the measured friction at well-characterised interfaces to an extent that depends sensitively on their hydration properties [26, 86, 87]. Intriguingly, despite this effect being fundamentally driven by confined water and salt, it appears to be rather well-approximated by considering the motion as an activated process that must overcome a free energy barrier [26, 85] (inset in Fig. 4.7), in an analogous manner to the PT model for dry friction (equation 4.3).

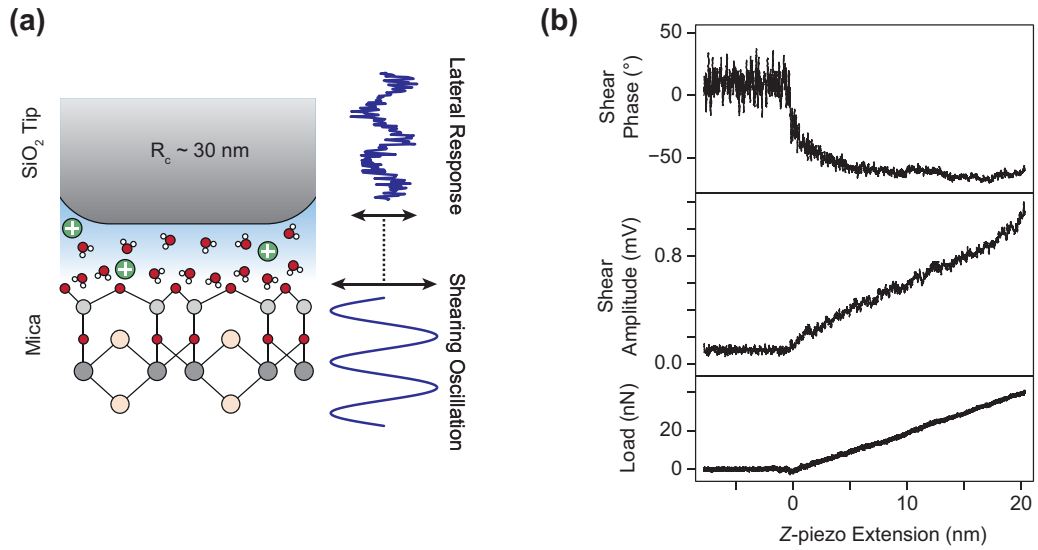


Fig. 4.8: (a) Schematic of shear-force spectroscopy, which is here used to probe the lubrication and dynamic properties of confined aqueous solutions. The AFM tip statically applies a normal load on the (structured) interfacial fluid while the sample is oscillated uniaxially. The fluid transmits this shearing motion to the tip, which pivots laterally at the same frequency with an amplitude and phase offset governed by the intervening fluid. Phase differences of  $\pm 90^\circ$  indicate the confined fluid dissipates energy in a viscous manner (“liquid-like”), while  $0^\circ$  indicates the fluid responds elastically. (b) A lock-in amplifier is used to extract the amplitude and phase of the cantilever response. As the normal load,  $F_N$  increases, the amplitude increases linearly and the phase tends towards a constant value.

#### 4.2.2 Dynamic response of confined ultrapure water and 150 mM KCl

##### *Shear force spectroscopy*

In the following section, we will explore the ability of confined water and electrolyte solutions to lubricate model systems, but with a specific focus on the dynamical behaviour of the interfacial layer and how it varies over different length- and timescales. This is because despite the wealth of studies exploring nanoconfined water and electrolytes, there is very little overlap between techniques in terms of frequency. Differential scanning calorimetry measurements that suggest confined water becomes more fluid are conducted in quasi-equilibrium [61, 89], while the oscillation frequencies of SFB and AFM tend to be of the order of Hz and kHz respectively. Computational studies [68, 69, 90, 91] are of course vital for gaining an atomistic picture of fluids’ lubrication under confinement but, despite rapid advances in computing power, are limited to shear speeds  $> \text{mm s}^{-1}$ , which exceed the vast majority of experimentally accessible values, with only a few exceptions [92].

To address this issue, we make use of shear-force spectroscopy, schematically outlined

in Fig. 4.8(a). This AFM technique uses the tip to apply a normal force statically (i.e. with no vertical oscillation) on the sample, putting pressure on the interfacial fluid. To probe the lubricating properties of this film, the sample is oscillated sinusoidally in its plane and perpendicularly to the cantilever's long axis with a frequency of  $\mathcal{O}(\text{kHz})$  (motion of the form  $A_d \sin(\omega t)$ ; (a), lower). Depending on the fluid's transmission of this motion, the tip will move laterally in response, causing the cantilever to twist with a component at the same frequency ( $A_s \sin(\omega t + \theta_s)$ ; (a), upper) that can be measured using the standard optical detection system (Fig. 2.1). A lock-in amplifier is used to compare the signal sent to the sample with the cantilever's response to produce the shearing amplitude,  $A_s$ , and phase lag,  $\theta_s$ .

This is illustrated in Fig. 4.8(b), which shows  $\theta_s$ ,  $A_s$  and normal load as function of  $z$ -piezo extension for a silica tip against a mica substrate. The shearing amplitude gives information relating to the lubrication of the fluid layer; that is, it can be converted to a lateral force (see section 4.4), which is then measured as a function of  $F_N$ . Before the normal pressure is applied to the sample (defined so that  $z < 0$ ), there is negligible shear amplitude and the phase oscillates around  $0^\circ$ , due to a lack of coupling between the two surfaces. For  $z > 0$ ,  $A_s$  is approximately proportional to the load, implying that the confined fluid has a well-defined  $\mu$  (see equation 4.2). The phase response tends asymptotically towards a value of  $\sim -60^\circ$  for high  $F_N$ . If we assume that the confined fluid is a linear viscoelastic material, the stress will have an in-phase and out-of-phase component with respect to the strain [93]. Physically, this allows us to relate  $\theta_s$  to how “fluid” the confined water is; at  $0^\circ$ , the tip is perfectly in-phase with the shearing oscillation, equivalent to an elastic contact, while at  $\pm 90^\circ$ , the interfacial fluid behaves in a purely viscous manner, dissipating energy [26]. The presence of at least one interfacial layer of water, as illustrated in Fig. 4.8(a), is exceedingly likely given the hydrophilicity of mica (it has a negligible contact angle) and the hydration repulsion routinely measured between mica surfaces [87]. Indeed, taking the affinity of water for mica to be  $W = 140 \pm 10 \text{ mN m}^{-1}$  [49], the energy needed to fully dehydrate an area on the scale of the tip radius,  $A$ , would be  $E_d = WA \sim 2500 \text{ eV}$ . Comparing this to the maximal energy due to the tip's exerted pressure on a monolayer of water,  $E_{\text{tip}} = P_{\text{tip}}V \sim 50 \text{ eV}$ , it is clear that  $E_{\text{tip}} \ll E_d$ ; i.e. the magnitude of  $W$  ensures there will always be a lubricating layer present. Even a strongly conservative estimate that accounts for the work done by the shearing, such that  $E_{\text{tip}} = \oint F_{\text{tip}} \cdot ds$  leads to maximal energies (for  $F_{\text{tip}} = 30 \text{ nN}$  and  $A_d = 5.0 \text{ nm}$ ) that are still 60% less than  $E_d$ . It should be noted that the latter calculation assumes that the confined water cannot dissipate energy through *any* mechanism over the course of a single shearing oscillation, which is physically implausible.

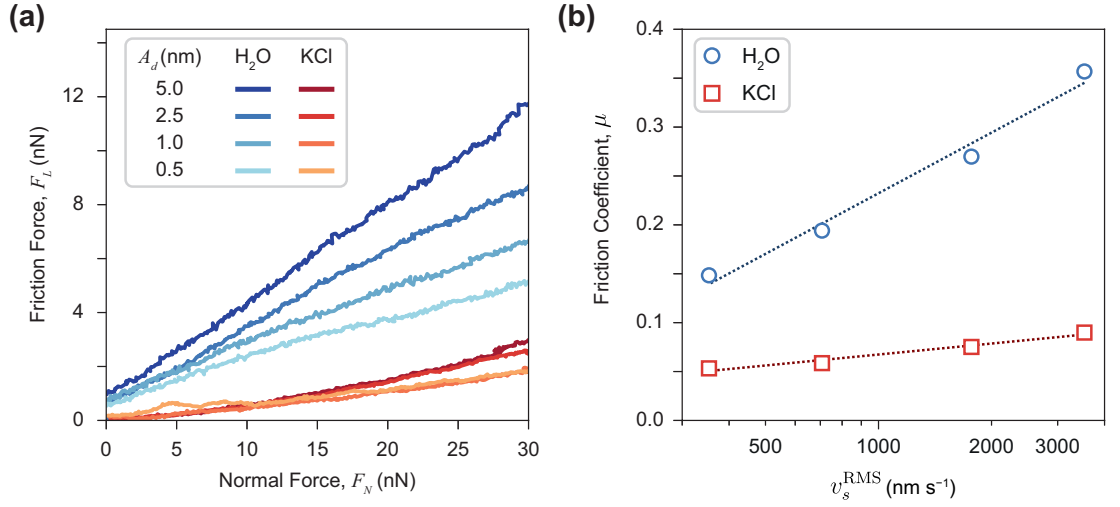


Fig. 4.9: (a) Lateral (friction) force,  $F_L$ , experienced by the tip as a function of the imposed normal force,  $F_N$ , for different oscillation amplitudes. In pure H<sub>2</sub>O, the friction is clearly dependent on the relative shearing velocity, as the coupling increases with  $A_d$ . The substitution of the pure water for 150 mM KCl dramatically reduces  $F_L$  in all cases, presumably due to the disruption of water’s well-structured hydrogen bond network (see text) at the mica surface. (b) Assuming a linear frictional response, the coefficient  $\mu$  increases linearly with the logarithm of the RMS velocity,  $v_s^{\text{RMS}}$ , (dashes). This implies that the confined fluids can be well described as an activated process, similarly to the PT model [79]. Each curve in (a) represents the average of at least 30 individual spectroscopic traces and the fitted uncertainties in (b) are smaller than the data markers.

#### Velocity-dependent friction and lubricating ability of $K^+$ ions

Spectroscopic measurements as in Fig. 4.8(b) give us an indication of the dynamics of the confined layer but only at a fixed velocity, shedding little light on the problem of how the film’s properties change as a function of the timescale probed. We thus investigated how its viscoelastic response was altered by the relative shearing velocity,  $v_s$ . Practically, this was achieved by varying the drive amplitude of the shearing signal,  $A_d$ , between 0.5 and 5.0 nm, which gave root-mean squared velocities of  $v_s^{\text{RMS}} = A_d\nu/\sqrt{2} \sim 350\text{-}3500 \text{ nm s}^{-1}$ , where the oscillation frequency  $\nu = 1 \text{ kHz}$ . We first investigate the model case of ultra-pure water confined between an amorphous silica tip and freshly-cleaved muscovite mica. The measured lateral force as a function of applied load at the various drive amplitudes is shown in Fig. 4.9(a) in blue. In all cases, it is clear that the linear relationship of  $F_L = \mu F_N$  holds, so that the load-dominated nature of the coupling between the surfaces is not affected by the altered shear amplitude. However there is a clear correlation between  $A_d$  and the frictional coupling. This shows that the dynamic response of the confined water layer – i.e. how rigidly it transmits the shear from substrate to cantilever – is strongly dependent on the relative velocity of the two plates.

To quantify this effect, the effective frictional coefficient for each  $A_d$  were extracted

by fitting a first-order polynomial to each curve; the results are presented in Fig. 4.9(b), plotted versus  $v_s^{\text{RMS}}$ . There is a clear evolution of the coefficient that follows  $\mu \propto \ln(v_s^{\text{RMS}})$ , which is highlighted by the dashed lines. Despite the presence of a nominally fluid layer of water between the tip and the mica, this is the same dependency as expected for “dry” friction that follows an activated Prandtl-Tomlinson model [78, 79], at least for relatively small velocities. In fact, similar results were found by Ma *et al.* when shearing two symmetric mica plates across an electrolyte layer (Fig. 4.7) [85]. Assuming validity of the PT model in this instance, we can extract the characteristic attempt frequency,  $f_0$ , for hopping over the periodic energy barriers presented by the mica’s crystal lattice. This is achieved by fitting equation 4.3 to our data (cast as  $F_L$  versus  $v_s^{\text{RMS}}$ ), with  $f_0$ ,  $F^*$  and  $\beta$  as free parameters. The results are presented in Table 4.1, and clearly show that applying more extreme loads strongly reduces  $f_0$ , emphasising the reduced kinetics associated with nanoconfinement. However, our data does not exhibit a plateau point in  $F_L$  (an important result of the thermal PT model) and as such, the fitting is rather under-defined. Hence, while generally agreeing with our interpretation, the physical validity of these parameters should be taken with caution.

Normal load, $F_N$ (nN)	$f_0$ (kHz)	$F^*$ (nN)	$\beta$ ( $\times 10^6 \text{ N}^{3/2} \text{ J}^{-1}$ )
12	$44 \pm 3$	$6.3 \pm 0.3$	$14 \pm 1$
20	$19 \pm 1$	$10.1 \pm 0.7$	$35 \pm 5$
28	$13 \pm 2$	$13.0 \pm 0.9$	$52 \pm 9$

Tab. 4.1: The characteristic attempt frequency,  $f_0$ , “zero temperature” friction force,  $F^*$ , and potential well constant,  $\beta$ , of the frictional behaviour of ultrapure water as a function of the normal load. These were found from implicit fitting of equation 4.3 to our results of Fig. 4.9. See ref. [79] for a full discussion of the physical meaning of each parameter.

The fixed oscillation frequency of  $\nu = 1$  kHz, gives an experimental timescale of  $\nu^{-1} = 1$  ms, which is positively glacial compared with the picosecond dynamics of  $\text{H}_2\text{O}$  molecules in bulk [38]. Our investigation of the slow in-plane diffusion and hydration behaviour of mica (section 4.1) suggests that the presence of a hydrophilic interface dramatically damps a fluid’s dynamic behaviour, allowing it to exhibit viscoelasticity even on long timescales such as these. This non-Newtonian behaviour of the strongly confined fluid can be further rationalised by considering that the film of water is likely to be only a few molecules thick, given the large normal forces applied here – assuming a contact area on the scale of the tip’s radius of curvature, the maximum pressure  $P_{\text{max}} \sim 10$  MPa. Hence the fluid, and its associated hydrogen bond network will be predominantly restricted to two dimensions, rather than its loosely tetrahedral structure in bulk [94]. This will increase the energy required for rearrangement of the network and thus is likely to suppress the interfacial relaxation times, as observed here (Table 4.1). Relaxation of confined water

films on millisecond timescales has in fact been observed *via* AFM previously [16, 26, 65, 95], but there is disagreement over to what extent this is velocity-dependent. Antognozzi *et al.*'s “transverse dynamic” force microscope found no dependence of their results on approach speed or shear frequency (for 1-20 kHz) [93]; the relaxation timescale of Li *et al.* decreased with increasing strain rate [95] and Khan *et al.* observed water to dynamically “solidify” when compressed above a threshold rate. These studies make use of different models to describe the confined fluid, as well as having different oscillation mechanisms and as such, objective comparison between them remains frustratingly difficult.

While we cannot unambiguously validate our results against the literature, we can test our hypothesis that the damped response of nanoconfined water is a result of its 2D hydrogen bond network. This was done by perturbing the interfacial fluid, by replacing the ultrapure water with a solution of 150 mM KCl. Alkali cations radically change the structure of the solid-liquid interface which influences the in-plane dynamics of the fluid as a whole, as discussed previously. Hence we expect that the ions will perturb the frictional response observed here by modifying both water's native hydrogen bond network and its relaxation times. Indeed, the red traces in Fig. 4.9 show that, not only does the inclusion of potassium ions reduce  $\mu$  by between 67-77%, compared to the pure water scenario, it also diminishes the dependence of the coefficient on  $v_s^{\text{RMS}}$  (i.e. the gradient of the dashed line is smaller for KCl). The observed effect is in good agreement with other studies finding that simple alkali cations can effectively reduce friction between atomically smooth surfaces – so-called hydration lubrication [26, 85, 87]. This regime is generally assumed to be driven by the disruption of water's native structure against the solid, which allows for weaker coupling between the tip and the sample, although counter-intuitively, it may involve the ions themselves being highly ordered [16].

#### *Viscoelastic modification of the nanoconfined fluids*

The rheological behaviour of the nanoconfined electrolytes is given by the tip's shearing phase and allows insight into the origin of the  $\ln(v_s^{\text{RMS}})$  dependency of  $\mu$  observed above. Fig. 4.10 shows  $\theta_s$  as a function of normal force and  $A_d$  for both solutions. In every case, the phase tends from a value close to  $0^\circ$ , at low confining pressures, towards  $\sim -55^\circ$  at high normal loads. However there are consistent trends in the evolution of  $\theta_s$  with  $A_d$  for both ultrapure water (a) and KCl (b). For a given  $F_N$ , as the shearing amplitude is increased (light to dark shades) the phase is pushed towards  $0^\circ$ , indicating a more elastic interaction, which can be rationalised by considering the *scale* of the periodic motion. For  $A_d = 0.5$  nm, the tip only slides over a single lattice site with each oscillation, requiring the motion of relatively few  $\text{H}_2\text{O}$  molecules and allowing the energy to be dissipated in a viscous manner. However, as  $A_d$  increases to more mesoscopic scales, the motion requires

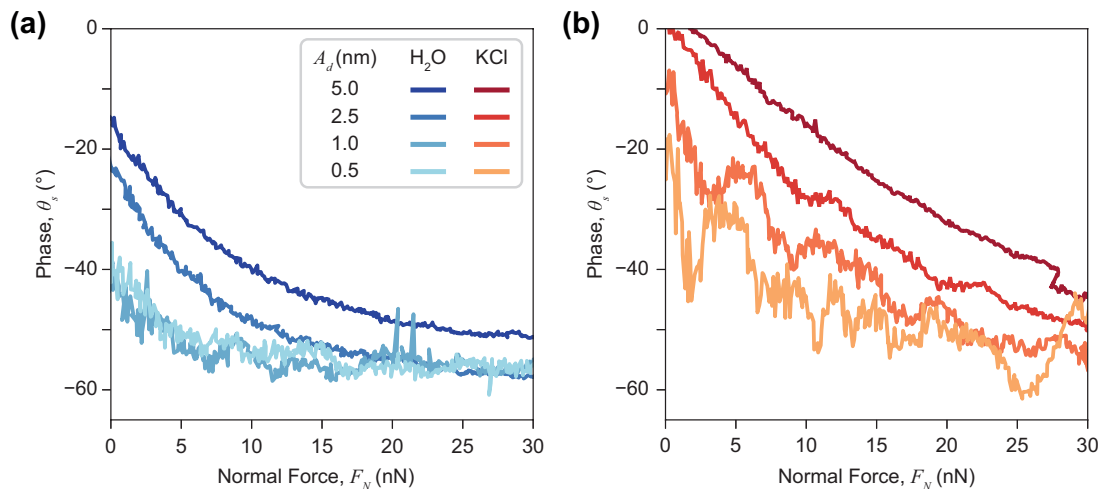


Fig. 4.10: The shearing phase reveals the origin of the non-linear tribological properties of the confined solutions. (a)  $\theta_s$  and its dependence on confining force and drive amplitude across pure water. For small confining forces ( $F_N < 15$  nN),  $\theta_s$  is well-separated with  $A_d$ . Higher values of  $A_d$  drive the phase closer to  $0^\circ$ , implying the increase in  $\mu$  (Fig. 4.9(b)) results from the interfacial water behaving in a more elastic, “solid-like” fashion. For  $F_N > 15$  nN,  $\theta_s$  tends towards  $\sim -55^\circ$  for all velocities. (b) Replacing the neat H<sub>2</sub>O with 150 mM KCl results in a similar dependence of  $\theta_s$  with  $F_N$  and  $A_d$ , but in general, there is a shift towards  $0^\circ$  relative to pure water, especially for the higher velocities.

the coordinated motion of interfacial fluid over many more energy barriers ( $\sim 10$  for  $A_d = 5.0$  nm) which thus increases the likelihood of the system “jamming”, leading to the elastic nature of the shear that we find here. The introduction of ions into the cavity Fig. 4.10(b) results in a similar trend, but with the phase in general closer to  $0^\circ$  compared to water at a given amplitude.

### 4.2.3 Stern layer structure and fluidity: $K^+$ concentration and length-scale dependence

The results presented above highlight the dramatic impact of simple monovalent ions on the dynamic properties of fluids at the interface. They especially highlight the charges’ propensity to make the liquid more “elastic” under large shear amplitudes. At first glance, this contradicts a similar AFM study which investigated a range of ions and found that they served to make the interface more viscous [26]. However, that particular case only probed one shear amplitude ( $A_d = 0.5$  nm), and later showed that this behaviour was concentration-dependent, breaking down above 75 mM. We thus explore the intervening concentrations between 0 and 150 mM in order to build up a picture of how the potassium ions progressively alter mica’s native hydration landscape.

We begin with traditional AM-AFM imaging and spectroscopy of the mica interface using a sharp tip and small amplitudes (section 2.3). This allows us to explore how the lat-

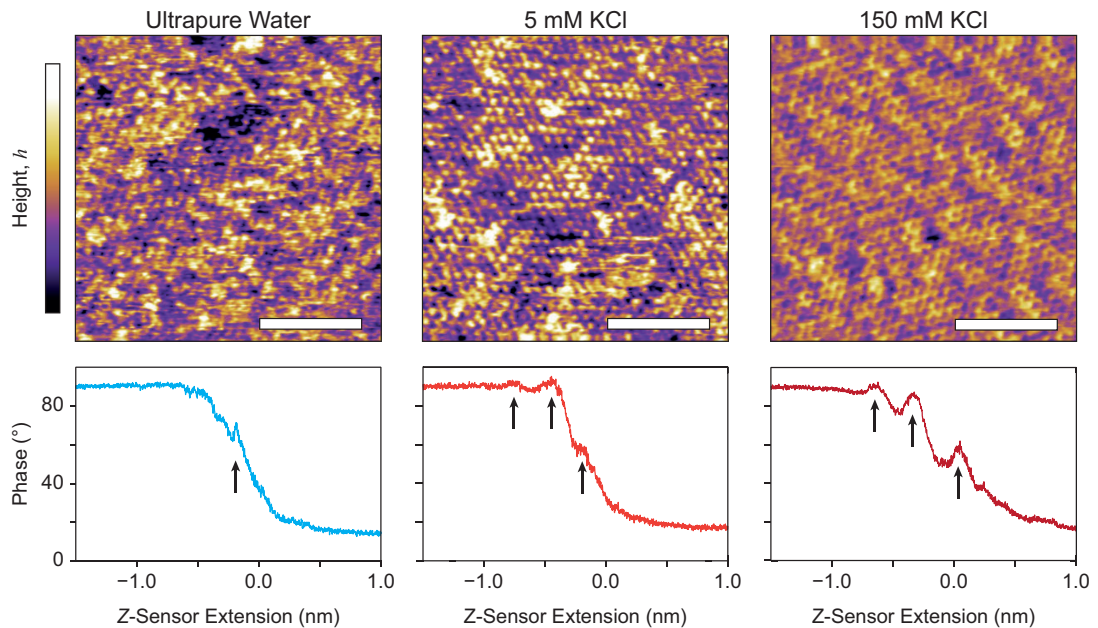


*Fig. 4.11:* AM-AFM imaging (upper) and spectroscopy (lower) illustrates the evolution of mica's Stern layer as the bulk concentration of KCl is increased up to 150 mM. The topography in pure water displays clusters of low height due to the specific hydration structure of water at the mica surface. This is reflected in the phase versus  $z$  curves having a single discontinuity (arrow) where the tip dissipates more energy as it removes water from the surface. In 5 mM KCl, the topography displays much larger variation and clusters of adsorbed  $K^+$  templated by the mica can be clearly resolved. The respective phase trace now demonstrates 3 anomalous peaks (arrows) due to the structuring of the ions vertically above the surface. However the low concentration renders the overall signal-to-noise ratio low. In 150 mM KCl, the topography is much smoother with a lower degree of noise. This is due to the well-formed Stern layer, presumably fully populated at this concentration, which generates three much stronger peaks in the phase. All length scale bars represent 5 nm and the height scale covers 320 pm. Phase traces represent the average of at least 30 independent force curves.

eral and vertical structure within the interfacial fluid is perturbed by the inclusion of alkali ions. Fig. 4.11 shows representative topographic images taken in solutions of increasing concentration of KCl. In ultrapure water (left), the topography variation is relatively low and the resolution of the underlying lattice is limited, reflecting the compact nature of the Stern layer in a similar manner to Fig. 3.3(f). This picture is reinforced by the tip oscillation phase spectroscopy curves (blue, now referring to the phase of the cantilever's vertical oscillation). Superposed on the smooth decrease from  $90^\circ$  expected for fluid damping near a solid surface is a spike (arrow) that represents an anomalous dissipation of energy by the tip as it traverses the strongly-bound hydration water. The traces presented are an average of at least 30 such curves, some of which had extreme deviations from the sigmoidal shape, but this was stochastic in nature and the average shows a rather small oscillation. When potassium ions are included in the electrolyte at 5 mM, they adsorb to the negatively-charged mica plane, forming clusters with a much greater height range,

due to their larger size. The corresponding phase trace (light red) still is dominated by the sigmoid, but there can now be observed three oscillations (arrows), representing the different coordinations available to the  $K^+$  ions. However, the amplitude of these oscillations shows that the Stern layer is not saturated, and many curves demonstrated only the single water “spike”. At 150 mM (dark red) the oscillations dominate, and are present in the majority of curves. Interestingly, the height variation of the scan at this concentration (top right) is much lower than the previous two images, implying that the topography represents a fully-formed interfacial layer of  $K^+$  ions.

Now having a clearer picture of the spatial organisation of the mica-electrolyte interface as the potassium density is increased, we repeat the shearing experiments but at a fixed  $A_d = 0.5$  nm over a range of ion concentrations between 0-150 mM. The variation of the shearing phase,  $\theta_s$ , with normal load is presented in Fig. 4.12(a). The results are all in the “second quadrant” (i.e.  $90^\circ < \theta_s < 180^\circ$ ), which was occasionally observed when using the AFM’s internal lock-in amplifier. This appeared to have no dependency on solution, cantilever or sample and so was assumed to be an artefact due to the symmetry of the tangent function (used to calculate  $\theta_s$ ) about  $\pm 90^\circ$ . Thus our interpretation of  $\pm 90^\circ$  as fluid-like and  $0^\circ, \pm 180^\circ$  as solid-like remains valid.

The traces presented in Fig. 4.12(a) display a large degree of noise, due to the small  $A_d$ , but for normal forces above  $\sim 5$  nN, the viscoelastic behaviour of ultrapure water is clearly distinct from that of the ionic solutions. We highlight this in (b) by plotting the phase as a function of potassium concentration at various  $F_N$  (dashed lines). While there is not a strong trend at finite concentrations, the key result is that  $\theta_s$  for ultrapure water is closer to  $180^\circ$  in all cases. This emphasises the ability of ions to make the interface more viscous and disordered, thus in line with the results of ref. [26]. We now have an apparent conflict – on the one hand Fig. 4.10 shows that the inclusion of ions makes the interface more elastic for a given  $A_d$ , but our conclusions from Fig. 4.12 are exactly the reverse! This discrepancy can be rectified by noting that the trend of Fig. 4.10 is only emphasised for large shear amplitudes above 0.5 nm; there is clearly a non-linear response of the solution that depends on the absolute scale of the motion relative to the crystal lattice.

We quantitatively show that this is the case by repeating the shearing “isotherm”, but this time with a fixed  $A_d = 2.5$  nm (Fig. 4.13). Now, the oscillatory motion requires the passing of 5 energy barriers in each half-period, increasing the likelihood of asymmetric motion (dashes in the schematic, top) as the nanoconfined fluid is unable to completely relax between clearing each lattice site. The phase versus normal force plot in Fig. 4.13(a) shows immediate contrast with the results taken at the smaller shearing amplitude. In all

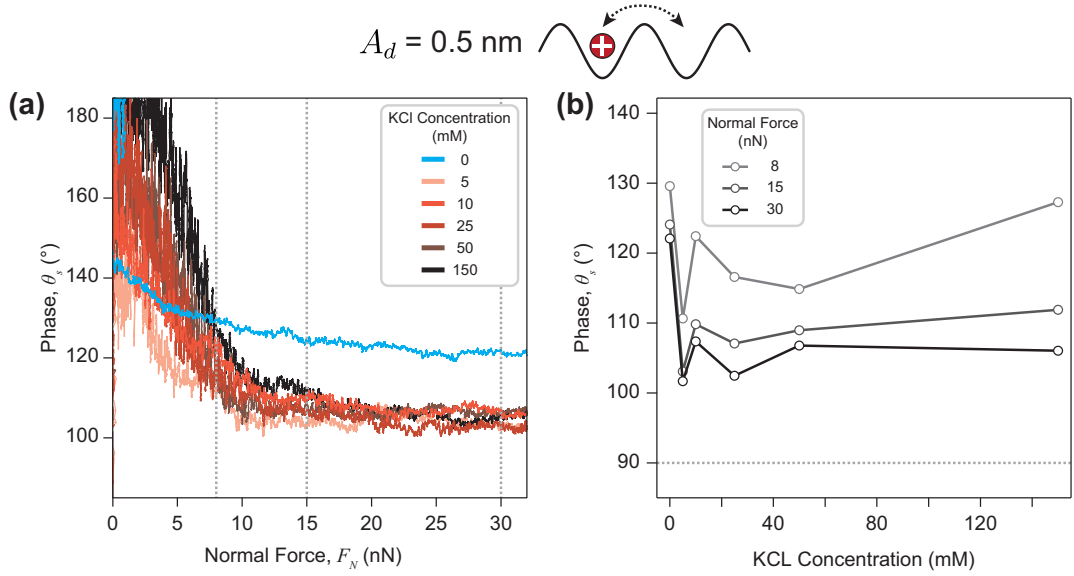


Fig. 4.12: Probing the effect of potassium concentration on the viscoelastic response of the confined electrolyte. (a) Shearing phase,  $\theta_s$ , as a function of normal force for a shear amplitude of  $A_d = 0.5 \text{ nm}$ . The small  $A_d$  leads to a large degree of noise, but for  $F_N \gtrsim 5 \text{ nN}$ , there is a clear separation between ultrapure water (blue) and the ionic solutions (red shades). By taking sections at the dashed lines, we plot  $\theta_s$  as a function of KCl concentration (b). In all cases, the addition of ions drives  $\theta_s \rightarrow 90^\circ$ , emphasising that, when rolling over a single lattice site (cartoon, top), the ions serve to make the interface more viscous, in good agreement with ref. [26]. Each trace in (a) is the average of at least 30 spectroscopy curves.

cases, even at small  $F_N$ , the phase of ultrapure water is closer to  $90^\circ$ . Further, there is a much stronger trend of  $\theta_s$  with KCl concentration; an increase in  $\text{K}^+$  broadly leads to a more elastic response for this value of  $A_d$  (b). Our results shed light on the intricate relationship between the kinetic behaviour of nanoconfined fluids, their ionic content and the absolute scale of motion investigated. We have shown that, for small oscillation amplitudes that encompass a lone energy barrier, potassium is effective in making the interface more liquid-like (relative to ultrapure water) by driving  $\theta_s \rightarrow 90^\circ$ . This presumably is a result of the ions' tight binding of their hydration waters, which allows them to roll across the energy barrier (Fig. 4.12, top) in a smoother, pseudo-harmonic manner. Conversely, when larger oscillation amplitudes are employed, the extended size of the mica-potassium Stern layer (compare e.g. the blue and dark red curves in Fig. 4.11) and its complex hydration structure require the clearing of many energy barriers. At the mesoscopic scale of  $A_d = 2.5 \text{ nm}$ , the wider  $\text{K}^+$  network is continually disrupted over each period, which increases the potential for anharmonic jamming due to the inability of the ionic solution to relax. As the water has a much more compact Stern layer, this jamming is reduced, leading to a more viscous interface.

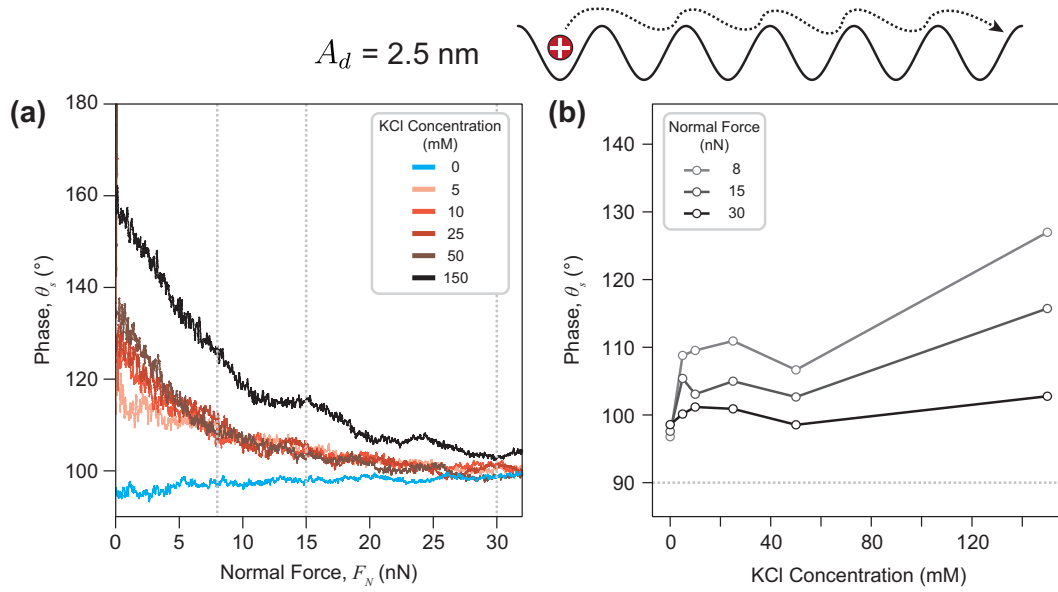


Fig. 4.13: Increasing the shearing amplitude to  $A_d = 2.5$  nm dramatically changes the response of the confined layer. In contrast with Fig. 4.12, solutions of ultrapure water always have  $\theta_s$  closer to  $90^\circ$  than those with ions in, highlighted by the sections presented in (b). This implies that the *scale* of the motion is crucial when considering the solutions viscoelastic response; the concerted motion of many ions over multiple energy barriers may induce severe penalties when compared to water alone (cartoon, top), leading to a more solid-like response for  $K^+$ . Each trace in (a) is the average of at least 30 spectroscopy curves.

#### 4.2.4 Impact of finite tip size

Throughout the experiments presented in section 4.2 (apart from for the high-resolution AM-AFM – Fig. 4.11) we have made use of SD-R30-FM cantilevers with silicon tips of nominal radii of curvature,  $r_c \sim 30$  nm. The use of larger tips is common in such spectroscopic studies [16, 96], as it increases the interaction region between the tip and the substrate and therefore amplifies any coupling mediated by the interfacial region. We expect that the viscoelastic behaviour – that is, the phase-dependencies – should not be strongly dependent on the contact area, as  $\theta_s$  reflects the kinetic properties of the fluid. However, the frictional force (and thus  $\mu$ ) is likely to be related to the absolute tip size, as the resistance to sliding will depend sensitively on the number of interfacial bonds formed between the two surfaces.

The silicon cantilevers used here are not as resistant to wear when compared to the common  $Si_3N_4$  tips of other cantilevers. We were thus careful when collecting the results of Fig. 4.9 (conducted with a single cantilever) to ensure that there were no time-dependent effects that could be related to tip degradation. This was done for each immersing fluid by collecting multiple sets at each  $A_d$  in a random order. However, it is still necessary to quantify how the tip radius of curvature evolves as a result of the measurement, and

how this impacts upon the results. We go about this in three ways. Firstly, we used scanning electron microscopy (SEM) to image the tips after a set number of curves had been acquired in order to accurately gauge the tip radius of curvature. Secondly, using a new SD-R30-FM cantilever, multiple force curves were conducted in ultrapure water on mica, with a constant  $A_d = 5.0$  nm (thus representing an extremal wear on the tip, as our previous experiments varied  $A_d$ ), while recording the changes in shearing amplitude and phase. Thirdly, the shearing measurements were repeated, but with a tip composed of diamond-like-carbon (DLC). These tips are extraordinarily resistant to wear, and the model we make use is a single-crystal tip with a nominal radius of curvature of  $< 5$  nm, thus allowing us to see how the dynamics of electrolyte layers are affected when as few molecules are confined as possible.

#### *Tip wear and large radii of curvature*

The results of the first two methods are presented in Fig. 4.14. The SEM images of SD-R30-FM cantilevers used for  $\sim 300$  and  $\sim 1000$  force curves of varying  $A_d$  are shown in (a) and (b) respectively, with dashed circles highlighting the effective  $r_c$ . In the former case, even with the sputtered layer of  $\sim 1.5$  nm of gold (necessary to make the tip conductive for the imaging), it can be seen that  $r_c$  has not increased much from its nominal value of 30 nm. In fact, it requires around three times as many force curves to be performed before the tip starts to show serious amounts of wear (b), with  $r_c \sim 108$  nm. Performing  $\sim 200$  force curves with  $A_d$  constant at a high value of 5.0 nm shows that a rather strong dependency of  $A_s$  with tip wear (c). Specifically, the measured amplitude reduces as the number of curves (tip wear) increases. This contradicts equation 4.2, which implies that  $F_L$  should *increase* with interaction area. It appears that, for our system at least, the key parameter is the pressure applied by the tip: we keep the maximum force,  $F_N^{\max}$ , constant throughout at 30 nN and so, as the tip degrades and the contact area increases, the applied pressure will *decrease*, leading to the reduction in shear amplitude. Fig. 4.14(d) shows that the phase is also quite sensitive to the total contact area, with an increase of  $\sim 40^\circ$  between the first and the last curve taken, and the transition region ( $z \sim 0$ ) becoming less sharp. This is indicative of the interface become less fluid-like, and agrees with our conclusions thus far about the strongly-coupled motion of interfacial fluid (i.e. with many molecules being moved at once) behaving more like a glass. Fig. 4.14 emphasises the care which must be taken when drawing conclusions from such nano-tribological experiments, especially as control over tip size and geometry in AFM is notoriously difficult. However, our use of multiple, randomised sets of varying  $A_d$  when collecting data for Fig. 4.9 and 4.10<sup>3</sup> should mitigate this effect, ensuring the validity of our conclusions.

<sup>3</sup> Fig. 4.12 and 4.13 were independent experiments, each taken with a brand new SD-R30-FM cantilever.

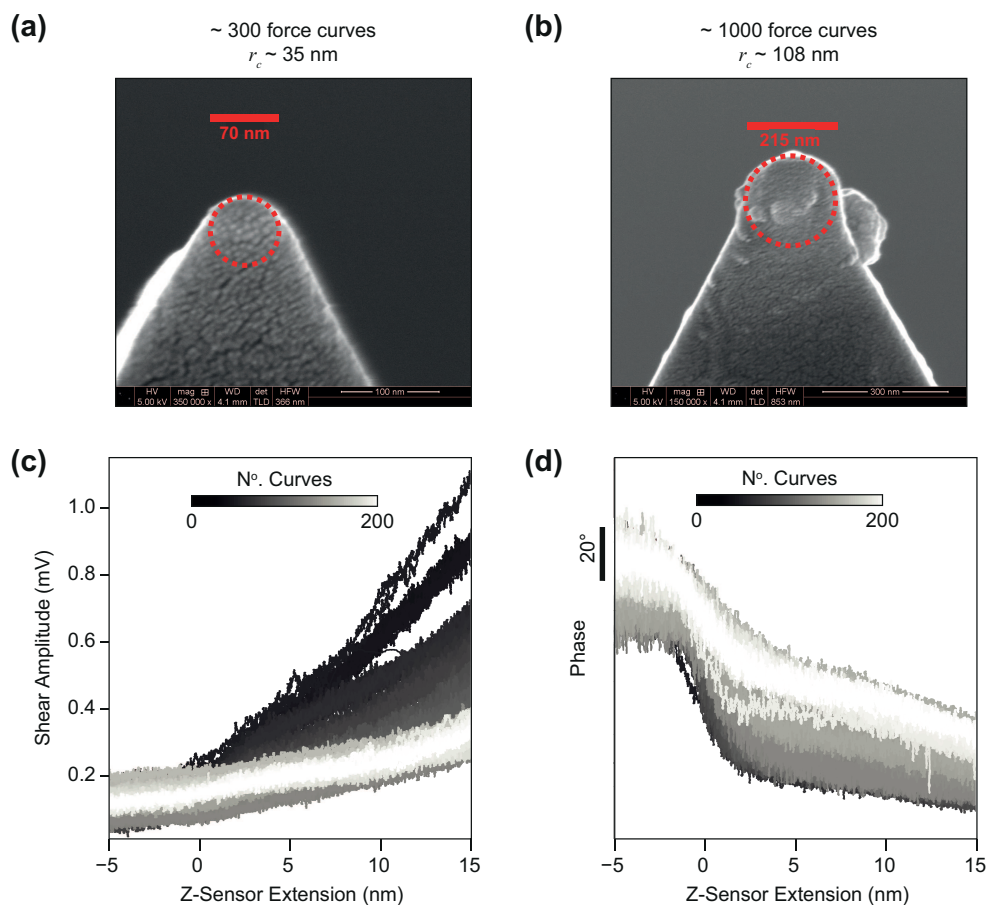


Fig. 4.14: Impact of shear force spectroscopy on the tip radius of curvature,  $r_c$  (a), (b) and (in separate experiments) on the measured shearing amplitude (c) and phase (d). Over a few hundred force curves in which  $A_d$  was varied between 0.5–5.0 nm, the tip's radius of curvature increases only by  $\sim 3.5$  nm (after accounting for the sputtered gold layer). After taking in order of 1000 force curves however, the radius has increased approximately threefold. Separate experiments, which tracked  $A_s$  and  $\theta_s$  over time while applying an extreme shear of  $A_d = 5.0$  nm show that total *pressure*, rather than interaction area is a key parameter when modelling the lateral force, as  $A_s$  decreases with increasing radius (see text). The phase is also rather sensitive to tip wear, with the transition around  $z = 0$  becoming less sharp over time.

*Ultrasharp tips and minimal confinement areas*

As well as understanding the impact of *increasing* tip size, it is also necessary to explore the other extreme; how does confining aqueous electrolytes affect their dynamics when the lateral confinement area is kept as small as possible? This is an interesting question as we move away from mesoscale, 2D networks of confined fluids and approach the kinetics of only a handful of trapped molecules. In these cases, there is still strong confinement in  $z$ , but there is the possibility of significant flux at the edges of the confined region. We tackle this problem using an ultrasharp tip ( $r_c < 5$  nm, illustrative image of ideal tip from manufacturer shown in inset to Fig. 4.15(b) [97]) that is composed of DLC. These cantilevers represent the sharpest commercially available probes with which to perform the experiments and further, the tip material is robust enough to withstand the wear observed on silica tips.

The results using this tip are presented in Fig. 4.15 with each trace reflecting the average of as least 30 individual spectroscopy curves. Comparing the shear amplitudes in (a), (b), it can be seen that the general linear relationship between  $A_s$  and  $F_N$  is maintained in both solutions. However, the ordering that was observed in Fig. 4.9 is now absent when using a sharp probe; there appears to be no correlation between the driving oscillation and the cantilever's response. This reflects the stochastic nature of the experiment; as the confinement includes many fewer molecules than previously, the individual  $A_s$  versus  $F_N$  curves varied a great deal and thus their averages cannot be meaningfully compared. This can be seen in the inset to (b), where the shear amplitude and deflection are plotted versus  $z$ .  $A_s$  is extremely non-linear, with at least four plateau regions characterised by sharp transitions. Further, the amplitude is non-zero well before the deflection signal changes ( $z \sim -2$  nm), indicating substantial tip-sample interactions prior to contact. Neither of these effects were observed with the blunt silica tips and it was assumed that this resulted either from the difference in interaction area, or the reduced cantilever stiffness of the DLC tips. Despite this, the overall lubricating effect of alkali ions is still apparent, with the amplitude (and thus frictional force,  $F_L$ ) in 150 mM KCl (b) consistently lower than for ultrapure water (a).

The shearing phase results while using ultrasharp tips are presented in Fig. 4.15(c) and (d). Despite the host of experimental differences between this system and that of the blunted tip, we observe strikingly similar trends to those of Fig. 4.10. Firstly, for a given solution, increasing  $A_d$  results in a decrease in  $|\theta_s|$ , showing that the nanoconfined fluids still “stiffen” when sheared over large distances, despite the interaction area being dramatically reduced. Further, the impact of  $K^+$  networks is evident; for the larger  $A_d$ ,

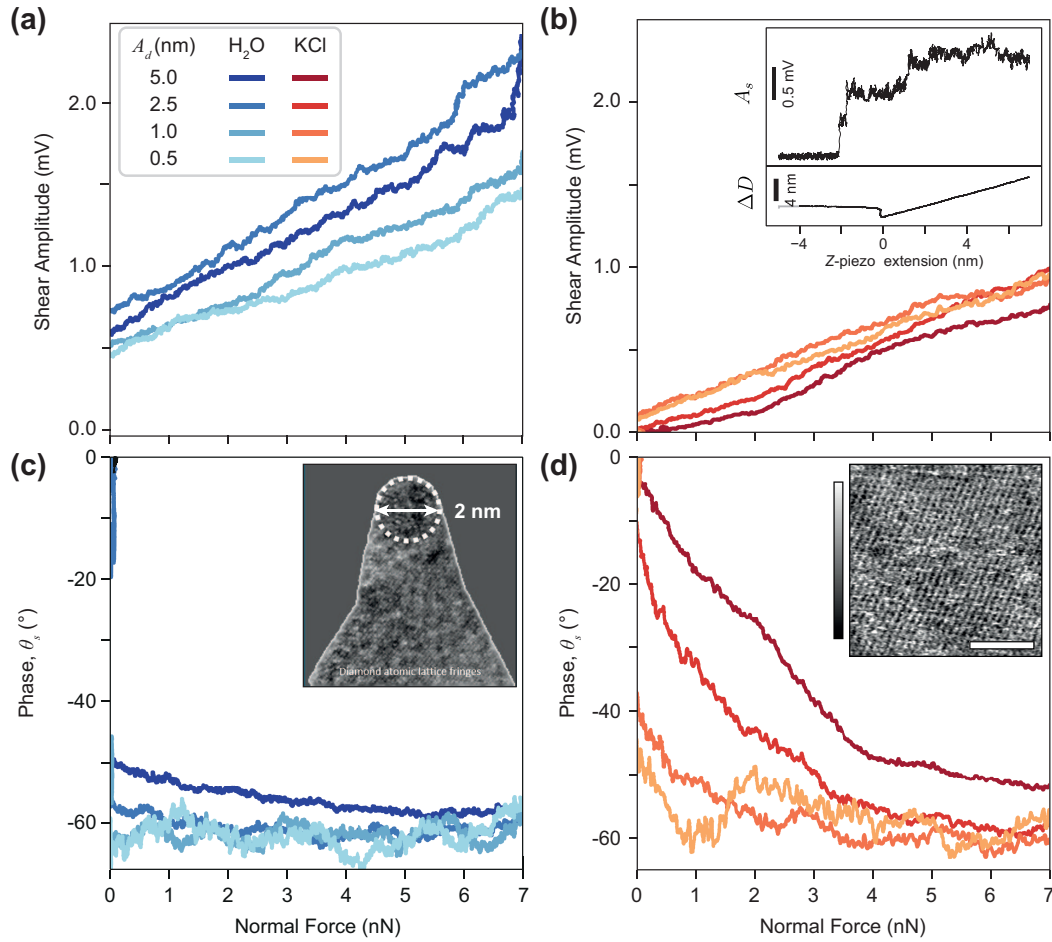


Fig. 4.15: We make use of ultrasharp tips composed of diamond-like-carbon (DLC; Adama, AD-2.8-SS, manufacturer's image shown in inset to (c) [97]) to probe the kinetics of nanoconfined solutions while retaining the smallest possible contact area. Comparing the shearing amplitudes (a), (b), it can be seen that there is no longer the clear trend with  $A_d$  that was observed in Fig. 4.9(a), due to the stochastic nature of the individual force curves (e.g inset to (b)). The lubricating ability of  $K^+$  ions is still present however, with the shearing amplitudes in (b) consistently lower than in ultrapure water. The shearing phase,  $\theta_s$  is presented in panels (c) and (d) for  $H_2O$  and  $KCl$  respectively. In contrast with the shearing amplitude, these curves replicate all the effects seen previously; smaller oscillation amplitudes (or  $v_s^{RMS}$ ) lead to a more viscous response of the interfacial fluid ( $\theta \rightarrow 90^\circ$ ), which is given more opportunity to fully relax. At larger  $A_d$ , the addition of potassium makes the dynamic response more solid-like due to the formation of ordered ionic networks. High-resolution imaging of the mica surface in 150 mM  $KCl$  (inset to (d)), performed immediately after the force spectroscopy, confirms the tip's retention of atomic level sharpness. Colour scale covers 100 pm and length scale bar represents 5 nm.

the addition of ions decreases the sharpness of the transition (more gradual descent to  $-60^\circ$ ) and generally results in a more solid-like interaction than compared to an interface composed only of  $\text{H}_2\text{O}$ . We confirm the ability of DLC tips to retain their sharpness, even after hundreds of force curves are collected, by acquiring high-resolution images of the mica surface in 150 mM KCl (inset to (d)) immediately after the experiment. Indeed, the hexagonal lattice of the mica crystal can clearly be observed, showcasing the resilience of these cantilevers to wear even at the nanoscale. Overall, the results of Fig. 4.15 complement those acquired with a blunt tip; they emphasise that the dynamic solidification of confined aqueous interfaces is rather general, even when interaction areas are reduced to just a few square nanometres, as well as showcasing the ability of  $\text{K}^+$  to substantially reduce the frictional forces. However, there remain stochastic events which cannot be described by the linear relation  $F_L = \mu F_N$  (inset to (b)) and hint at single-molecule friction effects. These, unfortunately, would require techniques other than AFM to fully characterise and so we avoid further speculation.

#### 4.2.5 Nanoconfinement against amorphous interfaces

The above results allow a great deal of insight into the dynamics of confined fluid molecules, as the use of crystalline mica allows the validation of 1D friction models, exhibited here with the modified Prandtl-Tomlinson (Table 4.1). Such interfaces have well-defined crystal length scales, and their interaction with water and electrolytes has been characterised with many different techniques over the years (section 1.3). However, the vast majority of solid-liquid interfaces found in nature, at least in a geological context, are amorphous oxides that are rough on many length-scales, chemically heterogeneous and less hydrophilic than our previous model system. To understand the impact of such complexity on the kinetic behaviour of nanoconfined electrolytes, we replaced the mica substrate used previously with a silicon crystal with a 100 nm layer of  $\text{SiO}_2$  thermally grown on it. The topography of these surfaces was found to vary on the scale of 10s-100s of nanometers (see inset to Fig. 4.16) with a roughness of around 0.2 nm. However, given our shear amplitudes,  $A_d < 5.0$  nm, we expect that it is not this mesoscale roughness that will dominate our measurements, but instead the complex surface chemistry that results from under-coordinated silicon and oxide bonds. This can produce diverse groups that each interact with the interfacial water in a distinct manner [98], thus making our substrate “complex” at the molecular level. We note that globally, the silica interface is much less hydrophilic than mica, with a contact angle of  $70\text{-}90^\circ$  routinely observed when performing shear-force experiments.

The evolution of the friction force with load and with  $A_d$  for symmetric silica surfaces

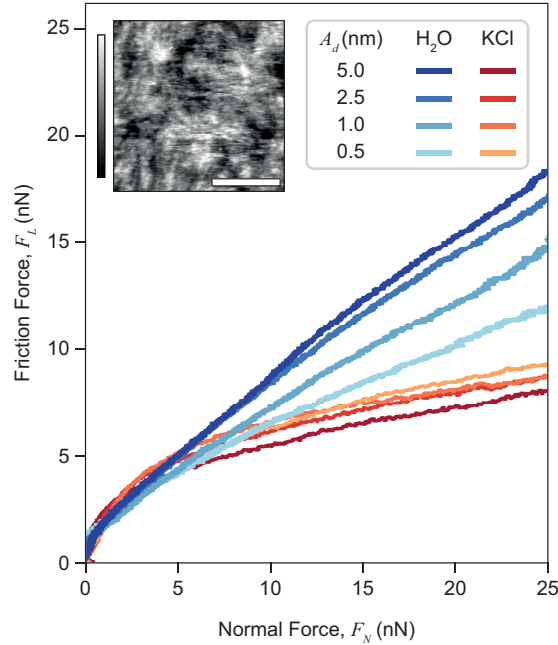


Fig. 4.16: The velocity-dependent shear response of fluids restricted to a crystalline surface is replicated when the confining walls are composed of amorphous  $\text{SiO}_2$ . The frictional force at the silica interface does not obey a linear relationship, as in Fig. 4.9, but instead appears to plateau for high  $F_N$ . However, the absolute frictional forces are larger than those on mica, likely due to the increased surface roughness (topography at 100 nm scale shown in inset). For confined  $\text{H}_2\text{O}$ , there is still a velocity-dependence, with  $F_L$  increasing as the shear amplitude is increased, but this is not observed when KCl is introduced into the cavity. Height colour scale of inset covers 1 nm and length scale represents 40 nm.

separated by ultrapure water and 150 mM KCl are presented in Fig. 4.16. For both solutions, the response of  $F_L$  is not quite linear but begins to plateau with increasing  $F_N$ . This precludes the calculation of an effective friction coefficient but, when comparing with Fig. 4.9, it is clear that  $F_L$  is greater on silica than mica, for a given  $F_N$ . This is likely a result of the interfacial “roughness” of silica discussed above, which presents an increased resistance to shear. The separation with  $A_d$  is still present in  $\text{H}_2\text{O}$ ; larger RMS velocities produce the greatest  $F_L$ , but the separation is smaller than for mica and, when potassium ions are included in the solution, the trend is lost. In the latter case, we observe both a reduction in the total lateral force and an increase in the plateau effect that is only hinted at in  $\text{H}_2\text{O}$ , confirming once more the lubricating ability of these ions.

The corresponding shearing phase plots are shown in Fig. 4.17. These demonstrate the viscoelastic properties of the silica-confined fluids are different in almost every way when compared with the case of mica. Firstly, the  $\theta_s$  traces do not all tend to the same value at high confining pressures, suggesting that the velocity-dependence (separation with  $A_d$ ) is more stable under large loads. Secondly, the addition of ions drives the phase towards  $-90^\circ$  relative to pure water, even at the largest oscillation amplitudes of 5.0 nm. Finally,

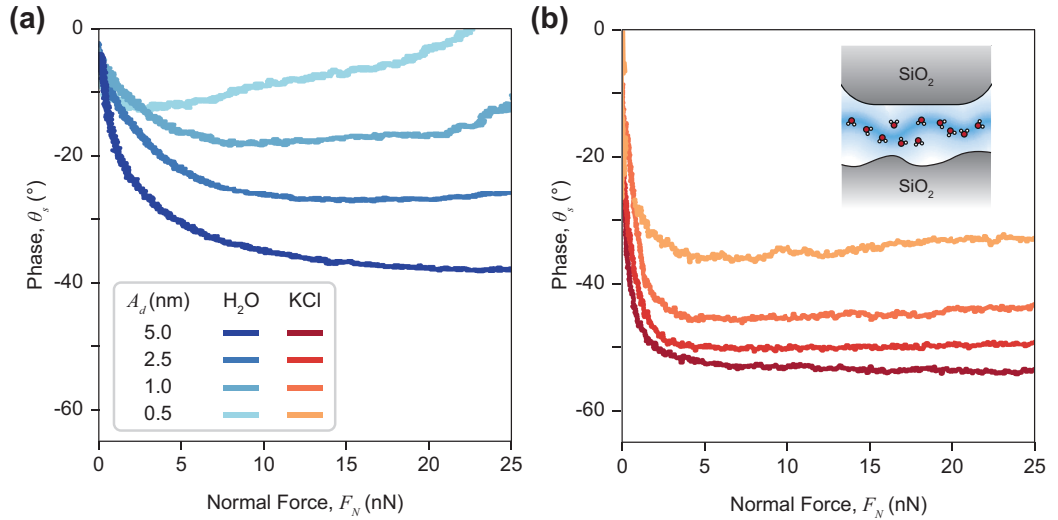


Fig. 4.17: The shearing phase response of silica-confined electrolytes highlights large changes from the silica-mica system.  $\theta_s$  in both ultrapure water (a) and 150 mM KCl (b) solutions do not converge for high loads, but tend towards different values that depend on  $A_d$ . Crucially, these show that increasing  $A_d$  (or  $v_s^{RMS}$ ) makes the confined film more fluid-like, in contrast with hydrophilic, crystalline surfaces. This trend-reversal is also seen in the case of potassium ions, with their phase being closer to  $90^\circ$  than ultrapure water, even for large shear amplitudes. We attribute the remarkable reversal of these results to the less hydrophilic nature of the silica surface, which may result in a depletion layer at its surface, precluding the formation of a well-ordered interfacial structure.

and perhaps most intriguingly, the trend of phase with  $A_d$  is completely reversed; larger driving amplitudes lead to  $\theta_s \rightarrow |90^\circ|$ , implying that the interface is more liquid-like at higher shear speeds. All these features are consistent in both ultrapure water and 150 mM KCl. This represents a dramatic shift in the dynamic characteristics of the confined films, which are decidedly non-trivial to unpack. We attribute the differences observed between Fig. 4.10 and 4.17 to a combination of silica's disordered interfacial chemistry and its smaller affinity for water molecules. Both of these reduce the likelihood of finding an ordered, ice-like layer of H<sub>2</sub>O molecules at the silica-water interface, which has consequences for the local fluid's density and dynamics. Indeed, molecular dynamics simulations have shown that that hydrophobic surfaces display a so-called depletion layer, with a reduced water density in the first few Ångströms above the solid's edge [99]. This then has direct consequences for the local fluid velocity and dielectric profile [63, 100], with hydrophobic surfaces demonstrating larger in-plane velocities than their hydrophilic equivalents [99]. This observation can be used to rationalise our discrepancy; the silica-confined fluid interacts less with the substrate than in the case of mica, and so increasing  $v_s^{RMS}$  increases the relative importance of fluid-fluid (lateral), compared with fluid-substrate (normal) interactions. Thus, in the limit of negligible hydrophilicity, increasing the velocity will tend towards a perfectly fluid response with  $\theta_s = \pm 90^\circ$ . This concept is illustrated in the inset to Fig. 4.17(b), with water molecules preferentially occupying the cavity region between

the silica surfaces in a disordered state.

#### 4.2.6 Frequency- and velocity-dependence of dynamic behaviour

So far in section 4.2, we have seen that confined aqueous solutions display a great variety of dynamic responses, depending on the amplitude of the driving shear oscillation,  $A_d$ , the chemistry of the confining surfaces and the extent of the confinement. The discussion has predominantly been couched in terms of the relative RMS velocity between the tip and the sample, as this is the key parameter for many models of friction [79, 101]. We changed  $v_s^{\text{RMS}}$  by altering the shearing amplitude while keeping the frequency constant at  $\nu_s = 1$  kHz. Although our conclusions should not be affected, it is clear that in doing so, we simultaneously probe the effect of a change of velocity as well as lengthscale, making it difficult to de-convolute these two parameters. This was further limited by the fact the AFM stage's piezo used to drive the oscillations resonated at a frequency of  $\nu_0 \sim 3$  kHz; increasing the frequency beyond 1 kHz would have pushed the piezo outside of its linear region and there would have been reduced control over the absolute value of  $A_d$ .

To overcome this problem, we augmented the commercial AFM stage with a secondary piezo actuator, optimised for shear motion along one axis only (P-121.01, Physik Instrumente, Germany) which thus had a much higher nominal resonance of  $\nu_0 = 330$  kHz. Even with the manufacturer's recommendation that the actuator not be used above  $\nu_0/3$ , this allows for a much broader range of frequencies and velocities to be explored, independently of changing the oscillation amplitude. After fixing a steel disc to one side of the piezo and a polymer disc to the other with epoxy resin, a mica crystal could be mounted and the ensemble inserted into the AFM sample chamber as usual. A calibration between the voltage applied to the piezo and its amplitude,  $A_d$ , was conducted at low frequencies, using high-resolution AM-AFM imaging and the periodicity of the mica lattice as a "standard candle" (see materials and methods, section 4.4). Assuming that this calibration remained valid in the actuator's linear region ( $\nu_0 \lesssim 110$  kHz), this system allows us to independently disentangle the conclusions drawn previously in this section.

#### *Ultrapure water*

Fig. 4.18 shows the results of such a shear experiment, conducted using the blunt SD-R30-FM cantilever (as previously) in ultrapure water on mica, using the same range of values of  $A_d$  and at constant normal force,  $F_N = 20$  nN. Using an external lock-in amplifier (MFLI, Zurich Instruments, Switzerland) to both drive the piezo and analyse its response, the frequency,  $\nu_s$ , was swept between 0.5-110 kHz, with a total of 3 sweeps per  $A_d$ ; the figure displays every result laid on top of one another. The higher frequency range ( $\nu_s > 18$  kHz)

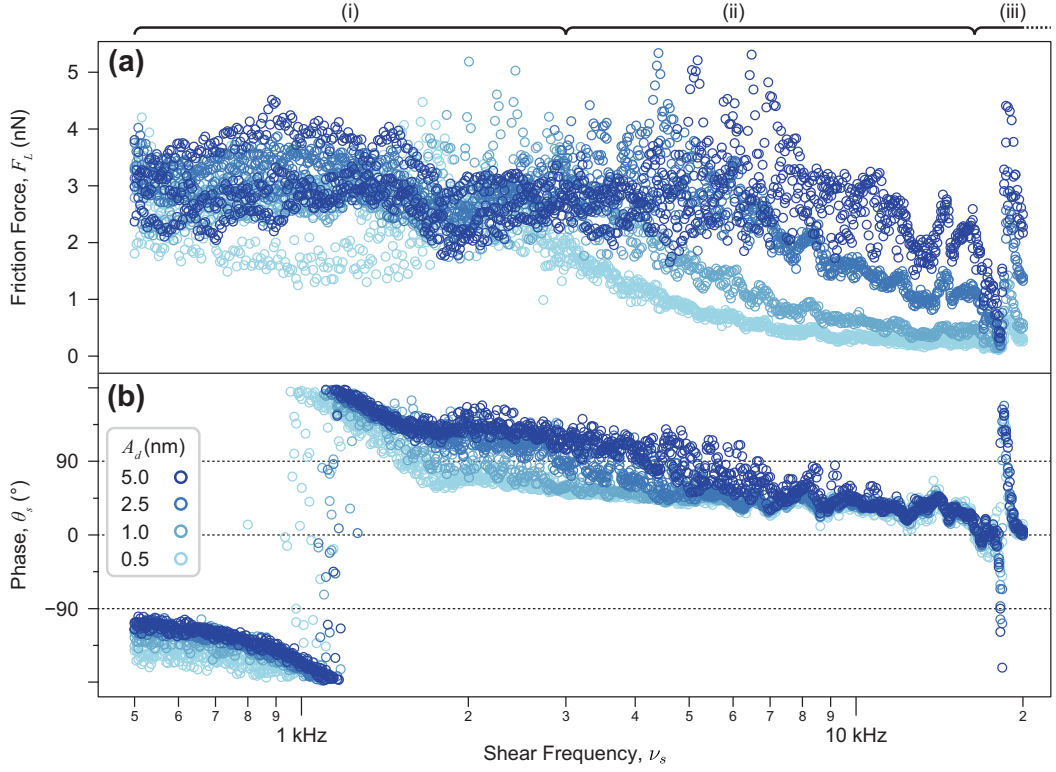


Fig. 4.18: The frequency-dependence of the frictional response (a) and shearing phase (b) of nanoconfined ultrapure water as probed by shear-force spectroscopy, using an external piezo actuator. Three sweeps were taken for each each  $A_d$  and all data are plotted here. Three regions can be distinguished: (i)  $0.5 \lesssim \nu_s \lesssim 3$  kHz,  $F_L$  is roughly constant while  $\theta_s$  varies and is “more positive” for higher  $A_d$  (see text). (ii)  $3 \lesssim \nu_s \lesssim 18$  kHz, the friction force decreases with frequency to an extent that depends on the shear amplitude. This agrees with our previous single-frequency result. The phase in this region is still separated by  $A_d$ , but converges rapidly with increasing frequency. (iii)  $\nu_s \gtrsim 18$  kHz,  $F_L$  is characterised by broad resonance-like peaks in which  $\theta_s$  varies rapidly with frequency, but has no  $A_d$  dependence. We tentatively attribute these peaks to spurious interactions between the cantilever and substrate or other mechanical couplings, and so only plot the beginning of this region.

demonstrated many peaks that we associated with spurious mechanical resonances and/or fluid-mediated coupling between the cantilever and the sample (see Fig. 4.24 and 4.25), and so we plot only the results for  $0.5 < \nu_s < 20$  kHz. There are key differences between these and the single-frequency data, but there is a lot of information contained within the results, which we shall first discuss, before comparing them with our previous conclusions.

We first observe that Fig. 4.18 shows there to be three regions of frequency (loosely marked by (i), (ii) and (iii), above figure) that are typified by different behaviour in the lateral force (a) and the shear phase (b), as a function of shearing amplitude,  $A_d$ .

- Region (i),  $\nu_s \lesssim 3$  kHz

In this section, the lateral force generally overlaps for each  $A_d$ , and is rather flat with fre-

quency. There is a possible feature at  $\sim 1.5$  kHz, but the noise and variation within data sets (three measurements are plotted for each  $A_d$ ) does not allow any full analysis of this. Conversely, within region (i), the phase shows a clear oscillation amplitude dependency; as  $A_d$  is increased,  $\theta_s \rightarrow -90^\circ$  (for  $\nu_s \lesssim 1$  kHz) or  $\theta_s \rightarrow 180^\circ$  (for  $\nu_s \gtrsim 1$  kHz). This reflects the traversal of  $\pm 180^\circ$ ,  $\pm 90^\circ$  and  $0^\circ$  by  $\theta_s$  in a continuous manner, making unambiguous assignment of the confined liquid's response difficult.

- Region (ii),  $3 \lesssim \nu_s \lesssim 18$  kHz

This region demonstrates correlation between the oscillation amplitude and the resulting frictional force felt by the tip, in agreement with that observed at a fixed frequency: shearing over multiple lattice sites results in a greater extent of “jamming” among the sheared molecules, which increases  $F_L$ . As well as this trend with  $A_d$ , region (ii) shows that the overall frictional force decreases smoothly with increasing frequency, to almost zero in the case of  $A_d = 0.5$  nm. The phase in this region still shows a trend with  $A_d$ , in that  $\theta_s(5.0 \text{ nm}) > \theta_s(0.5 \text{ nm})$ , but it is the opposite of that suggested by e.g. Fig. 4.9. At the highest frequencies in this region, the phase traces converge to be equal within error.

- Region (iii),  $\nu_s \gtrsim 18$  kHz

The third zone runs up to the highest frequencies studied here (110 kHz) and is typified by many peaks in  $F_L$  that coincide with the phase passing through  $0^\circ$  or  $\pm 90^\circ$  and so we associate them with resonances of the system. Their number of these peaks, as well as their breadth and relatively low frequency imply that these are not related to the physical properties of the nanoconfined film, but are instead part of the system's mechanical response to the shear. This view was reinforced by some of the resonances being observed in “control” trials where the lateral tip motion was monitored with a tip-sample separation of over 150 nm. We present the high-frequency data related to region (iii) in the materials and methods section (Fig. 4.24), but without a comprehensive analysis of the cantilever's lateral transfer function and its variation with tip-sample separation, little physical information can be gleaned from it.

### *Effect of alkali ions*

Repeating the experiment with 150 mM KCl as the intervening fluid does not bring about any dramatic changes to the frictional behaviour when using the external piezo actuator, as is shown in Fig. 4.19. For every oscillation amplitude (a)-(d), the addition of ions

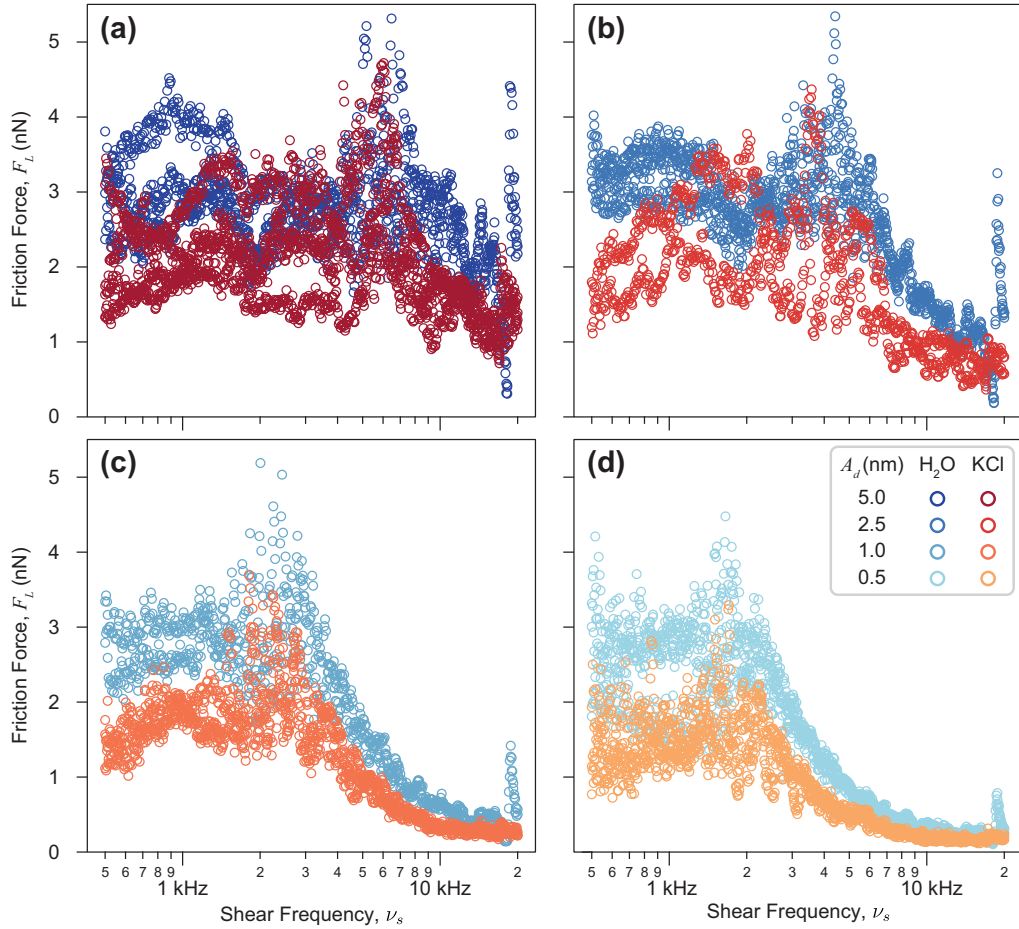


Fig. 4.19: Using the external shear piezo, we again confirm the ability of 150 mM KCl to lubricate the interface between the tip and the sample at oscillation amplitudes of 5.0 nm (a), 2.5 nm (b), 1.0 nm (c) and 0.5 nm (d). Similar behaviour is displayed for all  $A_d$ ; a plateau in friction force at low frequencies followed by a smooth decrease after  $\nu_s \sim 3$  kHz, although it is noisy in (a) for the largest amplitudes. All panels are plotted against the same axes, with the same scales and the ultrapure water data sets are reproduced from Fig. 4.18(a).

reduces the measured frictional force, but  $F_L$  follows the same trend with  $\nu_s$ ; a constant value for low frequencies, followed by a smooth decrease after 3 kHz. Shear amplitudes of 5.0 nm (a) display both the greatest amount of noise in the measurement and the least difference between ultrapure water and the electrolyte solution, potentially a result of mechanical noise introduced *via* the piezo which would scale with the voltage applied. The shearing phase for ultrapure water and 150 mM KCl is identical, within the noise limit, for a given  $A_d$  and so we do not plot it here.

#### Functional form of frequency-dependent $F_L$

The dynamic response of confined water and potassium is clearly a non-trivial function of frequency and shear amplitude, with no straightforward linear dependency akin to that

observed in subsection 4.2.2. Despite this complexity, each trace can be broadly described by a low-frequency plateau followed by a transition to a low-friction regime, with the onset of this decrease depending on  $A_d$ . This behaviour can be approximated by fitting the data with a function of the form  $F_L = K + F_0 \exp(-(\nu - \nu_0)/\lambda)$ , where  $K$  represents a fitted offset in  $F_L$ , a constant frequency offset of  $\nu_0 = 3$  kHz is used to focus on region (ii), and the fit is over all frequencies up to 18 kHz. The ultrapure water frictional data (averaged for each  $A_d$ ) is plotted in Fig. 4.20(a), along with the functional fits (black curves). The data is described relatively well, although the entire decay for  $A_d = 5.0$  nm is masked by the high-frequency resonances, which leads to large fitted uncertainties in  $\lambda$  and  $F_0$ . The overall behaviour is reminiscent of the Stribeck curve for fluid-mediated lubrication (Fig. 4.6), although in this case the transition is likely to be between a hydration lubrication region (low  $\nu_s$ ) and an anomalous regime with almost negligible friction (high  $\nu_s$ ). We postulate that the observed decrease in  $F_L$  is a result of the tip having enough inertia to avoid falling into the mica's crystalline potential wells. Thus, at high  $\nu_s$ , the effective PT potential energy landscape (c.f. Fig. 4.5(b)) is dominated by the spring term, rather than the oscillating potential.

The transition onset,  $\lambda$ , is plotted in Fig. 4.20(b) as a function of shear amplitude for both ultrapure water and 150 mM KCl and can be seen to increase approximately linearly in both cases. This is consistent with our interpretation of (a) in light of the PT model; at low  $A_d$  the oscillating motion is more “viscous” and  $F_L$  falls off rapidly with frequency, represented by a low value of  $\lambda$ . Conversely, for high amplitudes, the film behaves in a solid-like manner such that the crystalline term in the PT potential dominates at higher frequencies, and increases the extracted  $\lambda$ . The DC frictional force ((b), lower) reflects the extent of hydration lubrication, at low frequencies and increases with  $A_d$ , but converges for water and potassium at high amplitudes.

#### *Comparison with fixed-frequency results*

A significant conclusion of ref.s [78, 79, 85] as well as e.g. our Fig. 4.9 was that the effective friction coefficient,  $\mu$ , (or equivalently, the friction force,  $F_L$ ) scaled as  $\ln(v_s^{\text{RMS}})$  for crystalline surfaces, due to a combination of the periodic potential produced by the substrate, and thermal effects. If this was generally true, we would expect to find a similarly linear relation between  $F_L$  and  $\ln \nu_s$ , as the RMS velocity is proportional to the frequency. Fig. 4.18(a) demonstrates that this is patently not the case. In region (i), the frictional force remains roughly constant with  $\nu_s$  and in region (ii), it actually *decreases* as discussed above. We also note that the absolute frictional forces observed in Fig. 4.18(a) are slightly lower than those observed for the same  $F_N$  in Fig. 4.9(a), but this is not wholly unsurpris-

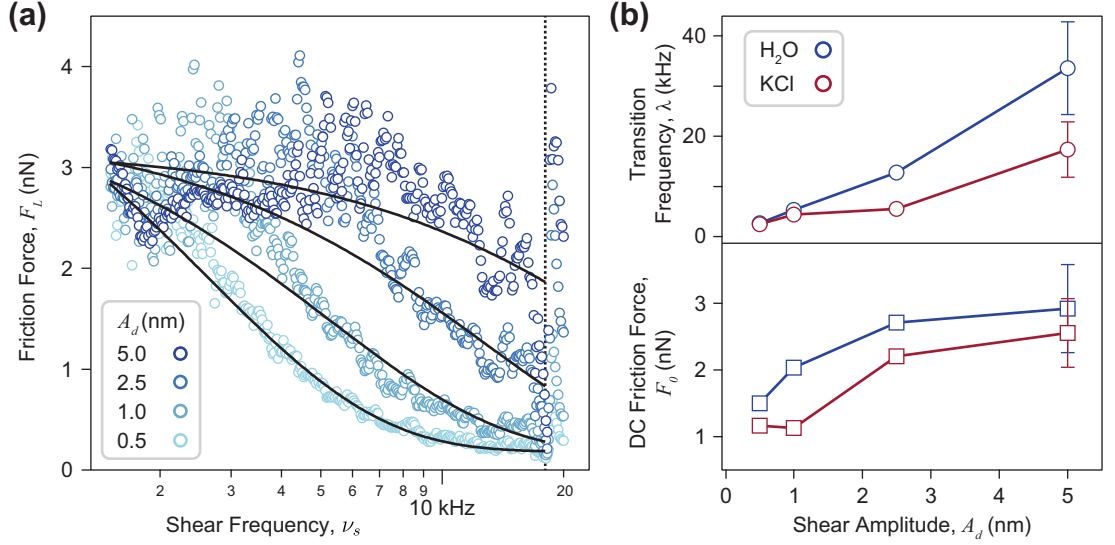


*Fig. 4.20:* Quantifying the frequency-dependence of the frictional forces of confined fluids. (a) Averaged data from region (ii) in Fig. 4.18(a) is reproduced, along with exponential fits up to 18 kHz (dashed line, see text) that capture the broad trend relatively well for varying  $A_d$ . (b) Extracted decay rates,  $\lambda$ , (upper) and “DC” amplitude of the friction force,  $F_0$ , (lower) demonstrate the evolution of these quantities with shearing amplitude.  $\lambda$  increases with  $A_d$  for both ultrapure water and 150 mM KCl solutions, indicating that the transition to a low friction regime (analogous to the Stribeck curve) is strongly lengthscale-dependent.  $F_0$  also increases with  $A_d$ , in agreement with our fixed-frequency results, with the water and potassium curves converging for high shear amplitudes. Error bars for  $A_d \leq 2.5$  nm are smaller than the data markers.

ing, given the different blunting methods of each experiment and the strong dependence of  $A_s$  on the tip radius of curvature (see Fig. 4.14).

When comparing the viscoelastic behaviour of the confined fluids, we re-iterate that the continuous traversal of  $0^\circ$ ,  $\pm 90^\circ$  and  $\pm 180^\circ$  observed in Fig. 4.18(b) means that a well-defined interpretation of  $\theta_s$  and its dependence on either  $A_d$  or  $\nu_s$  is not possible. For example, at 900 Hz, it could be claimed that larger shearing amplitudes result in a more viscous confined film ( $\theta_s \rightarrow -90^\circ$  with increasing  $A_d$ ), which seems physically improbable if precisely the reverse is true when  $\nu_s$  is increased to 1.3 kHz. This lack of a straightforward interpretation may result from the use of different lock-in amplifiers, with their separate filters and electronic characteristics, but it also hints at the limits of applying a linear rheological model to such microscopic layers of fluids.

We note that despite operating the external shear actuator well below its nominal resonance frequency, its electrical characteristics will strongly influence the frequency-dependence of the phase. Specifically, the piezo acts as a capacitor with finite charging times that depend on its capacitance,  $C$ , and the circuit’s resistance,  $R$ . As the shear frequency is increased, the piezo may not have sufficient time to charge, which would intro-

duce significant phase delays to the measured oscillation. To a first-order approximation, the circuit's impedance comes from the two connections to the lock-in amplifier/signal generator, each of  $50 \Omega$ . Thus, with a nominal piezo capacitance of  $1.4 \text{ nF}$  [102], the time constant is  $\tau = 0.14 \mu\text{s}$ , equivalent to a cut-off frequency of  $\nu_c = (2\pi\tau)^{-1} \sim 1.14 \text{ MHz}$ . This value is clearly much higher than our actuator's available bandwidth, implying that, in principle, the measured phase dependence relates only to physical changes in the nano-confined fluid and AFM tip/sample. It is certainly possible that the internal electronics of the AFM optical detection system introduce further resistance to the effective circuit, but as an in-depth characterisation of each component was not possible, we avoid further speculation.

### *Frequency response on amorphous interfaces*

Finally, we investigate the impact of amorphous, aperiodic interfaces such as silica, on the frequency-dependent shear response of our system. The results of three separate frequency sweeps at each amplitude are presented in Fig. 4.21, collected with the same tip as in Fig. 4.18 and at a normal load of  $F_N = 20 \text{ nN}$ . The friction force (a) demonstrates frequency-dependent regions with rather different characteristics to those observed for the mica-confined water. The first is at low-frequency ( $\nu_s \lesssim 1.4 \text{ kHz}$ ), where the frictional response increases with both shear amplitude *and* frequency. These features are both what would be expected from the results for mica and the thermally activated PT model but instead appear to have manifested themselves in a totally amorphous system. To emphasise the importance of this result, we plot  $F_L$  versus the RMS velocity in the inset to (a), highlighting the near-overlap of each shear amplitude in its low  $\nu_s$ , linear region. The low-frequency phase response is generally noisy, but collapse onto a single curve for  $\nu_s > 1 \text{ kHz}$ . The phase in this system appears to be much more restrained than for mica, ranging only from  $-50 < \theta_s < 180^\circ$ .

The second region is at high  $\nu_s \gtrsim 2 \text{ kHz}$ , and follows a transition at  $\sim 1.5 \text{ kHz}$ , where  $F_L$  drops rapidly and  $\theta_s$  passes through  $90^\circ$ . This crossing of the designated boundary between "solid-like" and "liquid-like" responses may be indicative of a different mode of shearing between the surfaces, as discussed regarding Fig. 4.20, with reference to the Stribeck curve. After this transition, the lateral force plateaus briefly for every  $A_d$ , before converging at high frequency, in a similar manner to region (ii) in the mica-confined system. The phase here is identical, despite changes in the oscillation amplitude, although with varying levels of noise.

Our use of a high-resonance shear piezo to pick apart differences in shearing frequency, velocity and lengthscale on the dynamic behaviour on confined fluids has illustrated a

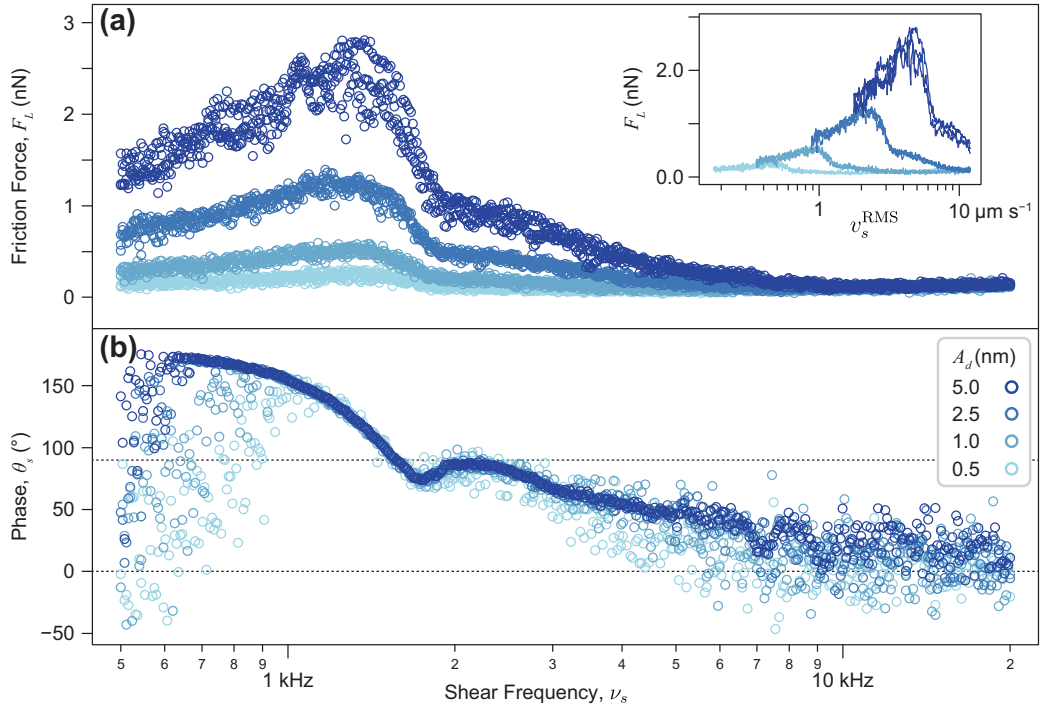


Fig. 4.21: Frictional response (a) and shearing phase (b) versus shearing frequency for ultrapure water nanoconfined between two amorphous silica surfaces. Three regions in  $\nu_s$  can still be determined, similarly to Fig. 4.18, but the behaviour is quite distinct. At low  $\nu_s$ , of  $\lesssim 1.4$  kHz, the frictional force is well-separated with  $F_L$  and also increases linearly with frequency.  $\theta_s$  is also dependent on  $A_d$  in this region, with smaller amplitudes more negative for a given frequency, but they collapse onto a universal line. Then follows a transition region, where  $F_L$  drops rapidly and the phase passes through  $90^\circ$  (upper dashed line). We finally observe a behaviour similar to region (ii) on mica, where the frictional force decreases gradually with frequency, and converges for each  $A_d$ . Plotting  $F_L$  versus  $v_s^{\text{RMS}}$  (inset) shows the low-frequency linear regions to approximately join up with one another, implying the existence of a master curve with velocity, at least for this particular system.

great diversity of responses. It appears that separation of  $F_L$  and  $\theta_s$  with shearing length-scale (i.e.  $A_d$ ) are relatively common, at least in subsets of frequency, but a global trend of  $F_L \propto \ln(v_s^{\text{RMS}})$  is only observed for fluids confined between amorphous silica at low  $\nu_s$ . On mica, we instead observe, for both water and confined electrolyte solutions, a plateau of  $F_L$  with frequency for below  $\sim 3$  kHz and a smooth decrease above that, possibly indicating a different form of motion that is less constrained by specific interactions of the fluid with the underlying energy wells. The form of this frictional transition is well-captured by an exponential decay that bears similarities to the Stribeck curve, despite the shearing film being just molecules thick.

Throughout our experiments in section 4.2, the stage's motion has been sinusoidal and we have assumed that we can directly correlate an effective root-mean squared velocity,  $v_s^{\text{RMS}}$ , with the linear velocity of e.g. refs. [79, 85], with which we compare many of our

conclusions. This may not be the case, as, in our set up, there will clearly be stationary points in the tip’s motion when the velocity drops to zero, which may encourage pinning or nucleation of different interfacial clusters. However, this remains difficult to resolve, as we only have access to the time-averaged  $A_s$  and  $\theta_s$ , rather than the direct series.

### 4.3 Conclusions

In this chapter, we have explored two ways AFM can be used to investigate the in-plane dynamics of  $\text{H}_2\text{O}$  molecules and cations at interfaces. Small-amplitude AM-AFM has been used to track the dynamics of single rubidium ions as they diffuse in the interfacial region adjacent to a crystal of mica. We observe the adsorbed charges to have a diffusion timescale of the order of 100 ms – significantly reduced when compared with that of the bulk, and easily long enough to resolve even with our AFM’s time resolution of  $\sim 25$  ms. This dramatic reduction can be rationalised by considering the bulk diffusion to be moderated by a factor depending on the ion’s free energy of adsorption to the solid, but we find that their interaction with waters and  $\text{H}_3\text{O}^+$  is also a crucial determinant for the structure and dynamics at the Stern layer. The native hydration landscape on mica in the absence of ions is seen to evolve on much slower timescales, due to the greater affinity and proximity of the waters to the surface groups when compared to  $\text{Rb}^+$ . Our results emphasise the importance of local hydration behaviour on the organisation and kinetics of interfacial species.

We have also made use of shear-force spectroscopy to study the collective dynamics of nanoconfined water and electrolytes. By monitoring the effective frictional response of the AFM tip, as well as its shearing phase, the dynamic behaviour of the intervening fluid under different conditions, such as pressure and shear rate, can be investigated. Using a fixed frequency, we see that both ultrapure water and 150 mM KCl display strong viscoelastic behaviour, even at these timescales of  $\nu_s^{-1} = 1$  ms. When confined between the tip and mica, the fluids obey a  $\ln(\nu_s^{\text{RMS}})$  scaling behaviour, compatible with a simple, 1D interaction model. This is seen to be largely related to the absolute *lengthscale* of the oscillation relative to the mica crystal lattice. However, investigating silica-confined fluids and the use of a secondary shearing actuator reveal the system to be much more nuanced and complex. There is no global  $\nu_s^{\text{RMS}}$  scaling (apart from for small regions in  $\nu_s$  in silica-confined water), but instead we generally find that  $F_L$  is constant or even decreases as the shearing frequency is increased. The findings are rich and contain much information about the kinetics of such “2D” fluids under pressure, but do not appear to be easily quantifiable in a single model. Instead, ours is the first study, to our knowledge, that independently probes the effect of lengthscale, shearing velocity, and interfacial chemistry

on the dynamics of nanoconfined aqueous solutions.

## 4.4 Materials and methods: chapter 4

### 4.4.1 *Sample preparation*

- Ultrapure water (AnalaR NormaPur ISO 3696 Grade 3 analytical reagent) was bought from VWR (UK) and used without further filtration or purification.
- KCl and RbCl (both anhydrous, ACS reagent, purity > 99%) were bought from Sigma Aldrich and made up to 150 mM and 1 mM stock solution respectively with ultrapure water. For the experiments at varying KCl concentration (subsection 4.2.3), the stock solutions were diluted with the appropriate volume of ultrapure water.
- HCl was purchased at a dilution in water of 37 wt% (ACS reagent grade, Sigma Aldrich), diluted further to 0.5 M and used to acidify the ultrapure water from its natural pH of  $\sim 5.5$  for the experiments of Fig. 4.4
- Muscovite mica (grade IV, SPI supplies, PA, USA) was glued with epoxy to a steel support disc. It was cleaved 3 times, or until mirror smooth, before the shearing solution was pipetted onto its surface.
- The silica substrate used as part of the shear-force spectroscopy experiments was created by growing a 100 nm thick SiO<sub>2</sub> layer on top of a 76.2 mm silicon wafer. The wafer was cut with a diamond scribe and then cleaned by sonication for 10 minutes each in diluted detergent, ultrapure water, isopropyl alcohol (Fisher Chemical, certified ACS,  $\geq 99.5\%$  purity) and finally ultrapure water before drying under a stream of nitrogen. In each case, sufficient rinsing was conducted to ensure that none of the previous fluid remained before sonicating again. The silica was then glued to a steel disc using epoxy resin.

### 4.4.2 *Time-resolved AM-AFM Imaging (section 4.1)*

A commercial Cypher-ES AFM (Asylum Research, CA, USA) with a temperature-controlled Peltier stage (set to  $25 \pm 0.1^\circ\text{C}$ ) was used without further modification. The principal cantilevers used were Arrow UHF AuD (Nanosensors, Neuchâtel, Switzerland), which were driven photothermally in small-amplitude operation in order to obtain spatial resolution on the scale of single Rb<sup>+</sup> ions (see section 2.3). The sample was oscillated uniaxially at 40 Hz, and images were line-by-line flattened to produce plots such as Fig. 4.2.

### *Image processing and drift analysis*

Fig. 4.3(a) shows the partial results of the image processing that occurred prior to analysis described in the main text. This involved line-by-line flattening along the length (vertical) axis and then averaging the pixels that were associated with each mica lattice site. This averaging was achieved using a 1D Fourier analysis that also allowed each site to be tracked for the duration of the data collection period. Hence, using this procedure, the lateral drift (parallel to the scan axis) could be straightforwardly corrected for.

The drift perpendicular to the scan direction,  $D_{\perp}$ , was more difficult to quantify as it could only be observed when the scan axis “jumped” onto a different crystalline row of the mica (illustrated in Fig. 4.22). Due to the mica’s hexagonal symmetry, a jump perpendicular to the scan direction results in a vertical shift in the topography peaks by half the lattice parameter (0.26 nm). Tracking these jumps across the experiment allows an estimate of the drift velocity of the measurement, here found to be  $D_{\perp} \sim 9 \text{ pm s}^{-1}$ , allowing us to rule out drift as having any significant impact on our results for the diffusion of  $\text{Rb}^+$ .

### *4.4.3 Shear-force spectroscopy*

A Cypher-ES AFM was used as above. The principle cantilevers used were SD-R30-FM (Nanosensors, Neuchâtel, Switzerland). These had nominal flexural stiffnesses of  $k_1 = 2.8 \text{ N m}^{-1}$  and silicon tips with radii of curvature,  $r_c = 30 \text{ nm}$ . For the experiments with diamond-like-carbon (DLC) tips, Adama AD-2.8-SS cantilevers were used, with  $r_c < 5 \text{ nm}$ , and  $k_1 = 0.8 \text{ N m}^{-1}$  (the latter measured using the cantilever’s thermal spectrum and  $S_l$  (see section 2.4). Prior to each experiment, the cantilever and its holder were bathed for  $> 30$  minutes in IPA, rinsed with ultrapure water and bathed in the same, again for  $> 30$  minutes. Both were then dried and  $\sim 30 \text{ }\mu\text{l}$  of the shearing fluid was pipetted onto the cantilever. Approximately  $80 \text{ }\mu\text{l}$  of the fluid was pipetted onto the freshly-cleaved mica or cleaned silica substrates.

The basic principle of the shearing experiments is illustrated in Fig. 4.8(a) and has been described elsewhere [26, 66, 103] but will be summarised briefly here. The  $y$ -piezo of the AFM stage was driven by a sinusoidal signal of frequency  $\nu_s = 1 \text{ kHz}$ . The cantilever (aligned such that its long axis was perpendicular to the stage’s motion) was extended towards the substrate at  $1 \text{ nm s}^{-1}$  until the tip exerted a normal force of  $30 \text{ nN}$ . During this process, the torsional twisting of the cantilever due to the stage’s motion was recorded via a laser reflected on the cantilever’s end to a four-quadrant photo detector. The AFM’s internal lock-in amplifier was used to extract the amplitude and phase of the photode-

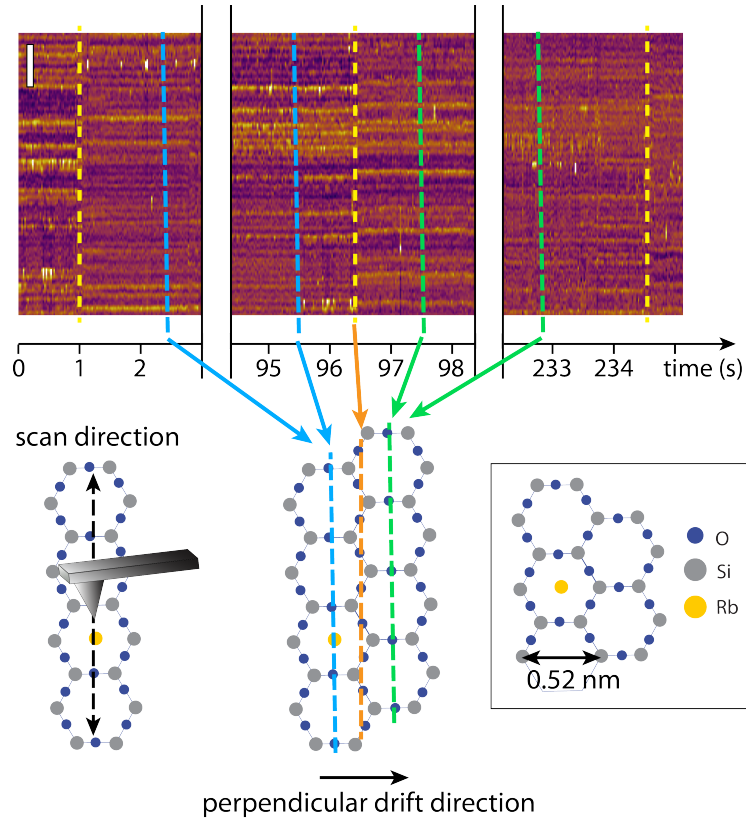


*Fig. 4.22:* Evaluation of the tip drift rate perpendicular to the scanning direction. The yellow dashed lines show transition points where the scanning tip drifts from a row of lattice sites (dashed blue lines) to the adjacent row (green dashed lines). Due to the hexagonal mica lattice, the two adjacent rows are offset by half the lattice periodicity ( $\sim 0.26$  nm). The transition (yellow dashed lines) therefore translates as a sudden vertical shift of 0.26 nm in the imaged profiles. After the transition, new sites appear occupied while previously occupied sites appear suddenly vacant, confirming that tip images a different lattice row. Assuming a drift distance of 0.52 nm between two subsequent transitions and knowing the associate time lapse  $T_{\perp}$ , it is possible to derive an upper estimate for the drift rate  $D_{\perp}$ , perpendicular to the scan direction. We found  $D_{\perp} \sim 9$  pm s $^{-1}$  ( $T_{\perp} = 117 \pm 20$  s). The value of  $T_{\perp}$  varied between measurements suggesting that the drift is not continuous and unidirectional, but oscillate around an “equilibrium” position similarly to the parallel drift. We note that this remarkable stability is, on our opinion, due to the excellent temperature control (better than 0.1 °C) and the design of the AFM. These experiments allow us to fully exclude drift as a potential influence on our results since most sequences are shorter than  $T_{\perp}$ . Drift parallel to the tip scan direction is also unimportant because the analysis procedure tracks the evolution of each site with time, and hence compensates for parallel drift. The data presented in this figure comes from a single continuous sequence acquired at 40 Hz in 1 mM RbCl. The scale bar is 3 nm.

tector’s lateral signal relative to the driving stage signal. This amplitude (in volts) was converted first into a cantilever twist in radians by the angular optical lever sensitivity,  $S_{\theta}$  (in V rad $^{-1}$ , analogous to  $S_l$  in section 2.4). The lateral force on the tip apex could then be calculated with knowledge of the cantilever geometry (thickness,  $t$ , and tip height,  $h$ ) and the lateral spring constant,  $k_L$  (in N m $^{-1}$ ), via the expression [104]:

$$F_L = k_L \frac{h + t/2}{S_\theta} \Delta V. \quad (4.4)$$

Here, the lateral photodetector signal is  $\Delta V$ . The optical lever sensitivity and lateral spring constant were found using Wagner *et al.*'s method [104] (or, equivalently, that of Mullin *et al.* [105]) to be  $S_\theta = 198 \text{ V rad}^{-1}$  and  $k_L = 203 \text{ N m}^{-1}$ , evaluated over several cantilevers. Each trace in Fig. 4.9(a), 4.10, 4.12, 4.13, 4.15 and 4.16 and 4.17 represents the average of at least 30 force curves.

For the results taken with the external actuator, the AFM's feedback loops were active in contact mode, such that a normal force of  $F_N = 20 \text{ nN}$  was applied, regardless of vertical drift. Reliable results were obtained for the  $A_s$  and  $\theta_s$  versus  $\nu_s$  plots when the SD-R30-FM tips were blunted prior to taking the measurement. This was done by scanning in contact mode while applying a harsh normal force of 350 nN for two frames of  $(3 \times 3) \mu\text{m}^2$ . Thus holding a constant  $F_N$  constant at 20 nN would not affect the tip sharpness dramatically. After this blunting procedure, the same cantilever was used to collect the data for Fig. 4.18, 4.19 and 4.21.

#### *Calibration of external shear actuator*

The fixed-frequency shearing data made use of the Cypher's internal actuator, which already had a reliable calibration. This allowed the straightforward setting of  $A_d$  to values between 0.5-5.0 nm. The external actuator had no such calibration on the nanometre scale, and so a relationship between the voltage applied to it and the subsequent shearing displacement needed to be found. This was done (in separate experiments) by operating the AFM in amplitude modulation mode above a mica sample affixed to the piezo, with the tip and sample fully immersed in 150 mM NaCl. The feedback loops were kept on, so that the tip was continually held just above the crystal, but only the external actuator was used to move the sample uniaxially at  $\nu_s = 4.88 \text{ Hz}$ . The tip thus tracked the topography of the mica lattice, which allowed the absolute distance of the piezo's motion to be found. The results were noisy and so, to improve the reliability of such a measurement, we performed line-by-line fast Fourier transforms of the scans at various applied voltages to better highlight the periodicity induced by the mica's corrugations.

The results are shown in Fig. 4.23 and a distinct peak is highlighted by dashed lines in all but two applied voltages (4.5 V and 6 V). When plotting the peak location against the applied voltage (inset), a linear relationship is found, as expected for the low shear frequencies and voltages that are used here. The gradient of this plot,  $G$ , has units of inverse pixel-Volts, and can be used to find the length calibration factor,  $F$ , by multiplying

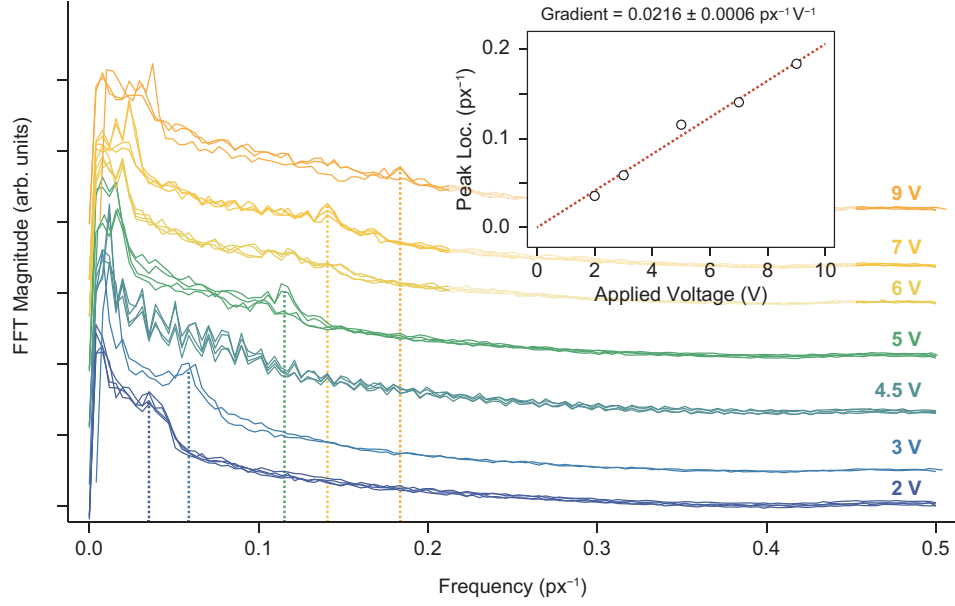


Fig. 4.23: Calibrating the shear extension of the external actuator. By operating the AFM with AM feedback, and scanning the sample laterally  $\mathcal{O}(\text{nm})$  only with the external piezo, the mica sample’s lattice induces corrugations in the measured topography. Although noisy, these can be seen as peaks in the 1D FFTs of the images, plotted here in units of inverse pixels. Increasing the voltage applied to the actuator alters the position of this peak in a linear manner (inset), which can be used to calibrate the actual motion of the sample in nanometres (see text). FFTs are offset vertically for clarity.

by the number of pixels per scan line,  $n$ , and by the lattice parameter of mica,  $a$ . That is:

$$\begin{aligned}
 F &= G [\text{px}^{-1}\text{V}^{-1}] \times n [\text{px}] \times a [\text{nm}] \\
 &= 0.0216 \times 256 \times 0.52 \\
 &= 2.74 \text{ nm V}^{-1}
 \end{aligned} \tag{4.5}$$

### High frequency shear actuator results

Although the external actuator used in subsection 4.2.6 could ostensibly access frequencies of  $\nu_0/3 \sim 110$  kHz while remaining in its linear regime, we reliably observed a dramatic change in behaviour in both shearing amplitude and phase for  $\nu_s \gtrsim 18$  kHz. These were characterised by many broad peaks in amplitude for which the absolute value was determined by  $A_d$  (see Fig. 4.24). These peaks were not well-separated in frequency and coincided with  $\theta_s$  passing through  $0^\circ$ ,  $\pm 90^\circ$  or  $\pm 180^\circ$ , and we thus associated them with mechanical “resonances” of the system, with uncertain origin.

Some of the resonances could be explained by fluid-mediated coupling between the tip and the oscillating mica sample. This was shown by recording the amplitude and phase of the cantilever’s lateral motion but with a separation of 160 nm between it and the sample (Fig. 4.25).  $A_s$  is at the noise level for all low frequencies, but above 18 kHz demonstrates

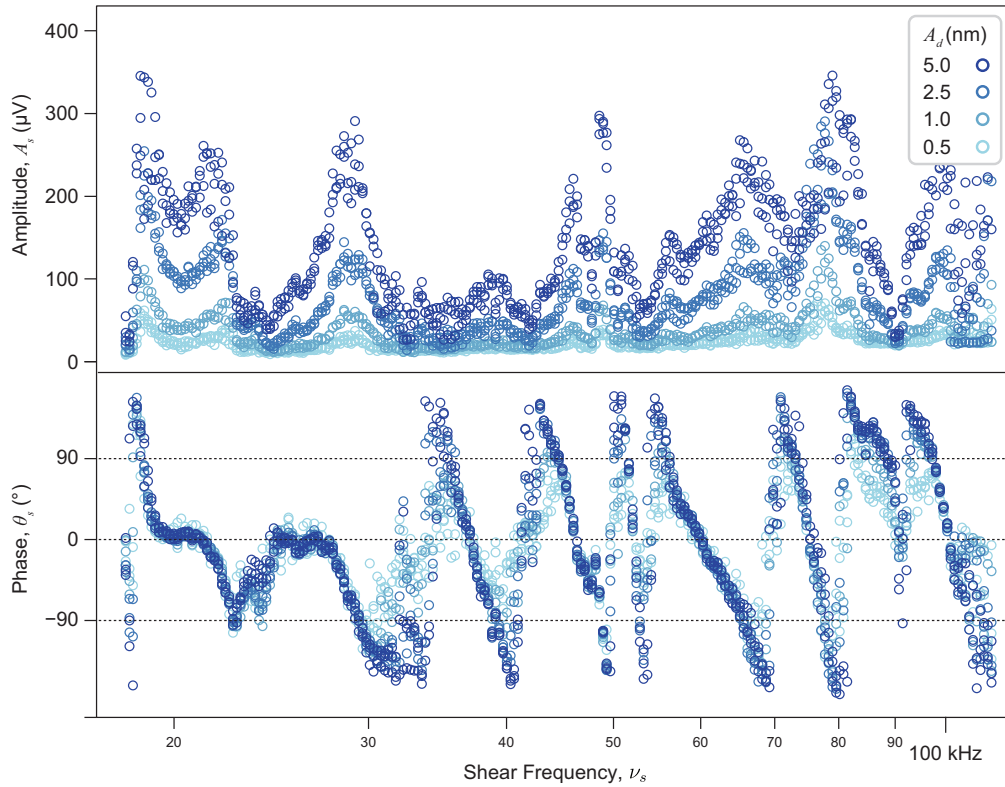
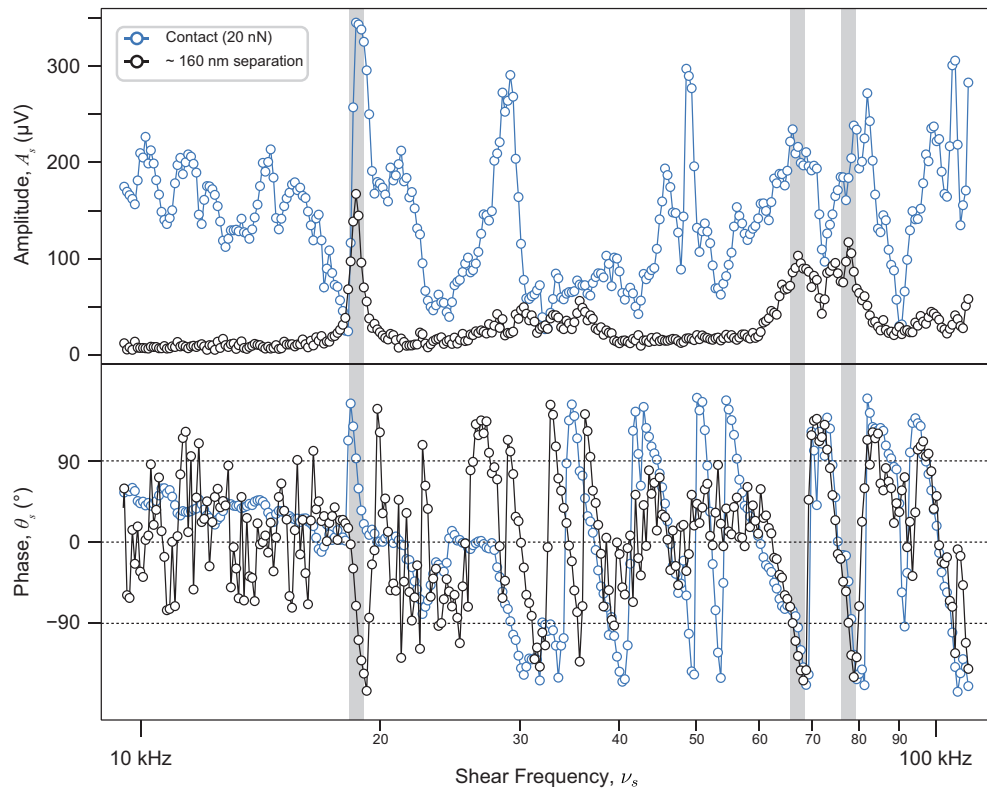


Fig. 4.24: The high frequency range (region (iii)) accessible to the external shear actuator demonstrates many “resonances” where  $A_s$  peaks and the phase moves through either  $0^\circ$ ,  $\pm 90^\circ$  or  $180^\circ$ . These are likely to be related to mechanical excitations of the system induced by the actuator’s high energy oscillations, rather than physically interesting phenomena.

peaks of similar magnitude to the measurement with  $F_N = 20$  nN (grey bars). In these regions, the  $\theta_s$  is less noisy and at the highest frequencies it is indistinguishable from the actual measurement phase. These imply that for this  $\nu_s$  range (our so-called region (iii) in Fig. 4.18), the actuator’s motion induces substantial vibrations in the system that do not reflect the dynamic behaviour of the nanoconfined fluid. In principle, these resonances could be corrected for by measuring the cantilever’s transfer function (i.e. its frequency-dependent lateral oscillations as a function of  $z$ -height), but this would require highly accurate knowledge of  $z$  down to sub-nanometre separations. As the data in e.g. Fig. 4.25 took several minutes to collect, there was finite drift in  $z$ , which rendered a complete characterisation impossible.



*Fig. 4.25:* The mechanical excitations at high frequency are emphasised by measuring the coupling between the tip and substrate at “macroscopic” separations where the intervening fluid is unconfined (at least, on a molecular scale) and should behave in a fluid manner. In these cases (black), for low  $\nu_s$ , the amplitude is at the noise level and the phase is undefined and so oscillates about  $0^\circ$ . However at higher frequencies, there are clear peaks in  $A_s$  (grey bars), of the same order of magnitude as the measurement itself (blue) and with  $\theta_s$  passing through  $-180^\circ$ . These show that at least some of the high frequency signal are in fact artefacts generated by mechanical vibrations.



## REFERENCES: CHAPTER 4

- [1] J. Peng, D. Cao, Z. He, J. Guo, P. Hapala, R. Ma, B. Cheng, J. Chen, W. J. Xie, X.-Z. Li, P. Jelínek, L.-M. Xu, Y. Q. Gao, E.-G. Wang, Y. Jiang, “The effect of hydration number on the interfacial transport of sodium ions”, *Nature* **2018**, *557*, 701–705.
- [2] J. Klimeš, D. R. Bowler, A. Michaelides, “Understanding the role of ions and water molecules in the NaCl dissolution process”, *J. Chem. Phys.* **2013**, *139*, 234702.
- [3] E. Gouaux, “Principles of Selective Ion Transport in Channels and Pumps”, *Science (80-. )*. **2005**, *310*, 1461–1465.
- [4] A. Phan, D. R. Cole, R. G. Weiß, J. Dzubiella, A. Striolo, “Confined Water Determines Transport Properties of Guest Molecules in Narrow Pores”, *ACS Nano* **2016**, *10*, 7646–7656.
- [5] C. Merlet, C. Péan, B. Rotenberg, P. A. Madden, B. Daffos, P. L. Taberna, P. Simon, M. Salanne, “Highly confined ions store charge more efficiently in supercapacitors”, *Nat. Commun.* **2013**, *4*, 2701.
- [6] R. B. Schoch, J. Han, P. Renaud, “Transport phenomena in nanofluidics”, *Rev. Mod. Phys.* **2008**, *80*, 839–883.
- [7] L. Bocquet, P. Tabeling, “Physics and technological aspects of nanofluidics”, *Lab Chip* **2014**, *14*, 3143–3158.
- [8] H. Zhang, A. A. Hassanali, Y. K. Shin, C. Knight, S. J. Singer, “The water–amorphous silica interface: Analysis of the Stern layer and surface conduction”, *J. Chem. Phys.* **2011**, *134*, 024705.
- [9] R. Hartkamp, B. Siboulet, J. F. Dufrêche, B. Coasne, “Ion-specific adsorption and electroosmosis in charged amorphous porous silica”, *Phys. Chem. Chem. Phys.* **2015**, *17*, 24683–24695.
- [10] C. J. Slevin, P. R. Unwin, “Lateral Proton Diffusion Rates along Stearic Acid Monolayers”, *J. Am. Chem. Soc.* **2000**, *122*, 2597–2602.
- [11] J. Zhang, P. R. Unwin, “Proton Diffusion at Phospholipid Assemblies”, *J. Am. Chem. Soc.* **2002**, *124*, 2379–2383.
- [12] A. Page, D. Perry, P. R. Unwin, “Multifunctional scanning ion conductance microscopy”, *Proc. R. Soc. A Math. Phys. Eng. Sci.* **2017**, *473*, 20160889.
- [13] L. H. Klausen, T. Fuhs, M. Dong, “Mapping surface charge density of lipid bilayers by quantitative surface conductivity microscopy”, *Nat. Commun.* **2016**, *7*, 12447.
- [14] D. Argyris, D. R. Cole, A. Striolo, “Ion-specific effects under confinement: The role of interfacial water”, *ACS Nano* **2010**, *4*, 2035–2042.
- [15] J. Song, T. H. Kang, M. W. Kim, S. Han, “Ion specific effects: decoupling ion–ion and ion–water interactions”, *Phys. Chem. Chem. Phys.* **2015**, *17*, 8306–8322.
- [16] S. H. Khan, E. L. Kramkowski, P. M. Hoffmann, “NaCl-Dependent Ordering and Dynamic Mechanical Response in Nanoconfined Water”, *Langmuir* **2016**, *32*, 10802–10807.
- [17] S. H. Khan, P. M. Hoffmann, “Diverging Effects of NaCl and CsCl on the Mechanical Properties of Nanoconfined Water”, *J. Electrochem. Soc.* **2018**, *165*, H114–H120.
- [18] U. Raviv, P. Laurat, J. Klein, “Time dependence of forces between mica surfaces in water and its relation to the release of surface ions”, *J. Chem. Phys.* **2002**, *116*, 5167.

- [19] M. Ricci, P. Spijker, K. Voitchovsky, “Water-induced correlation between single ions imaged at the solid-liquid interface.”, *Nat. Commun.* **2014**, *5*, 4400.
- [20] S. S. Lee, P. Fenter, C. Park, N. C. Sturchio, K. L. Nagy, “Hydrated cation speciation at the muscovite (001)-water interface”, *Langmuir* **2010**, *26*, 16647–16651.
- [21] H. Sakuma, K. Kawamura, “Structure and dynamics of water on Li<sup>+</sup>, Na<sup>+</sup>, K<sup>+</sup>, Cs<sup>+</sup>, H<sub>3</sub>O<sup>+</sup>-exchanged muscovite surfaces: A molecular dynamics study”, *Geochim. Cosmochim. Acta* **2011**, *75*, 63–81.
- [22] R. W. Impey, P. A. Madden, I. R. McDonald, “Hydration and mobility of ions in solution”, *J. Phys. Chem.* **1983**, *87*, 5071–5083.
- [23] B. S. Swartzentruber, “Direct Measurement of Surface Diffusion Using Atom-Tracking Scanning Tunneling Microscopy”, *Phys. Rev. Lett.* **1996**, *76*, 459–462.
- [24] S. Koneshan, J. C. Rasaiah, R. M. Lynden-Bell, S. H. Lee, “Solvent Structure, Dynamics, and Ion Mobility in Aqueous Solutions at 25 °C”, *J. Phys. Chem. B* **1998**, *102*, 4193–4204.
- [25] S. S. Lee, P. Fenter, K. L. Nagy, N. C. Sturchio, “Real-time observation of cation exchange kinetics and dynamics at the muscovite-water interface”, *Nat. Commun.* **2017**, *8*, 15826.
- [26] C. Cafolla, K. Voitchovsky, “Lubricating properties of single metal ions at interfaces”, *Nanoscale* **2018**, *10*, 11831–11840.
- [27] L. T. Kong, L. J. Lewis, “Transition state theory of the preexponential factors for self-diffusion on Cu, Ag, and Ni surfaces”, *Phys. Rev. B* **2006**, *74*, 073412.
- [28] C. Park, P. Fenter, K. Nagy, N. Sturchio, “Hydration and Distribution of Ions at the Mica-Water Interface”, *Phys. Rev. Lett.* **2006**, *97*, 016101.
- [29] M. Ricci, W. Trewby, C. Cafolla, K. Voitchovsky, “Direct observation of the dynamics of single metal ions at the interface with solids in aqueous solutions”, *Sci. Rep.* **2017**, *7*, 43234.
- [30] C. Park, P. a. Fenter, N. C. Sturchio, K. L. Nagy, “Thermodynamics, interfacial structure, and pH hysteresis of Rb<sup>+</sup> and Sr<sup>2+</sup> adsorption at the muscovite (001)-solution interface”, *Langmuir* **2008**, *24*, 13993–14004.
- [31] R. M. Pashley, “DLVO and hydration forces between mica surfaces in Li<sup>+</sup>, Na<sup>+</sup>, K<sup>+</sup>, and Cs<sup>+</sup>-electrolyte solutions: A correlation of double-layer and hydration forces with surface cation exchange properties”, *J. Colloid Interface Sci.* **1981**, *83*, 531–546.
- [32] S. S. Lee, P. Fenter, K. L. Nagy, N. C. Sturchio, “Monovalent Ion Adsorption at the Muscovite (001)-Solution Interface: Relationships among Ion Coverage and Speciation, Interfacial Water Structure, and Substrate Relaxation”, *Langmuir* **2012**, *28*, 8637–8650.
- [33] P. J. Scales, F. Grieser, T. W. Healy, “Electrokinetics of the Muscovite Mica-Aqueous Solution Interface”, *Langmuir* **1990**, *6*, 582–589.
- [34] C. Zhao, D. Ebeling, I. Siretanu, D. van den Ende, F. Mugele, “Extracting local surface charges and charge regulation behavior from atomic force microscopy measurements at heterogeneous solid-electrolyte interfaces”, *Nanoscale* **2015**, *7*, 16298–16311.
- [35] B. M. Lowe, C.-K. Skylaris, N. G. Green, “Acid-base dissociation mechanisms and energetics at the silica-water interface: An activationless process.”, *J. Colloid Interface Sci.* **2015**, *451*, 231–44.
- [36] S. M. R. Akrami, H. Nakayachi, T. Watanabe-Nakayama, H. Asakawa, T. Fukuma, “Significant improvements in stability and reproducibility of atomic-scale atomic force microscopy in liquid.”, *Nanotechnology* **2014**, *25*, 455701.
- [37] L. Cheng, P. Fenter, K. L. Nagy, M. L. Schlegel, N. C. Sturchio, “Molecular-Scale Density Oscillations in Water Adjacent to a Mica Surface”, *Phys. Rev. Lett.* **2001**, *87*, 156103.
- [38] H. J. Bakker, “Structural dynamics of aqueous salt solutions”, *Chem. Rev.* **2008**, *108*, 1456–1473.
- [39] D. E. Moilanen, N. E. Levinger, D. B. Spry, M. D. Fayer, “Confinement or the nature of the interface? Dynamics of nanoscopic water”, *J. Am. Chem. Soc.* **2007**, *129*, 14311–14318.
- [40] V. Parsegian, T. Zemb, “Hydration forces: Observations, explanations, expectations, questions”, *Curr. Opin. Colloid Interface Sci.* **2011**, *16*, 618–624.

- [41] S. H. Park, G. Sposito, “Structure of Water Adsorbed on a Mica Surface”, *Phys. Rev. Lett.* **2002**, *89*, 085501.
- [42] S. Pronk, E. Lindahl, P. M. Kasson, “Dynamic heterogeneity controls diffusion and viscosity near biological interfaces”, *Nat. Commun.* **2014**, *5*, 1–7.
- [43] K. Kimura, S. Ido, N. Oyabu, K. Kobayashi, Y. Hirata, T. Imai, H. Yamada, “Visualizing water molecule distribution by atomic force microscopy”, *J. Chem. Phys.* **2010**, *132*, 194705.
- [44] K. Miyazawa, M. Watkins, A. L. Shluger, T. Fukuma, “Influence of ions on two-dimensional and three-dimensional atomic force microscopy at fluorite–water interfaces”, *Nanotechnology* **2017**, *28*, 245701.
- [45] D. Laage, T. Elsaesser, J. T. Hynes, “Water Dynamics in the Hydration Shells of Biomolecules”, *Chem. Rev.* **2017**, *117*, 10694–10725.
- [46] M. Ricci, P. Spijker, F. Stellacci, J.-F. Molinari, K. Voïtchovsky, “Direct Visualization of Single Ions in the Stern Layer of Calcite”, *Langmuir* **2013**, *29*, 2207–2216.
- [47] K. Miyazawa, N. Kobayashi, M. Watkins, A. L. Shluger, K.-i. Amano, T. Fukuma, “A relationship between three-dimensional surface hydration structures and force distribution measured by atomic force microscopy”, *Nanoscale* **2016**, *8*, 7334–42.
- [48] T. Fukuma, B. Reischl, N. Kobayashi, P. Spijker, F. F. Canova, K. Miyazawa, A. S. Foster, “Mechanism of atomic force microscopy imaging of three-dimensional hydration structures at a solid-liquid interface”, *Phys. Rev. B* **2015**, *92*, 155412.
- [49] K. Voïtchovsky, J. J. Kuna, S. A. Contera, E. Tosatti, F. Stellacci, “Direct mapping of the solid-liquid adhesion energy with subnanometre resolution.”, *Nat. Nanotechnol.* **2010**, *5*, 401–405.
- [50] W. H. Briscoe, “Aqueous boundary lubrication: Molecular mechanisms, design strategy, and terra incognita”, *Curr. Opin. Colloid Interface Sci.* **2017**, *27*, 1–8.
- [51] M. Ricci, R. A. Quinlan, K. Voïtchovsky, “Sub-nanometre mapping of the aquaporin–water interface using multifrequency atomic force microscopy”, *Soft Matter* **2017**, *13*, 187–195.
- [52] H. Stanley, S. Buldyrev, P. Kumar, F. Mallamace, M. Mazza, K. Stokely, L. Xu, G. Franzese, “Water in nanoconfined and biological environments”, *J. Non. Cryst. Solids* **2011**, *357*, 629–640.
- [53] R. Sorkin, N. Kampf, Y. Dror, E. Shimoni, J. Klein, “Origins of extreme boundary lubrication by phosphatidylcholine liposomes”, *Biomaterials* **2013**, *34*, 5465–5475.
- [54] R. Sorkin, Y. Dror, N. Kampf, J. Klein, “Mechanical Stability and Lubrication by Phosphatidylcholine Boundary Layers in the Vesicular and in the Extended Lamellar Phases”, *Langmuir* **2014**, *30*, 5005–5014.
- [55] J. Sotres, T. Arnebrant, “Experimental Investigations of Biological Lubrication at the Nanoscale: The Cases of Synovial Joints and the Oral Cavity”, *Lubricants* **2013**, *1*, 102–131.
- [56] G. R. Medders, F. Paesani, “Water Dynamics in Metal–Organic Frameworks: Effects of Heterogeneous Confinement Predicted by Computational Spectroscopy”, *J. Phys. Chem. Lett.* **2014**, *5*, 2897–2902.
- [57] M. D. Scanlon, J. Strutwolf, A. Blake, D. Iacopino, A. J. Quinn, D. W. M. Arrigan, “Ion-Transfer Electrochemistry at Arrays of Nanointerfaces between Immiscible Electrolyte Solutions Confined within Silicon Nitride Nanopore Membranes”, *Anal. Chem.* **2010**, *82*, 6115–6123.
- [58] B. Moeremans, H.-W. Cheng, Q. Hu, H. F. Garces, N. P. Pature, F. U. Renner, M. Valtiner, “Lithium-ion battery electrolyte mobility at nano-confined graphene interfaces”, *Nat. Commun.* **2016**, *7*, 12693.
- [59] R. Tivony, S. Safran, P. Pincus, G. Silbert, J. Klein, “Charging dynamics of an individual nanopore”, *Nat. Commun.* **2018**, *9*, 4203.
- [60] M. Erko, G. H. Findenegg, N. Cade, A. G. Michette, O. Paris, “Confinement-induced structural changes of water studied by Raman scattering”, *Phys. Rev. B* **2011**, *84*, 104205.
- [61] G. H. Findenegg, S. Jähnert, D. Akcakayiran, A. Schreiber, “Freezing and Melting of Water Confined in Silica Nanopores”, *ChemPhysChem* **2008**, *9*, 2651–2659.
- [62] P. T. Cummings, H. Docherty, C. R. Iacovella, J. K. Singh, “Phase transitions in nanoconfined fluids: The evidence from simulation and theory”, *AIChE J.* **2010**, *56*, NA–NA.

- [63] A. Schlaich, E. W. Knapp, R. R. Netz, “Water Dielectric Effects in Planar Confinement”, *Phys. Rev. Lett.* **2016**, *117*, 048001.
- [64] J. Hou, D. H. Veeregowda, J. de Vries, H. C. Van der Mei, H. J. Busscher, “Structured free-water clusters near lubricating surfaces are essential in water-based lubrication”, *J. R. Soc. Interface* **2016**, *13*, 20160554.
- [65] S. H. Khan, G. Matei, S. Patil, P. M. Hoffmann, “Dynamic Solidification in Nanoconfined Water Films”, *Phys. Rev. Lett.* **2010**, *105*, 106101.
- [66] D. Ortiz-Young, H.-C. Chiu, S. Kim, K. Voitchovsky, E. Riedo, “The interplay between apparent viscosity and wettability in nanoconfined water”, *Nat. Commun.* **2013**, *4*, 2482.
- [67] G. Tocci, L. Joly, A. Michaelides, “Friction of Water on Graphene and Hexagonal Boron Nitride from Ab Initio Methods: Very Different Slippage Despite Very Similar Interface Structures”, *Nano Lett.* **2014**, *14*, 6872–6877.
- [68] E. Chiavazzo, M. Fasano, P. Asinari, P. Decuzzi, “Scaling behaviour for the water transport in nanoconfined geometries”, *Nat. Commun.* **2014**, *5*, 4565.
- [69] K. Falk, F. Sedlmeier, L. Joly, R. R. Netz, L. Bocquet, “Molecular origin of fast water transport in carbon nanotube membranes: Superlubricity versus curvature dependent friction”, *Nano Lett.* **2010**, *10*, 4067–4073.
- [70] T.-D. Li, H.-C. Chiu, D. Ortiz-Young, E. Riedo, “Nanorheology by atomic force microscopy”, *Rev. Sci. Instrum.* **2014**, *85*, 123707.
- [71] J. N. Israelachvili, *Intermolecular and Surface Forces*, Third, Elsevier, **2011**.
- [72] Q. Li, Y. Dong, D. Perez, A. Martini, R. W. Carpick, “Speed Dependence of Atomic Stick-Slip Friction in Optimally Matched Experiments and Molecular Dynamics Simulations”, *Phys. Rev. Lett.* **2011**, *106*, 126101.
- [73] Y. Lei, Y. Leng, “Stick-slip friction and energy dissipation in boundary lubrication”, *Phys. Rev. Lett.* **2011**, *107*, 1–5.
- [74] K. Tian, N. N. Gosvami, D. L. Goldsby, Y. Liu, I. Szlufarska, R. W. Carpick, “Load and Time Dependence of Interfacial Chemical Bond-Induced Friction at the Nanoscale”, *Phys. Rev. Lett.* **2017**, *118*, 076103.
- [75] U. D. Schwarz, H. Hölscher, “Exploring and Explaining Friction with the Prandtl–Tomlinson Model”, *ACS Nano* **2016**, *10*, 38–41.
- [76] M. Urbakh, J. Klafter, D. Gourdon, J. Israelachvili, “The nonlinear nature of friction”, *Nature* **2004**, *430*, 525–528.
- [77] A. Vanossi, N. Manini, M. Urbakh, S. Zapperi, E. Tosatti, “Colloquium: Modeling friction: From nanoscale to mesoscale”, *Rev. Mod. Phys.* **2013**, *85*, 529–552.
- [78] E. Gnecco, R. Bennewitz, T. Gyalog, C. Loppacher, M. Bammerlin, E. Meyer, H.-J. Güntherodt, “Velocity Dependence of Atomic Friction”, *Phys. Rev. Lett.* **2000**, *84*, 1172–1175.
- [79] E. Riedo, E. Gnecco, R. Bennewitz, E. Meyer, H. Brune, “Interaction Potential and Hopping Dynamics Governing Sliding Friction”, *Phys. Rev. Lett.* **2003**, *91*, 084502.
- [80] E. Riedo, E. Gnecco, “Thermally activated effects in nanofriction”, *Nanotechnology* **2004**, *15*, S288–S292.
- [81] D. Perez, Y. Dong, A. Martini, A. F. Voter, “Rate theory description of atomic stick-slip friction”, *Phys. Rev. B* **2010**, *81*, 245415.
- [82] K. Tian, D. L. Goldsby, R. W. Carpick, “Rate and State Friction Relation for Nanoscale Contacts: Thermally Activated Prandtl–Tomlinson Model with Chemical Aging”, *Phys. Rev. Lett.* **2018**, *120*, 186101.
- [83] M. Ratoi, H. A. Spikes, “Lubricating Properties of Aqueous Surfactant Solutions”, *Tribol. Trans.* **1999**, *42*, 479–486.
- [84] J. Klein, “Hydration lubrication”, *Friction* **2013**, *1*, 1–23.
- [85] L. Ma, A. Gaisinskaya-Kipnis, N. Kampf, J. Klein, “Origins of hydration lubrication”, *Nat. Commun.* **2015**, *6*, 6060.

- [86] B. C. Donose, I. U. Vakarelski, K. Higashitani, “Silica Surfaces Lubrication by Hydrated Cations Adsorption from Electrolyte Solutions”, *Langmuir* **2005**, *21*, 1834–1839.
- [87] A. Gaisinskaya-Kipnis, L. Ma, N. Kampf, J. Klein, “Frictional Dissipation Pathways Mediated by Hydrated Alkali Metal Ions”, *Langmuir* **2016**, *32*, 4755–4764.
- [88] D. Jing, Y. Pan, D. Li, X. Zhao, B. Bhushan, “Effect of Surface Charge on the Nanofriction and Its Velocity Dependence in an Electrolyte Based on Lateral Force Microscopy”, *Langmuir* **2017**, *33*, 1792–1798.
- [89] S. Cervený, F. Mallamace, J. Swenson, M. Vogel, L. Xu, “Confined Water as Model of Supercooled Water”, *Chem. Rev.* **2016**, *116*, 7608–7625.
- [90] P. J. Feibelman, “Viscosity of Ultrathin Water Films Confined between Alumina Surfaces of Kaolinite: Ab Initio Simulations”, *J. Phys. Chem. C* **2013**, *117*, 6088–6095.
- [91] A. Schlaich, J. Kappler, R. R. Netz, “Hydration Friction in Nanoconfinement: From Bulk via Interfacial to Dry Friction”, *Nano Lett.* **2017**, *17*, 5969–5976.
- [92] P.-A. Thorén, A. S. de Wijn, R. Borgani, D. Forchheimer, D. B. Haviland, “Imaging high-speed friction at the nanometer scale”, *Nat. Commun.* **2016**, *7*, 13836.
- [93] M. Antognozzi, A. D. L. Humphris, M. J. Miles, “Observation of molecular layering in a confined water film and study of the layers viscoelastic properties”, *Appl. Phys. Lett.* **2001**, *78*, 300.
- [94] Y. Marcus, “Effect of ions on the structure of water: Structure making and breaking”, *Chem. Rev.* **2009**, *109*, 1346–1370.
- [95] T.-D. Li, E. Riedo, “Nonlinear Viscoelastic Dynamics of Nanoconfined Wetting Liquids”, *Phys. Rev. Lett.* **2008**, *100*, 106102.
- [96] I. Siretanu, D. Ebeling, M. P. Andersson, S. L. S. Stipp, A. Philipse, M. C. Stuart, D. van den Ende, F. Mugele, “Direct observation of ionic structure at solid-liquid interfaces: a deep look into the Stern Layer.”, *Sci. Rep.* **2014**, *4*, 4956.
- [97] Adama Innovations Product Home, accessed 2018-12-17, <http://www.adama.tips/products/>.
- [98] G. Vigil, Z. Xu, S. Steinberg, J. Israelachvili, “Interactions of Silica Surfaces”, *J. Colloid Interface Sci.* **1994**, *165*, 367–385.
- [99] D. J. Bonthuis, R. R. Netz, “Beyond the Continuum: How Molecular Solvent Structure Affects Electrostatics and Hydrodynamics at Solid–Electrolyte Interfaces”, *J. Phys. Chem. B* **2013**, *117*, 11397–11413.
- [100] D. J. Bonthuis, S. Gekle, R. R. Netz, “Dielectric profile of interfacial water and its effect on double-layer capacitance”, *Phys. Rev. Lett.* **2011**, *107*, 1–5.
- [101] H. Spikes, W. Tysoe, “On the Commonality Between Theoretical Models for Fluid and Solid Friction, Wear and Tribochemistry”, *Tribol. Lett.* **2015**, *59*, 21.
- [102] Physik Instrumente UK Product page, accessed 2019-05-11, <https://www.physikinstrumente.co.uk/en/products/piezoelectric-transducers-actuators/shear-actuators/p-111-p-151-pica-shear-actuators-102900/#specification>.
- [103] K. Voitchovsky, “Effect of temperature on the viscoelastic properties of nano-confined liquid mixtures”, *Nanoscale* **2016**, *8*, 17472–17482.
- [104] K. Wagner, P. Cheng, D. Vezenov, “Noncontact Method for Calibration of Lateral Forces in Scanning Force Microscopy”, *Langmuir* **2011**, *27*, 4635–4644.
- [105] N. Mullin, J. K. Hobbs, “A non-contact, thermal noise based method for the calibration of lateral deflection sensitivity in atomic force microscopy”, *Rev. Sci. Instrum.* **2014**, *85*, 113703.



## 5.0 IONIC IMPACT UPON BIOMIMETIC MEMBRANES

In this chapter, we characterise the interactions of a model anionic lipid membrane (DPPA) with the monovalent cations  $\text{Na}^+$ ,  $\text{K}^+$  and  $\text{Rb}^+$  using electrophoresis, molecular dynamics simulations and high-resolution AM-AFM. These techniques provide complementary information about the molecular-level structuring of single ions at the electrolyte-lipid interface, the effective energy barriers that modify the ions' kinetics, and how the mechanical properties of the bilayer are strongly modified at the Ångström lengthscale as a result.

We begin with electrophoretic measurements of the potential at the slip plane ( $\zeta$ -potential) of lipid vesicles from which, with continuum-level models of the ionic distribution (subsection 1.2.1), the global binding strength of each cation to the lipid headgroups,  $K$ , is calculated. These are found to follow a Hofmeister-like ordering of  $K_{\text{Na}^+} > K_{\text{K}^+} > K_{\text{Rb}^+}$  and the data also suggest that there is an attractive correlative energy between ions that aids their binding, emphasising the need for an interrogation that goes beyond just mean field assumptions. High resolution AFM scans as well as small-amplitude spectroscopy confirm that the variation in binding constant results from the distinct structure of the ions at the interface. In fact,  $\text{Na}^+$  and  $\text{K}^+$  form stable 2D networks, which are shown by the MD simulations to be strongly correlated with the organisation of the water in each case. The long timescale of the AFM scans allows further interrogation of the network kinetics within the Stern layer and demonstrate that outer-sphere ions are correlated with one another, with an effective energy well of  $-0.4 k_{\text{B}}T/\text{ion}$ . This compliments the similar result acquired by electrophoresis, although the energies relate to subtly different modes of correlation. Finally, using a novel AFM technique, we conclude, with similar Ångström-level resolution, that these outer-sphere networks actively reduce the membrane stiffness *via* their water-mediated interactions. The work builds upon the recognition in chapter 4 that the presence of an interface hinders the diffusion of ions and increases the importance of water-mediated interactions.

## 5.1 Coordination of ions at lipid headgroups

Biological systems are exquisitely sensitive to electrostatic interactions, partly because of the ubiquity of charged or polar interfaces and partly due to the quantity and species of ions dissolved within the aqueous media. This manifests itself in, for example, the organisation of DNA [1] and the folding and hydration of proteins [2] – the latter being the original focus of the experiments that discovered the Hofmeister ordering of ions [3]. The significance of ionic interactions is perhaps most obvious in the case of cell membranes, where electrostatic gradients are actively maintained [4], and ions can initiate signaling cascades [5] as well as modulate tension [6], which can itself strongly influence membrane gating processes [7]. Clearly these effects are dependent on the specific interactions of ions with the membranes in question, as well as the membrane's local, dynamic response. Experimentally, isolating and quantifying ionic interactions *in vivo* remains difficult due to the sheer diversity of molecular species and the complex feedback systems between them. For this reason, it had previously been assumed that the vast majority of cell function was carried out by proteins, with lipids remaining passive and structural (known as the lipid-mosaic model). However, this perspective has been challenged in recent years [8] by the understanding that lipids can intrinsically drive organisational [9], functional [10] and dynamic [11] processes in membranes and thus their specific interaction with ions is of great importance.

Cell membranes are composed of many types of lipid, but the most prevalent by far are phospholipids; amphiphilic molecules composed of two hydrophobic acyl chains connected *via* a glycerol backbone to a hydrophilic headgroup (see Fig. 5.1 for a schematic bilayer and representative lipid) [12]. Many lipids found in bacteria and the inner leaflet of mammalian membranes are negatively charged [7], and even those that are globally neutral tend to produce a negative surface potential [13]. Thus they strongly perturb the waters and ions in their vicinity, as partially discussed in section 1.3. The specific details of ion complexation are sensitive to local, molecular-scale perturbations in the hydration landscape of lipid bilayers, but such binding events can simultaneously have consequences for global membrane properties such as stiffness and surface tension. Thus the response of lipids to ions in solution has received a great deal of attention with techniques that focus on a wide range of lengthscales.

Many independent techniques have shown the propensity of ions to alter the motion and organisation of lipids globally. For example, fluorescence recovery after photo-bleaching (FRAP) [14] and fluorescence correlation spectroscopy (FCS) [15] have quantified the diffusion coefficients of lipids within membranes, showing that ions tend to retard their

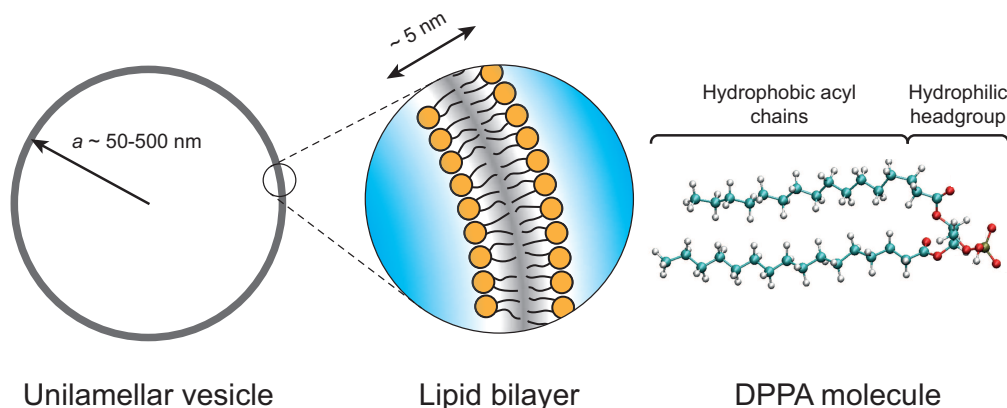


*Fig. 5.1:* The varying scales of lipid bilayers. In solution, lipids form large membranes which extend over hundreds of nanometres to microns (left), at which scale they can be treated as thin, 2D films with a well-defined stiffness and compressibility. At smaller scales (schematic, centre), the finite thickness of the bilayer and edge effects must be taken into account when describing membrane behaviour. Finally, at the single-lipid scale, the specific inter- and intra-molecular interactions of the headgroup with other lipids, waters and solutes become significant in determining the interfacial structure and bilayer properties. This is highlighted by the structure of dipalmitoyl phosphatidic acid (DPPA), right, which is used as a model lipid in this study. Its headgroup and carbonyl oxygens enable diverse hydrogen bonded networks to form. Carbons are shown in cyan, hydrogens in white, oxygens in red and phosphorus in gold.

dynamics by forming hydrogen-bonded networks. Ions can further structure lipid bilayers by inducing spontaneous phase-separation [16–19], vesicle tubulation [20], aggregation [21] and budding [22], which provides an intriguing mechanism for cells to induce membrane ordering with little energy cost. Despite the fact that the ionic composition of biological electrolytes varies dramatically, with e.g. sodium and potassium primarily located in the extra- and intracellular fluid of mammalian cells respectively, larger-scale experimental studies often focus solely on the former ion, with little acknowledgement of Hofmeister effects such as those discussed in chapter 1.

At the nanoscale, MD simulations agree that smaller cations penetrate deep into the membrane of both zwitterionic and negatively charged lipids [15, 23, 24], associating either with phosphate or carbonyl groups, often with little significant anionic adsorption. This intimate cationic interaction tends to modify headgroup orientation and bilayer thickness [25], as well as induce a great variety of lipid-ion, lipid-water and lipid-lipid complexes to form, depending on the lipid charge [24], ion valency [26] and physical membrane properties [6, 14]. In particular, there is mounting evidence that these cations are able to form 2D networks within the membrane’s Stern layer, despite their similar electric charge [24, 27]. This is likely to be mediated by hydration interactions: lipid-ion binding is an endothermic process (i.e. driven by the entropy of liberated waters) [6, 28, 29] that alters the

activation energy of water diffusion by the order of  $0.5 k_B T$  [30], and similar hydration-mediated networks have been directly observed on mica [31]. However, the nature of these networks has remained difficult to study directly, and their stability and dynamics on long timescales are still uncertain. This is especially pertinent considering the non-trivial energetics of charge transport along membranes [32–34] which may play a crucial role in bio-energetics [35].

In general, we must take a multi-scale approach to the interactions of bio-membranes with salts; in order to understand the larger-scale biological implications such as signalling and bilayer re-modelling, the continuum and molecular levels must be considered simultaneously and over long timescales. Further, the specific-ion effects that so commonly influence the global properties of lipid membranes [4, 21, 28, 36–38] must be assimilated at the scale of *single* ions and lipid headgroups. To address this, we make use of model lipid bilayers composed of purified dipalmitoyl phosphatidic acid (DPPA, structure illustrated in Fig. 5.1, right), the negatively-charged headgroup of which plays a key role in signal transduction and pH sensing [5, 11]. These roles are dependent on the complex hydrogen bonded network generated between neighbouring headgroups but also within the phosphate group itself and as such, the DPPA-electrolyte interface is sensitive to the local concentration of ions and water, as well as the global potential. Additionally, anionic lipids such as these are crucial for mediating protein interactions in the cytosol and signalling cell oncogenesis [7], and their strong electrostatic profile is likely to affect their mechanical response to ion adsorption [39].

## 5.2 Global interactions of alkali cations with DPPA; electrophoresis and continuum models

We first characterise the continuum electrostatic changes of small unilamellar vesicles (SUVs) of DPPA in varying aqueous alkali-chloride solutions using electrophoresis [40]. In brief, this consists of applying a voltage,  $V$ , to a solution of lipid vesicles (in our case of radius  $a \sim 60$  nm) and tracking their subsequent velocity,  $v$ , generated by this potential. The technique has variously been used to measure headgroup restructuring in response to ions [41], vesicle-size dependence of binding [42], as well as specific-ion interactions with lipids [37], thus making it well placed to investigate the DPPA-electrolyte interface.

### 5.2.1 Vesicle $\zeta$ -potential and charge density in electrolyte solutions

The electrophoretic mobility of a particle,  $\mu$ , is defined as the ratio of its velocity to the applied field and is assumed to be proportional to the potential at the vesicles' slip plane,

$\zeta$  as:

$$\mu \equiv \frac{v}{V} = \frac{2\varepsilon_0\varepsilon f(\kappa a)}{3\eta}\zeta, \quad (5.1)$$

where  $\eta$  and  $\kappa^{-1}$  are the solution's viscosity and Debye length, as defined in chapter 1. The relative size of the electric double layer and the vesicles is accounted for by the Henry function,  $f(\kappa a)$ . If the Debye length is much smaller than the radius (Smoluchowski limit,  $\kappa a \gg 1$ ),  $f(\kappa a) = 1.0$ , whereas if the reverse is true (Hückel limit,  $\kappa a \ll 1$ ), then  $f(\kappa a)$  tends to 1.5. As the Debye length strongly depends on the solution's ionic strength,  $I$ , which was varied as part of the experiment, neither of these limits was valid across the entire range of concentrations tested ( $0 \geq I \geq 145$  mM), and so a smooth function was assumed in a similar fashion to Maity *et al.* [29]:

$$f(\kappa a) = \begin{cases} 1.0, & \text{for } \kappa a < 1. \\ \frac{1}{6} \log(\kappa a) + 1, & \text{for } 1 < \kappa a < 1000. \\ 1.5, & \text{for } \kappa a > 1000. \end{cases} \quad (5.2)$$

Inherent in the derivation of equation 5.1 are the assumptions that neither the viscosity nor the dielectric constant of the solution change as a function of distance from the interface [37], neither of which are necessarily obvious (see discussion in chapter 1).

The  $\zeta$ -potential of DPPA vesicles of radius  $\sim 60$  nm was thus measured (see section 5.6) in aqueous solutions of NaCl, KCl and RbCl at different concentrations in order to probe the continuum changes these ions made to lipids' electrostatics. The results are presented in Fig. 5.2. As expected, the vesicles have a negative potential in pure water, and increasing the ionic strength serves to neutralise this *via* electrostatic screening and cation binding. At high concentrations, this effect saturates and the potential does not change dramatically. From ionic strengths of  $> 25$  mM, the extent of the change in  $\zeta$  is strongly dependent on the alkali species in solution, with  $\text{Na}^+$  having the strongest effect, followed by  $\text{K}^+$  and  $\text{Rb}^+$ . This result implies that the smaller an ion is, the greater its rate of accumulation on the lipid headgroups, in agreement with results obtained on similar negatively-charged and zwitterionic lipid systems [28, 29, 38, 43].

### 5.2.2 Calculation of cation binding constants

The variance between each ion's rate of accumulation can be quantified by the effective binding constant,  $K = [\text{PA} \cdot \text{M}]/[\text{PA}^-][\text{M}^+]$ , that describes the ratio of associated ( $[\text{PA} \cdot \text{M}]$ ) and disassociated species ( $[\text{PA}^-]$ ,  $[\text{M}^+]$ ) at the interface. This was achieved by calculating the relative coverage of charges adsorbed on the membrane at each bulk concentration

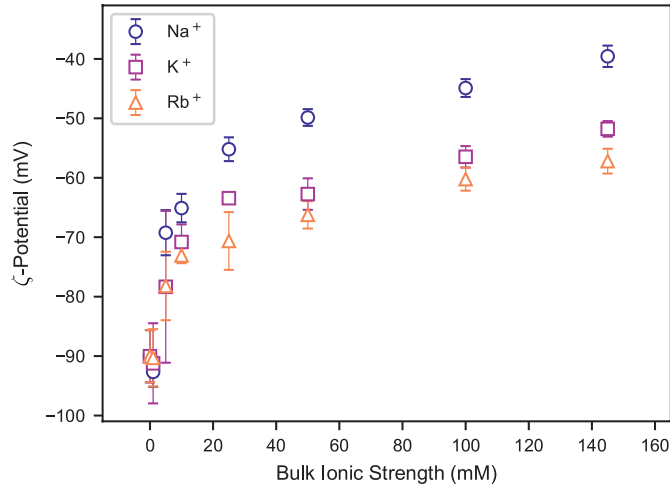


Fig. 5.2: Electrophoretic measurements quantify the global behaviour of ions near the surface of DPPA vesicles.  $\zeta$ -potential of  $\sim 120$  nm DPPA vesicles in varying concentrations of NaCl, KCl and RbCl solutions. As the bulk ionic strength is increased, the negative charge on the vesicles begins to be neutralised, but to an extent that depends upon the cation in solution.

and fitting this to an adsorption model. Firstly, the  $\zeta$ -potential values are assumed to correspond to the slip plane above the lipid headgroups at  $z = 2$  Å, in accordance with a condensed Stern layer that is appropriate for such vesicle systems [37, 44]. Then, the corresponding surface potentials,  $\psi_0$ , are extrapolated by inverting equation 1.4, and the equivalent net charge density,  $\sigma_{\text{net}}$ , obtained from equation 1.2. The charge density due solely to bound ions is simply found from  $\sigma_{\text{ion}} = \sigma_{\text{net}} - \sigma_{\text{bare}}$ . Here,  $\sigma_{\text{bare}}$  is the predicted charge density if there is no intrinsic binding of ions – i.e. using equation 1.2 and holding  $\psi_0$  constant at its value in ultrapure water. Finally, the total number of bound ions is converted to a fractional coverage,  $\Gamma$ , by

$$\Gamma = \frac{\sigma_{\text{ion}}}{e\rho_l}, \quad (5.3)$$

where  $\rho_l \sim 4 \times 10^{18} \text{ m}^{-2}$  is the areal density of the lipids in the bilayer as calculated from the AFM topograph FFTs in section 5.3. The results of this are shown in Fig. 5.3(a), and a similar trend to that of Fig. 5.2 is observed, with sodium showing a much greater coverage of the lipids for a given bulk concentration than potassium or rubidium respectively.

Given the adsorption behaviour of the ions to the lipid headgroups, a model can be used to extract effective interaction parameters between the two. A common choice is the Langmuir isotherm [45], which assumes that particles in solution bind as a non-interacting 2D gas with a single binding constant,  $K$ . We instead make use of the so-called Frumkin-Fowler-Guggenheim (FFG) isotherm [31, 45], which builds on the Langmuir model by allowing for ion-ion interactions *via* a correlation energy,  $E_c$ , and takes the form:

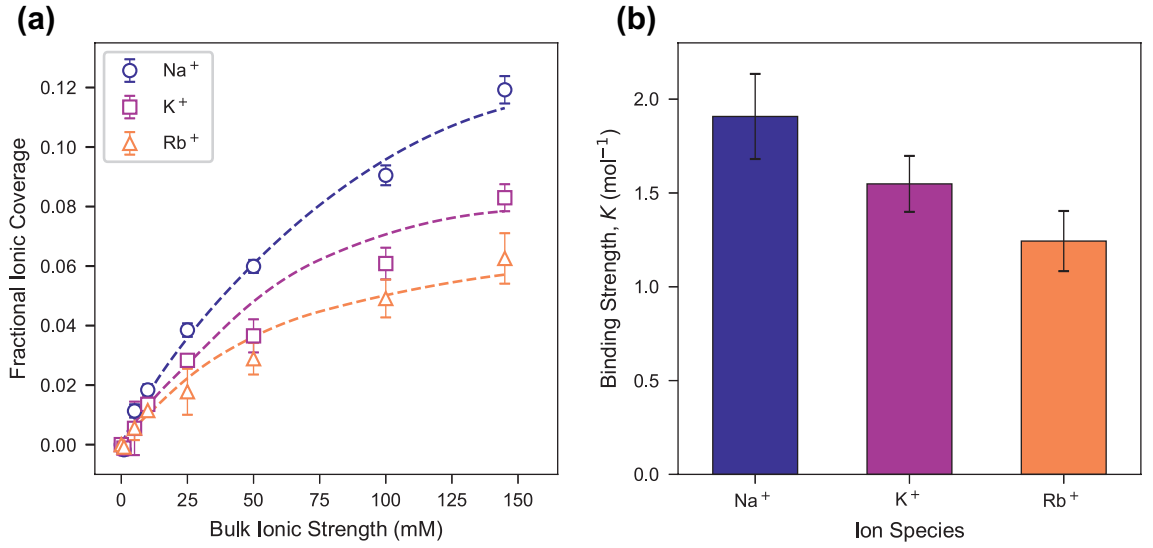


Fig. 5.3: From equation 1.4, 1.2 and the  $\zeta$ -potentials of Fig. 5.2 (see text), the fractional coverage of bound ions on the bilayer (a) can be obtained. These are described well by the Frumkin-Fowler-Guggenheim isotherm (dashed lines), but with a binding constant,  $K$ , that follows Hofmeister ordering;  $K_{\text{Na}^+} > K_{\text{K}^+} > K_{\text{Rb}^+}$  (b)

$$\Gamma = \frac{K \rho_{\text{ion}} \exp(nE_c \Gamma / k_B T)}{1 + K \rho_{\text{ion}} \exp(nE_c \Gamma / k_B T) + \text{p}K_a \rho_{\text{H}^+}}. \quad (5.4)$$

Here, the bulk ionic strength,  $\rho_{\text{ion}}$ , and proton/hydronium concentration,  $\rho_{\text{H}^+}$ , are in moles, and the  $\text{p}K_a$  of the  $\text{PA}^-$  headgroup here taken as 8.0 [12].  $n$  is the number of nearest neighbours of each binding site; we assume here that the lipids are hexagonally close-packed and that adsorbed ions form a 2D monolayer – i.e.  $n = 6$ . This is, however, an over-simplified picture of the interface, and these presumptions will be discussed further in subsection 5.3.3.  $E_c$  represents the effective correlation energy between ions at the interface and so accounts for hydration- and lipid-mediated interactions that affect ions' adsorption to the membrane. If  $E_c < 0$ , the ions experience attractive interactions between themselves; if  $E_c > 0$ , there is a mutual repulsion and if  $E_c = 0$ , then equation 5.4 reduces to the Langmuir adsorption model of a 2D gas.

The fits to equation 5.4 for each ion are shown in Fig. 5.3(a) as dashed lines and describe the data well, highlighting the suitability of the FFG model for describing the vesicle-cation interaction. The respective values of  $K$  extracted from the fits are displayed in Fig. 5.3(b) and Table 5.1 and indeed show that the ions' binding strength is dictated by their atomic weight – i.e. they display Hofmeister-like ordering;  $K_{\text{Na}^+} > K_{\text{K}^+} > K_{\text{Rb}^+}$ . The relative strengths and order of magnitude agree very well with previous measurements of binding constants to anionic lipids [4, 37]. Reported absolute values tend to be a little lower ( $K \lesssim 1.0$ ) but we note that our model system is in gel phase and thus has a smaller area per lipid (greater charge density), which is likely to encourage ion binding. We com-

pared the extracted values to those from a simple Langmuir fit (also shown in Table 5.1), which similarly demonstrated the Hofmeister ordering observed for the FFG isotherm. Its binding constants are closer to literature values for monovalent ions, but comparing the reduced  $\chi^2$  values for each reveals that the Langmuir model is too simplistic to capture the non-trivial adsorption behaviour of the charges.

The FFG correlation energies are also shown in Table 5.1 and are all negative, demonstrating that the ions experience an attractive interaction amongst the lipid headgroups, despite their similar charges. The value of  $E_c$  increases with ion size which emphasises the role of hydration interactions; sodium has the highest charge density and so the electrostatic energy is larger relative to water-driven attraction. Conversely, rubidium's large size results in a reduced electrostatic contribution, allowing correlative interactions to play a greater part, and increasing  $E_c$ .

Cation	FFG Isotherm			Langmuir Isotherm	
	$K$ ( $\text{mol}^{-1}$ )	$E_c$ ( $k_B T$ )	$\chi^2$	$K$ ( $\text{mol}^{-1}$ )	$\chi^2$
$\text{Na}^+$	$1.9 \pm 0.2$	$-1.1 \pm 0.2$	3.2	$1.10 \pm 0.09$	13.2
$\text{K}^+$	$1.5 \pm 0.2$	$-2.0 \pm 0.3$	1.8	$0.80 \pm 0.09$	12.4
$\text{Rb}^+$	$1.2 \pm 0.2$	$-2.9 \pm 0.5$	0.8	$0.58 \pm 0.08$	3.8

Tab. 5.1: Binding constants,  $K$ , and energies of correlation,  $E_c$  (see text), extracted from the FFG and Langmuir isotherms (the former displayed as dashes in Fig. 5.3(a)). In both cases,  $K$  decreases with increasing ionic radius as has been observed previously in lipid systems. Intriguingly, all  $E_c$  values are negative, indicating an attractive potential between the adsorbed ions, which *increases* with the atomic size of the alkali metal. The simpler Langmuir fits, which do not allow for ionic correlations, demonstrate a much larger reduced  $\chi^2$ , and imply that a single  $K$  is not sufficient to describe the adsorption process.

### 5.3 Molecular-scale structure and dynamics of ions around lipids

While the electrophoretic results are invaluable in describing the electrostatics at the vesicle scale (i.e. hundreds of nanometres) and grant insight into the adsorption and correlation behaviour of the ions, they give no insight into the mechanisms underlying the Hofmeister effects that were observed. Amplitude-modulation AFM and molecular dynamics simulations provide excellent tools to complement the  $\zeta$ -potential data and explore the nanoscale origins of Fig. 5.2 and 5.3, as highlighted in chapters 1 and 2. The former offers laterally-resolved, single-ion-level information about the topography and also energetic and mechanical properties of a sample [46]; the latter allows for detailed structural and dynamic information about every molecular species to be extracted, with no

perturbation (i.e. completely relaxed).

### 5.3.1 *Small amplitude AFM imaging and spectroscopy of DPPA-electrolyte interface*

#### *Hydration structure within the bilayer plane*

We begin by conducting high resolution AM-AFM scans of a pure DPPA bilayer supported on a mica substrate in 150 mM solutions of NaCl, KCl and RbCl (materials and methods in section 5.6). Representative ( $15 \times 15$ ) nm<sup>2</sup> height topographs (purple/yellow) and phase variation (blue/black) in each ionic solution are shown in Fig. 5.4. The small oscillation amplitudes,  $A_0$ , of the cantilever and high setpoint ratio probe just the headgroup-electrolyte interface [47, 48]. This, coupled with the fact that hydrophilic interfaces in aqueous electrolytes tend to generate very short-ranged solvation forces [49–52], ensure that only the headgroups and Stern layer contribute to the tip-sample interaction, resulting in interface-specific information. Hence, changes in height reflect the characteristic variations in the bilayer’s hydration landscape induced by the ions, as well as the underlying hexagonal symmetry of the gel-phase lipids (see, for example, the fast Fourier transforms (FFTs) in greyscale to the right of each image).

The nature of the interface clearly depends strongly on the cation species in solution. In 150 mM NaCl (Fig. 5.4(a)), amorphous clusters form two levels superimposed on the membrane. These reflect the fact that small ions rarely form a perfectly two-dimensional Stern layer at the interface and indicate the complexity of sodium’s binding states with the lipids; upper levels represent ions adsorbed in outer-sphere coordination with an intervening water molecule. These outer-sphere ions are loosely correlated with areas of relatively high phase (yellow arrows) that indicate a more viscous tip-bilayer interaction [47, 48]. Conversely, lower levels that relate to directly adsorbed ions are characterised by areas of reduced phase, reflecting a more elastic response (green arrows).

When the solution is replaced with 150 mM KCl, as in Fig. 5.4(b), the two adsorption states are still visible, but the interface’s topographic features are markedly more regular: the roughness (see chapter 3, equation 3.2) drops from  $R_q^{\text{Na}^+} = 0.037 \pm 0.003$  nm to  $R_q^{\text{K}^+} = 0.027 \pm 0.002$  nm. This reflects the fact that potassium ions (and larger cations in general) adsorb more frequently in an inner-sphere configuration [31, 53, 54] – that is, directly to lipid headgroups – due to their lower charge density. A similar correspondence of phase and topography was observed in KCl and RbCl, indicating that it is a rather general feature of ions within the Stern layer. This complements the discussion of section 4.2,

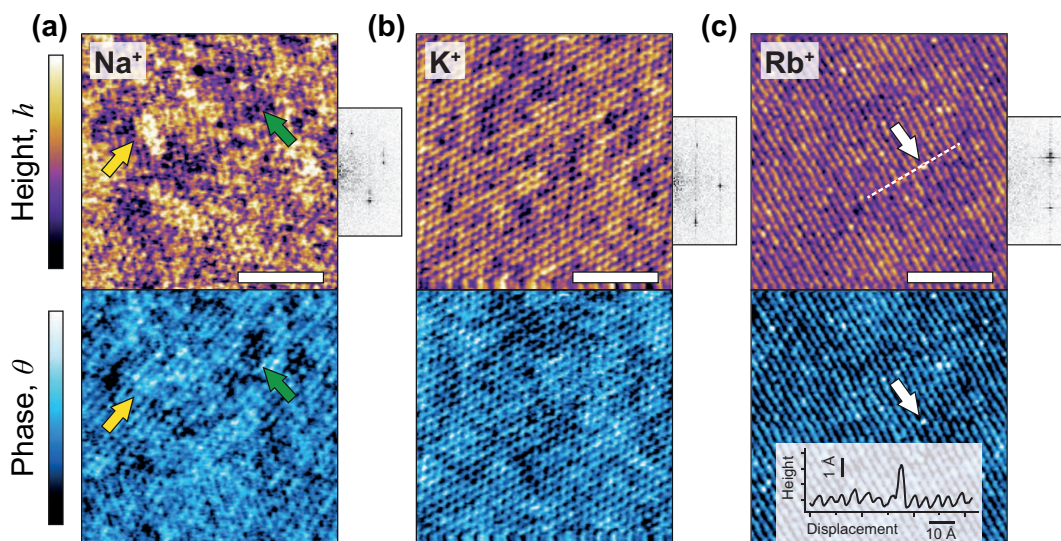


Fig. 5.4: AM-AFM illustrates the characteristic perturbation of the lipid-electrolyte interface by cations. Height topographs,  $h$ , (purple/yellow, upper) and phase differences,  $\Delta\theta$ , (blue/black, lower) of supported DPPA bilayers in 150 mM NaCl (a), KCl (b) and RbCl (c) solutions. In NaCl, two distinct height and phase levels are visible due to Na<sup>+</sup> adsorbing in inner- and outer-sphere complexes (green and yellow arrows respectively). The two levels are still present in KCl but to a lesser extent, with K<sup>+</sup> forming a much more “regular” Stern layer with reduced roughness (see text). Rb<sup>+</sup> presents single point defects of  $> 0.2$  nm in  $h$  and  $\Delta\theta$  (white arrows), highlighted by the section (dashed line and inset). These correspond to singly-adsorbed rubidium ions that are rare due to their relatively low binding constant. The remaining lipids are screened by hydronium and water dipoles, resulting in the appearance of molecular rows, rather than individual sites. Zoomed Fourier transforms for each ion’s image covering  $(3 \times 6) \times 10^{-18}$  m<sup>-2</sup> are shown in greyscale; colour scales represent 0.1 nm (height) and 5° (phase) and length scale bars are 5 nm.

as well as recent studies of nano-confined mono- and divalent ions, which revealed them to be consistently more viscous than pure water alone [55].

In RbCl solution (Fig. 5.4(c)), the topography predominantly takes the form of molecular rows, straddled by occasional large ( $> 2$  Å) protuberances, highlighted by the section (arrows and dashed line, inset). The size and location of these are consistent with them being inner-sphere Rb<sup>+</sup> complexes [53] that adsorb too rarely to show significant domain formation; the remainder of the bilayer must instead be screened by water dipoles and H<sub>3</sub>O<sup>+</sup>. This explains the row-like appearance of the majority of the topograph; waters are smaller and more dynamic than ions and generally present more of a challenge to image with AFM. Thus, the rows likely result from a direct interaction between the tip and the lipid headgroups or acyl chains themselves, in good agreement with 3D AFM images of hydration layers above DPPC [56].

The apparent non-random clustering of sodium and potassium into domains in Fig. 5.4(a)

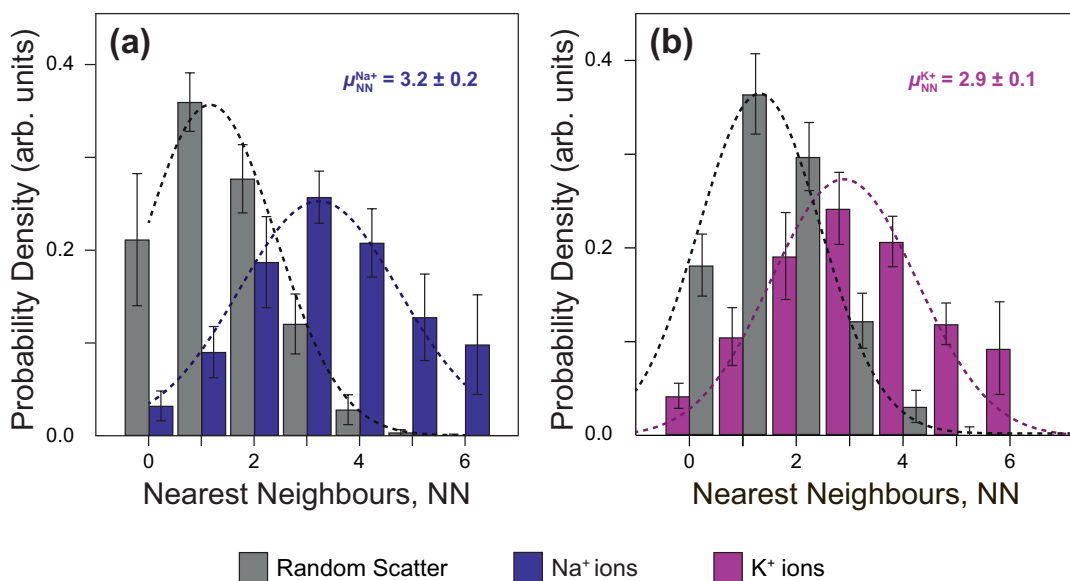


Fig. 5.5: Analysis of adsorbed outer-sphere Na<sup>+</sup> (a) and K<sup>+</sup> (b) from the AFM topographs allow the nearest neighbour distribution to be calculated for each ion. Fitting these with a Gaussian function (dashes) allows the extraction of the mean number of nearest neighbours, giving  $\mu_{NN}^{\text{Na}^+} = 3.2 \pm 0.2$ ,  $\mu_{NN}^{\text{K}^+} = 2.9 \pm 0.1$ . Both are much greater than a theoretical random distribution of equal coverage,  $\mu_{NN}^{\text{rnd}} = 1.3 \pm 0.1$ , quantitatively demonstrating the propensity of these ions to form domains that overcome their electrostatic repulsion.

and (b) was quantified by using a semi-automated algorithm based on height thresholding to identify the locations of adsorbed outer-sphere ions in the AFM topographs (further detail in methods subsection 5.6.4). Once the location of the ions was known, a simple procedure counted the number of nearest neighbours (NN) within a pre-defined radius (by inspection, 0.65 nm was found to give the most accurate determination of the number of nearest neighbours of each site). The NN distribution of the ions was then compared with a theoretical random distribution of equal coverage. The results from this analysis are presented in Fig. 5.5, along with Gaussian fits to histograms in order to calculate the mean number of nearest neighbours for each ion, which we refer to as  $\mu_{NN}$ . It is immediately obvious that the NN distribution for both sodium and potassium is weighted more towards clusters (high NN) than a random distribution; indeed we find that  $\mu_{NN}^{\text{Na}^+} = 3.2 \pm 0.1$ , compared with  $\mu_{NN}^{\text{rnd}} = 1.3 \pm 0.1$ . Potassium in fact demonstrates a slightly reduced mean of  $\mu_{NN}^{\text{K}^+} = 2.9 \pm 0.1$ . This analysis quantitatively confirms the cations' predilection to form non-random networks through the hydration water-mediated interactions which dominate at this scale [28, 31].

#### *Influence of AFM tip on apparent topography*

The topographs presented in Fig. 5.4 illustrate how the alkali metals alter the interface characteristically, in line with their atomic radius. However, since AFM is necessarily

a perturbative technique, the structures observed will not be truly equilibrated but will likely represent an “excited” state of the interface. We mitigated tip-specific effects to the best of our ability by using the same cantilever throughout and imaging using soft setpoint ratios of  $S_p \equiv A_w/A_0 \geq 70\%$ , which ensured that comparisons between each interface were meaningful. However, it is likely that a few of the most weakly-bound ions (especially those in outer-sphere) will be removed. To gauge the extent of this, a supported DPPA bilayer was imaged in identical conditions to those of Fig. 5.4, with a tip identical by design, but a spring constant less than half the value ( $k_1 = 0.7 \text{ N m}^{-1}$  c.f.  $k_1 = 1.7 \text{ N m}^{-1}$ ). A comparison between two representative images taken with each cantilever is presented in Fig. 5.6, with identical height colour scales. We use 150 mM RbCl to illustrate this as it provides the clearest contrast between adsorbed and desorbed ions, but the effect is still relevant for the other ions. Images taken with each cantilever have similar symmetries and lattice parameters but very different occupancies. This is highlighted by the sections (dashed lines), presented below each topograph. The softer cantilever (a) displays many more adsorbed ions with a few defects where an ion has been displaced, whereas the stiffer cantilever (b), in contrast, displays mainly row-like structures with only the occasional individually adsorbed ion of height  $> 0.2 \text{ nm}$ . This illustrates the impact of the AFM tip on the apparent topography; stiffer cantilevers dissipate more energy into the Stern layer per cycle than softer ones and thus displace more ions. However, our analysis of the *relative* changes in the Stern layer when the cation species is changed will remain valid, although we must assume that in each case the landscape reflects that of the strongly-bound charges.

In general, the above AFM data agree very well with the  $\zeta$ -potential results of Fig. 5.3. Sodium, as the smallest ion, has a high charge density and binds tenaciously to the DPPA membrane as well as to surrounding waters. This results in a complex hydration landscape due to the formation of inner- and outer-sphere complexes. Potassium is still able to form these ionic domains but results in a less rough, more “regular” topography. Rubidium has the weakest binding strength and, as such, is easily displaced by the AFM tip. However, even when using a soft cantilever, only a single binding location is observed, due to its large size.

### *Ionic structure perpendicular to the bilayer*

Our interpretation of the topography and phase images in Fig. 5.4, as well as the global binding constants in Fig. 5.3 can be directly confirmed by measuring each ions’ distortion of the hydration landscape perpendicular to the lipid bilayer. We achieve this using phase-distance spectroscopy, in which variations in the cantilever’s oscillation phase are measured as the cantilever is progressively moved towards the lipids. The cantilever was driven at amplitudes approximately corresponding to the diameter of a water molecule

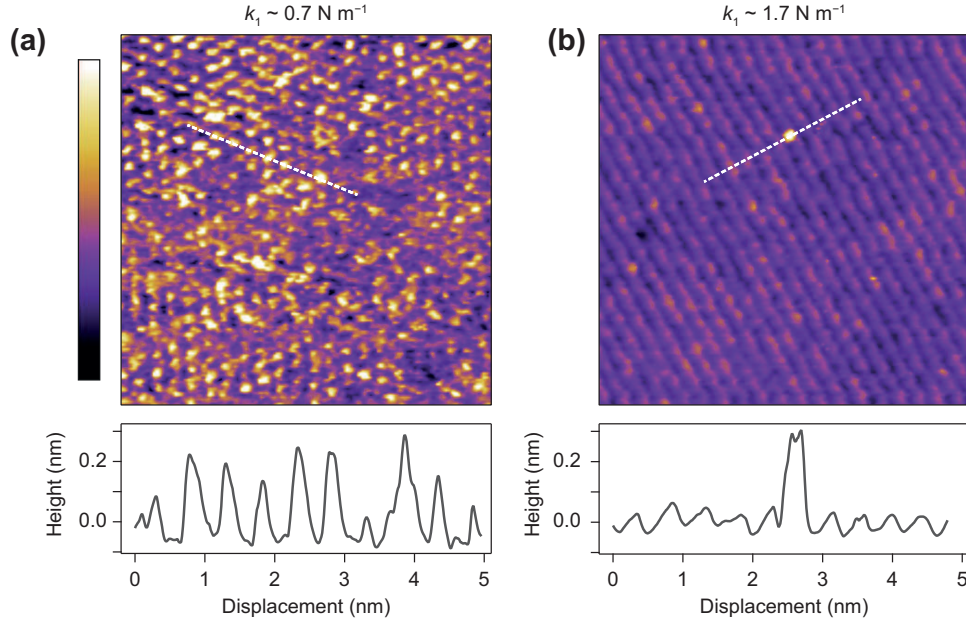


Fig. 5.6: The apparent Stern layer topography is dependent on the cantilever stiffness; comparison between  $10 \times 10 \text{ nm}^2$  height images taken with a low ((a),  $k_1 = 0.70 \text{ N m}^{-1}$ ) and high ((b),  $k_1 = 1.71 \text{ N m}^{-1}$ ) spring-constant cantilever in 150 mM RbCl. The stiff cantilever dissipates more energy per cycle into the solution and is thus able to remove a greater percentage of adsorbed ions. This results in an image with low height variation except for a few adsorbed  $\text{Rb}^+$  (section, below) that sit  $> 0.2 \text{ nm}$  above the membrane. Conversely, imaging with a soft cantilever allows more ions to remain in place, giving the appearance of a well-populated Stern layer, with only a few defects where ions are removed. Height colour scales both cover  $0.35 \text{ nm}$

( $\sim 2.5 \text{ \AA}$ ), in order to ensure the interaction force was as linear as possible (see chapter 2) while retaining sufficient signal-to-noise ratio. With these small amplitudes,  $\Delta\theta$  is particularly sensitive to variation in the density of waters and charges close to the bilayer (*via* equation 2.5) and highlights differences in the ions' coordination with the lipids. The true separation between the tip and lipids,  $d_{\text{tl}}$ , was computed using the standard relation for AFM spectroscopy between the vertical piezo extension,  $z$ , and the change in deflection,  $\Delta D$ :  $d_{\text{tl}} = z - \Delta D$ . The cantilever's motion far ( $> 1.5 \text{ nm}$ ) from the bilayer was assumed to be totally viscous such that the phase was set to  $90^\circ$  in this region.

An illustration of this procedure is given in Fig. 5.7(a) for the DPPA bilayer in 150 mM KCl. As the  $z$ -piezo extends and the tip is moved closer to the bilayer, the phase is smoothly reduced due to its increasing interaction with interfacial layers of fluid before “hard” contact is reached with the lipids (indicated by the sharp increase in static deflection). We approximate this smooth decrease as a sigmoidal function of the form

$$\theta(z) = \theta_0 + \frac{\theta_{\text{max}}}{1 + \exp((z_{\text{half}} - z)/\lambda)}, \quad (5.5)$$

presented as a dashed line in Fig. 5.7(a).  $\theta_0$  and  $\theta_{\max}$  are the baseline and maximum phases, and  $z_{\text{half}}$  and  $\lambda$  are the piezo's height-at-half-phase and sigmoid decay rate respectively. As well as this smooth decrease, the phase demonstrates reproducible oscillations that indicate an anomalous dissipation of energy which we associate with the removal of an ion from the interface by the oscillating cantilever. This is in line with Ricci *et al.*'s observations of discontinuities in  $\theta$  induced by the presence of 10 mM NaCl on calcite [57], as well as oscillatory behaviour in dynamic AFM operated in a diverse range of solutions and surfaces [49, 58–60]. We highlight this ion-specific energy dissipation by plotting the residuals,  $\Delta\theta$ , from the sigmoidal fit against the tip-lipid separation,  $d_{\text{tl}}$ , in Fig. 5.7(b). Each trace is the average of at least 15 such phase-distance curves that were aligned based on their deflection using a home-made least-squares fitting routine.

Far from the interface ( $d_{\text{tl}} > 1.0$  nm),  $\Delta\theta$  vanishes, as expected for bulk fluid with negligible structuring. However as the separation is decreased, sodium presents two peaks at  $d_{\text{tl}} < 0.3$  nm indicative of its condensed, complex binding conformation. However the perturbation here is relatively weak (its trace in (b) has been multiplied by a factor of four), likely related to sodium's non-trivial hydration structure [61] which generates the heterogeneous topography of Fig. 5.4(a). Potassium, in contrast, produces two well-defined peaks in  $\Delta\theta$  separated by  $\sim 0.3$  nm. The reproducibility of the signal reflects the more consistent imaging in Fig. 5.4(b), and their separation (about that of a water molecule) strongly imply that the peaks represent inner ( $d_{\text{tl}} = 0.1$  nm) and outer-sphere ( $d_{\text{tl}} = 0.4$  nm) coordinated  $\text{K}^+$ . Rubidium binds overwhelmingly in a single mode at  $d_{\text{tl}} = 0.3$  nm, the furthest initial peak of all the ions studied here. This reflects both its larger size and its preference to form just inner-sphere complexes due to its reduced charge density [54]. A shoulder is observed at 0.55 nm, which may indicate a small population of outer-sphere  $\text{Rb}^+$ , but it is within the spread of the initial peak and as such, no strong conclusions can be drawn.

### 5.3.2 Molecular dynamics simulations

#### *Simulation set-up*

The electrophoresis and AFM measurements clearly point to specific ion coordination and structured networks on the bilayer, but they do not permit truly atomic exploration of the in- and out-of-plane interfacial structures simultaneously. To address this, and gain further insight on our experimental results, we performed all-atom MD simulations using NAMD 2.11 [62]. The system consisted of 136 DPPA molecules in a free-standing, tensionless bilayer at 298 K and 1 atm pressure in direct contact with 150 mM NaCl, KCl or RbCl (Table 5.2 and Fig. 5.8), thus directly mirroring the experimental set up, but with

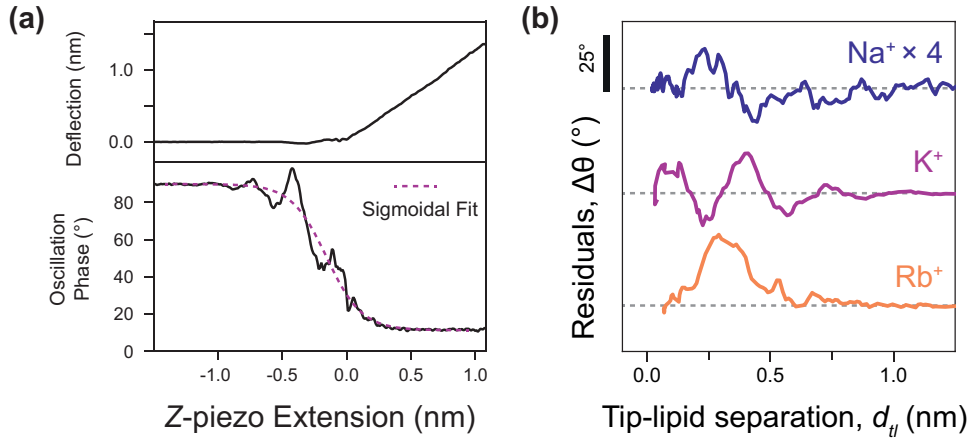


**Fig. 5.7:** Phase-distance spectroscopy reveals ion-specific coordination above the lipid headgroups. (a) Static deflection (upper) and phase (lower) of the cantilever as a function of  $z$ -piezo extension such that  $z \ll 0$  represents bulk electrolyte (here illustrated in 150 mM KCl). As the AFM tip approaches the bilayer, the increased interaction with the interfacial fluid dampens the phase. Ions within the Stern layer induce characteristic peaks in the phase that are highlighted by the subtraction of a sigmoidal fit (dashes). (b) The residuals from such fitting are strongly cation-dependent and agree with our interpretation of the AM-AFM scans presented in Fig. 5.4.  $\text{Na}^+$  forms heterogeneous, non-trivial complexes with the lipids that extend rather far into the solution;  $\text{K}^+$  binds in two modes at  $d_{t1} \sim 0.1$  nm and 0.4 nm;  $\text{Rb}^+$  binds overwhelmingly in a single mode at  $d_{t1} \sim 0.3$  nm (albeit with a small shoulder at 0.55 nm). Traces have been offset (dashes indicate  $0^\circ$ ) and sodium's trace multiplied by four for clarity.

a relaxed Stern layer (i.e. no AFM tip perturbation). We note that in both the AFM experiments and MD simulations, the area-per-lipid barely changes at all upon electrolyte exchange. This is to be expected for DPPA, which, unlike unsaturated, fluid-phase lipids, has highly ordered acyl chains that resist conformational changes.

	Cations	Anions	Waters	DPPA <sup>-</sup>	Total atoms	Bilayer surface area (nm <sup>2</sup> )
SimA	156 Na <sup>+</sup>	20 Cl <sup>-</sup>	6463	136	30231	30.0
SimB	156 K <sup>+</sup>	20 Cl <sup>-</sup>	6463	136	30231	30.3
SimC	156 Rb <sup>+</sup>	20 Cl <sup>-</sup>	6463	136	30231	30.5

**Tab. 5.2:** Composition of the systems considered in the MD simulations A snapshot representing the entire system for SimB is presented in Fig. 5.8

### *Radial distribution functions between ions and lipids*

We first probe the system by computing the radial distribution function (RDF,  $g(r)$ ) of headgroup oxygens within the phosphate group with each cation, presented in Fig. 5.9(a)-(c). There is clear structuring evident in the RDFs for each species which correspond to different modes of ion adsorption. The first peak represents direct binding between the

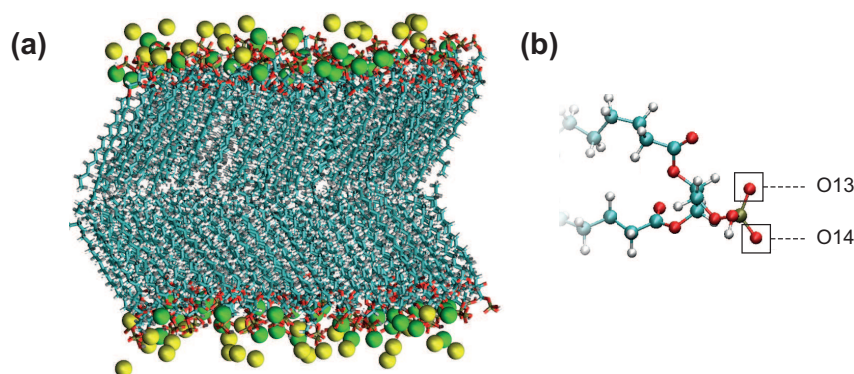


Fig. 5.8: (a) The simulation box: DPPA bilayer in 150 mM KCl. Lipids are shown in bond representation and adsorbed cations are displayed as spheres with their van der Waals radii. Waters, chlorides and non-adsorbed  $K^+$  are not shown for clarity. Inner-sphere ions are coloured green, whereas outer-sphere charges are coloured yellow, according to the radial distribution functions (RDFs) (illustrated in Fig. 5.9). (b) Snapshot of DPPA headgroup region with headgroup oxygens used for RDF analysis labelled.

headgroups and ions, limited only by the steric size of the participating atoms. The second peak indicates a preferred adsorption of ions, but further from the headgroups. This contains contributions from cations with a second lipid oxygen in their hydration shell (i.e. trivially generated by simulation geometry), but in the majority of cases, the peak represents ions which share a water with DPPA phosphate groups. That is, there is no *direct* interaction between lipid and ion, and the binding is determined by the intermediate water molecule. Thus the two peaks respectively correspond to the inner- and outer-sphere bindings identified in the AFM experiments earlier, confirming our interpretations. The third peak, where it exists, is related to the geometry of the simulation and is not physically relevant. Interestingly, and perhaps unsurprisingly for anionic lipid bilayers, no chlorides were found within the first coordination shell of the lipids, demonstrating that cations and waters are primarily responsible for generating the hydration landscapes observed.

The RDFs were used as part of an in-house analysis program to categorise ions, based on their environment, as being either directly or indirectly adsorbed. They were then coloured either green or yellow respectively and highlighted in the snapshots presented in Fig. 5.8 and 5.9(d). By analysing the relative proportions of each species, we find that the fraction of ions bound in the second mode decreases in the sequence  $Na^+ > K^+ > Rb^+$ , mirroring the binding affinities of Fig. 5.3 and Table 5.1. The inverse is true of the population of inner-sphere ions, as can be seen in Fig. 5.9(e). The two peaks are present for all cation species, even for  $Rb^+$  – for which AFM could not reliably identify an outer-sphere contribution – but we note that the simulations do find a dramatically reduced outer-sphere population. Previous simulations of  $PA^-$  lipids with divalent cations found only inner-sphere adsorption [26], suggesting that this multiplicity of adsorption states

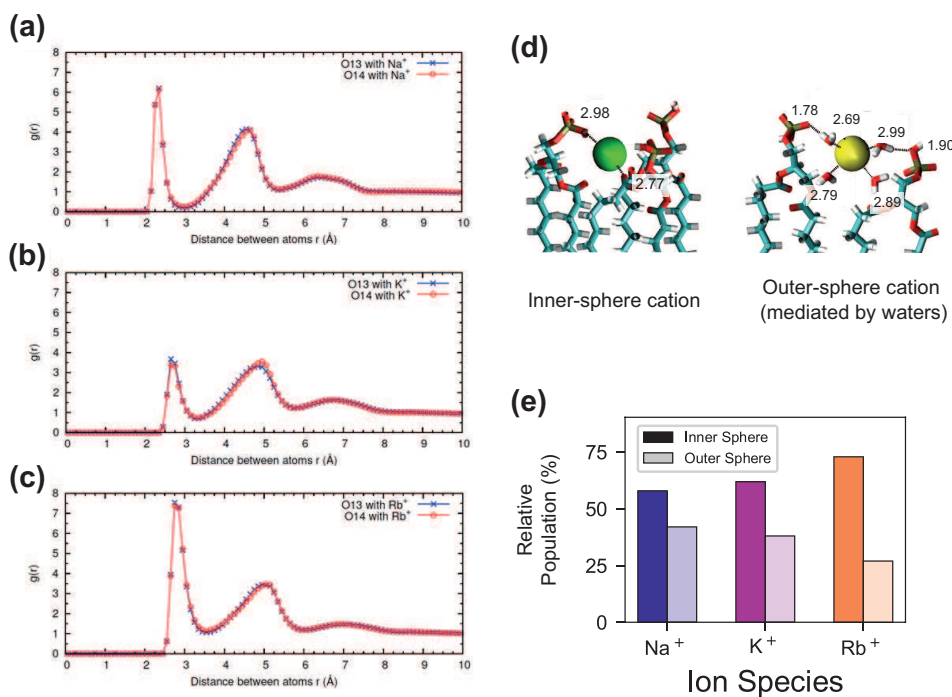


Fig. 5.9: Analysis of the RDFs of the lipid headgroup oxygens with Na<sup>+</sup> (a), K<sup>+</sup> (b) and Rb<sup>+</sup> (c) reveals considerable structure in their binding. The initial peak at 2.5-3 Å corresponds to directly-bound ions and is illustrated as a green sphere in (d), left. The second peak overwhelmingly represents ions that adsorb to the lipids *via* a water molecule (i.e. outer-sphere configuration) and an example snapshot is shown in yellow in (d), right. Bond lengths are annotated in Ångströms. There is no significant dependence of  $g(r)$  on the oxygen atom chosen for analysis. (e) The relative population of outer-sphere ions (lighter shades) decreases following the Hofmeister series as Na<sup>+</sup> > K<sup>+</sup> > Rb<sup>+</sup> due to the larger ions' reduced ability to interact beyond their first hydration shells.

may be unique to monovalent ions.

#### *Lateral correlations on the bilayer*

The simulations also revealed significant lateral correlations between the ions themselves; RDFs demonstrated coordination peaks at 0.35 nm, 0.42 nm and 0.46 nm for Na<sup>+</sup>, K<sup>+</sup> and Rb<sup>+</sup> respectively. These correspond to cation-oxygen-cation contacts, that is; ions interacting with each other *via* water molecules or lipids, as suggested by the correlation energies of Table 5.1. In fact, the majority of adsorbed ions share their solvation water with other ions, forming correlated chains as illustrated in Fig. 5.10(a), (b). These suggest that the domains observed in the AFM topographs are indeed induced by ionic networks at the bilayer interface. By using similar colours for ions that share water or lipid oxygens with one another in Fig. 5.10(c), we demonstrate that most ions belong to such nano-networks, with many forming larger-scale structures of four ions or more (dashed regions).

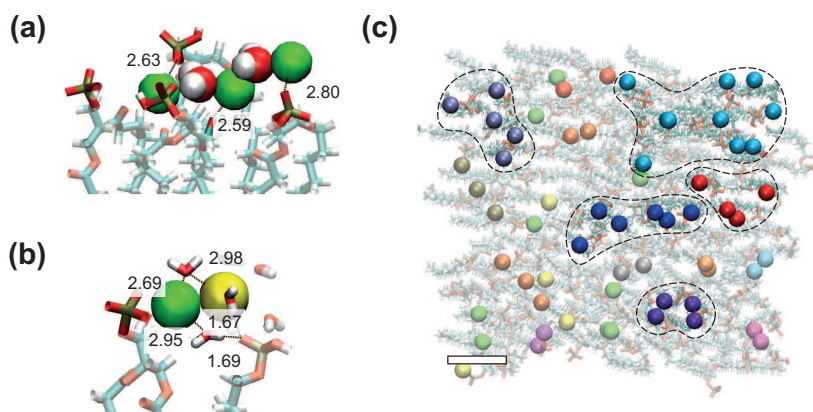


Fig. 5.10: MD simulation snapshots highlight lateral correlations of ions on the DPPA bilayer, either generating chains of ion/water pairs (a), or inner-/outer-sphere ion coupling (b). (c) Top view of simulation box with ions sharing water and lipid oxygens in their first hydration shell coloured the same. These demonstrate that the majority of ions on the bilayer participate in correlated domains. Larger-scale ( $> 4$ ) networks are enclosed with dashed lines. Scale bar represents 1 nm.

### 5.3.3 Time-resolved evolution of ionic domains

The MD simulations agree with the experimental results in terms of the relative ability of alkali cations to bind with the lipids and laterally organise themselves on the bilayer, especially the importance of water in these interactions. These ionic networks cannot be explained with traditional continuum theories and are believed to dramatically affect the charging [63] and dynamics [31] at aqueous interfaces (see also, chapter 4). Here, the MD results show ions to be essentially static at the bilayer surface once they bind, but the simulations'  $\sim 100$  ns length do not allow us to explore the evolution of the cationic networks over biologically relevant timescales (ms-s). However, the stability of the AFM scans such as those presented in Fig. 5.4 and 5.6 suggests that the ionic structures are remarkably long-lived, with dynamics that can be interrogated by AFM. Indeed observations of ions at the mica-electrolyte interface have shown that the energetics associated with ion adsorption generated relaxation times ranging from seconds [54] to minutes [64], although neither of those techniques allowed for direct identification of ionic networks, as is the case here. Fig. 5.11 shows the evolution of the networks observed by AFM with single-ion resolution over consecutive images. We objectively tracked the ions' locations using the same algorithm as of Fig. 5.5, but in successive images, thus allowing time-resolved information to be obtained. The ions are highlighted in (a) by white circles, and those participating in nearest-neighbour interactions are joined by red bars. Significantly, the image demonstrates that the ionic nano-networks persist long enough to be identified with AFM, in good agreement with the electrophoretic results, which predict attractive correlation energies of  $-2 < \Delta E_c < -1 k_B T/\text{ion}$  that can dominate over thermal fluc-

tuations. With the AFM scan rate being relatively slow, persistence of ionic domains between images implies they are stable on the order of tens of seconds, slow enough to influence many processes at bio-interfaces. However, there is clearly some size-dependence of the mobility of the domains (white boxes), with larger ionic networks typically more stable.

To better quantify the residence time of ions within nano-networks, as well as its dependence on network size, we computed the characteristic time necessary for a given ion to desorb as a function of its number of nearest neighbours (Fig. 5.11(b)). This was achieved by tracking for each outer-sphere ion the degree of correlation between consecutive frames. In practice, this meant computing the length of time,  $\Delta t$ , it took for the tip to return to the specific location of an outer-sphere adsorbed ion and then checking whether the ion was still present. We extract a characteristic timescale for each trace in (b) by fitting the data with a function of the form  $\Lambda(\Delta t) = \Lambda_0 + A \exp(-\Delta t/\tau)$ , where  $\Lambda_0$  and  $A$  are constants. As expected from our observations,  $\tau$ , depends strongly on the number of nearest neighbours (NN). Strikingly, the results show a linear relationship between  $\tau$  and NN for adsorbed ions (inset), further emphasising the fact that water-mediated ion-ion correlation dominates interactions and dynamics at this scale. The results are inconclusive for  $NN < 2$ , presumably due to dynamics faster than the temporal resolution of our AFM. From the dependence of  $\tau$  on NN, we estimated the free energy change associated with an adsorbed ion joining a domain on the bilayer. We assume a decorrelation time  $\tau_n \propto \exp(E_n/k_B T)$  [65], where  $E_n$  is the total correlated energy of  $n$  outer-sphere ions. We can then extract the change in free energy upon increasing the size of an existing network, which gives  $\Delta E_c \sim -0.38 k_B T$  per added neighbour. Making a further assumption that outer-sphere ions are maximally six-fold coordinated on the SLB (as in the analysis of subsection 5.2.2, with  $n = 6$  in equation 5.4) yields a total correlation energy,  $E_c^{\text{tot}} = 6\Delta E_c \sim -2.27 k_B T/\text{ion}$ , less than the value of 6-12  $k_B T/\text{ion}$  calculated from our electrophoretic measurements. This difference is expected, given the fact that our AFM analysis accounts only for the in-plane motion of outer-sphere ions. The  $\zeta$ -potential measurements, in contrast, are sensitive to both direct and indirect ionic interactions, and so accommodate 3D interactions (apparent in Fig. 5.7(b) and 5.10) that would increase the value of  $E_c$ . The assumed interaction with 6 nearest neighbours in both cases is thus rather naïve, but the order-of-magnitude agreement between these independent techniques is still remarkable.

The attractive nature of the ion-ion interaction measured here certainly agrees with the greatly reduced dynamics of Fig. 5.11(a), but a well of  $-0.38 k_B T/\text{ion}$  appears quite small (compared to the thermal energy), especially if it is to reduce the ions' dynamics to such a great extent. However, we show, using a minimal model based on Eyring dynamics

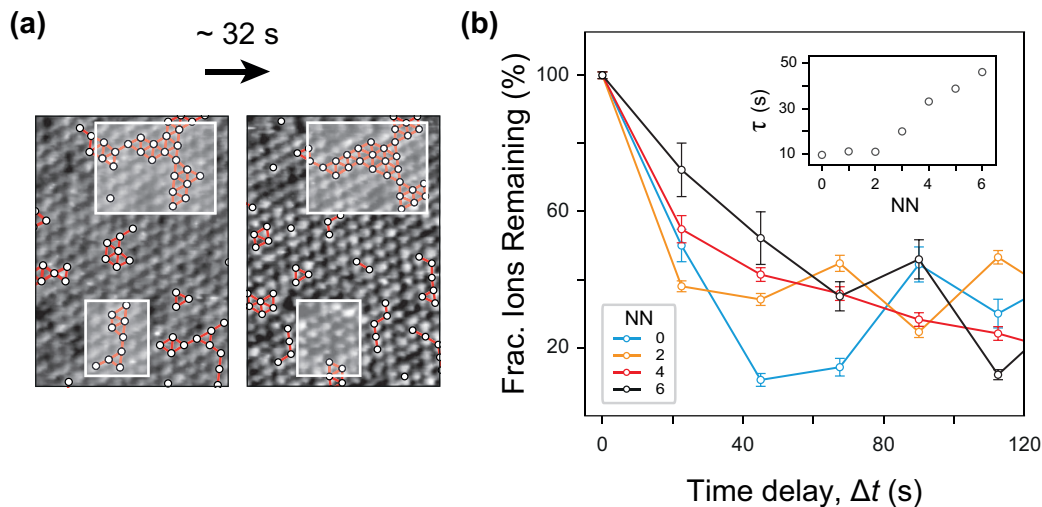


Fig. 5.11: AFM allows for long-timescale evaluation of the dynamics of ionic domains on the bilayer. (a) Consecutive topographs (original scan size of  $(15 \times 15) \text{ nm}^2$ ) of DPPA in 150 mM KCl with outer-sphere ions and nearest-neighbour connections, as defined by our algorithm, highlighted by white circles and red bars respectively. Larger domains (top right) tend to be more stable in shape and size between scans than smaller ones (bottom left). (b) To quantify this observation, we track the relative degree of correlation between ions in consecutive frames according to how many nearest neighbours each has, shown for even NN. Ions deep within the domains (high NN) remain more stable, which we quantify with a effective decorrelation time,  $\tau$ , (inset) from which a correlation energy of  $\Delta E_c = -0.38 k_B T$  is extracted.

that in fact, small contributions per ion can lead to very large timescale shifts when entire networks are considered. We begin with the assumption that the inverse timescale of the domains' motion,  $\tau^{-1}$ , is linked to the ions' microscopic jump frequency,  $\nu_0$ , (typically in the range of  $10^{10}$ - $10^{13} \text{ s}^{-1}$  [64]), and an effective activation energy,  $E_a$ , by the expression

$$\tau^{-1} = \nu_0 \exp\left(\frac{E_a}{k_B T}\right). \quad (5.6)$$

The activation energy depends upon the domain size,  $n_d$ , mean number of nearest neighbours ( $\mu_{\text{NN}}$ , as extracted from Fig. 5.5) and  $\Delta E_c$ , such that  $E_a = n_d \times \mu_{\text{NN}} \times \Delta E_c$ . Taking a reasonable estimate of  $n_d \sim 25$  ions by inspection of the AFM topographs, we arrive at  $E_a = -27.55 k_B T$ , which, for  $\nu_0 = 10^{11} \text{ s}^{-1}$ , leads to timescales of  $\tau \sim 10 \text{ s}$ , in excellent agreement with the order of magnitude observed experimentally. While undoubtedly representing an oversimplification, this model highlights the fact that for a single ion to desorb or diffuse requires the concerted motion of many waters, ions and lipid headgroups [52], especially for high biological ionic strengths of 150 mM. Thus, even a relatively small free energy well may, for larger ionic domains, result in the dramatically increased residence times found here.

Previous work on the mica-electrolyte interface has demonstrated that water can medi-

ate ion-ion correlations in similar conditions [31] (albeit with different ions), and slow the relaxation times of solitary ions down to almost a second (see chapter 4). There is, however, still no accepted consensus in the literature over the mobility of adsorbed ions [66], partly because water-mediated effects are usually ignored. Here, we have linked the ions' attractive correlation energy with specific nearest-neighbour group interactions that lead to greatly retarded dynamics for large ionic domains.

## 5.4 Mechanical perturbation of membranes by ions

We have demonstrated that the dynamics of monovalent ions are greatly retarded at the interface with anionic lipid bilayers, due to the formation of water-mediated networks that increase the energy needed for concerted motion. The collective timescales observed here are of the order of seconds and are thus likely to have profound implications for the behaviour of biomembranes *in vivo*. Of particular interest is the effect these domains may have on the physical properties of the bilayer, as these will in turn affect the function of membrane-bound proteins [6, 10, 67], as well as bilayer re-modelling events [7].

It is well-known that ions and electrostatics modulate the cohesive strength [68, 69] and bending or elastic moduli [38, 39, 70–73] of lipid bilayers, an effect usually assumed to be driven by molecular-level changes in headgroup hydrogen bond networks and liberation of waters. In these instances, ions tend to make bilayers more robust by neutralising bilayer charges and drawing lipids closer together [6]. While in general, there is consensus about the mechanical impact of increasing ionic strength, we must be careful about the particulars of the experiments; the AFM spectroscopy experiments by Garcia-Manyes *et al.* measure the force necessary to puncture the bilayer and thus reflect non-specific inter-lipid affinities. These contain complex contributions from van der Waals, electrostatic and entropic energies (especially for such cataclysmic, non-equilibrium experiments) [74]. The results are thus not directly comparable to experiments such as micropipette aspiration [75], X-ray spectroscopy [73] or vesicle shape fluctuations [71] that make use of mean-field frameworks such as the Helfrich Hamiltonian [76]. These latter will depend upon, for example, the effective thickness of the electric double layer, which may produce opposing effects for the lipids' mechanical properties [38, 73].

### 5.4.1 Extraction of bilayer mechanical parameters with AFM

#### *Bimodal AFM operation*

In order to ascertain the impact of ions on the physical properties of biological systems, AFM spectroscopy has been regularly used (along with necessary interaction models) to

characterise various mechanical properties of lipid bilayers, including the aforementioned breakthrough force [68, 69, 74], stiffness [77, 78] and compressibility modulus [79]. However, it is only recently with the advent of novel modes, that the extraction of physical attributes can be combined with lateral resolution and imaging speeds comparable to that of standard AFM operation [46, 77, 80–83]. Of these, the most straightforward to interpret (and most comparable to the data presented in section 5.3) is bimodal AFM. This technique is illustrated schematically in Fig. 5.12(a) and involves driving the cantilever simultaneously at its fundamental (left) and second harmonic (right). We make use of bimodal AFM with the first mode used in amplitude modulation, exactly as for Fig. 5.4 and 5.6. This ensures we probe the interfacial layer as before, maintaining single-ion level lateral resolution and times per frame of  $\mathcal{O}(10\text{ s})$ . The second mode is controlled by a feedback loop that keeps the phase locked at  $90^\circ$  and the oscillation at its resonance (i.e. frequency modulation).

We use the approach of Amo *et al.* [82] to extract quantitative information from the second mode. This involves using dynamic force reconstruction to relate the cantilever's motion to the maximum force,  $F$ , on the bilayer. Then, a contact mechanics model is required to link this force to the tip's indentation,  $\delta$ , and effective Young's modulus of the bilayer,  $E_{\text{eff}}$ . In this instance, we make use of the Hertz model ( $F_{\text{Hertz}} \propto E_{\text{eff}}\delta^{3/2}$ ), for both its simplicity and ubiquity in 1D AFM spectroscopic studies. Many operating parameters are required to reconstruct the effective modulus, but only two vary across a bimodal scan; the first mode's instantaneous amplitude,  $A_1$ , and the second mode's frequency shift (relative to the frequency where the tip force moves from attractive to repulsive regimes),  $\Delta\nu_2$ . The others are determined before a scan is taken. The equations (evaluated for every pixel of a scan) are:

$$\delta = \frac{1}{2} \frac{k_1\nu_2}{Q_1 k_2 \Delta\nu_2} (A_{0,1}^2 - A_1^2)^{1/2}, \quad (5.7)$$

$$E_{\text{eff}} = \frac{k_1}{Q_1 \delta^2} \sqrt{\frac{2A_1(A_{0,1}^2 - A_1^2)}{R}} \quad (5.8)$$

Here,  $k_1$  and  $Q_1$  are the stiffness and quality factor of the first mode, which are determined from simple harmonic oscillator fits to the cantilever's thermal spectrum (see Fig. 5.12).  $k_2$  and  $\nu_2$  are the stiffness and resonance frequency of the second mode and  $R$  is the radius of curvature of the tip, here nominally assumed to be 5 nm.  $A_{0,1}$  is the first mode's free amplitude and was evaluated at the same  $z$ -piezo height as  $\Delta\nu_2$ .

Fig. 5.13 shows representative bimodal AFM scans of a DPPA SLB, prepared identi-

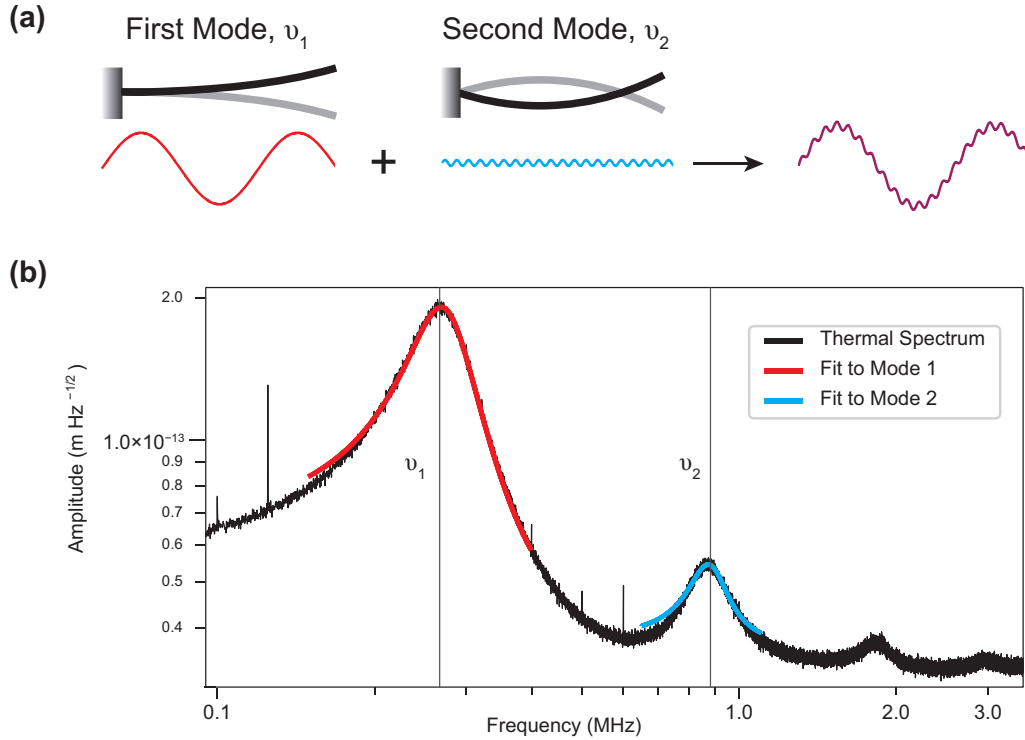
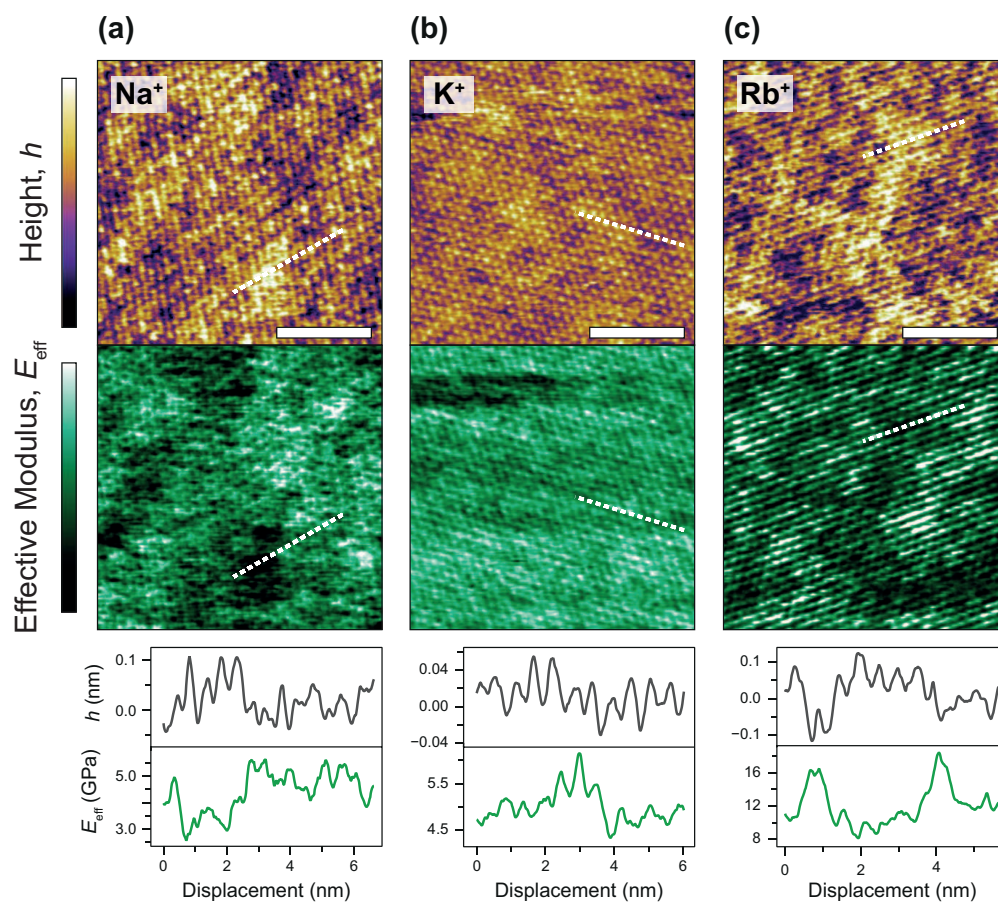


Fig. 5.12: (a) Illustration of bimodal AFM excitation. The cantilever is excited sinusoidally at its first resonant frequency (left, red trace), as normal with dynamic AFM. A second signal is sent that corresponds to the cantilever’s second mode of oscillation at a much higher frequency and smaller amplitude than that of the first (right, blue trace). Their combined signal is shown in purple; the first mode is used for imaging exactly as in our AM-AFM experiments earlier, while the second mode is used to extract quantitative mechanical information from the sample and is typically controlled *via* frequency-modulation [81, 82]. (b) Thermal spectrum of the Arrow UHF AuD cantilever; the first and second resonance frequencies ( $\nu_1$ ,  $\nu_2$ ) have been highlighted and simple harmonic oscillator fits to each mode are shown. Extracted cantilever quantities:  $k_1 = 0.956 \text{ N m}^{-1}$ ;  $Q_1 = 3.3$ ;  $k_2 \sim 7.07 \text{ N m}^{-1}$ .

cally to those used for the AM-AFM experiments and imaged using the same cantilever model. The effective modulus,  $E_{\text{eff}}$ , clearly reflects the periodicity and symmetry of the topography scan in each solution, confirming our hypothesis that ionic nano-domains modulate the mechanical properties of lipid bilayers. However, regions of high topography are correlated with a relatively *low* modulus (clear as e.g. dark green/black regions in (a) and (c)). Such outer-sphere ions reduce the Young’s modulus on the scale of domains of  $\mathcal{O}(10 \text{ nm}^2)$ , but also on that of individual charges ( $< 0.5 \text{ nm}^2$ ), as highlighted by the sections presented below each scan. This result, which appears general for all the ions studied here, agrees with our phase data in Fig. 5.4; networks of outer-sphere ions adsorbed *via* their hydration shells make the lipid-electrolyte interface more “fluid-like” ( $\theta \rightarrow 90^\circ$ ) and thus reduce the interface’s stiffness.

From the characteristic variation in lipid hydration landscape (Fig. 5.4 and 5.7), bind-



*Fig. 5.13:* Bimodal AFM reveals the molecular-level impact that ions have on SLB stiffness. Simultaneously recorded height (purple/yellow, upper) and effective Young's modulus ( $E_{\text{eff}}$ , green, lower) of a DPPA bilayer in 150 mM solutions of NaCl (a), KCl (b) and RbCl (c). In all cases,  $E_{\text{eff}}$  varies with the same periodicity and symmetry to the topography, showing that the ionic domains directly modulate the bilayer's mechanical properties. However there is an inverse effect; outer-sphere domains (yellow/white) induce relative softening of the membrane (dark green/black), especially clearly for  $\text{Na}^+$  and  $\text{Rb}^+$ . As well as this, sections (shown below each ion's trace) highlight the fact that *individual ions* (peaks in  $h$ ) reduce the membrane stiffness (troughs in  $E_{\text{eff}}$ ). Height and length scales cover 0.15 nm and 5 nm respectively for all ions.  $E_{\text{eff}}$  colour scales run from 3.3-6.2 GPa ( $\text{Na}^+$ ,  $\text{K}^+$ ) and 7.0-15.0 GPa ( $\text{Rb}^+$ ).

ing affinity (Fig. 5.3) and adsorption mode (Fig. 5.9), we similarly expect the Young's modulus to vary with the ion species. The bimodal scans demonstrate that this is indeed the case. Sodium (a) demonstrates large variations in height due to its multiple adsorption states and consequently the outer-sphere domains reduce the stiffness to about 3 GPa (left portion of section). Potassium's much more regular Stern layer generates a reduced variation in both topography and  $E_{\text{eff}}$  ((a) and (b) have identical height and stiffness colour scales). Interestingly, in the solution with  $\text{Rb}^+$ , the topography does not demonstrate such single ion perturbations as previously, although this may be due to the cantilever's reduced spring constant ( $k_1 \sim 1 \text{ N m}^{-1}$  c.f.  $k_1 \sim 1.7 \text{ N m}^{-1}$  used earlier, see discussion in subsection 5.3.1), or differences due to the bimodal operation. Clearly though, the modulus is greatly increased compared to the previous ions (note the increased colour scale and range of the section). This stiffening when rubidium is present is in fact expected when considering its specific coordination with the bilayer. We have shown that the large size of  $\text{Rb}^+$  makes it much more likely to bind directly to the lipids in an inner-sphere configuration. This means a larger fraction of headgroups are directly linked together by the metal, thereby resulting in an increase of  $E_{\text{eff}}$ . Sodium and potassium, conversely, participate to a greater extent in water-mediated binding that reduce the interface's stiffness by making it more fluid-like.

### *Static AFM force spectroscopy*

To confirm the validity of our bimodal measurements of the Young's modulus – especially whether or not there were any viscoelastic effects that arose from the high frequency ( $\sim 0.9 \text{ MHz}$ ) cantilever oscillations – we performed conventional static AFM force spectroscopy on a DPPA bilayer with the same model of cantilever (although in this case, the spring constant  $k_1 = 6.58 \text{ N m}^{-1}$ ). The  $z$ -piezo was used to lower the cantilever towards the bilayer, with no excitation. For each ionic solution, a map of  $12 \times 12$  curves were collected over an area of  $100 \times 100 \text{ nm}^2$ , that were converted into force versus sample indentation curves using Asylum Research's analysis software (v14.30.157) and knowledge of the cantilever's flexural stiffness and invOLS. From this, the same Hertz model as used in the bimodal analysis could be applied:

$$F_{\text{Hertz}} = \frac{4\sqrt{R}}{3} \frac{E_{\text{eff}}}{1 - \nu_{\text{lipid}}^2} \delta^{3/2}. \quad (5.9)$$

The Asylum Research software was used to apply the model with the assumption that the tip had a spherical geometry with  $R = 5 \text{ nm}$  and the bilayer had a Poisson's ratio of  $\nu_{\text{lipid}} = 0.33$ .

Fig. 5.14(a) displays exemplary force-indentation curves taken on the DPPA bilayer in

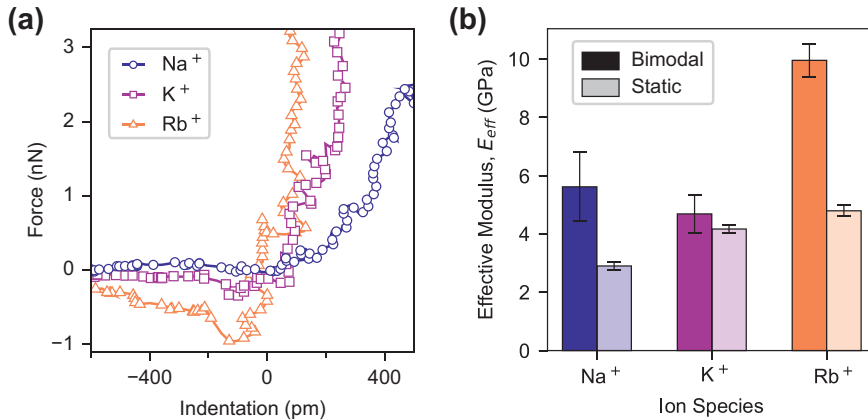


*Fig. 5.14:* The supported bilayer’s mechanical properties depend on the species of ion in solution. (a) Conventional AFM force spectroscopy highlights the different force gradients experienced by the tip when it compresses the DPPA membrane. Steeper gradients reflect a stiffening of the lipids. This effect can be quantified by fitting the curves with equation 5.9; results are shown in (b, lighter shades) alongside averaged  $E_{\text{eff}}$  extracted from bimodal scans (darker shades). In general there is good agreement between the two techniques’ order of magnitude and their Hofmeister-like ordering, although there are discrepancies (see text). Numerical values are presented in Table 5.3.

different electrolytes. The solutions clearly give rise to varying gradients in force; this is reflected in different values of  $E_{\text{eff}}$ , from fitting of equation 5.9. The average values thus extracted from the static force curves are presented in (b) (light shades), as well as the stiffnesses generated from the bimodal imaging (averaged over the entirety of  $> 10$  images for each solution) in darker shades. The static values indeed show that the stiffness is inversely related to the ion’s binding constant –  $E_{\text{eff}}^{\text{Na}^+} < E_{\text{eff}}^{\text{K}^+} < E_{\text{eff}}^{\text{Rb}^+}$  – in good agreement with the results of Fig. 5.13, as well as our interpretation of them. The Hofmeister-like trend is not as strong for the bimodal scans, and the value in sodium carries a large uncertainty; this could be related to the large variations in  $E_{\text{eff}}$  generated by the ionic domains (i.e. the large variation in Fig. 5.13(a)) which would not impact the “smeared-out” static spectroscopy.

While our effective stiffness values are broadly consistent, they are also rather high relative to previous AFM measurements of supported lipid bilayers [77, 84, 85], which find moduli in the tens to hundreds of MPa. It is of no particular surprise that our Hertz model, which assumes a semi-infinite sample and continuous elasticity throughout, becomes less reliable when confronted with a membrane just a few molecules thick and an indenter on the same lengthscale. However the same is, in principle, true of other studies that support lipids on mica (unless the precise behaviour of individual lipids is taken into account [79]), so it is unlikely that this is the reason for the discrepancy. Instead, we partially attribute the difference to our use of DPPA; the lipid is in gel phase at room temperature and thus is more ordered than fluid lipids and requires a larger force to compress. On top of this,

Cation	Bimodal $E_{\text{eff}}$ (GPa)	Static $E_{\text{eff}}$ (GPa)
$\text{Na}^+$	$6 \pm 1$	$2.9 \pm 0.1$
$\text{K}^+$	$4.7 \pm 0.7$	$4.2 \pm 0.1$
$\text{Rb}^+$	$10.0 \pm 0.6$	$4.8 \pm 0.2$

*Tab. 5.3:* Comparison of effective Young’s modulus extracted from bimodal scans (average across entire image) and from static (1D) force spectroscopy experiments. The data agree within an order of magnitude and both reproduce the Hofmeister trend. The absolute values are large relative to previously AFM measurements of SLBs ( $\mathcal{O}(10\text{-}100\text{ MPa})$  [77, 84]), but this could well be due to differences in the lipid phase, as well as the sensitivity of the cantilever and breakdown of the interaction models used.

the  $\text{PA}^-$  headgroup greatly changes the physico-chemical behaviours of the bilayer when compared to PC, as can be seen from its transition temperature being around  $65^\circ\text{C}$  [12]. This reflects the much larger energy needed to overcome the lipids’ intermolecular interaction than, say, DPPC, which melts at  $\sim 40\text{-}50^\circ\text{C}$  [86, 87], despite the molecules having identical acyl chains. This greater melting point suggests that DPPA would indeed have a higher stiffness than other, more commonly studied lipids. Finally, we use a relatively stiff cantilever throughout this study, as these were reliably found to generate high resolution images (see chapter 2). While this reduces the thermal noise contribution to the cantilever’s motion, it also reduces the sensitivity of the instrument (i.e. the force resolution is diminished). Thus high normal forces were necessary to reliably fit equation 5.9 to the curves of Fig. 5.14(a), and the effective modulus may be artificially inflated. That being said, the relative ordering of the effective moduli remains valid, as do our conclusions about the way the different ions’ binding modes affect the stiffness.

The present findings highlight the importance of specific-ion effects on many length-scales when investigating charge related modulation of biomembranes. In particular, we have shown that ions which adsorb more in outer-sphere configuration tend to soften the membrane relative to those which are able to form direct bonds linking lipid headgroups. Traditionally, dissolved salts are assumed to have a stiffening effect by forming hydrogen bond networks amongst lipids [6, 68, 70, 78]. Crucially however, and in contrast to many previous studies, the DPPA membrane is charged, inducing severe electrostatic repulsion at the headgroup level. Thus, the precise adsorption location of the ions will have a large impact on the membrane stiffness, an effect that is rarely taken into account. We can confirm this mechanism by lowering the pH of the solution. This increases the proportion of hydronium ions at the interface which compete with e.g. sodium for access to the lipid headgroups. As  $\text{H}_3\text{O}^+$  is essentially protonated water, it cannot bind in an outer-sphere configuration, and so decreasing the pH for a given NaCl concentration should allow more direct binding and stiffen the membrane. We conducted this experiment in a pH range where no (de)protonation of the lipid headgroups or silicon oxide cantilever tip are ex-

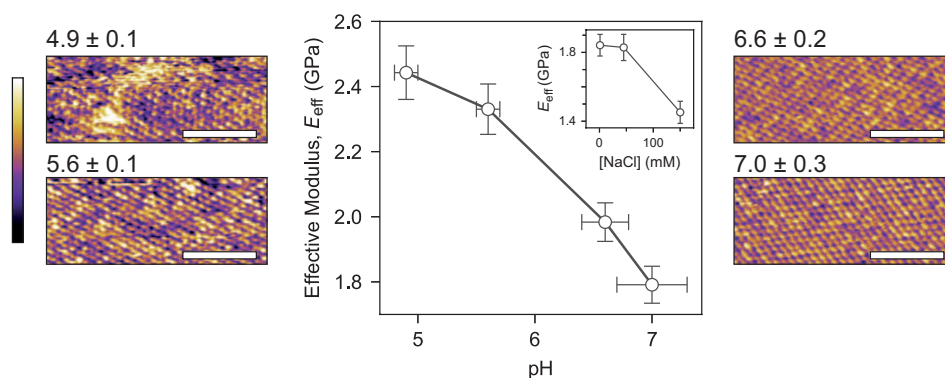


Fig. 5.15: The mechanism by which ions can soften the membrane is confirmed by repeating the static force spectroscopy experiments at fixed NaCl concentration (150 mM) but varying the pH. Unlike sodium,  $\text{H}_3\text{O}^+$  can only bind in inner-sphere coordination and thus increasing its relative density will decrease the proportion of outer-sphere bound ions. The spectroscopic results show that this indeed increases the measured  $E_{\text{eff}}$ , in line with our expectations. The effect of altering the global concentration also supports this interpretation (inset). High resolution topographs complement the modulus results by illustrating how the pH change affects the apparent Stern layer. In each AFM image, the length scale bar covers 5 nm and the colour scale covers 0.15 nm.

pected [12], hence allowing a straightforward analysis.

Fig. 5.15 shows the effective Young's modulus extracted from static force curves on a DPPA membrane in 150 mM NaCl. The solutions were titrated with HCl/NaOH to vary the pH, and high-resolution topographs that were taken in the same experiment are shown either side. The pH was measured immediately before and after the experiment to ensure it did not change significantly due to atmospheric  $\text{CO}_2$ . There is a clear stiffening associated with decreasing the pH that agrees with our hypothesis about the nature of inner-sphere ions. The inset shows the effect of varying the global NaCl concentration, which has a similar stiffening effect. Complementary high resolution images confirm that  $\text{H}_3\text{O}^+$  competes for access to the negatively charged phosphate groups; at pH 4.9, the topography appears rough due to the smaller size and faster dynamics of hydronium compared with  $\text{Na}^+$ . When the pH is increased to 5.6, the imaging becomes more stable (with fewer horizontal imaging artefacts), but the height still covers a broad range. Imaging the bilayer in pH 6.6 and 7.0, conversely, produces a remarkably regular interface that varies less, due to  $\text{Na}^+$  being allowed to form a more complete coverage on the lipid bilayer. Overall, this validates the manner in which ions in solution are able to locally reduce the stiffness of anionic lipid bilayers; they tend to form remarkably slowly evolving nano-networks on the membrane surface, mediated by water and competing with directly adsorbed charges.

## 5.5 Conclusions

We have combined experimental and computational methods to study the adsorption, coordination and dynamics of the alkali cations  $\text{Na}^+$ ,  $\text{K}^+$  and  $\text{Rb}^+$  at the interface with anionic lipid bilayers composed of DPPA. The continuum-scale electrophoresis experiments demonstrate that the charges adsorb to the membrane at rates dictated by their size and also that they experience an attractive ion-ion correlation. We then explore these distinctions at the nanoscale with AM-AFM, which highlights how each ion perturbs the Stern layer in a different manner, in good agreement with the binding constants. MD simulations confirm that hydration interactions dictate the ionic behaviour among the lipid headgroups and drive the formation of ion-specific outer-sphere correlations. This agrees with our AFM results, which demonstrate the propensity of sodium and potassium to form nanoscale networks that evolve over tens of seconds, driven by correlation energies of the order of  $-0.4 k_{\text{B}}T/\text{ion}$ . These networks induce a relative softening of the bilayer through local replacement of directly bound ions. Our model membrane is in gel-phase, in contrast to bilayers *in vivo*, but similar ion-dependent effects have been observed on fluid bilayers [14] and in principle. these effects could occur at any soft interface, as they rely only on water molecules mediating these common ions' interaction with themselves and with the lipids. At biological interfaces, we expect this mechanism to modulate the local viscoelastic properties on a timescale relevant for influencing processes such as molecular adsorption or the gating of mechanosensitive protein channels.

## 5.6 Materials and methods: chapter 5

### 5.6.1 Sample preparation

#### *Cleaning of glassware and apparatus*

A day prior to the each experiment, 5 ml glass vials, glass petri dish, tweezers, mini-extruder kit and 1 ml syringes (Avanti Polar Lipids, AL, USA) were bath sonicated for  $> 10$  minutes in ultrapure water (Merck-Millipore, 18.2  $\text{M}\Omega$  resistivity). The fluid was exchanged for isopropanol (Fisher Chemical, certified ACS,  $\geq 99.5\%$  purity) and the apparatus was sonicated for a further 10 minutes to remove any contaminant organic material. The isopropanol was drained, the equipment was rinsed thoroughly with ultrapure water until no observable trace of the solvent remained and it was then sonicated in the ultrapure water for 10 minutes. Finally, the water was drained and the equipment was covered and allowed to dry completely at a temperature of  $40^\circ\text{C}$ .

### *Small unilamellar vesicle (SUV) suspensions*

1,2-dipalmitoyl-*sn*-glycero-3-phosphate (DPPA) (Avanti Polar Lipids, AL, USA) was purchased in powder form and used without further purification. A mass of  $\sim 1$  mg of DPPA was measured into a 5 ml glass vial and diluted to a lipid concentration of  $1 \text{ mg ml}^{-1}$  with 150 mM NaCl (ACS reagent grade,  $\geq 99\%$ , Sigma Aldrich). For the electrophoretic measurements, the salt concentration and type was to be varied, so we carried out the below procedure with the lipids suspended in ultrapure water buffered with 5 mM sodium phosphate dibasic ( $\geq 99.0\%$ , Sigma Aldrich) to a pH of 7.45. The buffer was necessary because evaluation of the binding constants of each ion required precise knowledge of the concentration of protons in solution. Buffering agents were not used as part of the AFM experiments because these have been shown to alter the hydration structure at hydrophilic interfaces and interfere with high-resolution AFM imaging [88]. The solution was bath-sonicated for 30 minutes at  $55^\circ\text{C}$ , resulting in a milky, opaque colour due to the formation of multilamellar vesicles. These vesicles were held at  $-18^\circ\text{C}$  for 30 minutes, then sonicated at  $55^\circ\text{C}$  for the same period of time, resulting in a uniform, transparent solution. This “freeze-thaw” method encourages the break up of larger vesicles and tends to result in more well-defined, smaller lipid assemblies [39]. The solution was then diluted further with 150 mM NaCl to a final lipid concentration of  $0.1 \text{ mg ml}^{-1}$ . The cleaned extruder, along with a polycarbonate 100 nm membrane (WhatMan, Sigma Aldrich) were used to extrude the lipid vesicles at least 15 (but always an odd number) times at  $70^\circ\text{C}$  (in our case, the melting temperature for DPPA was  $T_m \sim 67^\circ\text{C}$  [12]). This results in a monodisperse SUV suspension, with vesicles of  $\sim 100$  nm diameter. The solution was then either used directly, or sealed in a glass vial and refrigerated for a maximum of one week.

### *Supported lipid bilayers*

Having produced the SUV suspension, the vesicle fusion method [89–91] was then utilised to produce supported lipid bilayers for the AFM experiments. This process involves pipetting the vesicle solution onto a stiff, hydrophilic support – in our case, muscovite mica (grade IV, SPI Supplies, PA, USA). The muscovite mica support had previously been affixed to a steel support with epoxy glue. The mica was cleaved 3 times with adhesive tape or until mirror-smooth to the naked eye. After extrusion, approximately 80  $\mu\text{l}$  of the DPPA SUV solution (see above) was pipetted onto the mica and the entire sample was incubated in a sealed glass petri dish with a damp cotton pad (to reduce evaporation of the sample) at  $80^\circ\text{C}$ . The sample was then cooled at a rate of  $2^\circ\text{C h}^{-1}$  to  $60^\circ\text{C}$ , and then cooled to  $25^\circ\text{C}$  at around  $6^\circ\text{C h}^{-1}$ . This elongated heating ramp ensured the lipids went through their phase transition from liquid disordered ( $L_\alpha$ ) to solid ordered ( $L_\beta$ ) state as close to equilibrium as possible. This procedure reliably produced at least one defect-free

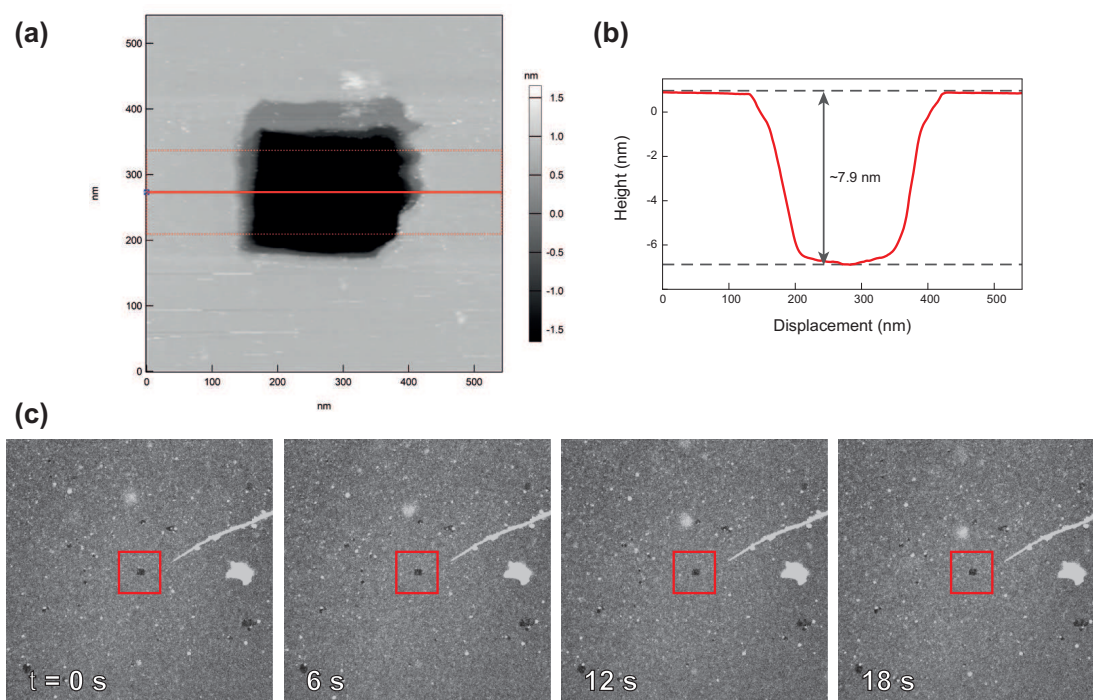


Fig. 5.16: Verifying the formation of DPPA supported lipid bilayers. (a)  $(550 \times 550)$  nm<sup>2</sup> topographic image showing the result of scanning a smaller area under “harsh” conditions in contact mode. The tip has clearly created a defect in the bilayer that extends down to the mica below. A section is taken at the thick red line that is laterally averaged between the two dashed red lines (b). The depth of the defect is double that expected for a bilayer, showing that our procedure has produced a stack of two membranes on the mica. (c) Representative  $(500 \times 500)$   $\mu\text{m}^2$  confocal microscopy scans of a fluorescently-labelled DPPA membrane with a central region of  $(10 \times 10)$   $\mu\text{m}^2$  bleached by repeated scanning (red boxes). The bleaching as well as the lack of recovery over 3 minutes confirms that the background fluorescence comes from a well-formed DPPA bilayer. Bright defects in centre-right of images were manually created with a sharp needle to create a reference point.

DPPA bilayer on the mica surface that could be checked via AFM, by applying large normal forces while scanning in contact mode to create holes in the membrane (see Fig. 5.16).

The robustness of this procedure to produce supported lipid bilayers on macroscopic lengthscales was further verified by fluorescence microscopy. This required including a fluorescently labelled lipid probe – 1,2-dipalmitoyl-*sn*-glycero-3-phosphoethanolamine-N-(lissamine rhodamine B sulfonyl), (16:0 Liss Rhod PE, Avanti Polar Lipids, AL, USA) – in the bilayer at a concentration of 0.1 mol%, a sufficiently low concentration such that the bilayer behaviour would not be significantly perturbed. The fluorescent probe was purchased in chloroform solution, which was thoroughly evaporated before combining with the correct mass of DPPA in power form. An identical procedure (see above) then followed to produce supported lipid bilayers on mica before loading into an EZ-C1 Confocal Microscope (Nikon UK, Kingston, UK) and imaging in reflection mode. A small,  $(10 \times$

10)  $\mu\text{m}^2$  region was raster-scanned repeatedly in order to bleach the rhodamine molecules, before imaging a zoomed-out region of  $(500 \times 500) \mu\text{m}^2$  at a rate of 1 s/image and a delay of 2 s between images. The presence of a bleached square (red boxes) that did not recover over the full 180 s of scanning (full data not shown) confirmed the successful formation of a large-scale gel-phase DPPA membrane on the mica surface.

### 5.6.2 Electrophoresis

The electrophoretic mobility of the DPPA SUV suspension was measured using a Zetasizer Nano ZS (Malvern Instruments, Worcestershire, UK) with a 4 mW He-Ne laser. The relative permittivity,  $\epsilon$ , and viscosity,  $\eta$ , in equation 5.1 were estimated for each ionic solution using the “solvent-builder” incorporated into the Zetasizer ZS software.

Measurement cells were initially rinsed with ultrapure water, followed by isopropanol and finally with ultrapure water once more, prior to the vesicles coming into contact with them. Approximately 100  $\mu\text{l}$  of the 0.1  $\text{mg ml}^{-1}$  vesicle solution was pipetted into a disposable low volume cuvette for the purposes of measuring  $a$ , and another 1 ml was transferred into a folded capillary zeta cell (both Malvern Instruments, Worcestershire, UK) to find  $\zeta$ .

The vesicles’ radii were obtained via dynamic light scattering (DLS), which relates the autocorrelation of light backscattered from the solution at rest to the Brownian motion of the vesicles. This then gives an estimate for the particles’ diffusion coefficient,  $D$ , which can be linked to the radius *via* the Stokes-Einstein relation;

$$a = \frac{k_{\text{B}}T}{3\pi\eta D}. \quad (5.10)$$

### 5.6.3 AFM imaging and spectroscopy

The AFM images and spectroscopy curves were all collected using a commercial Cypher ES AFM (Asylum Research, Santa Barbara, USA) using Arrow UHF AuD cantilevers (Nanoworld, Neuchâtel, Switzerland), which have tips with nominal radii of curvature of less than 10 nm. The stiffness of the cantilever used to produce the images and data of Fig. 5.4 and 5.11 was  $k_1 = 1.71 \text{ N m}^{-1}$ , calibrated from its thermal spectrum and subsequent measurement of the cantilever’s invOLS on a bare mica substrate (see chapter chapter 2). Similarly, the cantilevers used to produce the bimodal images and static Young’s modulus values had first-mode stiffnesses of  $k_1 = 0.956 \text{ N m}^{-1}$  and  $k_1 = 6.58 \text{ N m}^{-1}$  respectively. Calibrating the second-mode stiffness for the bimodal images,  $k_2$ , is less straightforward; there is no well-characterised method for achieving this, especially for

such unconventional arrow shaped levers. The value of  $k_2 \sim 7.07 \text{ N m}^{-1}$  was thus estimated from a thermal fit to the second mode (blue curve in Fig. 5.12), using the same invOLS as that of the first. As this is assumed constant throughout, the results of Fig. 5.13 and 5.14(b) still allow comparison between the different ion species, and their order-of-magnitude agreement with the static AFM spectroscopy implies that this is a valid approach.

A day prior to imaging, the cantilever was rinsed in isopropanol. Next, the cantilever and its holder were bathed in isopropanol overnight ( $> 12$  hours), followed by rinsing and bathing in ultrapure water for at least 30 minutes. This serves to remove any organic material or silicon oil from the tip that may have accumulated during its storage in its gel box [92], while minimising any alteration of tip geometry/size. The cantilever and tip were then wetted with  $\sim 50 \mu\text{l}$  of 150 mM NaCl. The supported lipid bilayers were removed from the oven at room temperature and rinsed by repeatedly pipetting 50  $\mu\text{l}$  of 150 mM NaCl into the fluid on top of the mica disc and then taking out the same volume. This procedure removes any unfused vesicles and ensures that the imaging solution is as clean as possible. The cantilever and sample were then brought into close proximity and the images and force spectroscopy curves were subsequently collected. When sufficient data had been acquired in the NaCl solution, the tip and sample were separated, with care taken to keep the SLB immersed at all times. The NaCl was then replaced with 150 mM KCl by rinsing 50  $\mu\text{l}$  at a time, with at least 500  $\mu\text{l}$  total fluid exchanged ( $\sim 8$  times the volume initially on the disc). Images and force curves were collected as before, and the procedure was then repeated for 150 mM RbCl.

All topography images were collected in amplitude modulation mode while fully immersed in each salt solution. Free (that is, when not interacting with the sample) first mode amplitudes,  $A_{0,1}$ , of 1-2 nm were used in all cases. The ratio between the working amplitude,  $A_w$ , used as part of the feedback loop and the free amplitude is known as the setpoint ratio,  $S_p$ , and was maintained at  $S_p \equiv A_w/A_{0,1} \geq 70\%$ , in order to mainly probe the fluid at the bilayer-electrolyte interface. Multiple images were taken in each ionic solution to confirm the effects observed in Fig. 5.4 were consistent and reproducible.

#### 5.6.4 Image analysis

All topography and phase images presented were line-by-line flattened and low-pass filtered for display to remove unwanted high-frequency noise. However, all quantitative analysis described was carried out on unfiltered images.

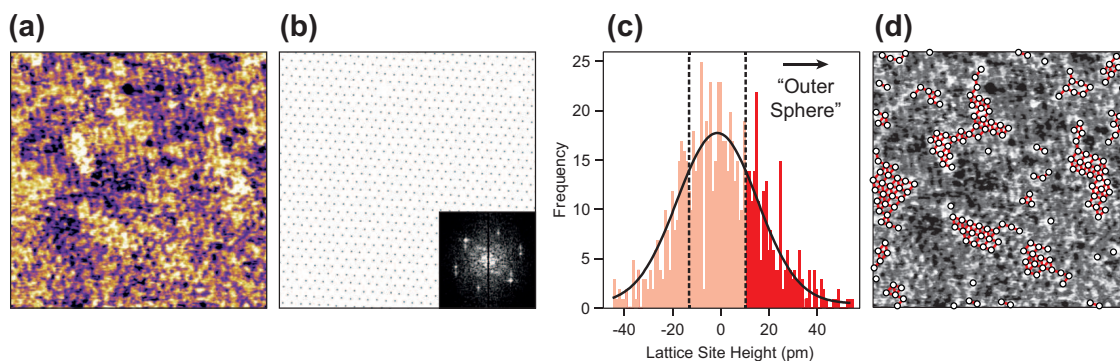


Fig. 5.17: Illustration of the process to identify nearest neighbour interactions of outer-sphere ions on the bilayer. (a) Original (flattened) image of DPPA bilayer in 150 mM NaCl. (b) Idealised lattice sites generated from FFT (inset). (c) Histogram of the average AFM topography height at the lattice site locations with Gaussian fit (black curve) and dashed lines showing the distinction between the “upper” category identified as outer-sphere ions (right hand side) and the lower lattice sites. (d) The algorithm identifies the highest, outer-sphere sites well, as shown here with white circles. The nearest-neighbour interactions are displayed with red bars.

### Identification of outer-sphere ions

The semi-automated categorisation of outer-sphere ions discussed above used the FFTs of the  $(15 \times 15) \text{ nm}^2$  AFM height scans to generate an idealised reference lattice (Fig. 5.17)(b)) that was used to define each lipid binding site. The height image was then passed through a square averaging filter with a kernel of 25 pixels (approximately corresponding to the area-per-lipid at this level of zoom) in order to reduce the impact of imaging noise on the calculation. A histogram of the height of the pixels lying on the reference lattice site (c) was then populated and fitted with a Gaussian function in order to determine the distribution’s mean,  $\mu_s$ , and width,  $\sigma_s$ . Those sites with heights of  $z(x_k, y_l) > \mu_s + \sigma_s/2$  (dashed line, right, in (c)) were interpreted as having an ion adsorbed in outer-sphere coordination. “Middling” and ‘low’ sites were respectively defined as having  $\mu_s - \sigma_s/2 < z(x_k, y_l) < \mu_s + \sigma_s/2$  and  $z(x_k, y_l) < \mu_s - \sigma_s/2$ , but the assignment of these levels is less straightforward and so our analysis focusses on just the upper category. These distributions were averaged over 12 images for the NaCl electrolyte and 15 for KCl. The principles of this procedure are illustrated in Fig. 5.17, and can be seen in (d) to locate the domains with good accuracy.

In order to generate the theoretical random distribution of ions of Fig. 5.5, the same procedure as above was repeated, but once the categorisation of the sites by their height was complete, a random number generator was used to shuffle the site categories. The newly mixed “high” sites were put through the same nearest neighbour analysis with identical parameters.

### *Simulations*

All chemical species were described using the CHARMM36 force field, with TIP3P parameters for water. DPPA molecules were assumed to have a net charge of  $-1$ , with atomic partial charges taken from standard values in the force field. For the ions, the improved CHARMM36 parameters of ref. [93] were used. The bilayer (of area  $65.45 \times 65.45 \text{ \AA}^2$ ) was first constructed using the CHARMM-GUI membrane builder [94]. Visual molecular dynamics (VMD) [95] was used to add solvation water and ions (with the Ionize plugin ensuring the total salt concentration was 150 mM). This configuration was then energy minimised using NAMD 2.11 [62].

The Newtonian equations of motion were solved using a time step of 2 fs. Electrostatic interactions were computed using the particle-mesh Ewald (PME) method with the usual settings in NAMD (1  $\text{\AA}$  resolution, updated every 2 time steps). Lennard-Jones interactions were truncated at 1.2 nm, employing a switching function starting at 1.0 nm. Periodic boundary conditions were employed in all directions. Temperature was kept constant at 298 K using a Langevin thermostat with a relaxation time of 1 ps. A pressure of 1 atm in the direction perpendicular to the bilayer was imposed using the anisotropic Nosé-Hoover-Langevin piston implemented in NAMD (oscillation period of 100 fs and decay time of 50 fs). The lateral pressure imposed by the barostat was adjusted to maintain the bilayer at zero tension, so our simulations correspond to the  $\text{NPT}\gamma$  ensemble. For each case shown in Table 5.2, we performed  $\sim 20$  ns of equilibration and  $\sim 100$  ns of production simulation.



## REFERENCES: CHAPTER 5

- [1] V. A. Bloomfield, "DNA condensation by multivalent cations", *Biopolymers* **1997**, *44*, 269–282.
- [2] F. Sheinerman, "Electrostatic aspects of protein–protein interactions", *Curr. Opin. Struct. Biol.* **2000**, *10*, 153–159.
- [3] P. Jungwirth, P. S. Cremer, "Beyond hofmeister", *Nat. Chem.* **2014**, *6*, 261–263.
- [4] G. Cevc, "Membrane electrostatics.", *Biochim. Biophys. Acta* **1990**, *1031*, 311–382.
- [5] J. J. Shin, C. J. Loewen, "Putting the pH into phosphatidic acid signaling", *BMC Biol.* **2011**, *9*, 85.
- [6] Y. A. Ermakov, K. Kamaraju, K. Sengupta, S. Sukharev, "Gadolinium Ions Block Mechanosensitive Channels by Altering the Packing and Lateral Pressure of Anionic Lipids", *Biophys. J.* **2010**, *98*, 1018–1027.
- [7] P. A. Janmey, P. K. Kinnunen, "Biophysical properties of lipids and dynamic membranes", *Trends Cell Biol.* **2006**, *16*, 538–546.
- [8] L. a. Bagatolli, J. H. Ipsen, A. C. Simonsen, O. G. Mouritsen, "An outlook on organization of lipids in membranes: Searching for a realistic connection with the organization of biological membranes", *Prog. Lipid Res.* **2010**, *49*, 378–389.
- [9] D. Lingwood, K. Simons, "Lipid rafts as a membrane-organizing principle.", *Science* **2010**, *327*, 46–50.
- [10] R. Phillips, T. Ursell, P. Wiggins, P. Sens, "Emerging roles for lipids in shaping membrane-protein function", *Nature* **2009**, *459*, 379–385.
- [11] B. P. Young, J. J. H. Shin, R. Orij, J. T. Chao, S. C. Li, X. L. Guan, A. Khong, E. Jan, M. R. Wenk, W. A. Prinz, G. J. Smits, C. J. R. Loewen, "Phosphatidic Acid Is a pH Biosensor That Links Membrane Biogenesis to Metabolism", *Science (80-. )*. **2010**, *329*, 1085–1088.
- [12] D. Marsh, *CRC Handbook of Lipid Bilayers*, Second, CRC Press, **2013**.
- [13] M. L. Berkowitz, D. L. Bostick, S. Pandit, "Aqueous Solutions next to Phospholipid Membrane Surfaces: Insights from Simulations", *Chem. Rev.* **2006**, *106*, 1527–1539.
- [14] L. Piantanida, H. L. Bolt, N. Rozatian, S. L. Cobb, K. Voitchovsky, "Ions Modulate Stress-Induced Nanotexture in Supported Fluid Lipid Bilayers", *Biophys. J.* **2017**, *113*, 426–439.
- [15] R. A. Böckmann, A. Hac, T. Heimburg, H. Grubmüller, "Effect of sodium chloride on a lipid bilayer", *Biophys. J.* **2003**, *85*, 1647–1655.
- [16] E. R. Lamberson, L. R. Cambrea, J. S. Hovis, "Controlling the charge and organization of anionic lipid bilayers: Effect of monovalent and divalent ions", *J. Phys. Chem. B* **2007**, *111*, 13664–13667.
- [17] L. R. Cambrea, F. Haque, J. L. Schieler, J.-C. Rochet, J. S. Hovis, "Effect of Ions on the Organization of Phosphatidylcholine/Phosphatidic Acid Bilayers", *Biophys. J.* **2007**, *93*, 1630–1638.
- [18] N. Shimokawa, M. Hishida, H. Seto, K. Yoshikawa, "Phase separation of a mixture of charged and neutral lipids on a giant vesicle induced by small cations", *Chem. Phys. Lett.* **2010**, *496*, 59–63.
- [19] D. R. Slochower, Y.-H. Wang, R. W. Tourdot, R. Radhakrishnan, P. a. Janmey, "Counterion-mediated pattern formation in membranes containing anionic lipids", *Adv. Colloid Interface Sci.* **2014**, *208*, 177–188.

- [20] B. Ali Doosti, W. Pezeshkian, D. S. Bruhn, J. H. Ipsen, H. Khandelia, G. D. M. Jeffries, T. Lobovkina, “Membrane Tubulation in Lipid Vesicles Triggered by the Local Application of Calcium Ions”, *Langmuir* **2017**, *33*, 11010–11017.
- [21] S. Ohki, S. Roy, H. Ohshima, K. Leonards, “Monovalent cation-induced phospholipid vesicle aggregation: effect of ion binding.”, *Biochemistry* **1984**, *23*, 6126–32.
- [22] W. B. Huttner, J. Zimmerberg, “Implications of lipid microdomains for membrane curvature, budding and fission”, *Curr. Opin. Cell Biol.* **2001**, *13*, 478–484.
- [23] R. Vácha, S. W. I. Siu, M. Petrov, R. A. Böckmann, J. Barucha-Kraszewska, P. Jurkiewicz, M. Hof, M. L. Berkowitz, P. Jungwirth, “Effects of Alkali Cations and Halide Anions on the DOPC Lipid Membrane †”, *J. Phys. Chem. A* **2009**, *113*, 7235–7243.
- [24] W. Zhao, T. Róg, A. a. Gurtovenko, I. Vattulainen, M. Karttunen, “Atomic-scale structure and electrostatics of anionic palmitoyloleoylphosphatidylglycerol lipid bilayers with Na<sup>+</sup> counterions.”, *Biophys. J.* **2007**, *92*, 1114–1124.
- [25] A. a. Gurtovenko, I. Vattulainen, “Effect of NaCl and KCl on phosphatidylcholine and phosphatidylethanolamine lipid Membranes: insight from atomic-Scale simulations for understanding salt-induced effects in the plasma membrane”, *J. Phys. Chem. B* **2008**, *112*, 1953–1962.
- [26] J. Faraudo, A. Travasset, “Phosphatidic Acid Domains in Membranes: Effect of Divalent Counterions”, *Biophys. J.* **2007**, *92*, 2806–2818.
- [27] T. Fukuma, M. Higgins, S. Jarvis, “Direct Imaging of Lipid-Ion Network Formation under Physiological Conditions by Frequency Modulation Atomic Force Microscopy”, *Phys. Rev. Lett.* **2007**, *98*, 106101.
- [28] B. Klasczyk, V. Knecht, R. Lipowsky, R. Dimova, “Interactions of Alkali Metal Chlorides with Phosphatidylcholine Vesicles”, *Langmuir* **2010**, *26*, 18951–18958.
- [29] P. Maity, B. Saha, G. Kumar, S. Karmakar, “Binding of monovalent alkali metal ions with negatively charged phospholipid membranes”, *Biochim. Biophys. Acta - Biomembr.* **2016**, *1858*, 706–714.
- [30] J. Song, J. Franck, P. Pincus, M. W. Kim, S. Han, “Specific Ions Modulate Diffusion Dynamics of Hydration Water on Lipid Membrane Surfaces”, *J. Am. Chem. Soc.* **2014**, *136*, 2642–2649.
- [31] M. Ricci, P. Spijker, K. Voitchovsky, “Water-induced correlation between single ions imaged at the solid-liquid interface.”, *Nat. Commun.* **2014**, *5*, 4400.
- [32] A. Springer, V. Hagen, D. a. Cherepanov, Y. N. Antonenko, P. Pohl, “Protons migrate along interfacial water without significant contributions from jumps between ionizable groups on the membrane surface.”, *Proc. Natl. Acad. Sci. U. S. A.* **2011**, *108*, 14461–14466.
- [33] E. Weichselbaum, M. Österbauer, D. G. Knyazev, O. V. Batishchev, S. A. Akimov, T. Hai Nguyen, C. Zhang, G. Knör, N. Agmon, P. Carloni, P. Pohl, “Origin of proton affinity to membrane/water interfaces”, *Sci. Rep.* **2017**, *7*, 4553.
- [34] T. H. Nguyen, C. Zhang, E. Weichselbaum, D. G. Knyazev, P. Pohl, P. Carloni, “Interfacial water molecules at biological membranes: Structural features and role for lateral proton diffusion”, *PLoS One* **2018**, *13*, (Ed.: C. Johnson), e0193454.
- [35] S. Antoranz Contera, K. Voitchovsky, J. F. Ryan, “Controlled ionic condensation at the surface of a native extremophile membrane.”, *Nanoscale* **2010**, *2*, 222–9.
- [36] S. A. Tatulian, “Binding of alkaline-earth metal cations and some anions to phosphatidylcholine liposomes.”, *Eur. J. Biochem.* **1987**, *170*, 413–20.
- [37] M. Eisenberg, T. Gresalfi, T. Riccio, S. McLaughlin, “Adsorption of monovalent cations to bilayer membranes containing negative phospholipids.”, *Biochemistry* **1979**, *18*, 5213–5223.
- [38] M. M. A. E. Claessens, F. A. M. Leermakers, F. A. Hoekstra, M. A. Cohen Stuart, “Opposing Effects of Cation Binding and Hydration on the Bending Rigidity of Anionic Lipid Bilayers”, *J. Phys. Chem. B* **2007**, *111*, 7127–7132.
- [39] M. M. Claessens, B. F. Van Oort, F. A. Leermakers, F. A. Hoekstra, M. A. Stuart, “Charged lipid vesicles: Effects of salts on bending rigidity, stability, and size”, *Biophys. J.* **2004**, *87*, 3882–3893.

- [40] J. C. Berg, *An Introduction to Interfaces and Colloids: The Bridge to Nanoscience*, 1st ed., World Scientific Publishing Co., **2009**.
- [41] K. Makino, T. Yamada, M. Kimura, T. Oka, H. Ohshima, T. Kondo, “Temperature- and ionic strength-induced conformational changes in the lipid head group region of liposomes as suggested by zeta potential data”, *Biophys. Chem.* **1991**, *41*, 175–183.
- [42] M. T. Roy, M. Gallardo, J. Estelrich, “Influence of Size on Electrokinetic Behavior of Phosphatidylserine and Phosphatidylethanolamine Lipid Vesicles”, *J. Colloid Interface Sci.* **1998**, *206*, 512–517.
- [43] S. Nir, C. Newton, D. Papahadjopoulos, “Binding of Cations to Phosphatidylserine Vesicles”, *Bioelectrochemistry Bioenerg.* **1978**, *5*, 116–133.
- [44] S. McLaughlin, N. Mulrine, T. Gresalfi, G. Vaio, A. McLaughlin, “Adsorption of divalent cations to bilayer membranes containing phosphatidylserine.”, *J. Gen. Physiol.* **1981**, *77*, 445–73.
- [45] H.-J. Butt, K. Graf, M. Kappl, *Physics and Chemistry of Interfaces*, Wiley-VCH, **2003**.
- [46] Y. F. Dufrène, T. Ando, R. Garcia, D. Alsteens, D. Martinez-Martin, A. Engel, C. Gerber, D. J. Müller, “Imaging modes of atomic force microscopy for application in molecular and cell biology”, *Nat. Nanotechnol.* **2017**, *12*, 295–307.
- [47] K. Voïtchovsky, J. J. Kuna, S. A. Contera, E. Tosatti, F. Stellacci, “Direct mapping of the solid-liquid adhesion energy with subnanometre resolution.”, *Nat. Nanotechnol.* **2010**, *5*, 401–405.
- [48] K. Voïtchovsky, “Anharmonicity, solvation forces, and resolution in atomic force microscopy at the solid-liquid interface”, *Phys. Rev. E* **2013**, *88*, 022407.
- [49] S. de Beer, D. van den Ende, F. Mugele, “Dissipation and oscillatory solvation forces in confined liquids studied by small-amplitude atomic force spectroscopy.”, *Nanotechnology* **2010**, *21*, 325703.
- [50] J. N. Israelachvili, R. M. Pashley, “Molecular layering of water at surfaces and origin of repulsive hydration forces”, *Nature* **1983**, *306*, 249–250.
- [51] J. N. Israelachvili, *Intermolecular and Surface Forces*, Third, Elsevier, **2011**.
- [52] V. Parsegian, T. Zemb, “Hydration forces: Observations, explanations, expectations, questions”, *Curr. Opin. Colloid Interface Sci.* **2011**, *16*, 618–624.
- [53] S. S. Lee, P. Fenter, K. L. Nagy, N. C. Sturchio, “Monovalent Ion Adsorption at the Muscovite (001)-Solution Interface: Relationships among Ion Coverage and Speciation, Interfacial Water Structure, and Substrate Relaxation”, *Langmuir* **2012**, *28*, 8637–8650.
- [54] S. S. Lee, P. Fenter, K. L. Nagy, N. C. Sturchio, “Real-time observation of cation exchange kinetics and dynamics at the muscovite-water interface”, *Nat. Commun.* **2017**, *8*, 15826.
- [55] C. Cafolla, K. Voïtchovsky, “Lubricating properties of single metal ions at interfaces”, *Nanoscale* **2018**, *10*, 11831–11840.
- [56] H. Asakawa, S. Yoshioka, K. I. Nishimura, T. Fukuma, “Spatial distribution of lipid headgroups and water molecules at membrane/water interfaces visualized by three-dimensional scanning force microscopy”, *ACS Nano* **2012**, *6*, 9013–9020.
- [57] M. Ricci, P. Spijker, F. Stellacci, J.-F. Molinari, K. Voïtchovsky, “Direct Visualization of Single Ions in the Stern Layer of Calcite”, *Langmuir* **2013**, *29*, 2207–2216.
- [58] A. Maali, T. Cohen-Bouhacina, G. Couturier, J.-P. Aimé, “Oscillatory Dissipation of a Simple Confined Liquid”, *Phys. Rev. Lett.* **2006**, *96*, 086105.
- [59] T.-D. Li, J. Gao, R. Szoszkiewicz, U. Landman, E. Riedo, “Structured and viscous water in subnanometer gaps”, *Phys. Rev. B* **2007**, *75*, 115415.
- [60] S. de Beer, D. van den Ende, F. Mugele, “Atomic force microscopy cantilever dynamics in liquid in the presence of tip sample interaction”, *Appl. Phys. Lett.* **2008**, *93*, 253106.
- [61] K. Kobayashi, Y. Liang, S. Murata, T. Matsuoka, S. Takahashi, N. Nishi, T. Sakka, “Ion Distribution and Hydration Structure in the Stern Layer on Muscovite Surface”, *Langmuir* **2017**, *33*, 3892–3899.

- [62] J. C. Phillips, R. Braun, W. Wang, J. Gumbart, E. Tajkhorshid, E. Villa, C. Chipot, R. D. Skeel, L. Kalé, K. Schulten, “Scalable molecular dynamics with NAMD”, *J. Comput. Chem.* **2005**, *26*, 1781–1802.
- [63] J. Wang, A. J. Bard, “Direct Atomic Force Microscopic Determination of Surface Charge at the Gold/Electrolyte Interface: The Inadequacy of Classical GCS Theory in Describing the Double-Layer Charge Distribution”, *J. Phys. Chem. B* **2001**, *105*, 5217–5222.
- [64] U. Raviv, P. Laurat, J. Klein, “Time dependence of forces between mica surfaces in water and its relation to the release of surface ions”, *J. Chem. Phys.* **2002**, *116*, 5167.
- [65] H. Yamashita, K. Voitchovsky, T. Uchihashi, S. A. Contera, J. F. Ryan, T. Ando, “Dynamics of bacteriorhodopsin 2D crystal observed by high-speed atomic force microscopy”, *J. Struct. Biol.* **2009**, *167*, 153–158.
- [66] I. C. Bourg, G. Sposito, “Molecular dynamics simulations of the electrical double layer on smectite surfaces contacting concentrated mixed electrolyte (NaCl–CaCl<sub>2</sub>) solutions”, *J. Colloid Interface Sci.* **2011**, *360*, 701–715.
- [67] A. Anishkin, S. H. Loukin, J. Teng, C. Kung, “Feeling the hidden mechanical forces in lipid bilayer is an original sense”, *Proc. Natl. Acad. Sci.* **2014**, *111*, 7898–7905.
- [68] S. Garcia-Manyes, G. Oncins, F. Sanz, “Effect of ion-binding and chemical phospholipid structure on the nanomechanics of lipid bilayers studied by force spectroscopy.”, *Biophys. J.* **2005**, *89*, 1812–26.
- [69] S. Garcia-Manyes, F. Sanz, “Nanomechanics of lipid bilayers by force spectroscopy with AFM: A perspective”, *Biochim. Biophys. Acta - Biomembr.* **2010**, *1798*, 741–749.
- [70] G. Pabst, A. Hodzic, J. Štrancar, S. Danner, M. Rappolt, P. Lagner, “Rigidification of Neutral Lipid Bilayers in the Presence of Salts”, *Biophys. J.* **2007**, *93*, 2688–2696.
- [71] H. Bouvrais, L. Duelund, J. H. Ipsen, “Buffers Affect the Bending Rigidity of Model Lipid Membranes”, *Langmuir* **2014**, *30*, 13–16.
- [72] J. J. L. Cascales, S. D. O. Costa, A. Garro, R. D. Enriz, “Mechanical properties of binary DPPC/DPPS bilayers”, *RSC Adv.* **2012**, *2*, 11743.
- [73] A. Hemmerle, G. Fragneto, J. Daillant, T. Charitat, “Reduction in Tension and Stiffening of Lipid Membranes in an Electric Field Revealed by X-Ray Scattering”, *Phys. Rev. Lett.* **2016**, *116*, 228101.
- [74] A. Alessandrini, H. M. Seeger, A. Di Cerbo, T. Caramaschi, P. Facci, “What do we really measure in AFM punch-through experiments on supported lipid bilayers?”, *Soft Matter* **2011**, *7*, 7054.
- [75] Y. Zhou, R. M. Raphael, “Solution pH Alters Mechanical and Electrical Properties of Phosphatidylcholine Membranes: Relation between Interfacial Electrostatics, Intramembrane Potential, and Bending Elasticity”, *Biophys. J.* **2007**, *92*, 2451–2462.
- [76] P. Bassereau, B. Sorre, A. Lévy, “Bending lipid membranes: Experiments after W. Helfrich’s model”, *Adv. Colloid Interface Sci.* **2014**, *208*, 47–57.
- [77] L. Picas, F. Rico, S. Scheuring, “Direct Measurement of the Mechanical Properties of Lipid Phases in Supported Bilayers”, *Biophys. J.* **2012**, *102*, L01–L03.
- [78] K. Voitchovsky, S. Antoranz Contera, M. Kamihira, A. Watts, J. F. Ryan, “Differential stiffness and lipid mobility in the leaflets of purple membranes.”, *Biophys. J.* **2006**, *90*, 2075–85.
- [79] C. Das, K. H. Sheikh, P. D. Olmsted, S. D. Connell, “Nanoscale mechanical probing of supported lipid bilayers with atomic force microscopy”, *Phys. Rev. E* **2010**, *82*, 041920.
- [80] E. T. Herruzo, H. Asakawa, T. Fukuma, R. Garcia, “Three-dimensional quantitative force maps in liquid with 10 piconewton, angstrom and sub-minute resolutions”, *Nanoscale* **2013**, *5*, 2678–2685.
- [81] M. Kocun, A. Labuda, W. Meinhold, I. Revenko, R. Proksch, “Fast, High Resolution, and Wide Modulus Range Nanomechanical Mapping with Bimodal Tapping Mode”, *ACS Nano* **2017**, *11*, 10097–10105.
- [82] C. A. Amo, A. P. Perrino, A. F. Payam, R. Garcia, “Mapping Elastic Properties of Heterogeneous Materials in Liquid with Angstrom-Scale Resolution”, *ACS Nano* **2017**, *11*, 8650–8659.

- [83] Z. Al-Rekabi, S. Contera, “Multifrequency AFM reveals lipid membrane mechanical properties and the effect of cholesterol in modulating viscoelasticity”, *Proc. Natl. Acad. Sci.* **2018**, *In Press*, 1–6.
- [84] F. W. Stetter, T. Hugel, “The Nanomechanical Properties of Lipid Membranes are Significantly Influenced by the Presence of Ethanol”, *Biophys. J.* **2013**, *104*, 1049–1055.
- [85] F. W. Stetter, S.-H. Hyun, S. Brander, J. M. Urban, D. H. Thompson, T. Hugel, “Nanomechanical characterization of lipid bilayers with AFM-based methods”, *Polymer (Guildf)*. **2016**, *102*, 326–332.
- [86] M.-C. Giocondi, D. Yamamoto, E. Lesniewska, P.-E. Milhiet, T. Ando, C. Le Grimmelc, “Surface topography of membrane domains”, *Biochim. Biophys. Acta - Biomembr.* **2010**, *1798*, 703–718.
- [87] A. Alessandrini, P. Facci, “Phase transitions in supported lipid bilayers studied by AFM.”, *Soft Matter* **2014**, *10*, 7145–7164.
- [88] W. Trewby, D. Livesey, K. Voitchovsky, “Buffering agents modify the hydration landscape at charged interfaces”, *Soft Matter* **2016**, *12*, 2642–2651.
- [89] M.-P. Mingeot-Leclercq, M. Deleu, R. Brasseur, Y. F. Dufrêne, “Atomic force microscopy of supported lipid bilayers”, *Nat. Protoc.* **2008**, *3*, 1654–1659.
- [90] R. Richter, A. Mukhopadhyay, A. Brisson, “Pathways of lipid vesicle deposition on solid surfaces: a combined QCM-D and AFM study.”, *Biophys. J.* **2003**, *85*, 3035–47.
- [91] I. Reviakine, A. Brisson, “Formation of supported phospholipid bilayers from unilamellar vesicles investigated by atomic force microscopy”, *Langmuir* **2000**, *16*, 1806–1815.
- [92] Y. S. Lo, N. D. Huefner, W. S. Chan, P. Dryden, B. Hagenhoff, T. P. Beebe, “Organic and inorganic contamination on commercial AFM cantilevers”, *Langmuir* **1999**, *15*, 6522–6526.
- [93] J. Yoo, A. Aksimentiev, “New tricks for old dogs: improving the accuracy of biomolecular force fields by pair-specific corrections to non-bonded interactions”, *Phys. Chem. Chem. Phys.* **2018**, *20*, 8432–8449.
- [94] E. L. Wu, X. Cheng, S. Jo, H. Rui, K. C. Song, E. M. Dávila-Contreras, Y. Qi, J. Lee, V. Monje-Galvan, R. M. Venable, J. B. Klauda, W. Im, “CHARMM-GUI Membrane Builder toward realistic biological membrane simulations”, *J. Comput. Chem.* **2014**, *35*, 1997–2004.
- [95] W. Humphrey, A. Dalke, K. Schulten, “VMD: Visual molecular dynamics”, *J. Mol. Graph.* **1996**, *14*, 33–38.



## 6.0 SUMMARY AND CONCLUSIONS

This thesis has explored the complexity associated with ionic interactions between solid or soft surfaces, and how dynamic AFM allows a unique insight into these systems. While simple, one dimensional frameworks such as Gouy-Chapman theory and the Stern layer are relatively successful in describing the electric double layer, there is clear evidence that these models simply aren't sufficient to describe the wealth of complexity associated with ions' structure and dynamics at the molecular scale. In these cases, the local surface chemistry and hydration interactions can often result in counter-intuitive behaviour, such as attractive correlations between like-charged ions and charge inversion. AFM has emerged as an ideal tool to investigate such interfaces, with its sub-nanometre spatial resolution and ability to probe relatively long timescales; chapter 2 thus focussed on charting the evolution of AFM techniques, from its static beginnings to dynamic operation modes. The use of appropriate models allows for quantitative physical information about the interface to be recovered, including the stiffness and the energy dissipated by the tip as it oscillates. These, along with a greater understanding of the role anharmonic motion plays in imaging resolution, have allowed small-amplitude AM-AFM to provide maps of the hydration landscape of various systems, which plays a significant role in this thesis' work.

Chapter 3 demonstrated the AFM principles outlined above in two particular applications. The first investigated the aggregation and structuring of buffering agents at hydrophilic interfaces, which revealed a broad range of behaviours, from epitaxial arrangement to amorphous aggregation, depending on the charge and steric properties of the buffer in question. The particular organisation was further shown to be sensitive to the local concentration of alkali salts and to impact the response of biomimetic membranes, highlighting the interplay between dissolved species and interfacial groups. The second application took advantage of the cantilever's dynamic motion to interrogate the viscosity and density of its surrounding fluid. This was shown to be an accurate method for calibration (despite breaking down in severely non-Newtonian fluids) and has potential in the field of diagnostics as it could be used to probe the interaction between biological assemblies in solution.

The structuring of solutes at hydrophilic interfaces strongly implies damped kinetic behaviour in this region, and chapter 4 demonstrated two ways in which AFM can characterise the dynamic properties ions and water at interfaces. First, high-resolution AM-AFM was used to visualise the in-plane diffusion of single rubidium ions on mica. Despite its time resolution being orders of magnitude smaller than traditional methods for studying ionic dynamics, the technique demonstrated that the adsorbed charges evolved on the surface with one timescale of  $\tau_1 \sim 100$  ms and a second – related to the mica’s hydration – of  $\tau_2 \sim 600$  ms. These extended timescales are related to the large free energy of adsorption to mica, itself sensitive to the coordination of water around  $\text{Rb}^+$ . Shear force spectroscopy was also used to probe the dynamic properties and relaxation of nanoconfined “2D” fluids. At fixed frequencies of  $\nu_s = 1$  kHz, both water and solutions of KCl demonstrate velocity-dependent friction and viscoelastic behaviour, compatible with a 1D model that reflects mica’s crystal symmetry. The inclusion of potassium strongly reduces the measured friction through the ions’ tightly-bound hydration shells, although the lateral networks formed at the interface give an absolute lengthscale to their “fluidising” effect on the interfacial layer. When varying the frequency with a secondary actuator, it is seen that a straightforward dependence on velocity is not sufficient to describe our results, with different viscoelastic regimes, depending on shearing frequency, amplitude and confining chemistry. In general, higher shear frequencies lead to lower friction regimes that may reflect changes in the effective energy landscape.

Biological systems are reliant on specific ion and hydration interactions, and model DPPA lipid membranes were shown in chapter 5 to exhibit starkly different binding modes between alkali ions and their phosphate headgroups. High resolution AFM imaging was combined with spectroscopy, continuum electrophoretic experiments and MD simulations to demonstrate that ions interact *via* hydrating waters that result in attractive, correlative energies of  $\sim -0.4 k_B T$  that allow the formation of long-lived networks. These networks modulate the mechanical properties of the membrane on the scale of both single ions and the mesoscale networks, allowing for precise control of the bilayer’s physical properties that can control membrane protein function.

## 7.0 OUTLOOK AND FURTHER WORK

The ability of dynamic AFM to explore molecular-scale hydration effects at solid and soft interfaces has come of age over the last decade; the understanding of mechanisms underpinning high-resolution imaging and spectroscopy now allow AFM to be exploited (using commercial machines) on a staggering array of systems relevant for biology, geophysics and electrochemistry. Further, the improvement of driving mechanisms (particularly photothermal excitation) and modelling of higher cantilever eigenmodes has allowed the interrogation of physical properties – usually inaccessible at this level of lateral resolution – while simultaneously imaging with gentle forces, as demonstrated in chapter 5. There remain, however, outstanding questions that require detailed investigation of novel experimental systems by AFM before a well-rounded, physical picture of ions at aqueous interfaces can truly be said to be achieved. Below, we will discuss aspects of the results presented in this thesis that merit further investigation, as well as presenting potential experiments and some preliminary results that complement the exploration of ionic structure and kinetics at interfaces.

- Unifying model for friction and viscoelasticity of confined fluids

While the results presented in chapter 4 were broadly consistent with reduced 1D representations of interfacial friction, the diverse behaviour of  $F_L$  and  $\theta_s$  with both frequency and shear amplitude suggest that more involved models are needed to capture the physical complexity of the system. This will require probing different crystalline systems with a variety of lattice spacings and affinities for water, such as calcite or highly-ordered pyrolytic graphite. Further, fully characterising the transfer function of the cantilever (see e.g. Fig. 4.25) is necessary before the high shear frequency data can be meaningfully interpreted. This will demonstrate whether the functional exponential decay implied by Fig. 4.20(a) is valid for  $\nu_s \geq 20$  kHz. A valid understanding of the confined fluids' properties also requires a physical interpretation for the viscoelastic reversal implied by  $\theta_s$  smoothly passing through  $0^\circ$ ,  $\pm 90^\circ$  and  $\pm 180^\circ$ . Monitoring the direct time series of the cantilever oscillations may shed some light on this and therefore give more weight to our categorisation of the nanoconfined solution as being either solid-like or liquid-like. Other than this, MD simulations offer a window onto the dynamics of water and the ions, but

currently only with shear speeds greatly in excess of those accessible experimentally.

- Correlative effect of mono- and divalent ionic species

Chapter 5 presented a deep look into the interactions of three alkali ions with a model bilayer, investigated separately in order to see their individual behaviours. Biological fluids are never this pure, but teem with many charged species in solution at any one time; special significance is attributed to divalent ions such as calcium, which can often provide signalling functions even at low concentrations. However, the collective, molecular-scale interactions of mixtures of divalent and monovalent ions has, to our knowledge, not been fully characterised. Preliminary AFM images of mica in solutions of KCl and either magnesium or calcium (Fig. 7.1) show that the low concentrations of divalent ions perturb the Stern layer, either reducing the roughness ( $\text{Mg}^{2+}$ ) or forming linear clusters ( $\text{Ca}^{2+}$ ) that appear to be highly directional. As has been stressed throughout this thesis, the evolution of such structures would likely influence the dynamic behaviour of many biological systems and a full characterisation of the relevant timescales of these interfacial layers would be a necessary first-step.

- Dynamics of nanoconfined fluids at lipid headgroups

The results of chapter 4 focussed on the dynamic behaviour of water and ions confined between solid surfaces such that the dynamic behaviour probed was due solely to the interfacial fluid. In biological contexts, where the concept of hydration lubrication is frequently invoked, the interacting surfaces are often fluid, as in the case of e.g. lipid bilayers. Thus there are timescales associated with any shearing motion that correspond to the motion of the surface/headgroups and the lateral diffusion of individual lipid molecules as well as the confined solution. Shear force spectroscopy may not be able to single-handedly discriminate between these different modes, but the use of different bilayers (gel/fluid phase) and confining fluids could directly show how bilayers can mediate lateral shearing motion. Preliminary results on a mica-supported POPC bilayer (Fig. 7.2) show that at  $\nu_s = 1$  kHz, no frictional force is observed whatsoever, presumably due to the lipids' in-plane fluidity. In fact, for high loads,  $A_s$  decreases below the noise level, which may be a result of the lipids effectively damping the lateral oscillations. Probing the influence of varying  $\nu_s$  and tip size, among others, would shed valuable light on the dynamics of the lipids as well as their interaction with the aqueous phase.

- Effect of external electric fields

The substrates used throughout this thesis have all had permanent negative charges that preferentially attract cations and structure the interfacial water accordingly. While

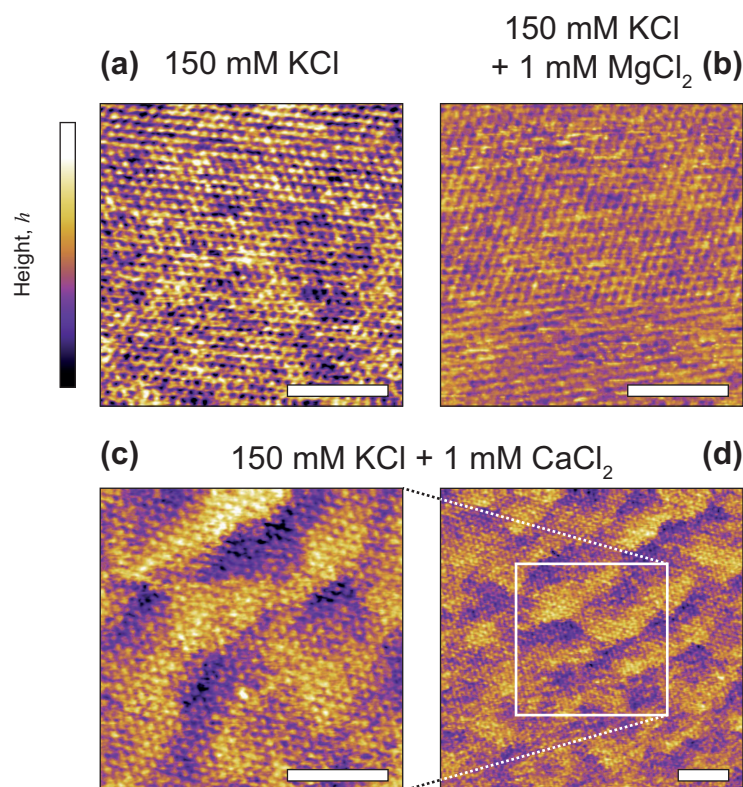


*Fig. 7.1:* High resolution AM-AFM topographs of mica in solutions of 150 mM KCl alone (a) and combined with small concentrations of MgCl<sub>2</sub> (b) and CaCl<sub>2</sub> (c),(d). In pure KCl, the interface is relative flat, agreeing with e.g. Fig. 4.11 and showing a well-defined Stern layer. The addition of magnesium results in a much smoother interface, perhaps because of the ion's high charge density that leads to a compact interfacial region. Calcium, in contrast, demonstrates a non-trivial, directional clustering with large height variations that is stable on larger scales (d). Length scale bars are all 5 nm and the height colour scale covers a range of 150 pm for all panels.

chapter 4 highlighted the difference between surfaces with large (mica) and small (SiO<sub>2</sub>) electric fields, a direct comparison between the two is confounded by their different chemistry. The ability to apply an external electric field that could be altered continuously while imaging with AFM would allow powerful insight into the energies involved in ion adsorption to different locations. Further, applying  $E$ -fields *parallel* to the sample plane would allow for 2D visualisation of biased ion diffusion in the Stern layer, augmenting the conclusions arrived at in section 4.1.

More generally, the recent commercialisation of specialised video-rate AFMs which allow the capture of 10 frames per second increase the available time resolution for tracking ions at the interface even further. Given the general disagreement outlined in chapters 1, 4 and 5 regarding the mobility of ions at interfaces, providing some overlap between “fast” techniques such as MD simulations and optical spectroscopies and “slow” scanning probe experiments is vital if these disputes are to be conclusively resolved.

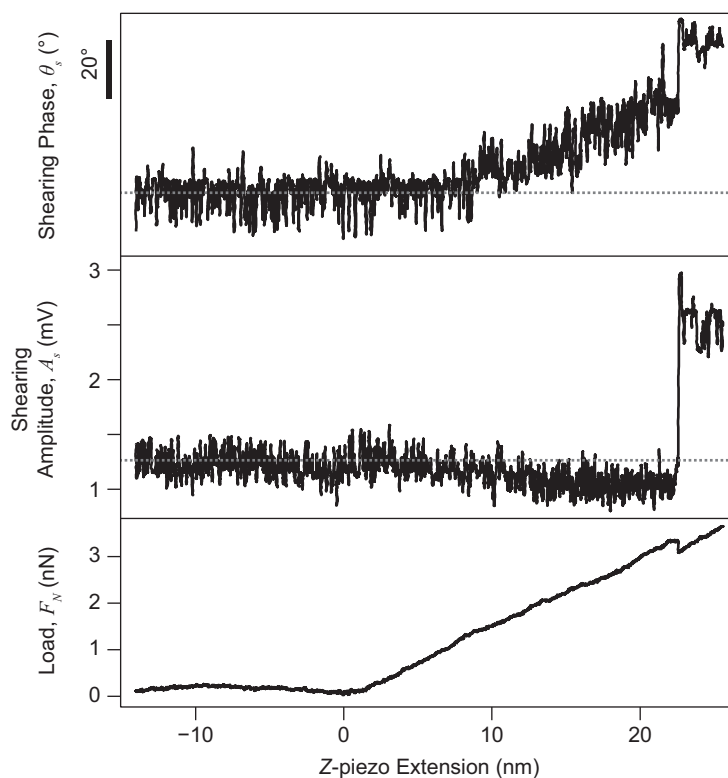


Fig. 7.2: Shear force spectroscopy of a fluid lipid bilayer composed of pure 1-palmitoyl-2-oleoyl-glycero-3-phosphocholine (POPC) using an RC800 PSA cantilever (Olympus, Japan). The shear frequency is  $\nu_s = 1$  kHz and amplitude is  $A_d = 5.0$  nm.  $A_s$  does not increase above the noise level (dashed line), even for finite loads, except when the cantilever breaks through the bilayer (step at  $F_N \sim 3$  nN). In fact, there is a small reduction for large loads, due to the lipids damping the tip's motion. The phase linearly increases upon contact ( $z = 0$ ), indicating a smooth change in the energy dissipated by the tip. Spectroscopy conducted in 150 mM NaCl solution, buffered by 10 mM Tris to pH 7.0.